12-14-2023

Catalyst-Free Epitaxy of Core-Shell Nanowire Arrays for Wavelength-Selective and Substrate-Free Optoelectronic Devices

Alireza Abrand

RIT

Catalyst-Free Epitaxy of Core-Shell Nanowire Arrays for Wavelength-Selective and Substrate-Free Optoelectronic Devices

by

Alireza Abrand

A dissertation submitted in partial fulfillment of the requirements for the degree of

Doctorate of Philosophy in Microsystems Engineering

Microsystems Engineering

Kate Gleason College of Engineering

Rochester Institute of Technology

Rochester, NY

December 14, 2023

Catalyst-Free Epitaxy of Core-Shell Nanowire Arrays for Wavelength-Selective and Substrate-Free Optoelectronic Devices

by

Alireza Abrand

Committee Approval:

We, the undersigned committee members, certify that we have advised and/or supervised the candidate on the work described in this dissertation. We further certify that we have reviewed the dissertation manuscript and approve it in partial fulfillment of the requirements of the degree of Doctor of Philosophy in Microsystems Engineering.

Dr. Parsian Katal Mohseni — Date:
Associate Professor, Electrical and Microelectronic Engineering

---

Dr. Stefan F. Preble — Date:
Professor, Electrical and Microelectronic Engineering

Dr. Seth M. Hubbard — Date:
Professor, Physics

Dr. Karl Hirschman — Date:
Professor, Electrical and Microelectronic Engineering

Certified by:

Dr. Stefan F. Preble — Date:
Director, Microsystems Engineering Program

Abstract

Kate Gleason College of Engineering

Rochester Institute of Technology

Degree: Doctor of Philosophy

Program: Microsystems Engineering

Author's Name: Alireza Abrand

Advisor's Name: Parsian K. Mohseni, Ph.D.

Dissertation Title: Catalyst-Free Epitaxy of Core-Shell Nanowire Arrays for Wavelength-Selective and Substrate-Free Optoelectronic Devices

This research is dedicated to advancing catalyst-free epitaxial growth methods for indium arsenide-based nanowires (NWs) on foreign substrates, including silicon and two-dimensional (2D) materials. The findings presented here demonstrate new methods for low-cost III-V semiconductor NW synthesis, manipulation of NW optical properties, and advanced techniques for modulation of NW geometry and composition during selective-area epitaxy (SAE).

The first part of this work explores the growth of InAs NWs with sub-lithographic dimensions on reusable Si (111), toward NW membrane-based optoelectronic devices such as infrared photodetectors (IR PDs). A SiO_2 masking template is first patterned using *i*-line photolithography, yielding hexagonal arrays of nanopores. InAs NW arrays are then grown through a novel localized self-assembly (LSA) method using metalorganic chemical vapor deposition (MOCVD). The yield of NWs is optimized through the introduction of a two-step flowrate-modulated growth technique. The NW arrays are embedded in a polymer membrane, delaminated, and transferred to carrier substrates. The process achieves ~100%

transfer yields, fully preserving NW position and orientation during transfer. The starting SiO_2-templated Si (111) substrates are then reused for LSA growth of subsequent NW generations, demonstrating reproducible global yields of >85% over wafer-scale areas. This substrate recycling approach aims to reduce the manufacturing costs of III-V NW-based membranes for large-area, flexible, and wearable optoelectronic devices.

Next, the influence of an integrated backside reflector on the optical properties of NW-based membranes is investigated. Simulations performed using the rigorous coupled-wave analysis (RCWA) technique are employed to demonstrate significant tunability of the IR absorption spectra of coaxially heterostructured NW arrays, where InAs core segments are partially encapsulated by $GaAs_{0.1}Sb_{0.9}$ shell layers. The integration of Au backside contact layers creates periodic evanescent fields between adjacent NWs, dependent on the NW core segment diameter and incident light wavelength. By introducing partial $GaAs_{0.1}Sb_{0.9}$ shell layers with dimensions aligned to the evanescent field, selective absorption of otherwise decoupled light in the 2 to 3 μm range is realized within the InAs NW core segments. This site-specific absorption, which can be engineered as a function of the NW shell segment geometry, offers new opportunities for the development of tunable IR photodetector device structures.

Lastly, we introduce a method to locally modulate the effective precursor flowrates during SAE growth by MOCVD in order to manipulate NW dimensions and compositions. Our findings demonstrate a significant growth rate modulation effect, resulting in an eight-fold volumetric enhancement ratio compared to control samples. This technique allows for the fabrication of III-V NWs with adjustable geometries on the same substrate, using only a single nanopore masking pattern. Furthermore, by leveraging the growth rate

enhancement effect, we demonstrate the ability to alter the composition of adjacent $Al_xIn_{(1-x)}As$ NW arrays within the $0.11 \leq x \leq 0.54$ range during a single SAE run. This provides new approaches for the growth and fabrication of NW-based optoelectronic devices, particularly beneficial for multispectral photodetector applications.

Acknowledgment

I express my deepest gratitude to my advisor, Dr. Parsian K. Mohseni, for his unwavering commitment, guidance, and encouragement throughout my doctoral studies. His support, granting me the freedom to explore uncharted territories, and insightful advice have been indispensable in shaping my academic journey. A special thanks to my doctoral thesis committee members, Dr. Stefan F. Preble, Dr. Seth M. Hubbard, and Dr. Karl D. Hirschman, for their constructive feedback and meaningful contributions to my research. I extend my appreciation to Dr. Stephen Polly for his essential guidance on MOCVD equipment and invaluable research advice. I am truly grateful to Dr. Nicklas Anttu for his collaboration and supporting me with his invaluable feedback on optical simulation. I sincerely appreciate the support and assistance of my colleagues at NPRL, SMFL, and the Microsystems Engineering program during my Ph.D. journey. Their help with my research, advice on problem-solving, and enjoyable moments have been invaluable to me. This includes Dr. Mohadeseh Baboli, Dr. Anastasiia Fedorenko, Dr. Thomas S. Wilhelm, Venkatesh Deenadayalan, Sami Znati, Ross Hisert, Salwan Omar and Anthony Mazur for their interesting collaborations and support. I want to acknowledge and thank the SMFL staff, including Thomas Grimsley, Patricia Meller, Sean O'Brien, Bruce Tolleson, John Nash, and Richard Battaglia for their consistent assistance and guidance throughout my experience in the cleanroom. On a personal note, I express my sincere thanks to my family, especially my parents. Their immense care and support leave me truly indebted. I also appreciate my closest friends who have been my pillars of strength, with special gratitude to Dr. Navid Safari for keeping me motivated. I acknowledge the Microsystems

Engineering Ph.D. Program and the National Science Foundation (NSF) for their crucial financial support, which has played a pivotal role in the success of this research

Dedicated to my parents, Soraya and Mohammad, with heartfelt gratitude.

Table of Contents

List of Figures

List of Tables

Chapter I

1 Introduction and Background

Nanotechnology has ushered in a revolutionary approach to research, empowering the precise design of materials at the atomic level to attain specific properties. Within this realm, the nanowire (NW) field has emerged as a highly dynamic area of exploration in nanoscience and nanotechnology, distinguished by their unique optical and electrical properties. Notably, semiconductor NWs present a promising avenue for the semiconductor industry, offering opportunities for novel device architectures and improved performance capabilities. This chapter provides an essential background on semiconductor NWs, focusing on the growth of III-V compound semiconductor NWs and their applications in light absorption-based technologies. Section 1.1 covers the general benefits of III-V semiconductor compounds, while Section 1.2 delves into specific advantages of III-V semiconductor NWs. Section 1.3 discusses the synthesis method, and the key advantages for absorption-based applications; specifically, light absorption (Section 1.4) and carrier collection (Section 1.5) are addressed. In Section 1.6, we review the recent developments in NW-based photodetectors as an example of the wider class of optoelectronics devices, and Section 1.7 offers a brief chapter overview in this dissertation.

1.1 III-V Compound Semiconductors

It is not an overstatement to assert that the progression of information technology owes much to the indispensable role played by semiconductor materials. Virtually all the electronic devices that have become integral to our daily lives, such as computers and cell phones, incorporate semiconductor components.

Solid-state materials, distinguished by their capacity to conduct electrical current, are broadly categorized into three groups: conductors, semiconductors, and insulators. According to band theory, conductors are those materials that conduct electricity using mobile electrons due to overlapping valence and conduction bands, which results in many free electrons in the equilibrium state. Electrons can flow through the material with minimal applied voltage. In contrast, insulators have large band gaps, typically exceeding 5 eV between their valence and conduction band edges, and they possess no free electrons for conduction [1].

Semiconductors materials have small bandgap less than 5 eV as shown in Figure 1.1. At a temperature of 0 K for semiconductors, all of the states in the valence band are fully occupied, indicating that electrons have filled all available positions in this band. Consequently, there are no free electrons in the conduction band, resulting in the absence of a net current. Under these conditions, semiconductors exhibit insulator-like behavior at low temperatures [1]. By introducing additional energy, such as thermal energy or incident photons, to semiconductor materials, electrons can be excited from the valence band to the conduction band. In the conduction band, these electrons gain the freedom to move, contributing to the generation of electrical current. As a result, these materials can exhibit

a behavior more akin to conductors. The conductivity of these semiconductors can be deliberately manipulated through various parameters, including the introduction of impurity atoms, adjustment of the bandgap, control of temperature, and exposure to illumination. This ability to modulate conductivity makes semiconductors highly versatile and forms the foundation for their extensive applications in electronic devices. [1].

Semiconductor materials exhibit diverse electrical and optical properties, and the tuning of these properties for specific applications is achievable through the alloying of multiple compounds. A notable class of semiconductor alloys is represented by the III-V compounds, which incorporate elements from group-III and group-V in the periodic table. This strategic combination of elements allows for precise adjustments in the material characteristics, facilitating tailoring to meet the requirements of various applications.

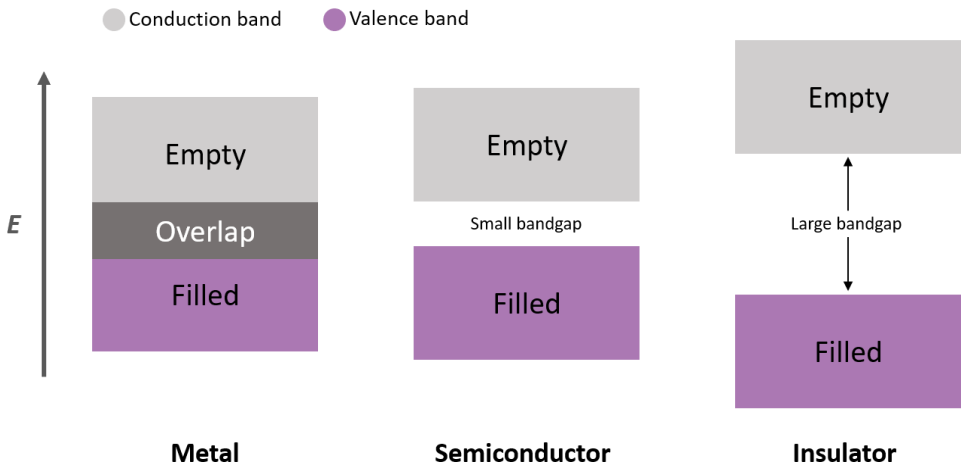

Figure 1.1. *Band structures of different materials: conductors, semiconductors, and insulator.*

III-V compounds emerge as promising materials for optoelectronic applications, due to their high carrier mobilities, extended carrier diffusion lengths, and favorable absorption coefficients. Additionally, their capability for bandgap engineering enhances their adaptability [2]. Through a flexible combination of III-V compounds, ranging from binary to quaternary alloys, it is possible to synthesize materials with bandgaps spanning from the ultraviolet (UV) to infrared (IR) ranges of the electromagnetic spectrum, as illustrated in Figure 1.2 [3], [4]. This diverse range of bandgaps renders these materials highly promising for a wide range of optoelectronic applications, including but not limited to photodetectors (PDs), photovoltaic (PV) solar cells, light-emitting diodes (LEDs), and lasers. The adaptability of III-V compounds positions them as key contenders for advancing technologies in these crucial areas.

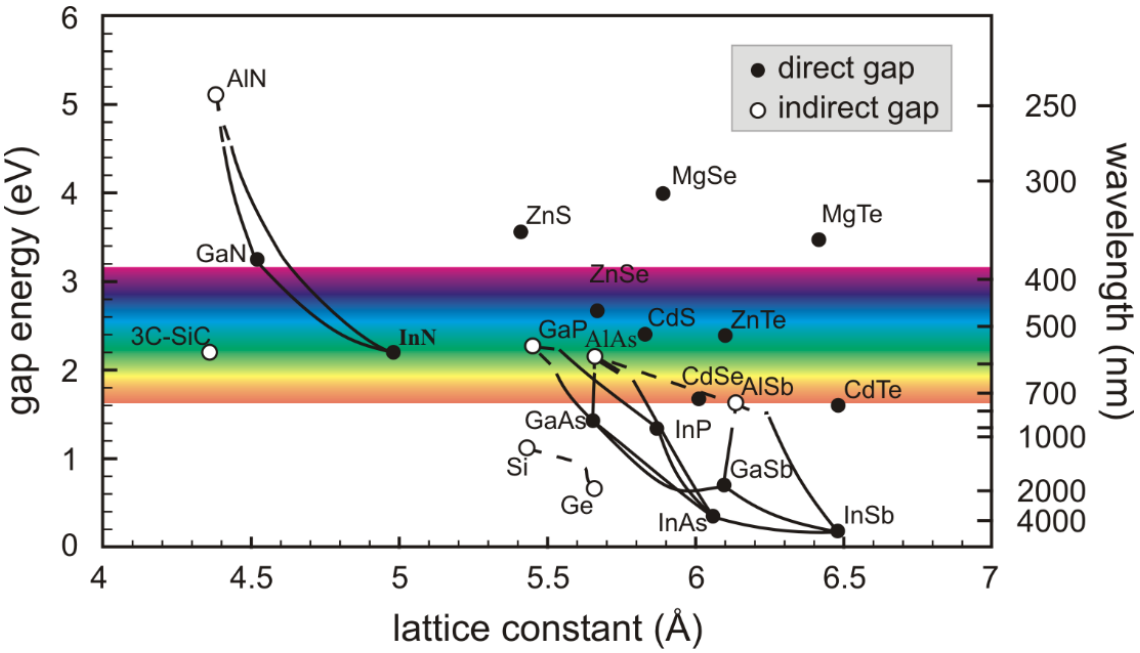

Figure 1.2. *Energy bandgap as a function of lattice constant of common semiconductors compounds. Adopted from Ref. [3].*

Given the demand for absorption-based applications such as PDs and PVs, this dissertation places its focus on the growth, optical design, and fabrication of innovative III-V NW systems that are promising for optoelectronic applications. More specifically, this dissertation aims to enable novel NW properties for PD applications. Moreover, the nanostructures presented here can be directly integrated with mainstream silicon technologies, ensuring compatibility with large-scale manufacturing methods and meeting a key requirement for III-V optoelectronic applications.

1.2 III-V Semiconductor Nanowires

Semiconductor NWs have received great research interest in the past two decades due to their great potential as next-generation materials for electronic and optoelectronic applications [5]–[7]. Nanowires are quasi one-dimensional (1D) nanostructures with diameters typically on the order of tens to hundreds nanometers and lengths on the order of a few microns [8]. In comparison to thin-films, NWs offer an additional dimension for strain relaxation along their sidewalls. Due to their large surface area-to-volume ratio and small footprint, NWs allow for more effective strain relaxation, particularly in the growth of heterostructures along the axial direction [9], [10]. The strain relaxation leads to an enhancement of the critical thickness criterion. It has been demonstrated that for diameters less than 45 nm, misfit dislocation-free InAs NWs, up to 450 nm in length, can be achieved on Si substrates, despite the 11.6% lattice mismatch, as illustrated in Figure 1.3 [11].

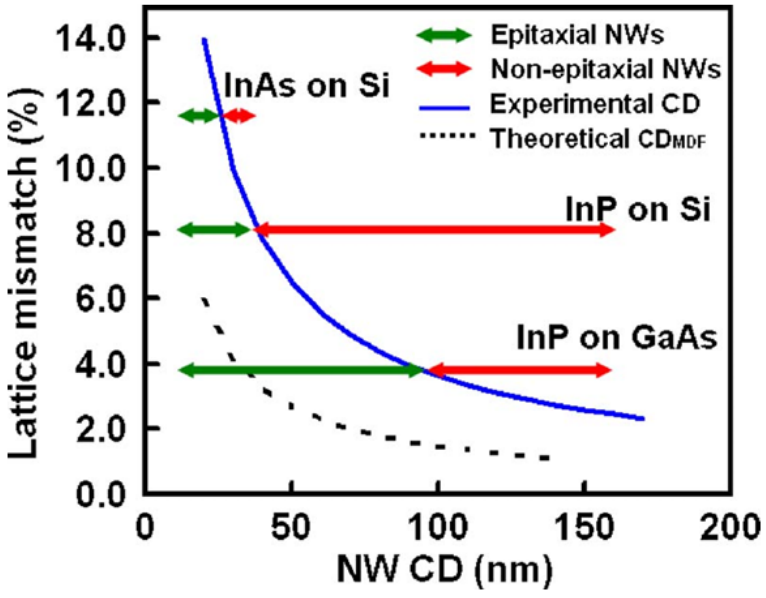

Figure 1.3. *Experimental critical diameter (CD) of NW compared to their corresponding theoretical CD as a function of lattice mismatch. Adopted from Ref. [11].*

The ability to fabricate defect-free nanostructures, particularly in scenarios of significant lattice mismatch, holds great promise for the monolithic integration of III-V semiconductor compounds with already mature and dominant silicon-based platforms. This capability opens novel prospects for advanced optoelectronic applications, bridging the technological strengths of III-V semiconductors with the well-established infrastructure of silicon-based platforms [12], [13]. This integration promises to pave the way for enhanced performance and expanded functionalities in optoelectronic devices, offering exciting avenues for innovation in the field. Furthermore, the exploitation of novel sub-wavelength optical phenomena, coupled with their small dimensions, quasi one-dimensional structure, and high surface area-to-volume ratio of NWs, positions them as strong candidates for a wide range of applications across diverse scientific and technological domains [14], [15].

Semiconductor NWs exhibit remarkable sensitivity to light, particularly in photoconductivity, making them promising for diverse applications like PDs, optical switches, and biological sensors [16], [17]. NW photoconductors maintain heightened light sensitivity beyond the quantum confinement size-regime, thanks to their large surface area-to-volume ratio and small dimensions. Considerable efforts have been dedicated to developing PDs using III–V NWs, driven by their high sensitivity and quantum efficiency. The distinct energy band gaps of III–V NWs enable PDs that can cover a range of detectable wavelengths. The inherent characteristics of III–V NWs result in higher light sensitivity compared to their bulk counterparts [18], [19]. NW-based PDs will be discussed in detail in Section 1.6.

Conventional thin film Si–based PVs, with thicknesses below 5 μm and utilizing cost-effective substrates like glass and metal foil, aim to reduce cell manufacturing costs; however, they face challenges related to light absorption and power conversion efficiency enhancement through surface treatments. In contrast, III-V-based PVs, surpassing the Shockley–Queisser efficiency limit (~32%), employ multiple *p-n* junctions for more efficient use of the solar spectrum [20], [21]. Despite their efficiency, III-V multi-junction solar cells are mainly used in space applications due to high costs and growth complexities arising from lattice mismatch. In this context, NWs have garnered interest for next-generation PVs due to strong light absorption and efficient carrier collection, making them promising for high-efficiency devices while also reducing the volume of rare materials used, such as indium-phosphide (InP) and gallium-arsenide (GaAs) [6], [22], [23].

Lighting and displays represent a substantial portion of our energy consumption. Contemporary semiconductor-based LEDs already showcase heightened efficiency and extended lifetimes [24]. The integration of NW technologies has the potential to further enhance efficiency, reduce material consumption, and enable precise tuning of material properties. NWs boost the light extraction efficiencies of LEDs and they can be synthesized with minimal structural defects, even when grown on foreign substrates [25]–[27]. This nanomaterials approach proves particularly advantageous for applications demanding ultra-bright and high-resolution displays, contributing significantly to progress in lighting and display technologies.

1.3 Nanowire Synthesis

Generally, NWs can be synthesized through two main approaches: top-down fabrication and bottom-up growth. In top-down methods, NWs are formed by etching bulk materials, like carving a statue from a block of stone [28]. Common techniques employed in this method include wet chemical etching and dry etching. However, this approach often overlooks one of the key advantages of NWs, their capability for heteroepitaxial growth across a broad range of material compositions. Additionally, fabricating small-diameter NWs via top-down methods, especially those with diameters less than 10 nm, faces challenges due to limitations in lithography and etching resolution [29].

In bottom-up methods, NWs can be epitaxially grown, favoring axial growth along the ⟨111⟩ direction of the crystal lattice rather than lateral growth, which can be further exaggerated through the modification of growth conditions. Precursors, most commonly in the vapor phase, are assembled layer-by-layer to form NWs, analogous to growing a plant from a seed. In contrast to top-down methods, the bottom-up approach enables the key aforementioned NW advantages to be realized and allows for controlled synthesis of a greater variety of material compositions and smaller geometries. The bottom-up method can be categorized into two main modes: catalytic growth and catalyst-free growth, which will be discussed in more detail in the subsequent sections. In these techniques, NWs synthesis is typically carried out in a vacuum reactor at elevated temperatures, which can be varied based on the materials and growth mechanism employed. In both cases, growth is initiated and ended by introducing and terminating the flow of desired gas-phase precursors into the reactor, respectively [15].

1.3.1 Catalytic Growth

In the catalytic growth mode, liquid-phase nanoparticles are required, which act both as a reactive catalyst and adatom sink. This growth mode is known as the vapor-liquid-solid (VLS) mechanism [30], [31]. Growth species in the vapor phase are absorbed by nanoparticle catalysts in the liquid phase. Once the nanoparticle becomes supersaturated, NW synthesis will be initiated by material precipitation, as depicted in Figure 1.4 [32]. Therefore, the position and diameter of NWs is related to the position and diameter of the catalyst. High growth rates, good control over NWs growth direction, and crystal structure engineering for either wurtzite or zinc-blende phases can be achieved through this mode [32], [33]. The catalyst can be either randomly distributed on the substrate or ordered in periodic arrays through lithographic patterning.

The catalytic growth mode can be sub-divided into foreign catalyzed and self-catalyzed growth approached. Gold (Au) is the most common foreign catalyst nanoparticle since it has a low melting point and, therefore, can form low-temperature liquid alloys with many desired materials. In addition, Au is resistive to oxidization, relatively inert, does not react with precursor carrier gases (e.g., nitrogen and hydrogen), and has good stability against changes in growth conditions [30], [33]. However, Au is not a desired element in some research areas, for instance in CMOS technologies due to introducing mid-gap traps and contaminating fabrication tools [34]. In addition, Au must be removed prior to shell growth since it permits continual VLS-based axial growth while sidewall or shell growth proceeds. Removing Au can introduce extra cost and contamination to NWs [35].

This problem can be eliminated by the self-catalyzed growth mode. For example, for III-V NW self-catalyzed growth, group-III elements are used as a nanoparticle catalyst due to

their low melting point and higher desorption temperature compared to group-V elements. In this mode, no contaminations will be introduced into the NWs via the catalyst droplet. Additionally, there will be no need to remove the catalyst droplet for shell growth, since the group-III catalyst can be consumed by only introducing group-V precursors into the reactor after NW growth termination [15], [29]. Both methods of catalytic NW growth suffer from graded junctions due to the reservoir effect of the catalyst droplet, unlike the catalyst-free growth mode [29].

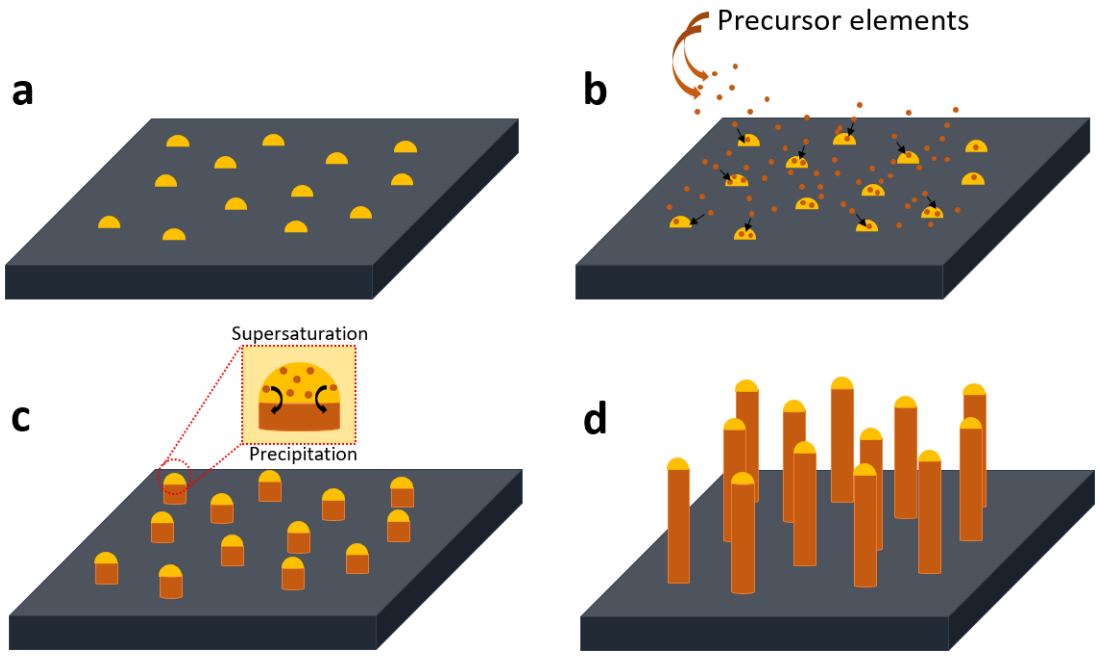

Figure 1.4. *Schematic representation of the VLS growth mode. (a) The bare substrate is decorated with Au particles that can be either patterned or randomly positioned; (b) Au particles capture gas-phase precursor species; (c) the alloyed particles become supersaturated leading to nucleation at the particle/substrate interface; and (d) NW growth occurs at the location of Au particles.*

1.3.2 Catalyst-Free Growth

In this growth mode, the substrate must be patterned by a masking template for growth of periodically positioned NWs that make up an array. A thin layer of amorphous dielectric material (such as SiO_2 or SiN_X) is deposited on the growth substrate, then patterned via lithography and etched (usually dry etching) through the masking dielectric to define pores with desired diameters, pitch, and geometry. This growth mode is referred to as selective-area epitaxy (SAE) [36], [37]. Adatoms can be introduced via different techniques, such as molecular-beam epitaxy (MBE), metalorganic vapor phase epitaxy (MOVPE), or chemical beam epitaxy (CBE). Due to the low sticking coefficient of adatoms on the masking film, growth species have longer diffusion lengths on the dielectric surface and can migrate until they reach the pores, where they nucleate and eventually form NW structures, as depicted in Figure 1.5 [36], [38]. In SAE growth, the density, position, and geometry of the NWs can be precisely controlled by density, position, and geometry of the pores, respectively. High crystal quality NWs, high NW uniformity and high growth yield can be achieved through this mode [39]. In addition, the SAE mode has the advantages of achieving abrupt junctions in axial or core-shell geometries compared to the catalytic growth mode since this mode operates according to a purely vapor-solid (VS) mechanism and gas-phases precursors directly contribute to the growth from vapor to solid phases [29].

The main disadvantage of this method is the substrate preparation, which includes mask deposition and mask pattering, most commonly via electron-beam lithography or nanoimprint lithography. It is not only costly and time consuming, but also any imprecision in the preparation procedure can undesirably affect the growth. The catalyst-free mode may

also be performed without the use of a masking layer for some specific material combinations (e.g., InAs NWs on Si substrates). This approach is known as the self-assembly (SA) growth mode [15]. In this case, the NWs are grown randomly on the substrate. The density and geometry of the NWs in SA growth can be controlled by growth conditions, but not nearly as precisely as in the case of SAE growth. In both catalyst-free methods, the native oxide of the substrate must be removed, which can be done using a common buffered oxide etch (BOE) procedure and high temperature baking before growth initiation. We will expand on this point in the context of experimental work on the localized self-assembly (LSA) growth mechanism, discussed in Chapter 3, and on the SAE research presented in Chapter 5.

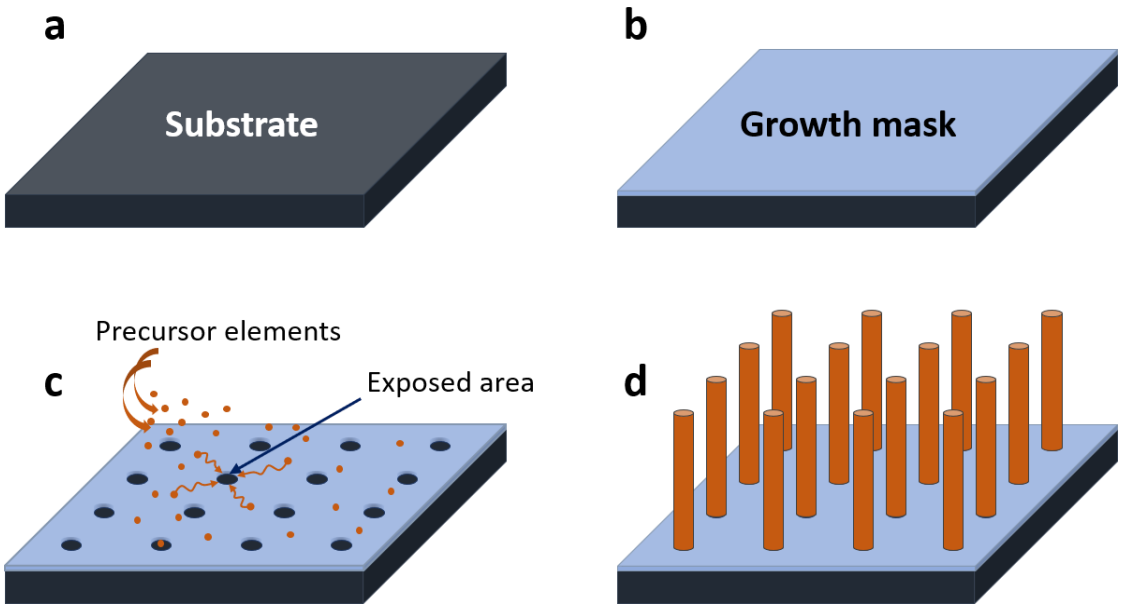

Figure 1.5. *Schematic representation of the SAE growth mode. (a) Bare substrate; (b) deposition of a masking dielectric film, most commonly SiO_2; (c) Nanopores are patterned through sequential lithography and dry etching, which serve as the sites for the collection of adatoms; (d) nucleation and vertical NW growth occurs at the location of nanopores.*

1.4 Light Absorption in NW Arrays

Light absorption is the first and most important step for optoelectronic devices such as PV solar cells and photodetectors. Efficient absorption is critical to photo-generation of charge carriers. Two primary types of absorption losses, namely reflection and transmission, play significant roles and degrade device performance. To mitigate these losses, common methods include the application of anti-reflection coatings, achieved through the deposition of a dielectric film on the device surface, and light-trapping techniques involving the texturing of both front and rear surfaces [40], [41]. As mentioned, NWs are promising type of materials for optoelectronic devices due to their strong light absorption capabilities compared to thin films of equivalent volume. This is mainly due to the extreme light trapping, high scattering, and inherent anti-reflection properties of the NWs [23], [42]–[44]. Garnett et al. demonstrated that etched Si NWs on 7.5 μm thick Si windows, with diameters of 390 nm and lengths of 2 μm and 5 μm, exhibit significantly reduced light transmission, especially for wavelengths exceeding 600 nm, when compared to a 7.5 μm thick Si thin-film window. This is illustrated in the wave-optics model shown in Figure 1.6(a) [23], [45]. Light can be coupled into NWs due to differences in the refractive index of NWs and their surrounded medium (i.e., waveguiding effect), which results in light absorption from a larger area than the physical cross-section of vertical NWs, as shown in Figure 1.6(b) [46].

Theoretical studies on optical properties of vertical NWs have demonstrated strong light absorption specifically in periodical NW arrays due to scattering, resonance and diffraction effects, which result in an increase of the optical path length; this results in

greater carrier generation and consequently improve device performance [7], [8], [47], [14].

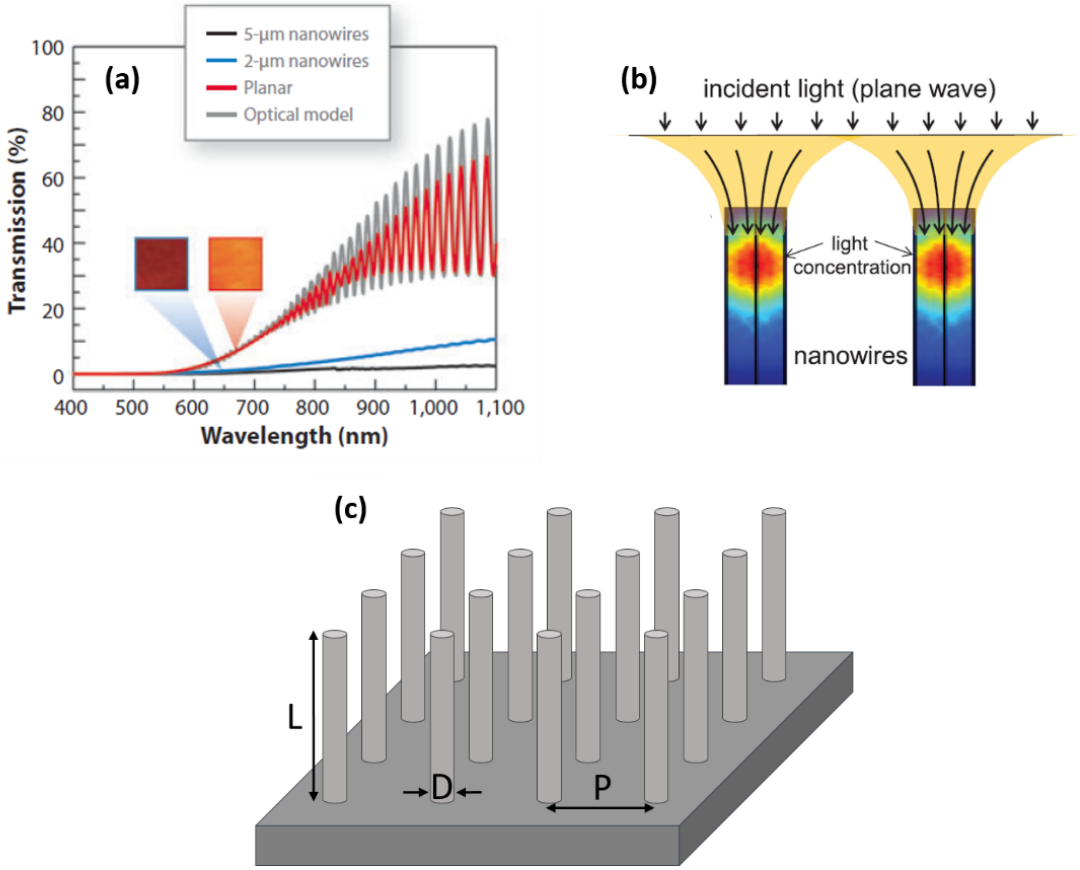

Figure 1.6. *(a) Transmission spectra for Si NW arrays with lengths of 2 μm (blue) and 5 μm (black) compared to a 7.5 μm-thick Si film. (b) Cross-section of simulated light absorption profile into the NW. (c) Geometrical properties of length (L), diameter (D), and pitch (P) of nanowire arrays. (a) and (b) are adopted from Ref. [23] and [46], respectively.*

In Figure 1.6(c), various parameters of periodic NW arrays, such as diameter (*D*), length (*L*), and pitch (*P*), are illustrated. The optical characteristics of these arrays are significantly influenced by these geometric parameters. Notably, absorption does not exhibit strong dependence on the array type, as similar absorption is observed in both square and hexagonal arrays, provided the nanowire density remains consistent across both configurations [48]. Nanowire arrays have attracted substantial theoretical attention,

revealing that, through judicious geometric selections, the nanowires can efficiently absorb incident light [47].

In NW arrays, light absorption is limited by reflection losses from top facet of NWs, which depends on D and P. This reflection loss decreases with a smaller D/P ratio, especially for broadband responses like the solar spectrum. To enhance light absorption, reducing the D/P ratio is desirable, as seen in sparse nanowire arrays achieving effective broadband light coupling [49]. However, decreasing the D/P ratio also reduces the amount of absorbing semiconductor material. Consequently, the optimal D/P ratio for absorption depends also on the length of NWs, with a larger L enabling a smaller D/P ratio, for optimized light absorption [14].

The NW diameter significantly influences the optical response. In the regime where D is much larger than the incident wavelength ($D >> \lambda$), geometrical optics apply, treating light as rays. For normally incident light, absorption is constrained by the NW area coverage (density $\times \pi D^2/4$) [50]. Conversely, when D is much smaller than the wavelength ($D << \lambda$), an electrostatic description reveals weaker absorption due to electrostatic screening, compared to a planar semiconductor layer. In the intermediate regime where D is comparable to the wavelength ($D \approx \lambda$), NWs function as optical waveguides with electromagnetic waveguide modes [51]. These modes depend on D but are less affected by P, unless in a very dense array where NW-to-NW coupling may influence mode dispersion. Waveguide modes distinctly occur, particularly when L exceeds half the wavelength ($L > \lambda/2$) [52]. For normally incident light, the HE_{1m} waveguide modes exhibit the strongest response in NW arrays. These HE_{nm} modes are hybrid modes, featuring non-zero longitudinal components of both the magnetic (H) and electric (E) fields. The azimuthal

dependence is denoted by *n*, while *m* indicates the radial dependence [51]. Based on the NW *D,* each HE_{1m} corresponds to a distinct wavelength-selective absorption peak. This behavior was initially observed for the HE_{11} mode in Si NW arrays [53]. As *D* increases, the waveguide mode becomes increasingly bound to the nanowire, resulting in enhanced absorption of the coupled light. However, this enhanced binding also reduces the overlap of the waveguide mode with the incident plane wave, resulting in less light coupling into the mode [54], [55]. Consequently, an absorption peak occurs for an intermediate value of *D*, driven by these opposing dependencies.

Nanowire array geometries must be optimized to obtain the highest light absorption while utilizing the minimum material volume. It has been demonstrated experimentally that InP periodic NW arrays with 2000 nm length and approximately 220 nm diameters with 400 nm pitch can absorb 94% of the incident light over the 400 to 900 nm wavelength range [56]. For PD device applications, the filling ratio of a NW array can impact the photogenerated current due to absorption. Increasing the filling ratio would also increase the reflection loss, whereas reducing the filing ratio increases transmission loss, especially at longer wavelengths [57]. This concept is relevant to the simulation-based research presented in this dissertation and will be discussed in greater detail in Chapter 4.

Another optical phenomenon arising from the interaction of incident electromagnetic waves with NW arrays is the occurrence of Fabry-Perot (F-P) modes. These modes result from reflections at the tips and bases of the NWs, leading to the formation of axial or longitudinal standing wave solutions through constructive interference of the guided wave [58]. These F-P modes manifest as localized peaks in the electric field amplitude along the axis of the NWs. It is worth reviewing the basic principles

of F-P based interference, as in Chapter 4 we will observe a phenomenon based on these principles.

The Fabry-Perot interferometer generates distinct interference peaks by leveraging the principles of multiple-beam interference. The measure of resonance sharpness, also known as the quality of the cavity, Q, can be defined as follows:

$$Q = \frac{v_0}{\Delta v_{1/2}} \tag{1.1}$$

where v_0 and $\Delta v_{1/2}$ are is the resonant frequency of the cavity and the corresponding full-width at half-maximum (FWHM), respectively. The cavity parameters can be written as:

$$v_0 = \frac{c}{\lambda_0} \tag{1.2.a}$$

$$\Delta v_{1/2} = \frac{c}{2\pi nd} \frac{1 - (R_1 R_2)^{1/2}}{\pi (R_1 R_2)^{1/4}} \tag{1.2.b}$$

where c is the speed of the light, n is the cavity medium refraction index, d is the length of cavity, R_1, R_2 are power reflectivity of cavity mirrors, and λ_0 the incident beam wavelength. Therefore, substituting Eq. 1.2.a and 1.2.b in Eq. 1.1 results in:

$$Q = \frac{2\pi nd}{\lambda_0} \frac{(R_1 R_2)^{1/4}}{1 - (R_1 R_2)^{1/2}} \tag{1.3}$$

Based on Eq. 1.2.b, the FWHM ($\Delta v_{1/2}$) decreases as the d and ($R_1 \times R_2$) increase [59].

1.5 Carrier Collection in NWs

Upon absorption of light, semiconductor materials undergo a process that generates carriers. The subsequent collection of photogenerated carriers then dictates many important device performance metrics, such as external quantum efficiency, responsivity, and detectivity in the case of photodetectors, as one example (discussed further in Section 1.6.4). In this context, the design and geometry of the material become crucial factors.

Semiconductor NWs emerge as a promising material system for efficient carrier collection, mainly due to the advantageous properties associated with their nanoscale geometry and tunable architectures. One notable advantage is the shorter diffusion length before recombination [18], [43]. The intrinsic small geometry of NWs enhances the probability of carriers reaching the collection electrode before recombination occurs. Additionally, the high mobility achievable in high-quality, defect-free single crystal NWs further contributes to their efficacy [30], [60]. These properties are particularly advantageous for applications where rapid and effective carrier collection is paramount, such as in PVs or PDs devices.

The unique characteristics of NWs not only contribute to enhanced carrier collection efficiency but also underscore the importance of tailoring nanostructure geometries for specific applications. The influence of the dimensions of individual NWs, the geometry of their core and shell segments, and their periodicity in an array become increasingly important as we delve deeper into optimizing the performance of absorption-based devices; they will be discussed in greater detail in Section 1.6 and they will critical to the research results presented in Chapters 4 and 5.

Generally, NWs can be designed with three different junction geometries: substrate junction, axial junction, and radial junction, as illustrated in Figure 1.7 [8], [43], [61]. In the substrate junction design, the NW and substrate would be doped differently, and the active region would be formed in both the NW and substrate. In axial junctions, *p*- and *n*-type segments would be grown on top of each other. So, the active region would be formed between the vertically aligned *p*- and *n*-type segments. In both configurations, not all of the advantages of NW structures, specifically light absorption and carrier collection, would be fully used. Principally, radial junction NWs (i.e., the so-called *core-shell* structures) are more promising for both PD and PV applications due to the orthogonalization of light absorption and carrier separation directions [62], [63].

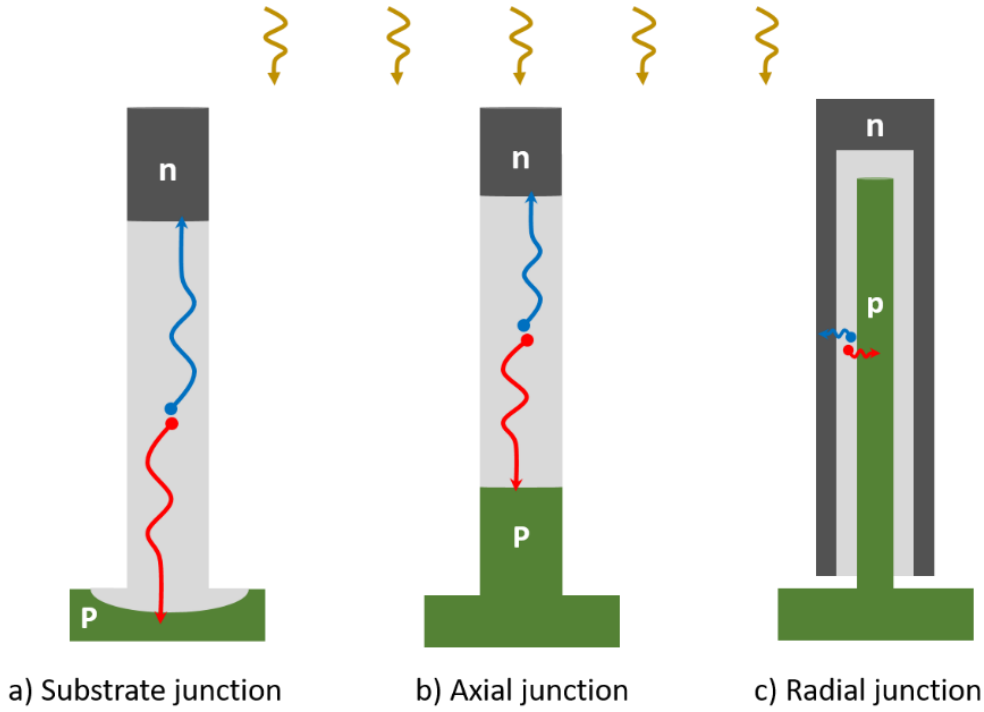

Figure 1.7. *Schematic of a) radial, b) axial and c) substrate junction, which is possible for NW-based solar cells.*

In the case of radial junction geometries, light absorption occurs along the NW length, while carrier collection occurs along the NW diameter. Therefore, photogenerated carriers need to travel much shorter distances (i.e., < 100 nm) before collection, as compared to axial or substrate junction design. This specific capability of core-shell structures makes it possible to improve the response speed of photodetectors. On the other hand, the active region is elongated in the light illumination direction (*z*-direction), so photons can be absorbed along the entire NW length. Since minority carrier diffusion lengths are typically much larger than or comparable to the thickness of the NW core and shell segments, carriers can efficiently reach the edge of the depletion region where they can be collected [8]. This concept holds significance in the simulation-based research presented in this dissertation and will be further elaborated upon in Chapter 4.

The research presented in this dissertation describes novel methods for the growth and fabrication of substrate-free InAs NW-based devices and unique strategies for manipulating the optical absorption properties of NW systems. It also explores the modulation of InAs NW dimensions and composition, along with the growth of mixed-dimensional heterostructures on foreign two-dimensional (2D) materials. The research outcomes pave the way for innovative designs and engineering of semiconductor NW materials, presenting opportunities for advancements in flexible and cost-effective optoelectronic devices. Each chapter's focus prioritizes a different aspect of NW-based IR photodetectors. This deliberate emphasis is primarily attributed to the distinctive characteristics of the InAs material system utilized throughout the entire research endeavor. The unique properties of InAs, characterized by a small band gap of 0.36 eV and high carrier mobility, position it as a promising candidate for IR PD applications. To provide

the reader with the necessary background on this target device application and to contextualize the research contributions presented here, the following section delves into the basics of photodetectors, their principles of operation, figures of merit, and reviews recent developments in NW-based PDs.

1.6 Use of Nanowires for Photodetector Device Applications

1.6.1 Introduction to Photodetectors

Photodetectors (PDs) are optoelectronic devices that absorb electromagnetic radiation and convert it to measurable photocurrent [59]. They are one the most ubiquitous type of devices in use today with a broad range of applications from TV receivers and automatic door sensors to cell phone cameras and optical communication that are used in commerce, industry, defense and research [64], [65]. Since there is a large variety in PD applications with unique requirements, there are different types of PDs with different material systems, device structure, characterization parameters, and costs [59], [64]. For instance, automatic door sensors, which normally operate in the infrared and microwave range, are relatively slow and less sensitive [66]. In contrast, optical communication sensors operate in infrared spectrum with wavelength in the 1.3 μm to 1.55 μm range, need to be extremely fast and sensitive to receive a large capacity of data [67], [68].

Generally, PDs can be divided to two main categories: thermal detectors and photon detectors. Thermal detectors detect incident photons via increases in the device temperature, which results in physical properties changes such as electrical conductivity and subsequent changes in the output electrical signal. This type of PD is mostly used for IR detection and suffers from low performance, specifically low spectral responsivity [1], [69]. Photon detectors operate by creating electron-hole pairs as a result of photon absorption and converting them to measurable photocurrent. Unlike thermal detectors, photon detectors need to be cooled for better device performance, specifically to increase the signal-to-noise ratio. There are different types of photon detectors based on the photocurrent generation mechanism, such as photoconductor, phototransistor, Schottky

junction photodiode, and photodiode [69], [70]. Among the photon detectors portfolio, photodiodes are attractive devices for various applications due to their high sensitivity to incident light, low noise, high speed of operation, and low operational power. They are generally based on inorganic semiconductor materials due to stability of their chemical and mechanical properties, materials variety, and mature established fabrication processes [64], [71].

1.6.2 Infrared Photodetectors

Electromagnetic radiation can be classified into different spectral ranges based on wavelengths ranging from radio waves to gamma rays. Solar radiation thermal effect studies by William Herschel in 1800 resulted in the discovery of invisible radiation with wavelengths longer than red light, which later came to be known as infrared (IR) radiation [72]. Infrared radiation that can be emitted and absorbed by objects in the surrounding environment extends across wavelengths from ~770 nm to 1 mm. This wide spectrum can be divided into five main sub-divisions, as follows:

- Near infrared (NIR): 770 nm – 1 μm
- Short wavelength infrared (SWIR): 1 – 3 μm
- Medium wavelength infrared (MWIR): 3 – 5 μm
- Long wavelength infrared (LWIR): 8 – 14 μm
- Far infrared (FIR): 16 μm – 1 mm

Detection of IR radiation has great importance in various fields such as astronomy, medical imaging, chemical sensing, surveillance, security, and optical communication

[73]–[75]. Photodetectors with high sensitivity and operation speed are desired for all above-mentioned applications.

1.6.3 Principles of Operation

Generally, PD operation can be divided into two main mechanisms: photoconductive or photovoltaic effects. The absorption of photons can generate electron-hole pairs by exciting electrons from the valence band to the conduction band, which increases the concentration of mobile charge carriers. This phenomenon increases the conductivity of the material, which is the photoconductive effect, or it can induce a current by accelerating the electron-hole pairs by the built-in electric field, which is the photovoltaic effect. In both cases, photogenerated current, which is proportional to photon flux can be extracted through an external circuit and results in detection of the incident light.

In this section the basic principle of depletion-mode PDs, which are either introduced by *p*-*n*, *p*-*i*-*n*, or Schottky junctions, will be summarized. The operation principle of depletion-mode photodetectors can be divided into three different processes: light absorption, carriers generation, and photogenerated carrier collection [1]. Incident light will be either reflected from the material's surface, transmitted through the material or absorbed in the material. Both reflection and transmission are considered as loss in PD systems and should be minimized to increase the photon absorption [59]. Photogenerated carriers (electrons and holes) within the depletion region can be separated by a built-in electric field at the junction, in which electrons and holes move to *n* and *p* regions, respectively, which is known as carrier collection process [1], [59]. Finally, carriers are

extracted to external circuit as measurable photocurrent. The entire process is shown in Figure 1.8 [2].

Not all photons are absorbed within the depletion region. Short wavelength photons are absorbed close to the semiconductor surface, whereas photons with longer wavelengths travel longer distance into the semiconductor [59]. Those carriers that are generated beyond one diffusion length of the depletion region cannot significantly contribute to photocurrent due to the absence of a charge-separating *E*-field, as illustrated in Figure 1.8 [76]. Diffusion proceeds more slowly compared to drift, and carriers generated at different distances from the edge of depletion region have different diffusion times, which results in undesirable signal distortion [76].

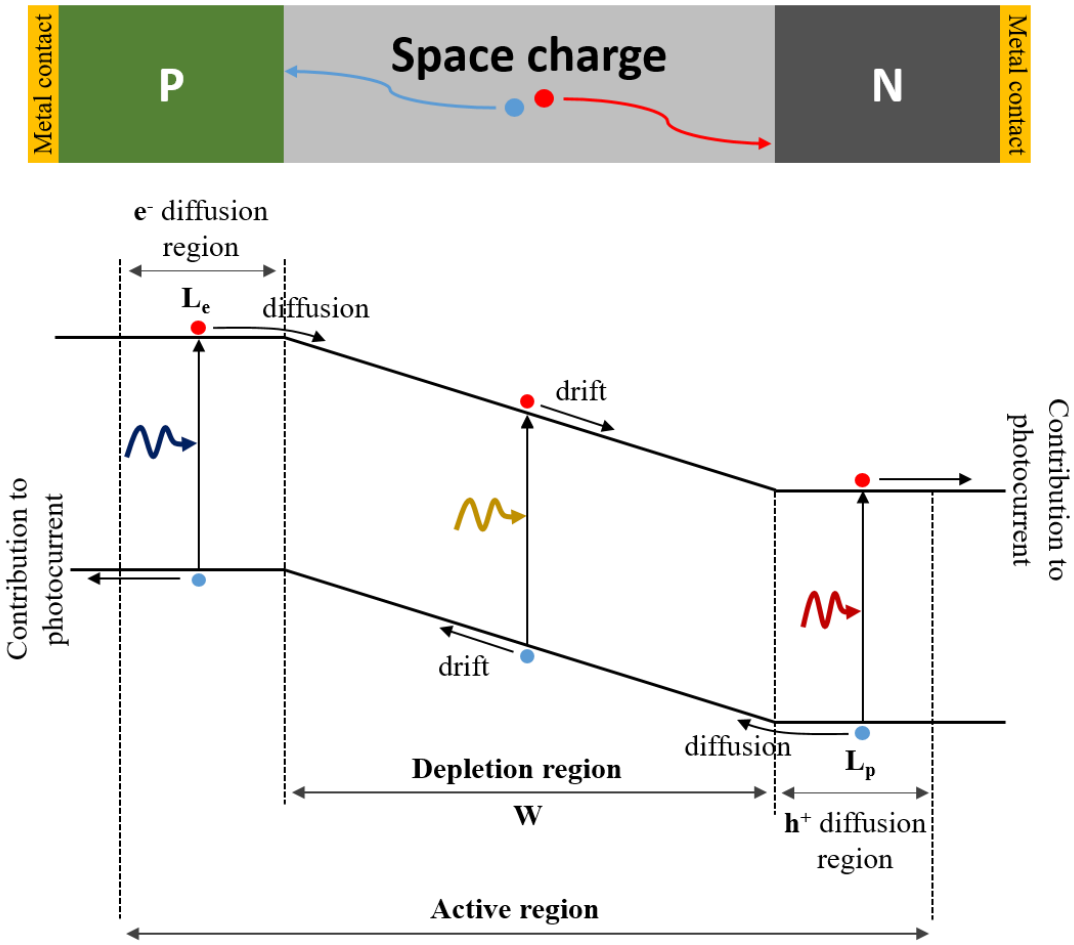

Figure 1.8. *Schematic of p-n NW structure and its related band diagram under illumination, showing the working mechanism of photodiodes.*

Depletion-mode PDs are usually operated under reverse-biased condition in the third quadrant of the I-V characteristics plot, unlike solar cells that operate in the fourth quadrant. The ratio of photo-generated to total current is much larger in the third quadrant as shown in Figure 1.9, which is favored for photodetection, especially for weak incident light. Reverse-biased mode increases the width of the depletion region thereby the active area of the device is expanded, and more carriers can be effectively collected. In addition, a larger depletion region leads to a stronger electric field and lower junction capacitance,

which reduces the transit time and improves the response speed of the device, as will be discussed in Section 1.6.4 in greater detail.

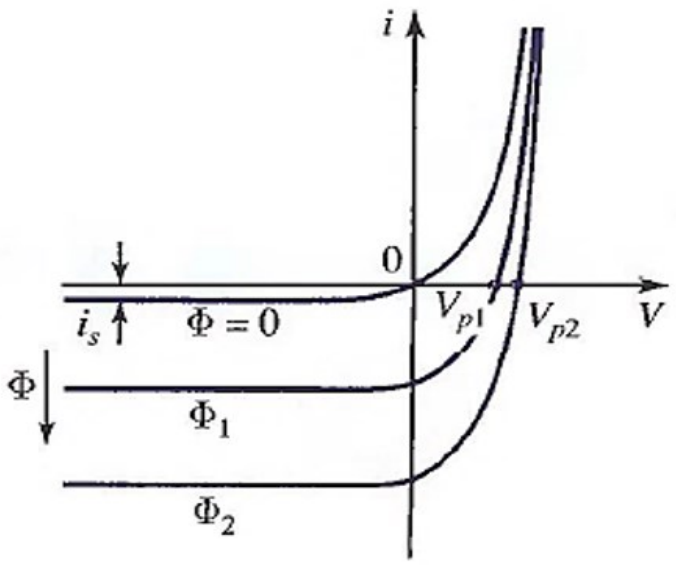

Figure 1.9. *I–V curve of a photodiode operating in reverse-biased mode under varying incident fluxes Φ_1 and Φ_2, where $\Phi_2 > \Phi_1$. Adopted from Ref. [1].*

The photocurrent response output to abrupt light pulses exhibits a decay tail as depicted in Figure 1.10. This tail is attributed to carriers in the diffusion region that are delayed in contributing to the photocurrent. An effective strategy to mitigate this phenomenon involves reducing the thickness of the diffusion regions. This can be achieved by lowering the dopant concentration in both the *n* and *p* segments, allowing the depletion region to extend closer to the electrodes. However, to maintain good Ohmic contact and facilitate efficient carrier extraction, thin heavily doped layers are essential at the electrode junctions. In this design, the very lightly doped middle region, in comparison to the heavily doped regions adjacent to the electrodes, can be designated as an intrinsic (*i*) region.

Devices featuring such a structure and design are commonly referred to as *p-i-n* photodiodes, representing the prevalent type of photodetectors [59], [76].

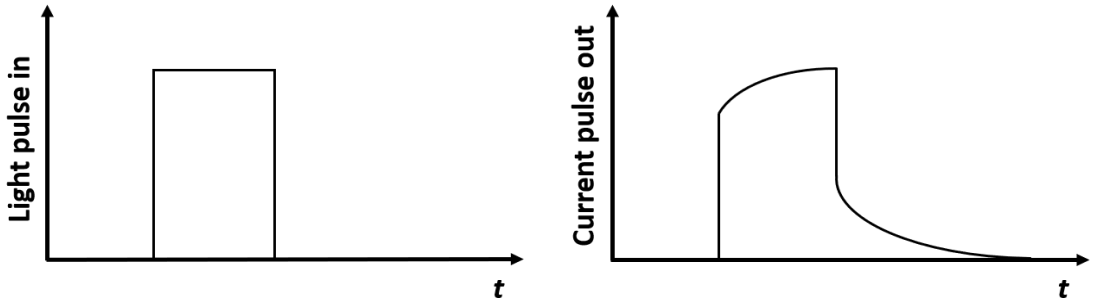

Figure 1.10. *Charge carriers created in the diffusion region give rise to a distortion in the photocurrent waveform.*

In *p-i-n* diodes, the depletion region width, *W*, is limited by the geometry of the device. Therefore, *W* can be modified by design rather than by the applied reverse bias. This ability allows device performance optimization for specific applications. For example, the *i*-region can be extended in order to increase the PD depletion region and path length for photon absorption, specifically for photons with wavelengths near the semiconductor's bandgap. Hence, increasing the *i*-region thickness results in more efficient carrier collection. However, by increasing the width of *i*-region, carriers need to transit longer distances before they can be collected, which decreases the response speed of the PD device [76]. This is the well-known efficiency-speed tradeoff in conventional *p-i-n* PDs [8], [76]. This efficiency-speed tradeoff can be broken in NW-based PDs to simultaneously improve quantum efficiency and response speed, which will be discussed more in details in Sections 1.6.4 and 1.6.5 [8].

In Schottky photodiodes, with a metal-*n*-n^+ configuration, light passes through a very thin metal layer (partially transparent) and is mostly absorbed in the *n*-region of the

semiconductor absorber. Generated carriers are separated by a built-in *E*-field induced at the semiconductor-metal junction. Like *p-i-n* photodiodes, the depletion region thickness can be adjusted via donor dopant concentration (N_D) to eliminate the diffusion tail in photocurrent response [76]. This type of PDs has some benefits over *p-n* and *p-i-n* PDs for some specific applications. A less complicated fabrication process is one of the main advantages. Due to the lack of a *p*-region, there would be no diffusion tail arising; therefore, the response time can be improved [76]. Another advantage of Schottky photodiodes is that a wide variety of semiconductor materials can be used for metal-semiconductor junctions, including wide band gap materials for UV detection. Schottky photodiodes, however, suffer from poor photons absorption, mainly caused by high reflection from metal surface especially at longer wavelengths. Therefore, their efficiency is lower compared to *p-i-n* photodiodes. Schottky photodiodes are mainly used for UV or high-speed detection applications [76].

1.6.4 Photodetector Figures of Merit

The device performance of PDs is evaluated by several different parameters and figures of merit, which will be described in this section.

Responsivity *([R] = [AW^{-1}])* is defined as the ratio of generated photocurrent (I_{ph}) to incident optical power (P_{in}) [8]:

$$R = \frac{I_{ph}}{P_{in}} = \eta g \frac{e\lambda}{hc} \tag{1.4}$$

Here, η is the external quantum efficiency (EQE), g is photelectric gain, e is the fundamental charge, λ is the wavelength of incident photon, h is Planck's constant, and c is the speed of light. The EQE is defined as the ratio of the number of generated carriers per second that contribute to photocurrent to the number of incident photons per second [8].

The photoelectric gain (g) describes the number of trips that carriers pass through the PD electrodes before recombination per absorbed photon [64] and can be defined as:

$$g = \frac{\tau}{\tau_t} \tag{1.5}$$

Here, τ is the excess-carrier recombination lifetime and τ_t is the carrier transit time between PD electrodes. Generally, NW-based PDs have been shown with high photoelectric gain due to a combination of the two following factors: (1) high carrier mobility due to quasi-1D geometry and high crystal quality achievable in NWs, which result in considerable reduction in τ_t; and (2) high surface to volume ratio in NW geometry, which results in excess-carrier recombination lifetime being prolonged due to surface trap states [18], [77].

Another important figure of merit is detectivity ($[D] = [W^{-1}]$), [8] which defines the sensitivity of the PD by determining smallest detectable signal with a signal-to-noise ratio of unity.

$$D = \frac{1}{NEP} \tag{1.6}$$

Here, *NEP* is noise-equivalent power. This defines the minimum incident optical power required to generate a signal-to-noise ratio of unity, and can be further expressed as:

$$NEP = \frac{I_N}{R} \tag{1.7}$$

Here, I_N is the PD noise current [8]. The noise current can be described as:

$$I_N = \left(2eI_d\Delta f + \frac{4kT\Delta f}{R_d}\right)^{1/2} \tag{1.8}$$

I_d is the dark current, which is defined as the current through a PD in the absence of incident optical power. Δf is the frequency bandwidth, which is defined as the frequency where the PD output electrical power has dropped 3 dB from a low-frequency reference. *T* and R_d are the temperature and differential resistance, respectively. The first term is related to shot noise due to random carriers collected by electrodes. The second term is related to thermal noise due to fluctuation of carriers. The detectivity is not a reasonable figure of merit for comparing device performance of different PDs since the effects of detector area and frequency bandwidth are not always considered [78]. To overcome this issue specific detectivity *($[D^*] = [cm\ Hz^{1/2}\ W^{-1}]$)* was introduced, which is the normalized signal-to-noise to an area of 1 cm^2 and an electrical bandwidth of 1 Hz [8]. It can be described as:

$$D^* = \frac{R(A\Delta f)^{1/2}}{I_N} \tag{1.9}$$

where *A* is the active area of PD. Substitution of Eq. (1.8) in Eq. (1.9) results in:

$$D^* = \frac{R}{\left(2eI_d + \frac{4kT}{R_d}\right)^{1/2}} \tag{1.10}$$

Importantly, I_d is exponentially dependent on temperature. So, to increase the specific detectivity, PDs can be operated at lower temperatures. Therefore, IR PDs are commonly cooled either by liquid nitrogen or thermoelectric coolers. NW-based PDs potentially can operate at room temperature due to their low material volume, which results

in low dark current. Response time is another important PD parameter, which is defined as the time required for a PD to rise from 10 % to 90 % of final output. We will expand on this point in the context of experimental and simulation works on the substrate-free applications, discussed in Chapters 3 and 4.

1.6.5 Nanowire-Based Photodetector Research

The conventional III-V PDs are based on thin film technologies. A thin absorber medium is desired to shorten carrier transit time, which results in the improvement of PD detection speed and noise reduction [71]. On the other hand, thin film structures can suffer from weak absorption, resulting in low carrier generation and, therefore, low quantum efficiency. This is known as traditional efficiency-speed tradeoff [71]. To overcome this problem, waveguide PDs or resonant structures have been developed to increase the light absorption, but such approaches limit device scaling and add more complexity to device fabrication and integration [79]. In addition, integration of III-V semiconductor devices on silicon (Si) is currently an attractive research topic due to the potential of combining the unique optical and electronic properties of III–V compounds with the low-cost and mature Si technology [80]. Heteroepitaxial growth of III-V compounds films on Si with a high crystal quality is difficult due to their lattice mismatch, dissimilar thermal expansion coefficient, and polarity differentials [29]. All the aforementioned challenges can be potentially overcome through the use of NW structures.

Semiconductor NWs have received great research interest in the last decade due to their potential as next-generation materials for electronic and optoelectronic applications [5]–[7]. The possibility of achieving high quantum-efficiency due to strong light absorption

and fast carriers collection due to small size and high carrier mobility in NW geometries makes them promising materials for novel PDs, most importantly by breaking the traditional efficiency-speed tradeoff with lower epitaxial volumes and higher quality of materials [8], [18], [77].

In this section, some of the current research on III-V NW-based PDs will be reviewed. This section is categorized by the detector's operating spectral range such as: UV, visible, and infrared (IR) regimes. The last example will be discussed in more detail as it can potentially cover both visible and IR regions in a multispectral operation mode.

1.6.6 Ultraviolet Photodetectors

Ultraviolet (UV) PDs are of interest because of their various applications in environmental and biological research, space communication, and military uses. III-V UV detectors are mainly based on GaN due to its large direct bandgap, high carrier mobility and good chemical stability with high melting point [19]. A great deal of research has already been dedicated to GaN-based detectors with low dark current and high responsivity. Coupling of metal nanoparticle in PDs has been shown to significantly enhance the detector performance due to localized surface plasmon resonance (LSPR), which results in strong light absorption and improvement in photocurrent intensity and detectivity of PDs, respectively [81]. Pt nanoparticles are expected to enhance GaN PD device performance due to LSPR in UV region, unlike Au and Ag nanoparticles that have been shown to exhibit LSPR in the visible and IR region, respectively.

Recently, X. Zhang et al. demonstrated significant improvement in single GaN NW-based UV detection by modification of Pt nanoparticles [81]. The GaN NWs were grown with effective combination of Pt nanoparticles through dispersion of a Pt colloid solution. Their specific design with Pt nanoparticles resulted in 126-fold photocurrent improvement compared with a bare GaN NW. The EQE of the detector also improved by two orders of magnitude. Moreover, the detector responsivity and sensitivity were increased by about 100 and 9 times, respectively, via Pt nanoparticle coupling. Additionally, GaN NW PDs coupled with Pt nanoparticle exhibited large reduction in rise time (τ_r) from 17.5 s to 1.1 s and decay time (τ_f) from 6.2 s to 0.65 s. The UV photoresponse improvements of GaN detectors can be attributed to the formation of the depletion region at the Pt/GaN interface, effective light scattering, and hot electron injection due to implantation of Pt nanoparticles. This strategy can be potentially applied to a wide range of PDs to improve device performance for detecting different wavelengths [81].

1.6.7 Visible to Near-Infrared Photodetectors

Gallium arsenide GaAs is a promising material for high-efficiency photovoltaics due to its near-optimal bandgap, aligning well with the single-junction Shockley-Queisser limit for theoretical maximum efficiency [21]. Also, its high absorption coefficient and high carrier mobility further contribute to its suitability for advanced photovoltaic applications. Another important application of GaAs is in PD devices for visible and NIR spectral ranges [82]. There are many research efforts dedicated to GaAs-based NW detectors. For instance, Wang et al. demonstrated an improvement in single undoped GaAs NW PDs using the metal-semiconductor-metal Schottky junction structure [83]. They

achieved a high photoconductive gain of 2×10^4 for the detector at the NIR operational range. Further studies by Hu's group revealed the single GaAs NW PD optoelectronic property dependence upon doping level [84]. They have shown for doping levels higher than 2×10^{17} cm^{-3}, the photocurrent and reverse bias voltage exhibited an abnormal linear relationship for NW-based Schottky junction devices. This was a good indication that *n*-type GaAs NW carrier lifetime can be decreased above a certain doping level.

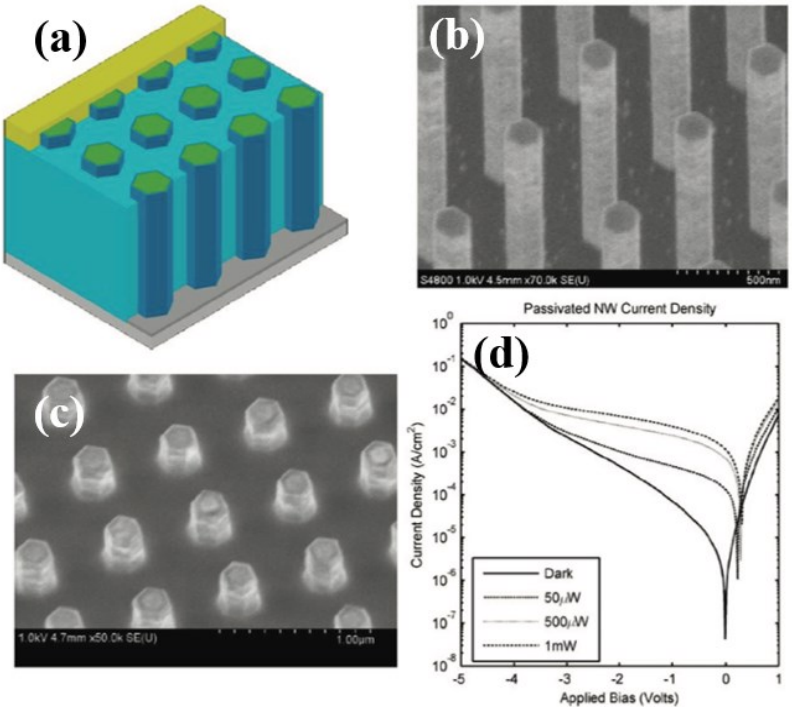

Figure 1.11. *(a) Schematic illustration of GaAs-AlGaAs core-shell NW arrays and PD device structure. SEM images of the NW arrays (b) after growth and (c) after planarization. (d) photocurrent density of NW array device under illumination with different intensities. Adopted from Ref. [85].*

Moreover, Seyedi et al. reported arrays of undoped GaAs NWs with AlGaAs shell segments as passivation layers, contacted with indium-tin-oxide (ITO) for Schottky-like heterojunction PDs, as shown in Figure 1.11 [85]. The device was designed to detect

incident radiation at a wavelength of 850 nm, which is important in data communication technologies. The device showed a responsivity of 0.5 AW^{-1} with signal-to-noise ratio as large as 7 dB. Furthermore, the reported device can be a promising candidate for high-speed optoelectronic device based on its capacitance-voltage characteristics.

The combination of GaAs and graphene makes it potentially possible to obtain highly sensitive NIR PDs. There are many investigations that have shown graphene-GaAs NIR PD with high response speed operating at low power. For instance, recently, Luo et al. reported NIR PD based on Schottky junction formation at a GaAs nanocone array/monolayer graphene interface. In this report, a monolayer of graphene was used as the top contact for top-down synthesized *n*-type GaAs nanocone arrays. Device characterization showed high-sensitivity performance at 850 nm with high response speed ($\tau_r = 72$ μs, $\tau_f = 122$ μs). Additionally, compared to other GaAs-based detectors, the device showed higher detectivity of 1.83×10^{11} cm $Hz^{1/2}$ W^{-1} [86].

Indium phosphide (InP) is another promising III-V compound for detection in this spectral range, especially in NIR region, due to its direct band-gap and high carrier mobility [82]. InP NW arrays have been experimentally shown to exhibit strong light absorption [56]. Pettersson and coworkers reported an efficient NIR PD based on p^+-*i*-n^+ InP NW arrays with p^+-segment length varying from 0 to 250 nm, grown on a p^+ InP wafer. They have shown that the NW's p^+-segment length strongly affects the detector performance. Increasing the length of the p^+-segment resulted in effective reduction of the substrate contribution to photocurrent for p^+-segments longer than 200 nm, as shown in Figure 1.12 [61]. Adding a thick p^+-segment into the NWs shifted the depletion region up and effectively separated the active region and substrate, which blocked carriers from funneling

from the substrate into the NWs. The detectors exhibited rectifying behavior with an ideality factor between 1.8 and 2.5 at room temperature and a small leakage current of 100 fA at 1 V [61].

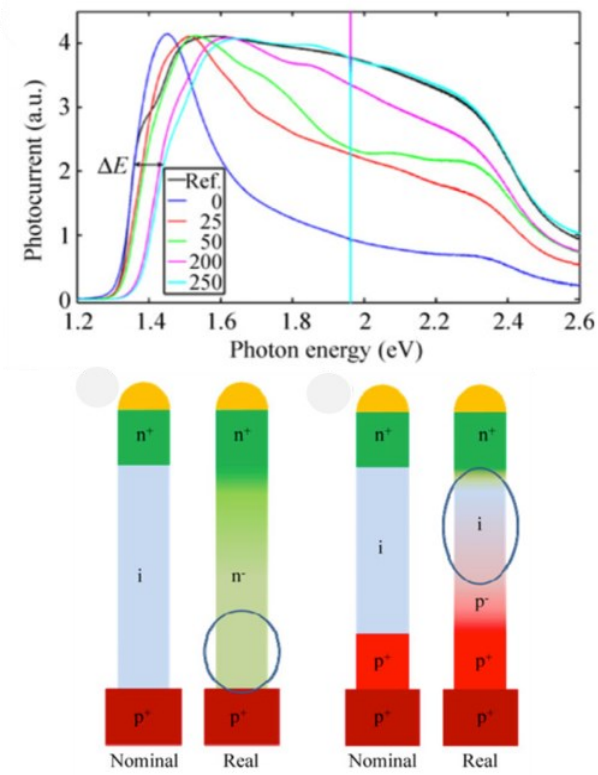

Figure 1.12. *Normalized photocurrent vs. photon energy for different samples with different p^+-segment length (from 0 to 250 nm) measured at 300 K and schematic of different NW device geometries. Adopted from Ref. [61].*

1.6.8 Infrared Photodetectors

There is great research interest in IR detection and sensing due to the broad variety of its application to manufacturing inspection, free-space communication, deep-space monitoring, medical imaging, environmental sensing, and missile tracking technologies. Mercury cadmium telluride (MCT) detectors are the most common and dominant available detectors in the market for IR sensing, especially for MWIR and LWIR detection [8].

However, MCT detectors suffer from yield and uniformity challenges for large area growth. Also, they are mostly grown on expensive CdZnTe substrates. In addition, there are environmental concerns due to the high toxicity of mercury. III-V NWs such as indium-gallium-arsenide (InGaAs), indium-arsenide (InAs), indium-antimonide (InSb), and induim-arsenide-antimonide (InAsSb) are promising materials for IR detection, which cover a wide IR spectral range through bandgap engineering [19], [87].

Theoretically, $InAs_{1-x}Sb_x$ (for $x = 0.65$) has the smallest bandgap of 0.1 eV amongst III-V compounds at room-temperature [54]. Sevensson et al. investigated InAsSb NW IR detectors with varying Sb content and diameters, as shown in Figure 1.13 [54]. NWs were grown by the VLS method on InAs substrates with different Sb content of $x = 0.04 – 0.76$. They showed that both composition and NW diameter greatly influence spectrally resolved photocurrent. Adjusting the diameter of the NWs resulted in peak absorption close to InAsSb bandgap, which was nearly one order of magnitude higher than thin-film absorption with same amount of material. Experimental data showed that the peak absorption was due to resonance effects within NWs that improve light coupling and absorption. Photocurrent under illumination in NWs with $x = 0.76$ was calculated to be 10 nA at 0.25 V [31]. Later, they demonstrated axially doped *p-i-n* $InAs_{0.93}Sb_{0.07}$ NW array detectors grown on Si operating in SWIR region. The NW structure consisted of a 250 nm *p*-type InAs segment followed by equally long 500 nm segments of *p-, i-* and *n*-type InAsSb. The device showed low leakage current density around 2 mA/cm^2 at room temperature [88].

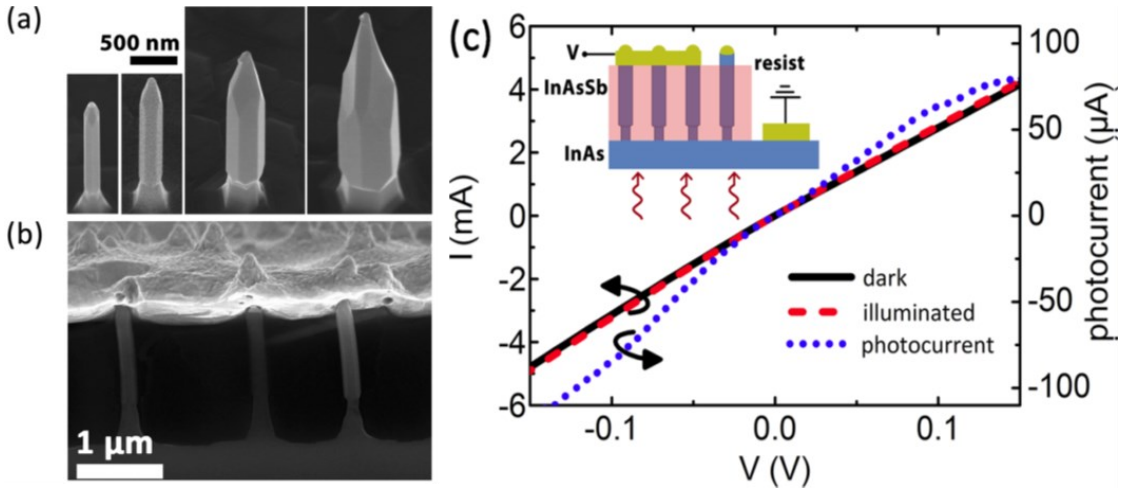

Figure 1.13. *(a) 30° tilted-view SEM images of $InAs_{1-x}Sb_x$ wires with x = 0.27 and different diameters. (b) Cross-sectional SEM image of $InAs_{1-x}Sb_x$ NW-based PD device. (c) I-V curve at 5 K of $InAs_{1-x}Sb_x$ NW PD with x = 0.76, d = 587 ± 60 nm, and length of 1.95 µm under dark (black) and backside illuminated (red) conditions. Adopted from Ref. [54].*

As mentioned above, the catalyst-free growth mode is preferred over VLS growth as it is more compatible with CMOS technology. However, growing catalyst-free InAsSb by MOCVD is difficult due to the low equilibrium vapor pressure, short diffusion length, and consequent condensation of Sb [89]. The Huffaker Group recently demonstrated high-quality, SAE-grown $InAs_{0.85}Sb_{0.15}$ NWs by MOCVD. They adjusted not only the growth conditions but also the masking template's pore diameter and pitch to eliminate Sb condensation in order to obtain their maximum Sb composition. Also, they recently reported room-temperature detectors based on SAE grown InAsSb NWs on InP substrates coupled with their unique 3-D nanoscale plasmonic grating with MWIR detection at 3.4 µm [90]. They performed *ex-situ* Al_2O_3 passivation to suppress surface recombination velocity to 10^3 cm/s, which resulted in enhancement of photoluminescence emission at room-temperature.

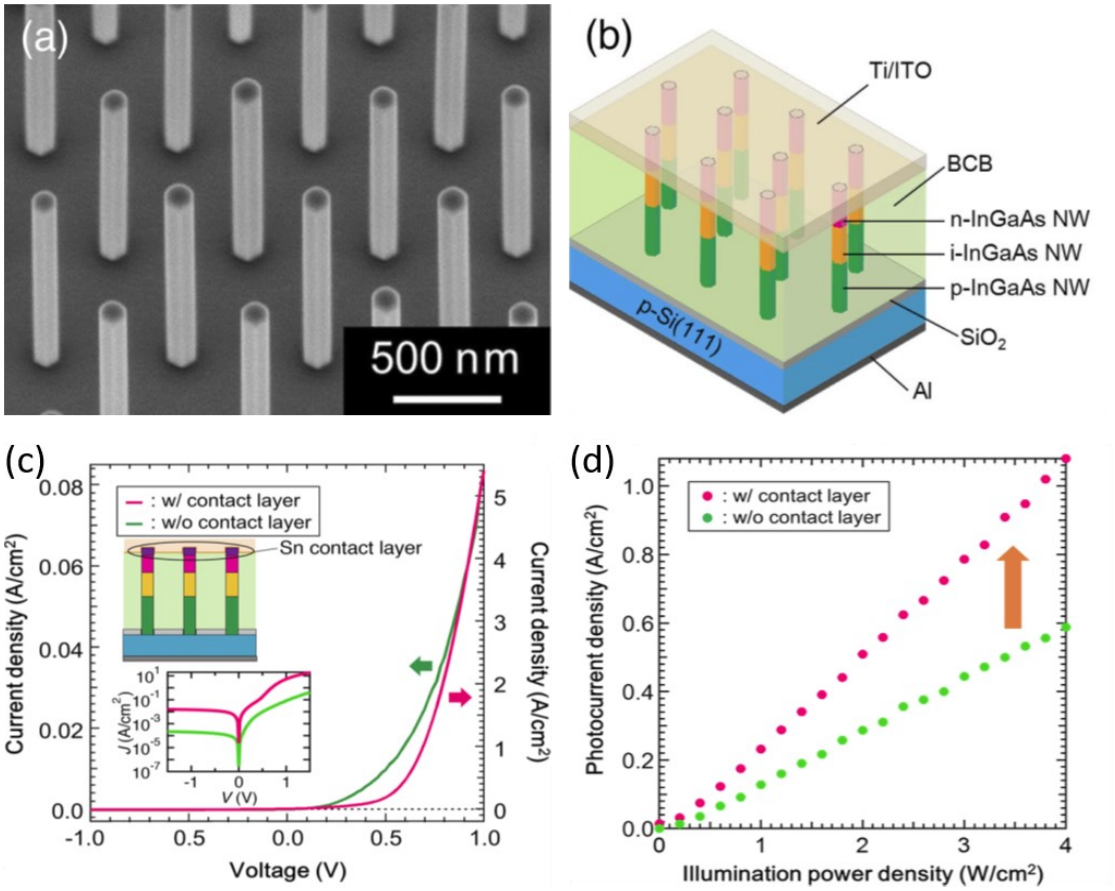

Figure 1.14. *(a) 30°-tilted SEM image of InGaAs NW array on Si after growth. (b) Schematic of fabricated InGaAs NW-based PD. (c) Current density vs. voltage characteristics of the device with and without a Sn-doped contact layer. The inset shows the same plot in logarithmic scale. (d) Photocurrent density vs. illumination power under 635 nm illumination and a reverse bias of −1 V. Adopted from Ref. [92].*

$In_xGa_{1-x}As$ is another ternary III-V semiconductor compound with tunable bandgap energy from 1.42 to 0.36 eV, depending on the indium content, x. It is a promising material for PD applications due to its direct bandgap (independent of x), high carrier mobility, and ability to tune its bandgap to cover a wide range from visible to SWIR wavelengths. InGaAs detectors show low leakage current in comparison to InAs or Ge operating in the NIR region [91]. Due to the InGaAs range of operation, its integration with Si can be very promising for optical telecommunications applications. Motohisa's group recently demonstrated *p-i-n* InGaAs NW array PDs on Si. The NWs were grown by SAE method

with approximately 53% In-content with *p*, *i*, and *n* segments of 600 nm, 400 nm, and 400 nm length, respectively. After growth, NWs were spin-coated with benzocyclobutene (BCB) as a spacer followed by RIE (using CH_4 and O_2 as reaction gases) to expose the tip of the NWs for top contacting. Next, Ti/ITO layers were deposited with 2 and 100 nm thickness as a top contact. A thin layer of Ti was deposited to improve the contact quality between InGaAs and ITO. Also, 100 nm of Al layer was deposited on the back of the Si substrate as a mirror to reflect transmitted light. The PD active area was 50 μm × 50 μm and contained 7000 NWs, as is shown in Figure 1.14 [92].

The device was tested under dark conditions and showed moderate rectifying behavior with turn-on voltage of 0.4 and ideality factor of 6.5. A dark current density of 0.2 mA/cm^2 was measured at -1 V. The device was illuminated by a laser with 635 nm wavelength and power density of 0.2 mW/cm^2. The NW-based PD showed a photocurrent density of 0.015 mA/cm^2 at zero bias voltage, which was a good indication of the NWs light response and presence of a *p*-*n* junction. The series resistance of the device was calculated as 1.06 Ω·cm^2. High resistance between NWs and Si or Ti/ITO contacts could be the reason for these high values. In order to improve device performance, they applied two different approaches. First, 200 nm-long segments of heavily Sn-doped InGaAs were grown at the tip of the NWs in order to reduce the contact resistance between the NWs and the Ti/ITO top contact. The series resistance dropped to 0.0345 Ω.cm^2, which represents a 30× improvement. The ideality factor also improved by roughly a factor of 2, as shown in Figure 1.14(c) [92]. Figure 1.14(d) shows that the photocurrent density increases linearly as a function of illumination power density. A responsivity of 0.25 AW^{-1} and quantum efficiency of 12.8 % were reported under illumination.

The second approach was to use NWs with InP surface passivation layers. A 10 nm InP shell was grown, and subsequently removed by RIE (with CF_4 and O_2) at the tip of the NWs after BCB etching. The surface passivation resulted in an increase in photocurrent density of roughly 20 times under 1.55 μm illumination due to the suppression of surface recombination, as shown in in Figure 1.15. The device achieved a photoresponsivity of 3 μAW^{-1} under illumination. The photoresponsivity decreased by 5 orders of magnitude compared to 635 nm illumination. This was attributed to the NW geometry (e.g., length, diameter, and pitch) not being suitably designed and optimized for absorption in IR region, which resulted in insufficient light absorption and resulted in low photoresponsivity.

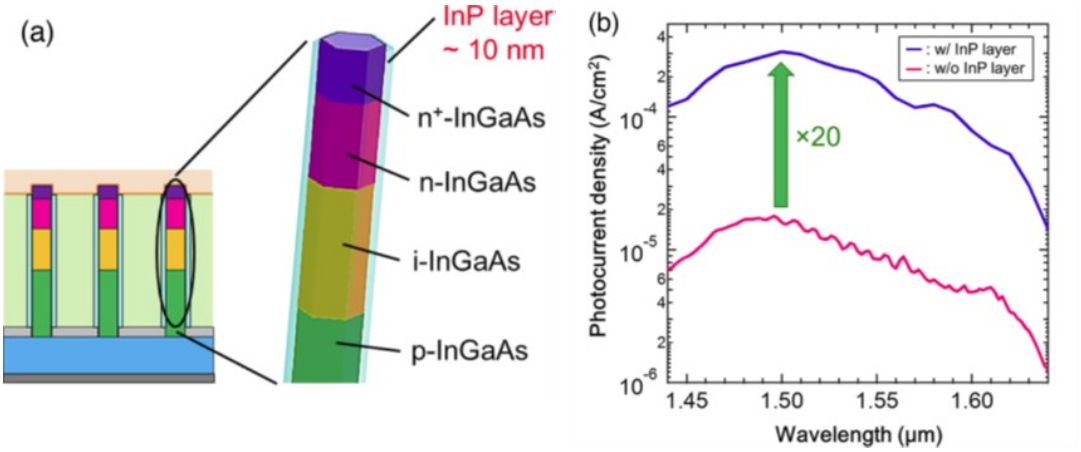

Figure 1.15. *(a) Schematic design of the core-shell structure of InGaAs-InP NW array PD. (b) Photocurrent spectra of the device with (blue) and without (gray) the InP shell layer. Adopted from Ref. [92].*

1.7 Approach and Framework

This research is centered around the epitaxial growth of catalyst-free InAs NWs on foreign substrates and novel approaches that strategically tune their physical properties for advanced optoelectronic device applications. The multifaceted approach encompasses considerations of manufacturing costs, functionality, and overall performance of substrate-free NW-based materials and devices. Through this comprehensive exploration, the research seeks to contribute advancements in the realm of NW-based optoelectronics, such as IR PDs, with respect to manufacturing costs, functionality, and performance.

In Chapter 2, we review the experimental procedures implemented throughout this research. The discussion initiates with an exploration of the theoretical foundations and experimental significance of the MOCVD crystal growth system for vertical NW growth. Subsequently, we direct our attention to the characterization methods utilized in our investigations. Notably, we delve into various electron microscopy techniques and surface characterization processes.

In Chapter 3, we introduce a novel localized self-assembly (LSA) method for growth of InAs NWs on reusable Si (111) wafers toward cost-effective and substrate-free applications. The process first involves *i*-line photolithographic patterning of hexagonal arrays of nanopores in a SiO_2 masking layer. InAs NW arrays are grown using MOCVD with a two-step flow-rate modulated growth technique, significantly enhancing global NW yield. Following growth, the NW arrays are embedded in a polymer membrane, delaminated from the growth substrate, and transferred to a new carrier wafer for further device fabrication with a transfer yield of ~100%. The masking template on the initial

growth substrates are then reused for subsequent NW growths, demonstrating regrowth without intermediate restoration steps. This process utilizes the remnant NW base segments on the parent substrate as preferential growth sites for regrowth, enabling the formation of second-generation InAs NWs with reproducible global yields exceeding 85% over wafer-scale areas.

In Chapter 4, we use the rigorous coupled-wave analysis (RCWA) simulation method and employ it to demonstrate significant tunability of the IR absorption spectra of coaxially heterostructured NW arrays, where InAs core segments are partially encapsulated by $GaAs_{0.1}Sb_{0.9}$ shell layers. Embedding the bases of InAs NWs in Au backside contact layers induces periodic evanescent fields between adjacent NWs, with optical characteristics dependent on the NW core segment diameter and incident light wavelength. Selective absorption of otherwise decoupled light is achieved over the 2 to 3 μm wavelength range in NW core segments by adding partial $GaAs_{0.1}Sb_{0.9}$ shell layers matching the evanescent field characteristics. Site-specific absorption in InAs NWs offers the potential of tailoring narrowband wavelength-selectivity in the SWIR range for IR PD applications.

In Chapter 5, we introduce a novel approach to locally manipulate effective precursor flowrates during NW SAE growth. This method takes advantage of a growth rate enhancement effect that depends primarily on the dimensions of the NW array, enabling the synthesis of InAs NWs with tunable geometries on the same substrate, while only using a singular nanopore masking pattern. Moreover, we leverage this growth enhancement effect to grow AlInAs NWs with variable Al content in a single growth run. The findings

in this chapter hold promise for achieving diverse absorption capabilities using NW structures, particularly beneficial for multispectral PD applications.

In Chapter 6, we summarize the key findings of this work and discuss possible future research avenues based on the presented results, as well as their associated challenges and prospective solutions.

Chapter II

2 Methodologies

This chapter describes the experimental procedures employed in the research presented within this dissertation. The methods under consideration encompass the following: (a) crystal growth via metalorganic chemical vapor deposition (MOCVD); (b) various electron microscopy-based approaches for the characterization of NW structure and chemistry, including scanning electron microscopy (SEM), transmission electron microscopy (TEM), and energy-dispersive X-ray spectroscopy (EDXS); and (c) atomic force microscopy (AFM) for surface analysis. To provide a comprehensive perspective on these techniques, each method will be discussed in terms of its theoretical background and related applications.

2.1 Metalorganic Chemical Vapor Deposition (MOCVD)

As introduced in Section 1.3, the approach for the synthesis of semiconductor nanostructures presented in this dissertation employs bottom-up crystal growth, whereby adatoms assemble and bond to a substrate and each other to form distinct single-crystalline NWs. This approach is achieved through epitaxial techniques, meticulously growing crystals atom by atom. Among various techniques, two prominent methods—molecular beam epitaxy (MBE) and metalorganic chemical vapor deposition (MOCVD)—are widely used for the epitaxial growth of semiconductor materials. The efficacy of an epitaxy growth method hinges on its capacity to produce uniform structures with sharp interfaces, achieve rapid growth rates, support the growth of diverse alloys, facilitate in situ monitoring, and scale for industrial manufacturing [93].

In MBE growth, elemental sources are heated, causing them to evaporate and form molecular beams within an ultra-high vacuum (UHV) reactor. These molecular beams deposit atoms onto a substrate, building crystalline structures layer-by-layer, involving a limited number of chemical reactions. This method is mostly used in academic research laboratories due to its unmatched purity and capability of achieving precise control over layer thickness, often down to a single atomic layer with atomically abrupt hetero-interfaces. In addition, the growth process can be monitored in real-time using techniques like reflection high-energy electron diffraction (RHEED), providing instant feedback on layer quality, crystal structure, and growth rate. However, the primary barriers to adopting MBE in industry is its scalability (i.e., the technique is not suitable for large wafer sizes and batch processing), and its operation within an UHV environment. The growth chamber

frequently requires venting for source replenishment or maintenance, leading to extended downtimes and increased costs [94].

In contrast, MOCVD is the predominant method for epitaxial growth of semiconductors in the industrial sector. This preference stems from its scalability, which is suitable for mass production, its material diversity that encompasses a wide range of semiconductor materials and complex multi-layer structures, and non-UHV environments with chamber pressures commonly in the 50 to 1000 mbar range. This reactor pressure range simplifies system maintenance and operation while ensuring high-quality and uniform growth. The primary drawbacks of MOCVD arise from the expenses and challenges associated with the use and storage of hazardous precursors. As depicted in the schematic in Figure 2.1, MOCVD has three main parts including supply, reactor, and exhaust which will be briefly described below [95].

Metalorganic (MO) precursors serve as the group-III supply in MOCVD. Examples include Trimethylindium (TMIn; $In(CH_3)_3$), Trimethylgallium (TMGa; $Ga(CH_3)_3$), and Trimethylaluminium (TMAl; $Al(CH_3)_3$), which are employed for the supply of In, Ga, and Al adatoms, respectively [93]. A specific container, known as a bubbler, is used to keep MO sources at a consistent temperature to ensure the correct vapor pressure. Typically, a non-reactive gas, primarily hydrogen (H_2), acts as the carrier to transport the MO vapor-phase precursors into the reactor. The H_2 is channeled through an inlet into the bubbler and as it flows through, it becomes saturated with the material inside. This saturated mixture then exits the bubbler through an outlet, which connects to pipelines. Generally, there are two main pipelines: the run lines, which link the bubblers directly to the reactor where growth occurs, and the vent line, which transfers the precursors directly to the exhaust

system. This dual-line configuration is designed to ensure a steady material supply, either at the commencement of growth or when switching between precursors, and they are controlled by manifolds. Each individual bubbler is equipped with a mass flow controller (MFC) to precisely control the precursor flowrates. Hydride (Hyd) precursors, such as arsine (AsH_3) and phosphine (PH_3) are used for the supply of group-V elements As and P, respectively [93]. In contrast, bubblers are not required for hydride sources, since they are stored in highly pressurized gas cylinders. Due to the toxicity of the hydride gas, more stringent safety protocols, such as exhaust and scrubbing systems for each gas cylinder, are needed.

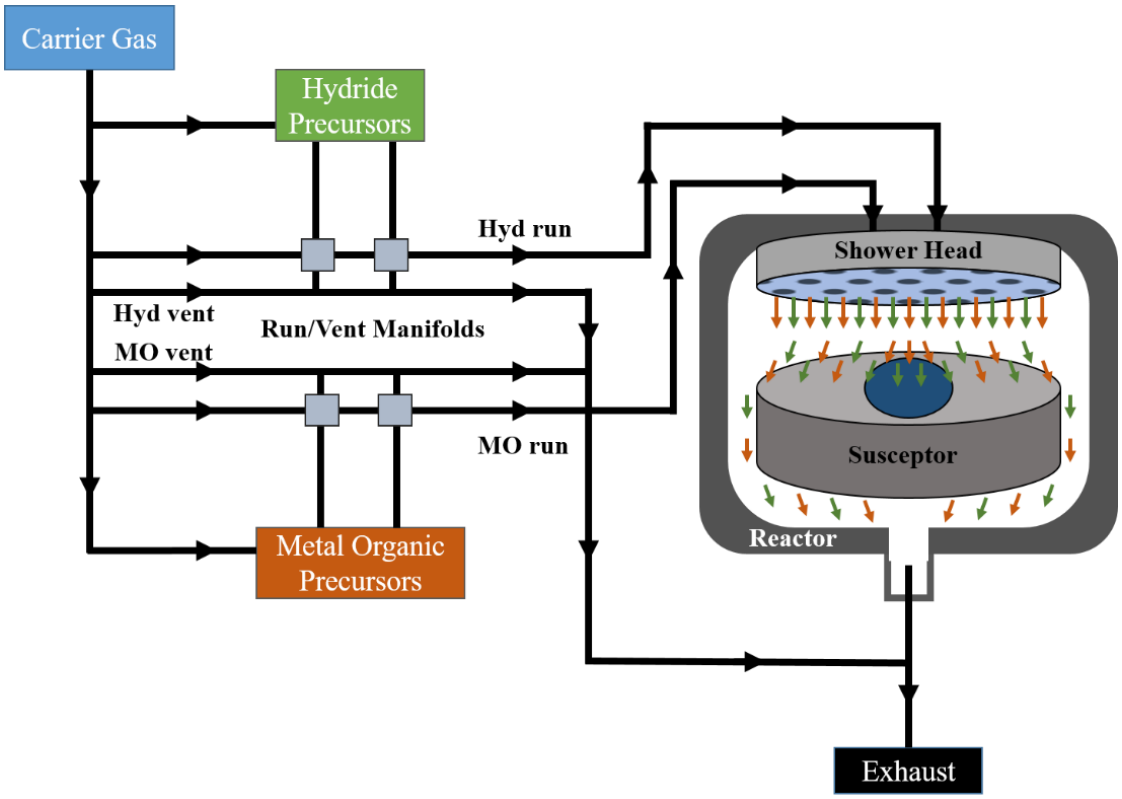

Figure 2.1. *Schematic of an MOCVD system: The carrier gas (H_2) delivers the metalorganic and hydride precursors to the reactor. Epitaxial growth occurs within the reactor, while the residual materials are directed to the exhaust. Arrows indicate the flow direction of the gas.*

The reactor is the main part of the MOCVD system where growth occurs at elevated temperatures, usually in the range of 500 °C to 1000 °C. A carrier gas delivers the precursors to the reactor via a showerhead, ensuring that they are evenly distributed over a susceptor. Samples are placed on this susceptor, which is locally heated to minimize undesired growth in other parts of the reactor. This setup is known as a cold-wall reactor configuration. When the precursors (e.g., TMIn) land on the sample surface, they decompose, leaving adatoms (e.g., In) adsorbed onto the surface. These adatoms then diffuse and can either encounter other adatoms to form a nucleation site, integrate into pre-existing growth sites, or desorb without contributing to the growth. The reaction rates in the reactor are primarily determined by gas concentration and growth temperature.

The last part of the MOCVD is the exhaust system, which is connected to the reactor via a throttle valve to keep the reactor under the desired pressure. Toxic materials are either burnt or neutralized within the exhaust system in a component referred to as the scrubber of the MOCVD before exiting.

In this work, all the samples were grown using an Aixtron 3×2" close-coupled showerhead (CCS) MOCVD reactor, as shown in Figure 2.2. The reactor is housed within a nitrogen glovebox, which serves a dual purpose. Firstly, it provides a secure barrier, safeguarding operators from potentially hazardous precursors. Secondly, it shields the reactor from exposure to oxygen, water, and other potential sources of contamination, ensuring its integrity and safety. The configuration is termed "close-coupled showerhead" because of the minimal gap, 20 mm, between the showerhead and the susceptor. This tight spacing ensures a uniform flow of precursors over the susceptor. Samples must be inserted

into the glovebox through a load lock to prevent contamination by isolating the main chamber from atmospheric conditions, ensuring high-quality thin film deposition.

Figure 2.2. *Aixtron 3×2" CCS MOCVD reactor operated within the NanoPower Research Laboratories (NPRL) at RIT.*

2.2 Electron Microscopy-Based Techniques

2.2.1 Motivations for Electron Microscopy

Fundamentally, an optical microscope consists of three key components: a light source, a magnifying lens, and a detector. Visible light, whether from a lamp or the sun, illuminates the specimen. The collected scattered light is then focused by optical lenses onto the eye, a screen, or a camera. According to the Rayleigh criterion [96], the resolution, δ, which describes the minimal distance between two distinguishable points, can be written as:

$$\delta = \frac{0.61\,\lambda}{n\,sin\beta} \tag{2.1}$$

where λ is the incident light wavelength, n signifies the effective refractive index of the lens, and β denotes the acceptance semi-angle of the magnifying lens. For instance, using green light with a wavelength of approximately 550 nm (to which the human visual system exhibits heightened sensitivity) yields a resolution of approximately 300 nm. In order to improve the resolution limit, the wavelength of the illumination source needs to be reduced. That can be realized by using electrons as the illuminating source, where their wavelength is dictated by their accelerating voltage (V_0), in accordance with a modified form of the de Broglie relation [97]:

$$\lambda = \frac{h}{\sqrt{2mqV_0}} \tag{2.2}$$

where h is the Planck constant, m is the electron mass, and q is the fundamental electron charge. This relationship can be reduced to $\lambda \sim 1.22/\sqrt{V_0}$, where wavelength and acceleration voltage are defined in units of *nm* and *V*, respectively. Hence, by tuning the

acceleration voltage (or, effectively, by adjusting the energy) of the incident electron beam, the microscope's resolution can be improved. At an acceleration voltage of 10 kV, typical for scanning electron microscopy, the electron wavelength is roughly 12 pm. However, for a 200 kV accelerating potential, typical for transmission electron microscopy, the electron’s non-relativistic wavelength becomes approximately 2.2 pm. Although this degree of resolution is not achieved in practice due to, for example, lens aberrations and source fluctuations, electron microscopes can practically achieve 4 orders of magnitude greater resolution than optical microscopes.

Electrons within an incident beam interact with a sample in multiple manners. They can either scatter elastically or inelastically, while each type of interaction provides distinct information about the sample. Figure 2.3 outlines the various signals produced when an electron beam interacts with a specimen. Generally, non-transmitted signals such as secondary electrons (SEs) and backscattered electrons (BSEs) are collected in scanning electron microscopy (SEM) [98].

On the other hand, transmission electron microscopy (TEM) employs transmitted electrons. Furthermore, when the electron beam interacts with the sample, it produces X-rays through inelastic interactions. This phenomenon can be harnessed to identify the sample's elemental composition using a method known as energy-dispersive X-ray spectroscopy (EDXS). The SEM, TEM, and EDXS methods are briefly discussed in Section 2.2.3, 2.2.4, and 2.2.5, respectively.

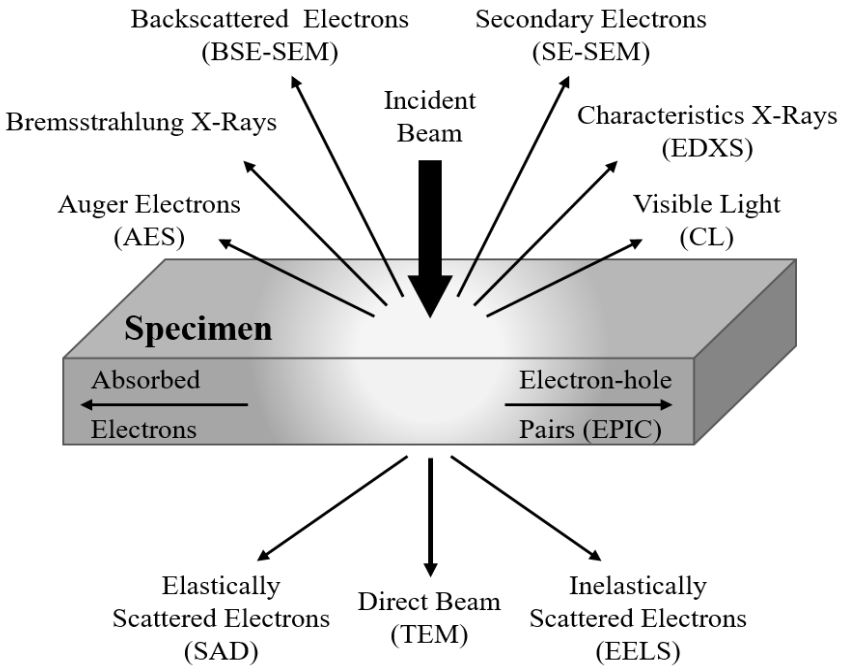

Figure 2.3. *Interaction of high-energy electron beam and thin-enough sample results in a variety of signals. The signals captured vary based on the microscopic or spectroscopic method utilized.*

2.2.2 The Instruments

The electron microscope is structured around three main components. Firstly, the electron gun assembly generates and accelerates electrons. Secondly, various lens systems tune the diameter of the primary electron probe and focus it onto the specimen. Thirdly, detectors convert electron signals into a magnified image.

Electron guns have three main mechanisms for electron emission: thermionic emission, Schottky emission, and field emission. In thermionic emission, a wire, typically made of tungsten or LaB_6, is heated until electrons exceed the material's inherent binding energy. The Schottky emission boosts thermionic electron emission by lowering the potential barrier on the cathode surface. A Schottky source typically consists of a V-shaped

tungsten filament coated with zirconium oxide to lower the work function [99]. Field emission, in contrast, utilizes an electric field to extract electrons from a tungsten tip. While thermionic and Schottky emitters are more cost-effective, our research tools mainly employ field emission guns because of their low operating temperature, enhanced beam brightness, and low energy spread of the generated electrons [97].

Electron microscopy necessitates the use of magnetic lenses rather than traditional optical lenses. The magnetic lenses are composed of symmetric pole pieces extending from a cylindrical high permeability ferromagnetic shell that encases current-carrying windings. Electron pathways through the lens are influenced by the magnetic field generated by this coil current. Electrons travel in a spiral pattern due to the generated Lorentz force, mimicking the focusing function of convex optical lenses. Similar to optical lenses, electromagnetic lenses have unavoidable defects and suffer from aberrations. Therefore, their resolution is often limited by the imperfections of electromagnetic lenses, such as spherical aberration, chromatic aberrations, and astigmatism, rather than the electron wavelength itself [97].

The primary factor limiting resolution in these lenses is the spherical aberration effects, which arise from the differences in focal length of electrons as a function of their distance from the central optic axis, resulting in image blurring. To address this, apertures are commonly introduced, in order to filter out these off-axis electrons to reduce the so-called “disk of least confusion”. Chromatic aberration, on the other hand, emerges as a result of the inherent and finite spread of the primary electrons energy [100]. To mitigate chromatic aberration, one can employ monochromators in the gun assembly, which is commonly used in TEM. Finally, astigmatism arises due to lens imperfections, which result

in an asymmetric probe and inconsistent focal lengths. In practice, astigmatism appears as image blurring. However, this issue can be effectively resolved by using stigmator lenses integrated into the electron column to generate an electron probe with a more circular profile.

2.2.3 Scanning Electron Microscopy

Scanning electron microscopy (SEM) is one of the most common techniques used to characterize the morphology of micro- and nano-scale samples. In this method, a focused beam of electrons is raster-scanned over the region of interest to produce an image. The sample must be conductive and sufficiently thick (>100 nm) to prevent charge accumulation and to stop the beam from passing through. The primary beam energies used in this technique commonly range from 2 keV to 30 keV. As the energy of the beam increases, the electrons penetrate deeper into the sample [99].

As previously mentioned, electrons can interact either elastically or inelastically with the atoms of the sample. Secondary electrons (SEs) are a type of signal resulting from inelastically scattered electrons. These electrons are valence electrons from the sample that acquire sufficient kinetic energy to break free and escape into the vacuum. Since the majority of these electrons possess energies less than 50 eV, a significant portion of them can be reabsorbed by the sample. As shown in Figure 2.4, only those SEs generated within approximately 50 nm of the sample surface manage to escape. Therefore, SEs provide only topological information of the sample surface. The yield of SEs that escape the sample is largely influenced by the angle between the incoming beam and the sample's surface. A

smaller angle results in a higher number of SEs being released from the sample. To capture these low-energy SEs, an electric field is employed, drawing them into a detector.

Electrons can also elastically scatter, meaning they deflect from their initial trajectory without significant energy loss. This happens when an electron experiences Coulomb scattering, getting deflected by the positively charged nuclei of the atoms. These electrons are referred to as backscattered electrons (BSE), as they can experience Rutherford scattering to angles much larger than 90° relative to their original travel path. Generating BSE requires a strong Coulomb interaction; therefore, the yield of BSEs mainly depends on atomic number (Z) [99]. Hence, they can be used to provide compositional information through Z-contrast, meaning that regions of a BSE-generated SEM image that contain higher atomic number constituents appear brighter. Due to their higher energy compared to the SEs, BSEs are able to escape the sample from much deeper within the sample, resulting in lower spatial resolution, as portrayed in Figure 2.4 [101]. Since BSE energies are comparable to the energy of the primary electron beam, they cannot be deflected as effectively as SEs toward the electron detector by an applied electric field. Therefore, only those projected toward the detector are collected.

In SEM, spatial resolution is determined by the diameter of the electron probe and the penetration range of primary electrons. The acceleration voltage of the microscope affects both of these factors, with the penetration depth also being influenced by the sample material. For instance, in semiconductor nanowires, different III-V materials have comparable penetration depths, but resolution is more influenced by acceleration voltage. A higher voltage typically results in deeper penetration, reducing the signal-to-noise ratio for SEs. Conversely, increased voltages offer greater control over the beam probe size,

enhancing spatial resolution. With the right imaging settings, it's possible to achieve a resolution down to a few nanometers on semiconductor samples. For optimal SEM imaging, samples should be conductive to prevent electrostatic charge accumulation that can distort images. Non-conductive specimens are often coated with a thin layer of carbon or gold to enhance conductivity. However, certain semiconducting materials, like III-V compounds, inherently possess sufficient conductivity, eliminating the need for additional coatings in SEM analysis.

In this research, two SEM systems, the Hitachi S-4000 and Tescan MIRA3 instruments, are used; the latter system is capable of EDXS mapping and point analysis.

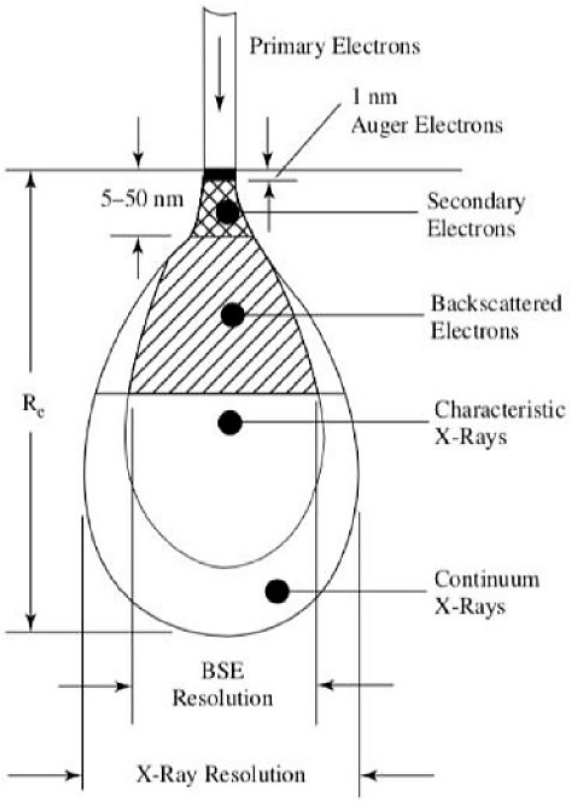

Figure 2.4. *The interaction volume of primary electron beam within sample. Adopted from Ref. [101].*

2.2.4 Transmission Electron Microscopy

Transmission electron microscopy (TEM) is a powerful technique that operates on the fundamental principle of transmitting a high-energy electron beam through a very thin specimen. This approach allows researchers to obtain detailed and high-resolution images of the sample's internal structure, down to the atomic scale.

In TEM, the electron beam is produced by an electron gun and then accelerated to energies, typically in the range of hundreds of keV. Proper sample preparation is crucial for TEM. Especially for semiconductors, the specimen must be ultra-thin, often less than 100 nm, ensuring the electron beam can penetrate the sample without major obstruction. As electrons pass through the sample, they undergo various interactions. Some electrons pass through without any interaction, maintaining their energy and trajectory, which then provides a "background" for the resulting image. The contrast in the image primarily arises from two mechanisms: mass-thickness contrast and diffraction contrast [99].

In a bright-field TEM image, the observed variation in intensity is directly correlated with the mass or thickness of specific regions within the specimen. Essentially, thicker sections of the specimen have a reduced electron penetration depth due to a higher absorption of primary electrons (PEs). Moreover, regions that contain elements with a higher atomic number (Z) tend to induce elastic scattering events at larger angles with respect to the optic axis. As a result of both phenomena, such electrons—either absorbed or scattered—are not detected, leading to dark contrasted areas in the TEM image. In the bright-field imaging mode, only the direct PEs, or unscattered electrons, are detected. Electrons that are diffracted or scattered at higher angles get excluded by a strategically placed aperture, ensuring the fidelity of the image. Within the context of this dissertation,

bright-field imaging serves as a tool for the qualitative assessment of nanowire morphology.

High-resolution TEM (HR-TEM) is a more advanced mode of TEM that pushes the technique's capabilities even further. It focuses on capturing the smallest details of the sample's structure, down to the atomic scale. This method involves collecting diffracted and transmitted beams with distinct amplitudes and phases, leveraging the Fourier sum of these signals to generate precise and highly detailed images [102]. HR-TEM enables the acquisition of clear images depicting the atomic column arrangement within crystalline structures, providing invaluable insights into material properties. This level of detail can highlight defects within the crystal, such as dislocations, vacancies, or impurities, which can have significant implications for the material's properties and applications.

Scanning transmission electron microscopy (STEM) is an imaging mode that combines both TEM and SEM techniques to obtain high-resolution images with detailed information about the structure and composition of the specimen. Unlike traditional TEM, STEM allows for the scanning of a focused electron beam to raster across a specimen, similar to SEM [102]. This enables the collection of various signals, such as transmitted electrons, from different regions of the specimen as the primary beam scans the sample surface. The technique offers high spatial resolution, allowing for the visualization of atomic arrangements and morphological details. Different imaging modes, including annular dark-field (ADF) and high-angle annular dark-field (HAADF) can be operated in STEM. These images are acquired based on electrons scattered at specific angles. ADF imaging involves electrons scattered within 10-50 mrad, while for HAADF, electrons scattered at angles larger than 50 mrad are detected [102]. This approach results in images

primarily formed based on Z-contrast, allowing a high degree of compositional differentiation.

2.2.5 Energy-Dispersive X-Ray Spectroscopy

One of the most informative outputs obtained when a sample is illuminated with an electron beam is characteristic X-rays. These X-rays offer a wealth of information about the composition of the specimen under examination [103].

Characteristic X-rays result from inelastic interactions between incident electrons and the atoms within the specimen. When high-energy electrons collide with atoms, they can eject electrons from the inner shells of these atoms. Consequently, electrons from higher energy levels in the outer shells occupy the vacant states in the inner shells, releasing the energy difference between the two energy levels in the form of X-ray photons. Since each element possesses a distinct electron configuration, the energy of the emitted X-rays reflects this unique arrangement, effectively serving as an elemental fingerprint [103]. Thus, by detecting these X-rays, we can obtain compositional information about the specimen, as depicted in Figure 2.5.

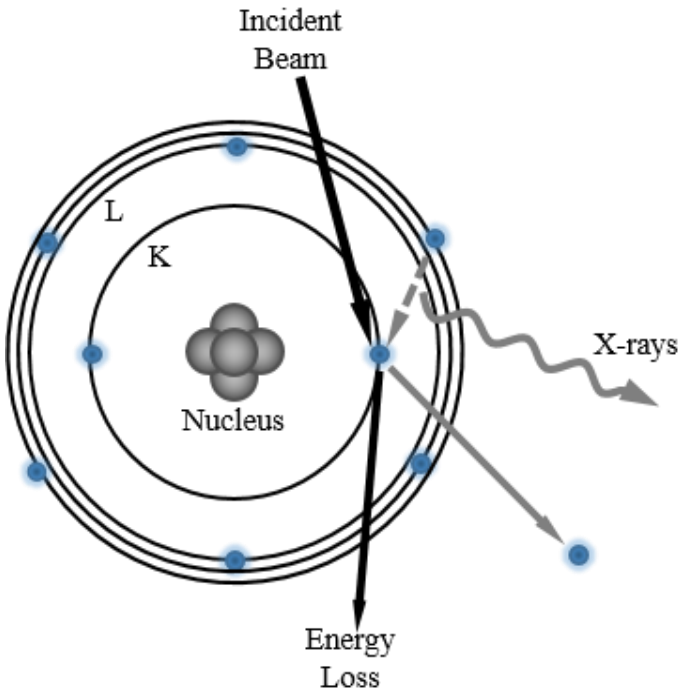

Figure 2.5. *This schematic shows an atom's K and L shells. In X-ray generation, the primary beam electrons displace core electrons. Relaxation of electrons from higher energy states results in the emission of characteristics X-rays, which are characteristic of each element and relaxation transition.*

EDXS is a technique that maps the characteristic X-ray energies emitted from a specimen against the number of detected X-rays. The characteristic X-rays, with energies on the order of one to tens of keV, produce distinct intensity spectra. When X-rays are collected by the EDXS detector, which is reverse biased, they generate a measurable charge pulse. The observed integrated intensity of characteristic X-ray in the generated spectrum is directly related to the concentration of each element. By determining the concentration of a given element in the specimen relative to others, the sample's composition can be defined. EDXS detectors can be equipped on both SEMs and TEM systems [103]. The interaction volume between the electron beam and the specimen is influenced by factors like the beam diameter and beam spreading. These, in turn, are determined by the beam

energy and sample thickness. To achieve spatially-resolved elemental information, a small probe size is typically chosen when scanning the electron beam across the specimen.

For analysis, users have the flexibility to choose either a single point or an area and then observe X-ray counts versus energy, resulting in a "*point and ID*" form of analysis. Alternatively, one can select a specific energy and scan over the entire specimen area, leading to counts of that distinct X-ray energy against different positions. These are termed compositional maps. Depending on the selection, these can be 1D elemental maps (line scans) or 2D elemental maps (area maps). In this research, the Tescan MIRA3 SEM equipped with an EDXS system was utilized to investigate the composition of NW samples.

2.3 Atomic Force Microscopy

Atomic force microscopy (AFM) is an advanced subset of scanning probe microscopy (SPM) that allows for the precise characterization of surface morphology at the nanometer scale. At the heart of the AFM is a cantilever equipped with a sharp tip with apex tip radius of ~10 nm. This cantilever oscillates near its resonance frequency, typically varying between 15 to 400 kHz [104].

To understand the operation of the AFM, one should be familiar with the principle of maintaining a consistent force between the cantilever's tip and the sample's surface. This force, denoted as *F*, is derived from Hooke's law:

$$F = -kX \tag{2.3}$$

Here, *k* represents the cantilever's spring constant, essentially indicating its stiffness, while *X* signifies the deflection or the distance that the cantilever bends. Generally, the force exerted during AFM measurements falls in the pico- to micro-Newton range, typically in an ambient atmosphere [104].

AFM operation can be broadly categorized into the three following modes:

- **Contact mode**: The tip is in constant "contact" with the sample, at a tip-sample separtion of < 10 Å, such that tip interacts with the sample's short-range repulsive field.
- **Non-contact mode**: The cantilever tip is lifted and hovers within a small distance (~50 Å to 150 Å) from the sample surface, such that it resides beyond the short-range repulsive field.
- **Tapping mode**: The tip hovers above the sample at a set deflection point beyond the short-range repulsive field, and oscillates at a constant frequency (near the fundamental

flexure resonance of the cantilever) at a constant, high oscillation amplitude. This mode is a favored mode for softer samples, as it imparts less damage compared to the contact mode, and concurrently offers more detailed data than the non-contact mode [104].

In the case of tapping mode AFM, the fundamental principle is relatively straightforward. As shown in Figure 2.6, the oscillating cantilever gently taps its sharp tip across the surface of the sample while a predefined region of interest is raster-scanned. This cantilever interacts with the sample, which rests on a piezoelectrically-actuated stage, and a laser beam is directed towards the cantilever's top surface, such that the reflected beam can be directed toward a quadrant-split photodiode detector. Feedback electronics measure and adjust the variable tip-to-sample distance in real-time. The reactive displacement of the stage then measures height variations, thereby tracking surface topography.

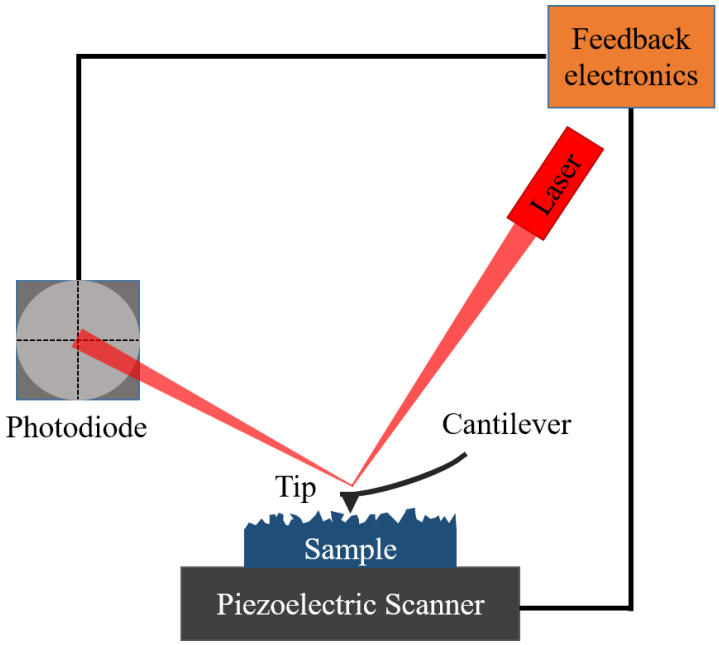

Figure 2.6. *Schematic of AFM setup where a cantilever with a sharp tip scans the surface. The deflection of the cantilever is measured through the reflection of a laser onto photodiode. A controller maintains constant tip oscillation or deflection via feedback electronics that adjust stage height.*

Chapter III

3 Localized Self-Assembly of InAs Nanowire Arrays on Reusable Si Substrates for Applications in Substrate-Free Optoelectronics

A low-cost and scalable approach is presented for synthesis of wafer-scale InAs nanowire (NW) arrays on photolithographically-patterned, reusable Si wafers using a localized self-assembly (LSA) epitaxial growth technique. Conventional *i*-line lithography is used to define arrays of 500 nm-diameter pores through 50 nm-thick SiO_2 layers, which serve as the LSA mask. A two-step, flowrate-modulated growth sequence is implemented to optimize selective-area self-assembly of NW arrays with over 80% yield and excellent control over placement of one NW, with mean diameter of 130 nm, inside each 500 nm pore. As-grown NW arrays are delaminated from the growth substrate, enabling fabrication of flexible membrane devices as well as reuse of Si wafers and growth masks while preserving the template pattern fidelity. Reuse of Si substrates for III-V epitaxy is demonstrated with and without pre-growth substrate restoration treatments. In both cases, the yield of NWs on reused wafers is comparable to that achieved in the original growth

run. Without substrate restoration procedures, the remnant base segments of NWs on parent wafers act as preferential sites for regrowth of vertical NWs. Transmission electron microscopy analysis reveals that the InAs lattice is coherently extended from the remnant NW base segments during regrowth. The delaminated InAs NW arrays are transferred to carrier wafers for fabrication of substrate-free photodetectors through use of an anchoring procedure, which preserves the original NW position and orientation. Under broadband illumination, the NW array-based photodetectors produce a photo-to-dark current ratio of 10^2, demonstrating the utility of the fabrication procedure employed. This work establishes a low-cost route toward III-V semiconductor-based flexible optoelectronics via LSA epitaxial growth of NW arrays on reusable Si wafers.

3.1 Background and Motivations

Semiconductor NWs have received great interest for optoelectronic applications due to their unique properties, as well as their controllable epitaxial growth and *in situ* doping [105]–[107]. In contrast to conventional bulk and thin-film geometries, a broad range of material compositions can be grown heteroepitaxially in NW form due to the small NW footprint and large free surfaces that allow efficient strain relaxation [15], [108], [109]. These unique properties provide great opportunities for electronic, optoelectronic, energy conversion, and energy storage applications [5], [43], [110], [111] with potential for incorporation within flexible device architectures [112]–[114]. In particular, III-V semiconductor NWs have received considerable interest as optoelectronic materials for photodetector (PD) applications. Using periodic arrays of coaxial NWs, the traditional tradeoff between external quantum efficiency and response speed can be overcome due to orthogonalization of the directions of photon absorption and carrier collection. Photodetectors that utilize NW array device geometries also benefit from highly selective resonant absorption and tunable spectral range of operation [18], [115], [58], [77].

Growth of periodically-arranged III-V NW arrays can be realized through various template-assisted epitaxial methods. One of the most common NW growth techniques is the Au-assisted VLS approach [116]. High growth rates, wide variability in dopant concentrations, and excellent control over NW crystal structure can be achieved using this growth mode [117]–[120]. However, the VLS approach faces several challenges, including: (a) compositional phase segregation effects, particularly during growth of ternary alloys;[121] (b) undesired incorporation of Au atoms from the catalyst; [34], [122] and (c) formation of graded junctions and compositionally-smeared heterointerfaces due

to the catalyst droplet reservoir effect [123], [124]. Moreover, in some cases, Au nanoparticles must be selectively etched in order to better accommodate the growth of coaxial NW architectures or to mitigate optical reflection losses [125], [35]. This introduces additional process complexity during synthesis and fabrication procedures. The above challenges can be either reduced or, at best, entirely overcome through growth of NWs via SAE. This growth mode enables several key advantages, including the ability to: (a) grow complex core-shell geometries and coaxial heterostructures; (b) realize abrupt junctions and heterointerfaces; and (c) avoid the need for Au nanoparticle deposition and selective etching steps [36].

Regardless of the growth mode, one of the main challenges for large-scale production of epitaxial III-V NW arrays is their synthesis cost [126], [127]. Some synthesis costs are inevitable; these include, for example, the costs of instrumentation, operation, and precursor sources. However, other major cost contributions, such as those associated with the growth substrate, are largely reducible and can be separated into two categories: (1) the cost of III-V wafers as the NW growth platform, and (2) the lesser cost of pre-epitaxial processing of masking templates used for position-controlled synthesis of periodic NW arrays. Novel nanofabrication procedures that can overcome both cost streams are desired for large-scale implementation of III-V NW-based technologies.

Key substrate requirements for most applications include epitaxial guidance for growth of vertically-oriented NWs and the ability to serve as a robust carrier platform for handling during device fabrication. Low-cost foreign substrates such as Si (111) wafers fulfil both of these requirements, and they have been routinely used instead of bulk III-V wafers in order to considerably curtail manufacturing costs [12], [128], [129]. However,

site-specific NW synthesis still requires the patterning of masking templates on starting wafers, which presents an additional cost barrier. A possible strategy for simultaneously reducing pre-growth processing costs and complexity is to reuse Si substrates with existing predefined growth masks for site-selective and seed-free growth of III-V NW arrays. Such a process requires delamination of as-grown NWs from the "parent" Si substrate and transfer to alternative handling platforms for further device processing in order to accommodate substrate reuse and preservation of the original masking template. Moreover, Si substrates would need to be reused fewer times than III-V substrates for recovery of wafer costs.

For conventional SAE growth, masking templates are used to define the number density, position, and periodic arrangement of the NWs [36]. Growth templates are typically defined by first depositing a thin SiO_x or SiN_x layer on the substrate and subsequently patterning arrays of nanopores, which expose the substrate through the masking layer and serve as sites for preferential nucleation and NW crystal growth. The nanopore arrays can be defined using various lithography techniques, such as electron-beam lithography (EBL), nanoimprint lithography (NIL), or nanosphere lithography (NSL), followed by either wet-etching or reactive-ion etching for substrate exposure inside the nanopores. Each of these lithographic approaches have their own limitations. For example, EBL is a costly and low-throughput approach, while NIL suffers from reproducibility challenges, and NSL faces limitations with respect to formation of patterns with long-range periodic order [130], [131]. Comparatively, conventional photolithographic patterning for fabrication of nanoporous masking templates is preferred with respect to cost, reproducibility, throughput, long-range order, wafer-scale

manufacturing, and compatibility with existing foundry processing lines. However, conventional photolithography is commonly prohibited for the synthesis of NWs due to the resolution limit.

Using a combination of the above strategies, in this study, we establish a procedure for low-cost and wafer-scale, "selective-area self-assembly" of III-V NWs with sub-lithographic dimensions on photolithographically-patterned and reusable Si substrates. This growth mode is henceforth referred to as the *localized self-assembly* (LSA) mechanism, and will be differentiated from both the conventional self-assembly and selective-area epitaxy modes for III-V NW synthesis in later sections of this chapter. We present an optimized growth parameter space with respect to the yield and aspect ratio of InAs NWs synthesized under a seed-free growth mode, whereby the NWs self-assemble inside predefined nanopores without occupying the full extent of each growth site. We chose InAs as a model material system for demonstration of this approach for two main reasons. Firstly, InAs serves as the binary basis for the growth of ternary III-V NW systems that enable tunability across a wide spectral range from short-wavelength infrared (SWIR; using ternary $In_xGa_{1-x}As$) to long-wavelength infrared (LWIR: using ternary $InAs_ySb_{1-y}$) for applications in photodetection. Secondly, the lattice-mismatch between InAs and the underlying Si substrate is sufficiently high to accommodate localized NW growth under a strain-limited, self-assembly regime (additional details regarding the growth mechanism are discussed in following Section 3.3 [132]–[137].

We provide a procedure for delamination of as-grown NW arrays, which allows for Si substrates to be reused without additional patterning of masking templates between subsequent regrowth steps. We demonstrate growth of NW arrays on recycled substrates

with comparable aspect ratio and yield upon regrowth. We provide two approaches for substrate reuse, including with and without the introduction of intermediate substrate restoration procedures, and we discuss the merits of both approaches. In the absence of an intermediate restoration procedure, remnant NW base segments left below the delamination fracture plane serve as preferential growth sites in subsequent growth runs. We show that the vertically-oriented InAs NW lattice is coherently extended along the axial growth direction during regrowth cycles. Lastly, we demonstrate a unique process flow for the fabrication of substrate-free NW-based infrared (IR) photodetectors that allows delaminated arrays to be transferred to foreign platforms while preserving the original position and orientation of the as-grown NWs.

The motivations outlined above provide strong incentives for exploring an innovative approach aimed at reducing the production cost of NWs for flexible IR PDs based on NWs. This comprehensive exploration considers all previously mentioned possibilities. Furthermore, the main focus of this work is the locally-confined self-assembly of InAs NWs with sub-lithographic dimensions on photolithographically-patterned Si wafers and the reuse of the parent wafers for subsequent III-V crystal growth runs without the need for intermediate processing steps prior to substrate reuse. This work enables the reduction of manufacturing cost of optoelectronic devices through LSA growth of III-V nanostructures on reusable Si substrates.

3.2 Substrate Pattering

Full 150 mm Si (111) wafers were used as growth substrate to grow NW arrays. The masking template for SAE growth was realized by first coating a parent Si wafer with a 50 nm-thick SiO_2 film via plasma-enhanced chemical vapor deposition (PECVD) with P5000 and deposition rate of 10 nm/sec. Afterwards AZ MIR 701 photoresist spin coating at 1000 rpm. Then conventional *i*-line ASML PAS 5500/200 stepper lithography was used with zero focal focus and 280 $mJ.cm^{-2}$ to expose the photoresist etch mask. After post exposure development, reactive ion etching (RIE) technique via P5000 was used to desirably etch the SiO_2 oxide mask and obtain wafer-scale arrays of hexagonally-arranged pores with 500 nm diameter and 1000 nm pitch. Optimized recipe with etch rate of 20 nm/min was used performed for 180 sec in order to make sure the pores are completely exposed, which is necessary for SAE growth. Figures 3.1(a) and 3.1(b) show the top-view and cross-section schematic of designed Si substrate with the masking templet, respectively.

In Figure 3.1(c), the tilted-view SEM image shows the fabricated Si substrate with a patterned growth mask. Pores, with a diameter of 500 nm, were selected based on the ASML stepper exposure limitation without applying anti-reflection treatment. Furthermore, a pitch of 1000 nm was chosen according to simulation studies that demonstrated, for longer wavelength strong absorption through periodical NW arrays, a larger pitch is more suitable [58].

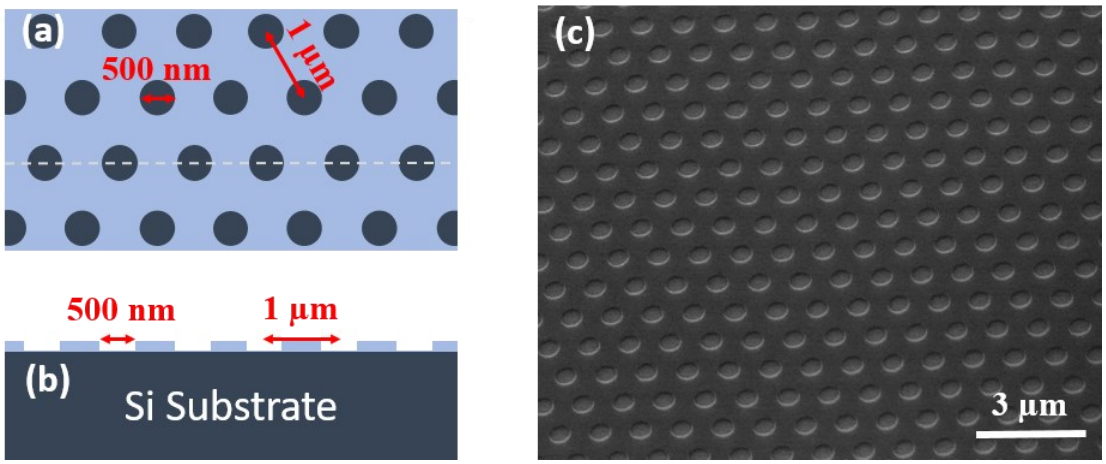

Figure 3.1. *Schematic of designed Si substrate with the masking templet (a) the top-view, (b) cross-section view, and (c) tilted-view SEM image of actual fabricated Si substrate with patterned growth mask.*

3.3 InAs Nanowire Growth and Optimization

Epitaxial growth of III-V NW arrays under the SAE regime is commonly carried out using oxide masking templates that are defined by electron-beam lithography (EBL) [92], [138], [139]. This technique provides excellent control over the position, growth rate, and, consequently, dimensions of the SAE NWs. However, EBL is also associated with high costs and prohibitively long processing times for wafer-scale template fabrication. To overcome these limitations, standard *i*-line photolithography is employed here to oxide masking templates on 150 mm-diameter Si wafers. The first objective of this work is to tune the MOCVD growth parameters in order to realize a high total yield of NWs with only single NW occupation per nanopore. Three different sets of LSA growth conditions are investigated toward optimization of yield and aspect ratio of InAs NWs. The samples grown under these three sets of conditions are referred to as Samples A, B, and C, as summarized in Table 3.1 and are described in the following paragraph.

Vertically-oriented InAs NW arrays were grown using a 3×2" close-couple showerhead AIXTRON metalorganic chemical vapor deposition (MOCVD) reactor. Three distinct sets of growth conditions were investigated (henceforth, referred to as Samples A, B, and C) under different group-III precursor flowrates in order to optimize NW yield and single NW per pore placement. Prior to loading in the MOCVD reactor, samples were rinsed with standard solvent and the native oxide of the Si substrate exposed through each pore was etched during a 5 s buffered-oxide etching (BOE) treatment. Trimethylindium (TMIn; $In(CH_3)_3$) and arsine (AsH_3) were used as gas-phase precursors for the supply of In and As growth species, respectively. All samples were first subjected to a 5 minute annealing treatment at 850 °C under AsH_3 flow in order to improve the growth yield,

similar to what was reported to favor NW growth along the vertical <111> direction over other equivalent <111> directions [140], [141]. Next, the reactor was cooled to a growth temperature of 700 °C. All temperature values reported here refer to the thermocouple-controlled reactor set-point value. The AsH_3 flowrate and the chamber pressure were maintained at 365 µmol/min and 100 mbar, respectively, for all growths. Table 3.1 summarizes the key growth conditions for the various samples investigated in this study. Sample A growth was performed using a TMIn flowrate of 1 µmol/min over a 25 minute growth duration.

Table 3.1. *Summary of relevant growth conditions and NW details for all samples.*

Sample	Pre-Growth Processing	Substrate Reuse	Growth Sequence	Growth Time (s)	TMIn (µmol/min)	V/III	NW Aspect Ratio	Single NW Occupation Yield (%)
A	Solvent Cleaning 5 s BOE	No	NW Growth	1500	1	365	100 ± 12	31.4
B	Solvent Cleaning 5 s BOE	No	Nucleation Step	60	16	22.8	11 ± 5	67.7
			NW Growth	1500	1	365		
C	Solvent Cleaning 5 s BOE	No	Nucleation Step	30	16	22.8	34 ± 9	81.3
			Growth Step	1500	1	365		
D	Citric Acid Etch Solvent Cleaning 5 s BOE	Yes	Nucleation Step	30	16	22.8	38 ± 10	75.1
			Growth Step	1500	1	365		
E	Solvent Cleaning	Yes	Growth Step	1500	1	365	61 ± 11	80.4

A two-step, flowrate-modulated growth sequence was introduced for Samples B and C to increase the NW yield. In order to increase the number of nucleation sites, during the first growth step (i.e., the nucleation step), the substrate surface was flooded with a high TMIn flowrate of 16 μmol/min for a period of 60 s and 30 s for Samples B and C, respectively. During the second step (i.e., the growth step), the TMIn flowrate was reduced to 1 μmol/min for a period of 25 minutes. Figure 3.2(a)-(c) represent tilted-view SEM images obtained from as-grown Samples A-C, respectively.

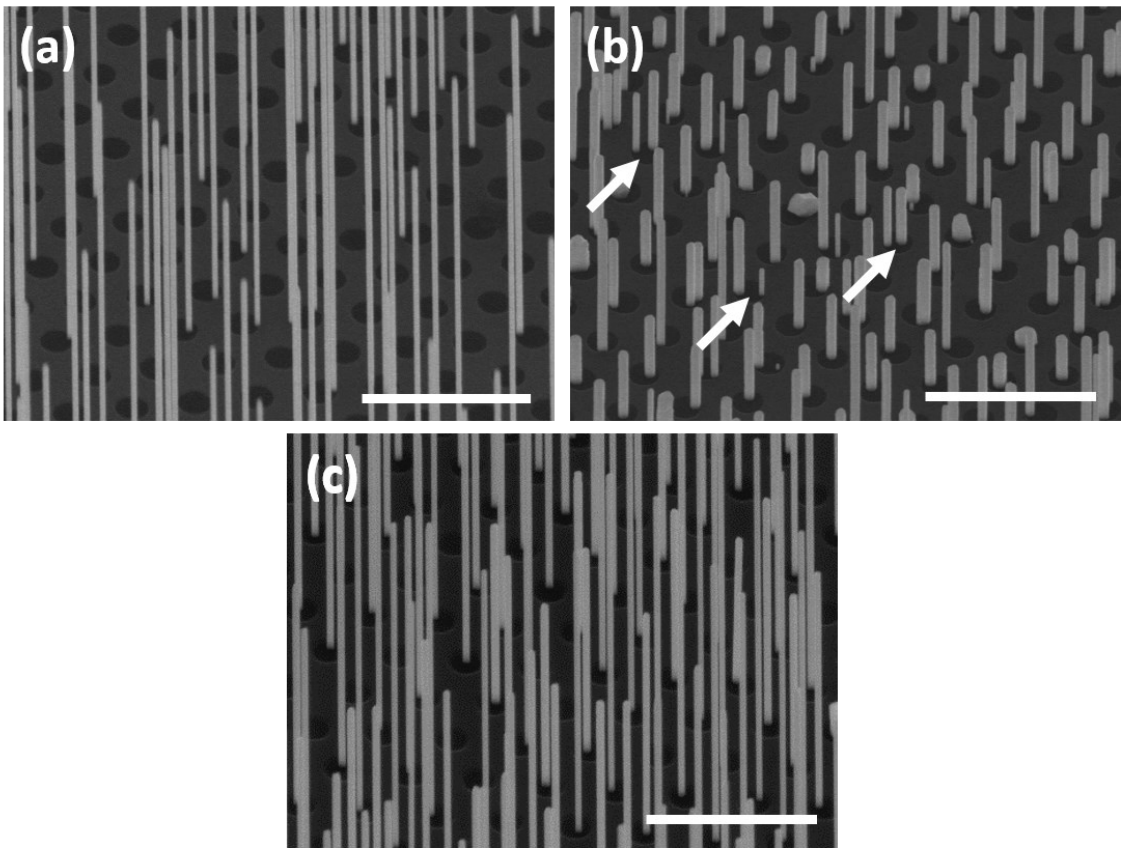

Figure 3.2. *Tilted-view SEM images of LSA-grown InAs NWs. (a) Sample A, grown in a one-step process without a separate nucleation step. (b) Sample B, grown using the two-step, flowrate-modulated sequence with 60 s nucleation step. Arrows point to three examples of nanopores in which more than one NW are formed. (c) Sample C, grown using the two-step sequence with 30 s nucleation step. Scale bars represent 3 μm.*

For each sample set, dimensional analysis is performed by measuring more than 100 NWs from different sample locations, while yield analysis is conducted based on the occupancy of more than 400 nanopores across four regions on each sample. Based on these measurements, the calculated mean NW aspect ratio (blue data points) and NW yield (gray bars) values for each of the three samples are presented in Figure 3.3. The yield measurements are sub-categorized as total yield, which is defined as the percentage of nanopores occupied by at least one vertical InAs NW (light gray bar), and as single NW occupation yield, which is defined as the percentage of nanopores occupied by exactly one vertical InAs NW (dark gray bar).

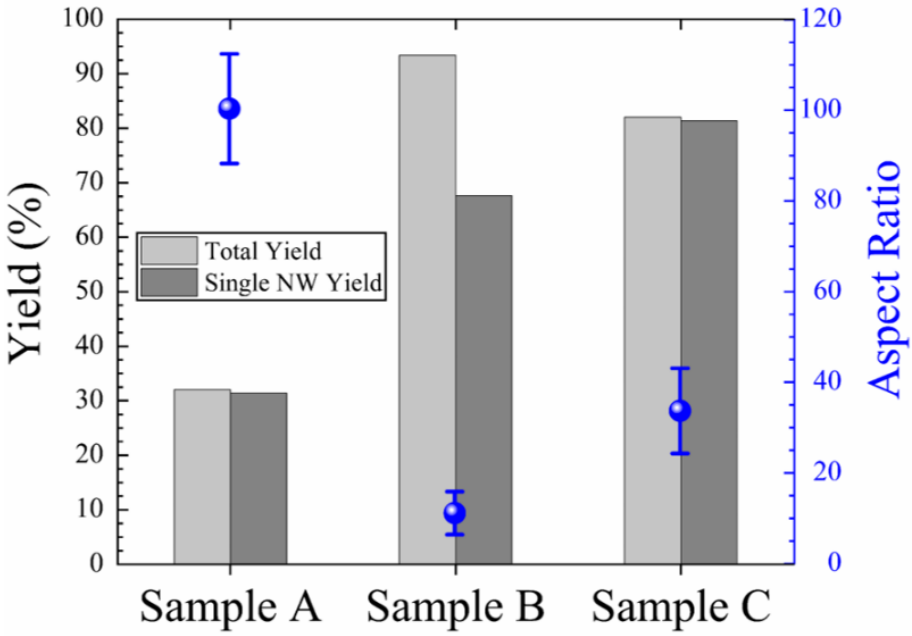

Figure 3.3. *Measured values for total yield (light gray bars) and single NW occupation yield (dark gray bars), as well as mean NW aspect ratio (blue data points; error bars represent ± one standard deviation from the mean) for Samples A – C.*

For Sample A NWs, which are grown without a high flowrate nucleation step, a mean length of 11320 ± 1250 nm and mean diameter of 113 ± 9 nm is measured (errors represent one standard deviation from the mean). We note from Figure 3.2 that most NWs are grown near the peripheral pore regions. While the exact basis of this effect is currently unclear, we speculate that it may be related to the higher capture probability of stable nuclei, which preferentially form at the edge of the pores due to a greater supply of diffusive adatoms from the neighboring oxide field. Yield analysis reveals that 32% of all patterned nanopores are occupied by NWs, while only a negligible fraction of nanopores are occupied by two or more NWs, resulting in a measured single NW occupation yield of 31%. To increase the number of occupied pores, a two-step sequence is introduced during growth of Sample B NWs. First, the substrate is flooded with a high TMIn flowrate of 16 μmol/min for 60 seconds in order to promote NW nucleation inside the exposed pores. Next, the TMIn flow is reduced to 1 μmol/min for a period of 25 minutes in order to promote adatom surface migration, leading to axial extension of the InAs lattice at each nucleation site. Sample B NWs, shown in Figure 3.2(b), exhibit a mean length of 2216 ± 548 nm and a mean diameter of 176 ± 21 nm. Use of the two-step growth sequence results in a total yield of 93%. However, a higher fraction of pores are occupied by more than one NW. The white arrows in Figure 3.2(b) point to three examples of nanopores in which two NWs are formed. This effect results in a single NW occupation yield of only 68% in Sample B.

The undesired multiple NW occupancy effect is resolved in Sample C, simply by reducing the duration of the initial high-flowrate nucleation step from 60 seconds to 30 seconds. A reduction in the number of nucleation sites and distribution of growth species

amongst correspondingly fewer NWs lead to the formation of higher aspect ratio structures in comparison to Sample B. This is quantified by a mean length of 4377 ± 878 nm and mean diameter of 132 ± 17 nm for Sample C NWs. Figure 3.2(c) shows an image of Sample C NWs, which exhibit a total yield of 82% and a single NW occupation yield of 81%, indicating that only a negligible fraction of the nanopores contain multiple NWs. This can be explained by nucleation probability based on two factors: TMIn flowrate and time. As the TMIn flowrate increases, the surface migration length of group-III adatoms decreases, consequently leading to an increased probability of nucleation, as it was observed in the case of Sample B with multiple NWs per pore. Nucleation can occur at any time during the growth process, and as time increases, the probability of nucleation also rises. Therefore, the duration of the so-called "nucleation" step was decreased while maintaining the higher TMIn flowrate (i.e., 16 μmol/min) in order to reduce the probability of multiple NW formation in each pore, while still achieving a high occupation yield. The growth conditions of Sample C provide a suitable basis, with respect to NW yield and aspect ratio, for additional Si wafer reuse and substrate-free device fabrication experiments discussed in Section 3.5. For all three samples, no parasitic crystal growth is observed on the oxide mask, which is one indication that growth may proceed under a selective-area regime.

During SAE growth, island nucleation occurs preferentially inside the patterned nanopores due to the large sticking coefficient differential between the masking layer (i.e., SiO_2) and the exposed substrate (i.e., Si). In the current work, the large lattice mismatch between InAs and Si (i.e., ~11.6%) and the corresponding lattice strain lead to a high interfacial surface energy, which limits lateral expansion of nuclei inside the template pores. Thus, direct InAs island nucleation from the vapor phase becomes energetically

favorable without wetting layer formation according the Volmer-Weber growth mode, which can proceed in the absence of metallic seeding agents [134], [135]. Since the InAs islands are epitaxially registered to an atomically flat Si substrate with (111) surface orientation, subsequent crystal growth proceeds preferentially along the vertical $\langle 111 \rangle$ direction of the InAs lattice [136]. Thus, vertical and free-standing NWs can be formed under a pseudo-Volmer-Weber regime [134], [135].

Due to the large pore size of 500 nm used here, strain-limited self-assembly results in NWs that do not fully occupy the exposed substrate area inside each pore [139]. This allows only coarse control over the exact position of NWs inside template pores of relatively larger diameter and, under certain conditions, can lead to the formation of multiple NWs in a single pore. This is in contrast to the case of a more closely lattice-matched system, such as GaAsP on Si, for which the SAE-grown nanocrystals extend across the full area of the template nanopores under otherwise comparable SAE conditions. For growth of InAs on Si, the fact that NW diameter is not strictly dictated by the template nanopore diameter also results in the formation of NWs with a range of heights. The large standard deviation values associated with the aspect ratio data shown in Figure 3.3 illustrates this point.

Figure 3.4 shows a comparison of different catalyst-free growth modes for epitaxy of InAs and GaAsP NWs on Si by MOCVD. Figure 3.4(a) shows a representative SEM image of InAs NWs grown on a bare Si (111) substrate with no masking template. This represents the direct self-assembly growth mode. Resulting NWs show large variances in diameter, length, and spacing. Due to the large lattice mismatch between InAs and Si, growth proceeds under a pseudo-Volmer-Weber growth regime, which results in

randomly-distributed individual NWs. Figure 3.4(b) show InAs NWs formed under the LSA regime on a Si (111) through an oxide masking template containing a hexagonal array of pores with 500 nm diameter and 1000 nm pitch. The growth template serves to define InAs nucleation sites inside the pores while the high lattice mismatch between InAs and Si inhibits lateral expansion of NWs under the growth conditions employed. This results in selective-area self-assembly of NWs that occupy only a fraction of the total pore area. In contrast, Figure 3.4(c) shows $GaAs_{0.73}P_{0.27}$ nanocrystals grown under the selective-area epitaxy regime on a Si (111) substrate containing the same oxide masking template as that used for InAs LSA growths. Nucleation is limited to the pore sites. Due to the smaller lattice mismatch between $GaAs_{0.73}P_{0.27}$ and Si (i.e., ~3.1%), the nanocrystals laterally extend to fully occupy all pores. Thus, the LSA growth mode exhibits a combination of the characteristics of the direct self-assembly and selective-area epitaxy regimes.

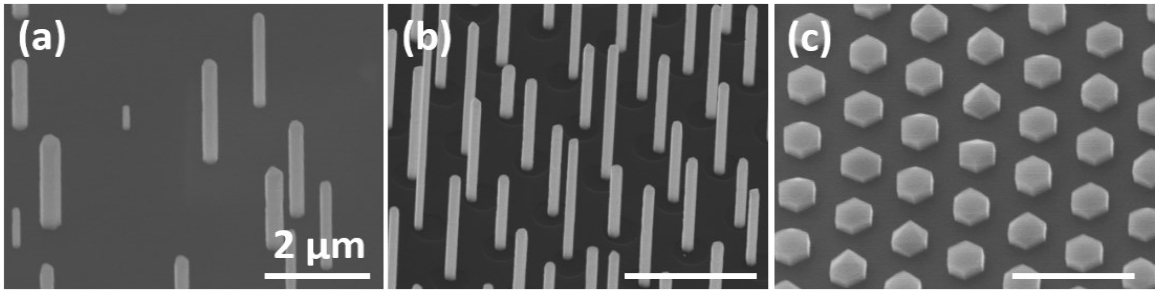

Figure 3.4. *Tilted-view SEM images of (a) direct self-assembly growth of InAs on bare Si (111) with no template, (b) localized self-assembly growth of InAs on Si substrate with masking template of 500 nm diameter pores with 1000 nm pitch, and (c) selective-area epitaxy of GaAsP on Si using the same masking template as shown in (b) and under otherwise similar growth conditions. Scale bars represent 2 µm.*

These features distinguish the current approach from the conventional NW SAE growth mode, where NW diameters are commonly equal to or exceed the nanopore dimensions. We emphasize this distinction by referring to our growth mode as "localized

self-assembly". A similar description was recently adopted by Dubrovskii et al. for Ga-droplet assisted epitaxy of GaAs NWs on Si substrates through microscale pores of oxide masking layers [142]. We also note that Gao et al. have reported a dual growth regime wherein InP NW epitaxy can simultaneously proceed via both SAE and VLS regimes under the same growth conditions depending on NW diameter [143]. To investigate the possibility of In-droplet mediated NW synthesis in the current work, we have carried out an additional growth under Sample C conditions, but in the absence of AsH_3 flow during the cooling stage. Thus, NW growth was terminated by simultaneously stopping both group-III and group-V precursor flows. Here, no isolated In phase (i.e., seeding droplet) was observed at the NW tip, as determined by TEM and EDXS analysis as shown in Figure 3.5. This is in contrast to the observation of In droplets at the tip of thinner InP NWs grown under otherwise SAE conditions reported by Gao and colleagues [143]. Given that our growth process precludes a group-III species pre-deposition step and that In droplets were not observed at the NW tip under AsH_3-free cooling conditions, we believe that the current LSA growth mode is more comparable to the seed-free SAE mechanism than localized VLS growth.

To better understand whether LSA growth of InAs NWs proceeds via the In droplet-assisted mechanism or the self-assembly mechanism, the tip structure of NWs is investigated. Since a potential In droplet at the NW tip will crystalize as InAs during the post-growth cooling stage under a continual supply of AsH_3, an additional growth is carried out under Sample C conditions, but growth is terminated by simultaneously stopping the supply of both TMIn and AsH_3 precursors. Any In droplets responsible for NW growth should be observable in such a sample, as has previously been observed by Gao and

colleagues [143]. After growth, NWs are removed from the growth substrate via sonication and deposited on lacey carbon TEM grids. Similar to previously published work [144], the tip segments of the deposited NWs can be identified under TEM based on a either truncated facet profile in the case of seed-free self-assembly growth or based on the presence of a separate In phase in the case of VLS growth. Figure 3.5(a) illustrates schematic representation of the growth sequence with temperature and precursor flows over time. Figure 3.5(b) shows TEM image of an InAs NW grown under the modified Sample C conditions with AsH_3-free cooling stage, and Figure 3.5(c) represents EDXS linescan showing X-ray signal intensities representative of elemental In (black) and As (red) as measured over the positions indicated by the white dotted line in (b). In Figure 3.5(b), no separate In droplet is observed at the NW tip. The EDXS linescans show no noticeable variation in the relative In and As signal intensities along the tip of the NW. This indicates that the tip region is composed of a single InAs phase. We believe the absence of a separate In phase at the NW tip demonstrates the likelihood that growth of InAs NWs in the current work does not proceed via the VLS mode

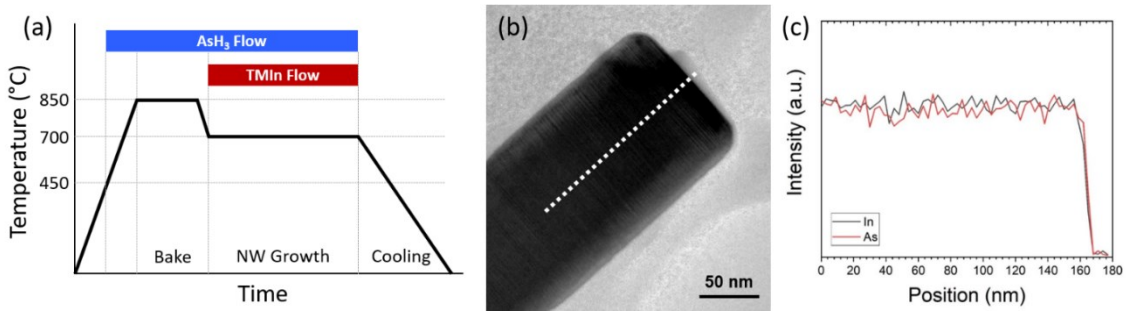

Figure 3.5. *(a) Growth sequence employed for InAs NW growth with simultaneous termination of AsH_3 and TMIn precursors. (b) TEM image of the tip of an InAs NW grown under the sequence depicted in (a). (c) EDXS linescan corresponding to location marked by a white dotted line in (b). Elemental counts of In and As are shown in black and red, respectively.*

3.4 Delamination Procedure, Substrate Restoration, and Reuse

3.4.1 Si Substrate Reuse

After optimizing the growth conditions, the next step involves NW arrays delamination to enable reusing the native patterned substrate in subsequent growth generations. In this section, we will delve into the details of the delamination process and the restoration of the substrate for subsequent growth.

For delamination of InAs NW arrays, the Colorless First Contact^{TM} (CFC) polymer was applied to as-grown samples by drop-casting small volumes of the polymer solution. After drying under ambient conditions for ~24 h, the NW array-embedded membranes were mechanically delaminated from their native growth substrates through shear-induced fracture. After delamination, all substrates were treated with the First Contact^{TM} Thinner solution to ensure dissolution of residual CFC polymers on the surface. Then, two different methods were investigated for substrate reuse. In the first method, substrate restoration to the pre-growth state was investigated. In this case, substrates were treated with either a citric acid or a piranha solution in order to selectively etch the InAs NW base segments that remained attached to the substrate in each pore (i.e., below the NW fracture plane). After rinsing with standard solvents and a pre-growth BOE treatment, the restored substrates (i.e., Sample D) were loaded in the MOCVD reactor for reuse and growth of second generation InAs NW arrays using a two-step growth sequence (i.e., same growth sequence as Sample C). In the second substrate reuse method, post-delamination wafers (i.e., Sample E) were simply rinsed with standard solvents and then directly reloaded in the

MOCVD reactor for growth of second generation InAs NW arrays without intermediate substrate restoration steps to etch the remnant NW base segments formed during the initial growth cycle. Sample E NWs were grown under otherwise identical growth conditions as Sample A NWs.

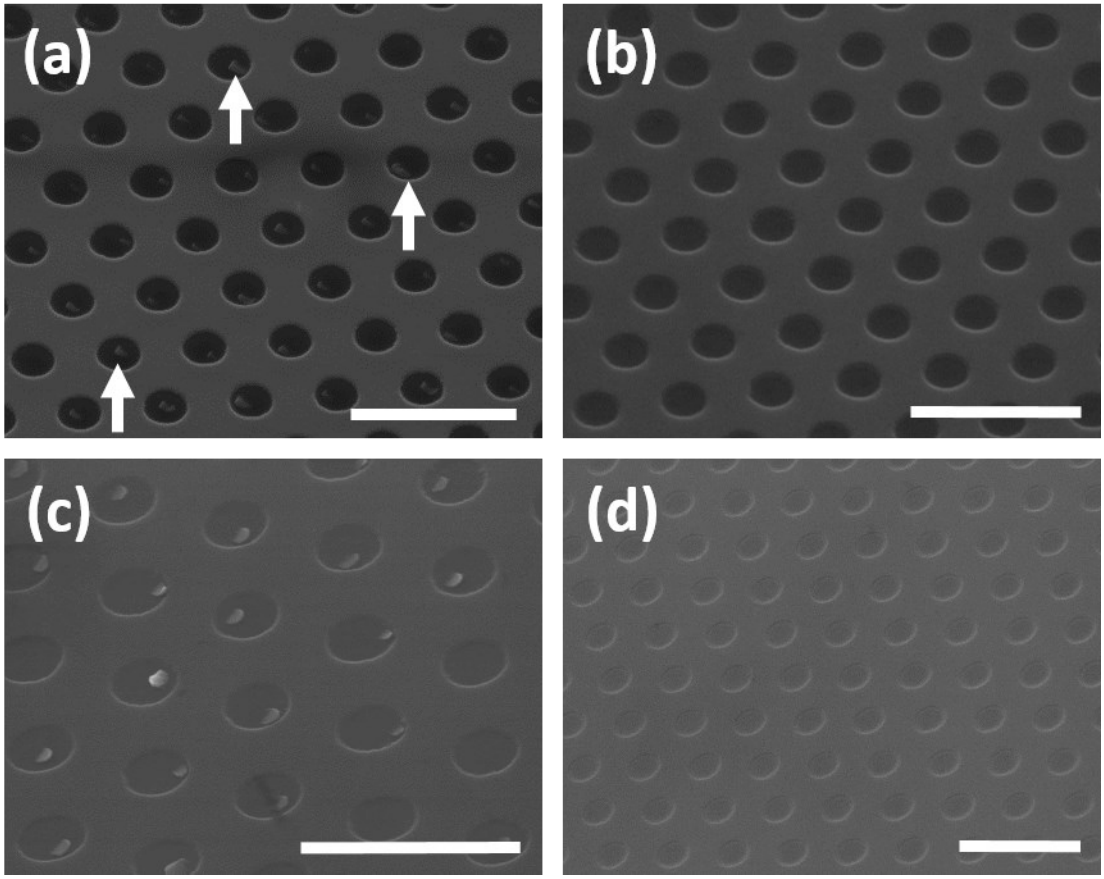

Figure 3.6. *Tilted-view SEM images of the parent SiO_2-templated growth substrate (a)and (c) immediately after NW array delamination, and (b) and (d) after restoration via a citric acid and Piranha wet-etching treatment, respectively Arrows in (a) point to three examples of pores in which remnant NW base segments can be seen. Scale bars represent 2 µm for (a), (b) and (c), whereas scale bars represent 3 µm for (d)*

Before investigating the reuse of Si substrates for multiple III-V crystal growth runs, Sample C NW arrays are delaminated from the parent wafer. Figures 3.6(a) and 3.6(c) show SEM images of the Sample C Si substrate and oxide masking template immediately

after the delamination step. After NW array peel-off, the oxide masking layer remains fully intact. However, short NW base segments are observed inside the pores, which reveal the fracture plane induced during delamination. Three examples of clearly identifiable remnant NW base segments are indicated by white arrows in Figure 3.6(a).

The fracture surface profile and average height of the remnant base segments after NW delamination were measured using AFM. A Bruker DI-3000 atomic force microscope (AFM) was used in the intermittent contact mode for imaging and NW base segment height profilometry. Figure 3.7(a) shows an AFM image of a representative nanopore in which a NW base segment is visible after the delamination step. The height profile of this base structure is shown in Figure 3.7(b), which corresponds to the line segment spanning points A to B marked in Figure 3.7(a). A graded fracture profile is observed and a base segment height of ~16 nm is measured at its apex (i.e., maximum height relative to substrate surface baseline). Based on similar analysis of over 30 pores, a mean apex height of 20.6 ± 5.1 nm is measured for the NW base segments after peel-off.

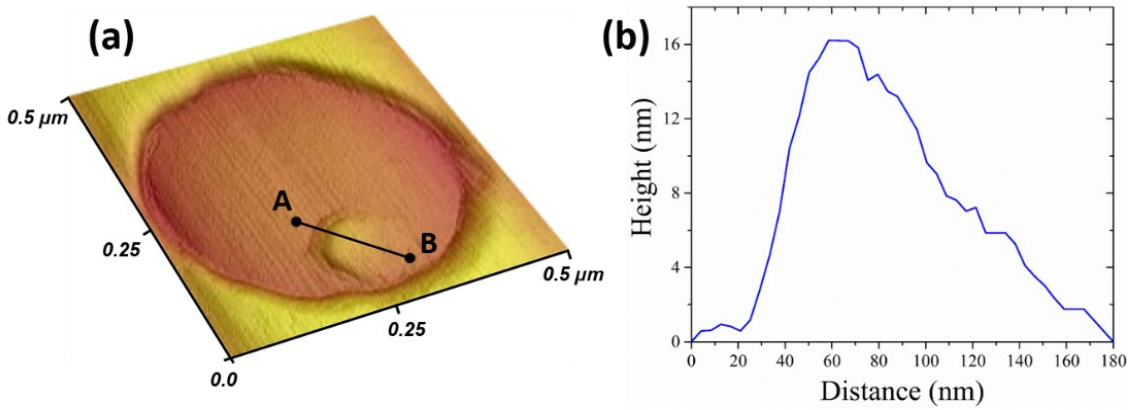

Figure 3.7. *(a) AFM image collected along a masking template nanopores after NW array peel-off, revealing a NW base segment inside the pore that was left behind below the NW's fracture plane. The hexagonal cross-section profile of the NW can be seen toward the left-hand side of the base segment. (b) Corresponding AFM height profile measured across points A and B in (a).*

For Si substrate reuse investigations, two different strategies are employed. In the first approach, the post-delamination growth substrates were subjected to a citric acid ($C_6H_8O_7$:H_2O_2, 20:1) treatment for 5 minutes to selectively etch the remnant InAs NW base segments inside the template nanopores. Figure 3.6(a) shows the surface of the parent Si wafer immediately after NW array delamination. As shown in Figure 3.6(b), the citric acid treatment fully restores the Si substrate to its initial pre-growth state without damaging or unintentionally inducing porosity in the oxide masking template. In the second approach, the growth substrates were treated by Piranha solution (C_2SO_4:H_2O_2, 3:1) for 5 minutes to return the oxide-templated parent substrate to its pre-growth condition. Figures 3.6(c) and 3.6(d) show the post-delamination parent substrate and after Piranha solution treatment, respectively. In both cases, no InAs crystallites are observed after the selective etching treatments and the masking template is preserved for reuse. The citric acid treatment is favored over the piranha solution treatment in this work due to chemical compatibility with subsequent device fabrication processes; namely, for the height adjustment process to chemically etch extended InAs NW tip segments, which will be discussed in detail in Section 3.5.

In order to verify the feasibility of the restoration process as an intermediate step toward reuse of Si substrates with masking templates, the flowrate-modulated LSA sequence (i.e., under Sample C growth conditions) is performed on parent Si wafers after InAs NW array delamination and citric acid treatment. Figure 3.8(a) shows a representative SEM image of as-grown NWs on a restored and reused Si substrate; henceforth, referred to as Sample D. A mean length of 5065 ± 1244 nm and mean diameter of 133 ± 16 nm (i.e., aspect ratio of 39 ± 10) are measured in the case of Sample D NWs. Total yield and single

NW occupation yield values are measured to be 77% and 75%, respectively, on the reused substrates after the restoration treatment. Thus, similar NW dimensions and yield values are realized in the preliminary growth run on parent substrates (Sample C) and in the secondary growth run on reused substrates (Sample D). Compared to conventional substrate reuse methods for thin films that are intended to mitigate the high cost of III-V wafers, such as the epitaxial liftoff (ELO) technique[145], the NW array delamination and wet chemical etching approach reported here offers the following advantages: (a) liberation of active device structures without the need for either growth or subsequent chemical etching of sacrificial release layers; (b) elimination of the additional processing steps, dedicated instrumentation, and high costs associated with chemo-mechanical polishing (CMP) procedures (we note that prior demonstration of an ELO procedure without use of CMP has also been presented by Cheng et al. [146]); and (c) replacement of starting III-V wafers with reusable Si substrates.

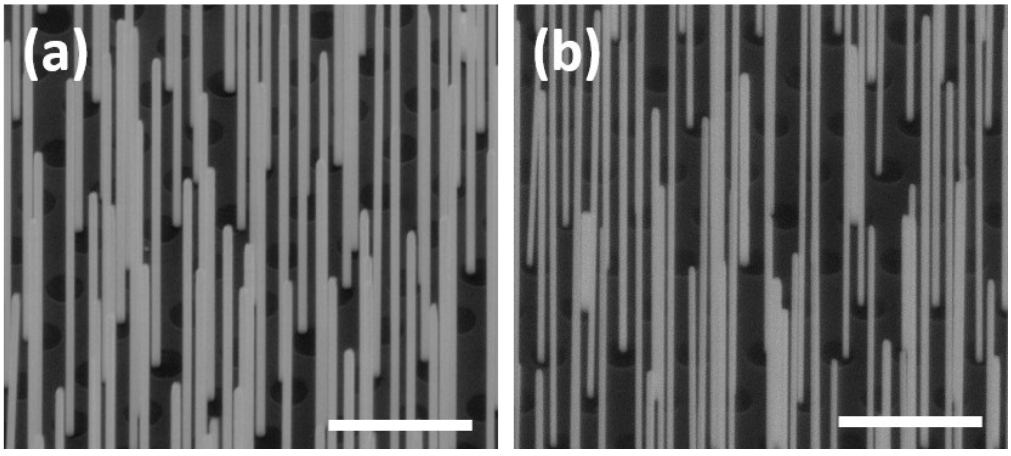

Figure 3.8. *Tilted-view SEM images of InAs NW arrays grown on reused Si substrates. (a) Sample D, grown following a citric acid restoration procedure and BOE treatment. (b) Sample E, grown directly after delamination of the parent NW array without an intermediate restoration procedure or BOE treatment (only solvent cleaning). Scale bars represent 2 µm.*

However, the substrate reuse approach described for Sample D has a critical drawback. Due to the formation of a native oxide layer inside the nanopores of the LSA making template after substrate restoration, a pre-growth BOE treatment is needed prior to loading the reused substrates in the growth reactor. This imposes a limit on the number of times each oxide-templated substrate can be reused due to continual dissolution of the masking layer, which has an etch rate of ~80 nm/min in the BOE solution employed here [147]. We were able to reuse the patterned Si substrate three times when employing the intermediate citric acid treatment and BOE procedure before the SiO_2 template was dissolved as a result of the pre-growth oxide etching step. One approach for extending the longevity of the masking layer is to use a silicon nitride template [27], which allows a high etch rate selectivity of the native oxide over the LSA mask [148]. However, an even simpler alternative is adopted here. This alternative approach involves elimination of the substrate restoration procedure and pre-growth BOE step, such that parent Si wafers with masking templates and remnant NW base segments are reused after NW array delamination. Here, the remnant NW base segment inside each pore serves as a preferred growth site for direct extension of the InAs lattice along the substrate normal direction (i.e., axial NW growth direction). This approach potentially allows a greater number of substrate reuse cycles to be realized compared to a procedure that requires pre-growth wet etching of the substrate native oxide.

To investigate the potential for direct re-growth, Sample E substrates are loaded in the MOCVD reactor following the NW array delamination procedure and a solvent rinsing step. Since the template pores are occupied by remnant NW base segments that serve as preferential growth initiation sites, the nucleation step, which is necessary in the case of

Samples B – D, is eliminated from the Sample E growth sequence. Figure 3.8(b) shows a representative tilted-view SEM image of as-grown Sample E NWs after growth on reused substrates with no restoration procedure. Vertical extension of the remnant base segments is realized, leading to the growth of NWs with mean length of 6285 ± 1474 nm and mean diameter of 99 ± 11 nm. Total NW yield and single NW occupation yield values of 81% and 80% are measured for Sample E, respectively, which match well with the yield values of the initial LSA growth run on parent substrates (i.e., Sample C). A comparison of NW aspect ratio and yield data for Sample D (substrate reuse after citric acid restoration) and Sample E (substrate reuse without restoration) is shown in Figure 3.9. In both substrate reuse approaches, the original pattern fidelity and NW verticality are preserved.

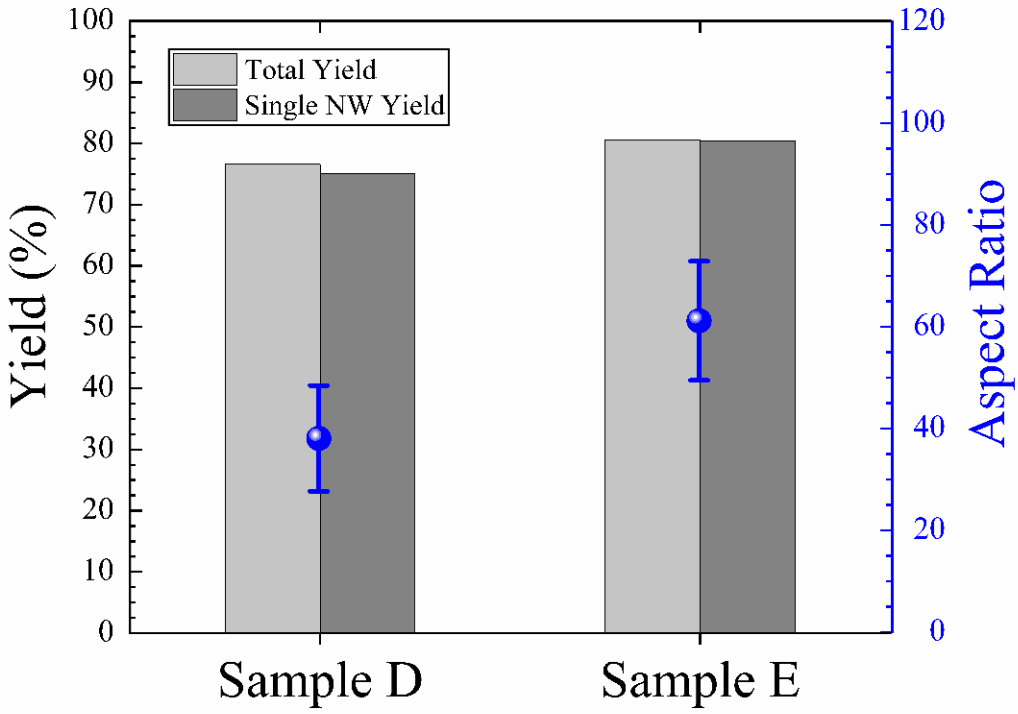

Figure 3.9. *Measured values for total yield (light gray bars) and single NW occupation yield (dark gray bars), as well mean NW aspect ratio (blue data points) for Samples D and E.*

Next, the crystal structure of Sample E NWs that are extended from the remnant base segments on reused Si wafers is investigated using TEM. A FEI Strata 400 STEM focused ion beam (FIB) was used for preparation of lamellae for analytical transmission electron microscopy (TEM) experiments. Emphasis is placed on inspecting the crystal structure along the NW base region about the anticipated delamination fracture plane. As noted above from AFM analysis, this region of interest is located ~20.6 ± 5.1 nm from the InAs/Si interface and serves as the location of InAs lattice extension during the regrowth sequence. Figure 3.10(a) shows a low-magnification, bright-field TEM image of two neighboring vertical InAs NWs on the reused substrate, where the SiO_2 masking template is false-colored in blue. Figures 3.10(b) and 3.10(c) show higher-magnification bright-field and HR-TEM images, respectively, collected along the reused substrate/InAs interface of the NW seen on the left-hand side of panel (a).

In Figure 3.10(c), the substrate interface is marked by a white dashed line, while the region corresponding to the anticipated delamination fracture plane (i.e., regrowth initiation region) is marked by a white border. Figures 3.10(d) and 3.10(e) show bright-field and HR-TEM images, respectively, collected along a segment of the same NW that is located approximately 500 nm from the Si/InAs interface. Along the entire length of the NW, including the regions corresponding to the remnant base segment of the parent NW and the regions above the regrowth initiation plane, a mixed crystal structure consisting of a combination of zinc-blende and wurtzite phases is observed. Fast Fourier transform (FFT) patterns generated from the lattice-resolved HR-TEM images are shown in Figure 3.11.

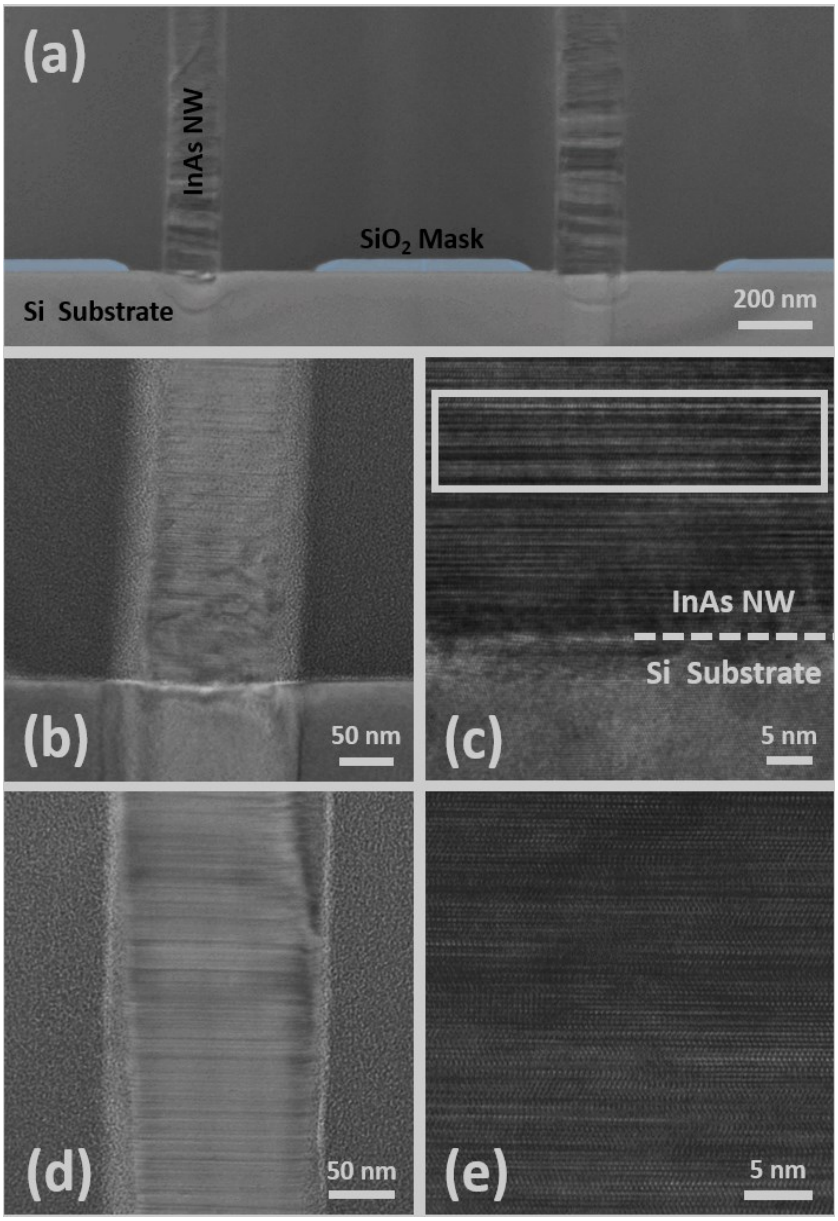

Figure 3.10. *TEM images of InAs NWs grown from remnant base segments on parent Si substrates, which were reused without restoration procedures. (a) Low-magnification bright-field image of two adjacent NWs. The oxide masking layer between NW is false-colored in blue. (b) bright-field TEM and (c) HR-TEM images collected at the InAs NW/Si substrate interface. The white box in (c) indicates the anticipated region of InAs lattice extension during the regrowth sequence. (d) bright-field TEM and (e) HR-TEM images collected along a region approximately 500 nm above the NW/substrate interface.*

The coincident symmetries of the FFT patterns and comparable streaking along the growth direction confirm the mixed phase lattice arrangement that is common to both

remnant base and regrowth segments. This polytypic crystal structure is characteristic of InAs NWs grown under both SAE [149], [150] and self-assembly [134], [151] growth modes on various substrates. Considering that the polytype crystal structure is commonly observed under the growth condition used in this study [140], [151], [152], no additional lattice discontinuities, variations in the crystal structure, or extended defect phases are introduced as a result of the regrowth procedure. A higher magnification image and corresponding SAED pattern obtained at the interface between the regrown NW and reused substrate, along with elemental linescans and maps obtained using EDXS, are provided in Figure 3.11.

Analytical TEM of InAs NW Growth on Reused Si Substrate was performed. Figure 3.11(a) shows a HR-TEM image obtained along the InAs/Si interface. The InAs lattice extends along the vertical growth direction and stems from the remnant base of a NW on the parent Si substrate, allowing substrate reuse without restoration. Figure 3.11(b) shows a selected-area electron diffraction (SAED) pattern collected at the InAs/Si interface along the $\langle 1\bar{1}0 \rangle$ zone axis. Three sets of distinguishable diffraction spots are indexed. These include reflections from the Si substrate (white) as well as a combination of diffraction spots stemming from zincblende InAs (yellow) and wurtzite InAs (blue) segments. The superposition of SAED patterns characteristic of both cubic and hexagonal InAs phases and visible streaking along the $\langle \bar{1}\bar{1}\bar{1} \rangle$ direction highlight the mixed-phase crystal structure of NWs grown under the selective-area self-assembly mode. Figures 3.11(c) and 3.11(d) show FFT patterns generated from HR-TEM images collected at the InAs/Si interface (i.e., representative of the InAs NW remnant base segment) and along the NW body (i.e., representative of the “regrown” InAs lattice), respectively. The matching

FFT pattern symmetry and consistent streaking along the $[\bar{1}\bar{1}\bar{1}]$ direction indicates that the mixed phase crystal structure is common to both the originally grown and the regrown NW segments. Figure 3.11(e)-(h) show a HAADF-STEM image and elemental In, As, and Si maps with superimposed linescans, respectively, from the corresponding area collected using EDXS.

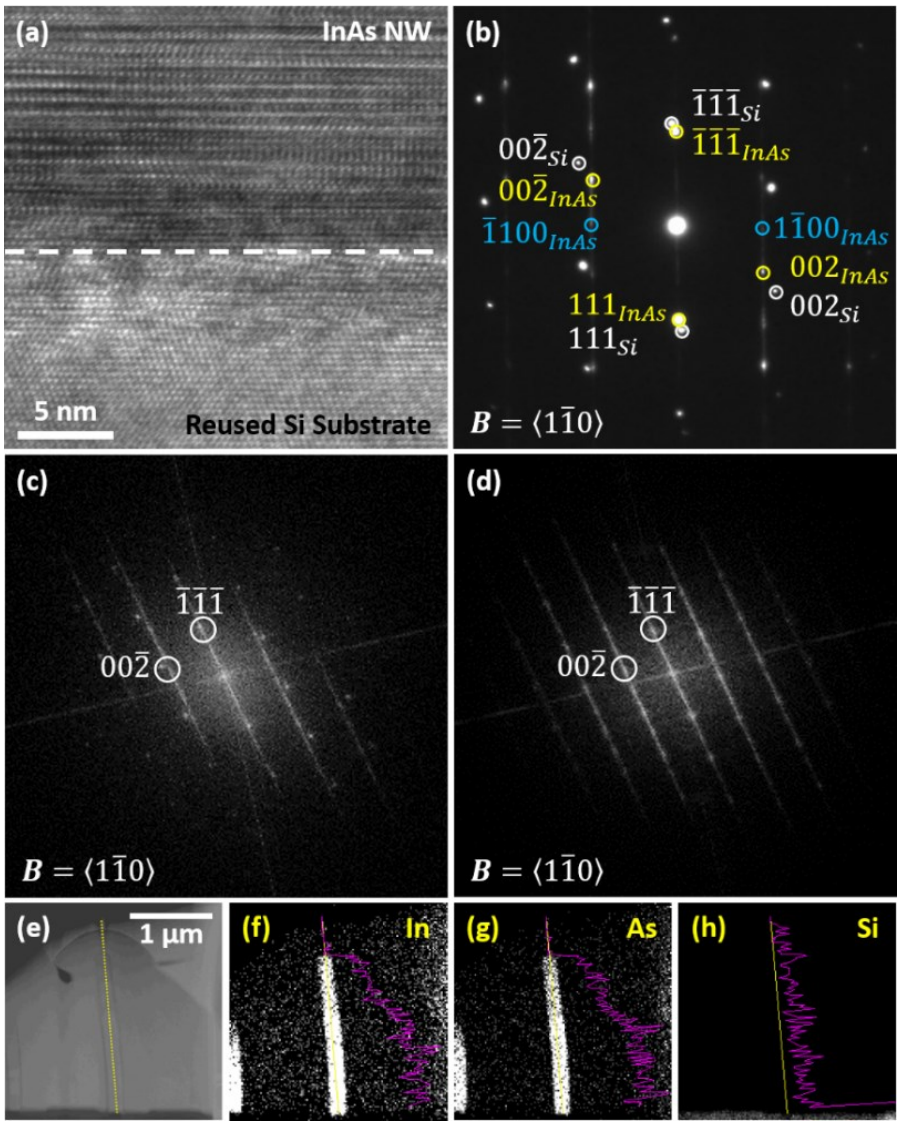

Figure 3.11. *(a) HR-TEM image and (b) SAED pattern collected along the interface of a regrown InAs NW and parent Si substrate. FFT patterns generated from HR-TEM images collected at (c) the InAs/Si interface and (d) near the longitudinal midpoint of the regrown NW. (e) HAADF-STEM image and (f)-(h) corresponding area EDXS maps with superimposed linescans representing counts of elemental In, As, and Si, respectively.*

The yellow line indicates the EDXS linescan location, corresponding to the NW axial direction. The slight reduction in elemental In and As linescan intensity near the top of the NW is due to the reduced thickness of the wedge-shaped TEM lamella. A uniform InAs NW composition is confirmed in Figures 3.11(f) and 3.11(g). No lattice discontinuities are observed along the anticipated regrowth plane location in (a), nor are changes in composition observed near the base of the NW in (f) and (g). A sharp contrast change below the NW basal plane in (e) and corresponding rapid increase in elemental Si counts in (f) are indicative of an abrupt InAs/Si interface.

3.4.2 Single-Layer Graphene (SLG) Substrate Reuse

Heterogeneous integration of III–V nanostructures on inert two-dimensional monolayer materials such as single-layer graphene (SLG) enables novel hybrid nanosystems with unique properties [151]. Self-assembly (SA) of InAs NWs on SLG has been previously investigated in our research group [151]. Here, the re-use of SLG as a growth substrate for InAs NWs was investigated. In order to grow SA InAs NWs, first SLG on Si substrates were cleaned by conventional procedures in the order: acetone, methanol, and isopropanol each for 15 seconds. Then, the SLG samples were loaded in the MOCVD chamber. Growth was performed at 650° C under TMIn and AsH_3 flow of 16 and 365 μmol/min, respectively. Figure 3.12(a) shows the results after 25 minutes of growth. In order to delaminate the as-grown NWs, polydimethylsiloxane (PDMS) was spin-coated at 1000 RPM. Afterwards, the samples were observed under SEM, as shown in Figure 3.12(b).

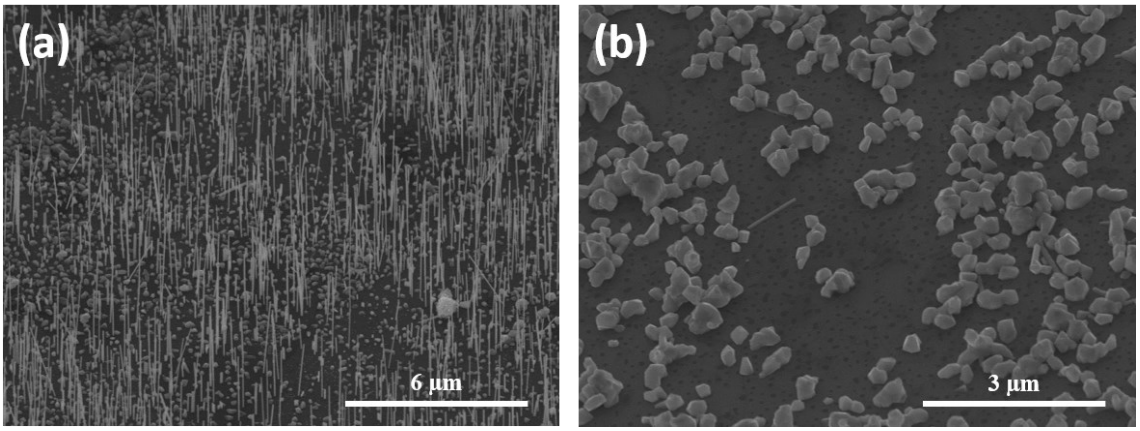

Figure 3.12. *Tilted-view SEM images of self-assembly InAs NW arrays (a) grown on SLG (b) growth substrate after NWs delamination via PDMS membrane.*

After delamination, three different SLG re-use procedures were performed including: (1) loading SLG into the chamber after delamination as-is; (2) restoring the SLG surface using citric acid solution; and (3) restore the SLG surface using Piranha solution. For the first procedure, samples were loaded in the chamber after delamination followed by conventional cleaning. Growth was performed under the same conditions as the original sample and the results are shown in Figure 3.13(a). The parasitic islands act as preferred growth sites, and the NWs are grown out of them. Since those islands can have multiple of different facets; therefore, the (111)-oriented NWs are randomly aligned in different directions. For the second and third procedures, substrates were treated with citric acid ($C_6H_8O_7$:H_2O_2, 20:1) and Piranha solution, respectively, for 5 minutes, in order to chemically etch the InAs material left on the substrate after the delamination process. The results are shown in Figures 3.13(b) and 3.13(c), respectively. As shown, there is a significant difference in the growth yield between the two different samples. The citric acid-treated substrate, shown in Figure 3.13(b), resulted in a higher growth yield compared

to the Piranha-treated substrate, shown in Figure 3.13(c), which was mostly covered by parasitic islands.

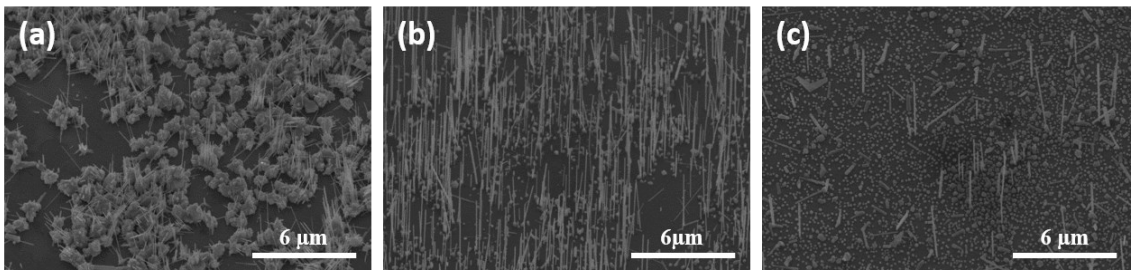

Figure 3.13. *Tilted-view SEM images of regrown InAs on: (a) SLG substrate after delamination without treatment, (b) after regrowth on citric acid-treated SLG substrate, and (c) after regrowth on Piranha-treated SLG substrate.*

To determine the root of the differences observed in the case of the citric acid-treated and Piranha-treated SLG samples, Raman investigations were performed on the different samples. A new SLG substrate was used as the reference. Raman measurement was performed on SLG substrates after InAs growth and also after delamination in order to investigate the growth and delamination process effects on the SLG substrate. A new SLG sample was treated with citric acid and Piranha solution and measured to observe their effects on SLG. Finally, samples after growth, delamination, and critic acid treatment were measured to be compared with all the other samples. Figure 3.14 shows all of the Raman spectroscopy results. For the control SLG sample, the 2D and G peaks are observed at 2677 and 1585 cm^{-1}, respectively. The same two peaks were observed on the other sample including, after growth; after growth and delamination; after citric treatment; and after growth, delamination, and citric treatment. This proves that the growth, delamination, and citric acid treatment do not impact SLG. However, as shown in Figure 3.14 for Piranha-treated SLG, no peaks have been observed. The difference in regrowth results for SLG

treated with Citric acid and piranha can be explained with these Raman results such that the Piranha treatment etched the SLG. Therefore, only the citric acid treatment enabled restoration of the SLG surface to a condition suitable for the regrowth of InAs NWs.

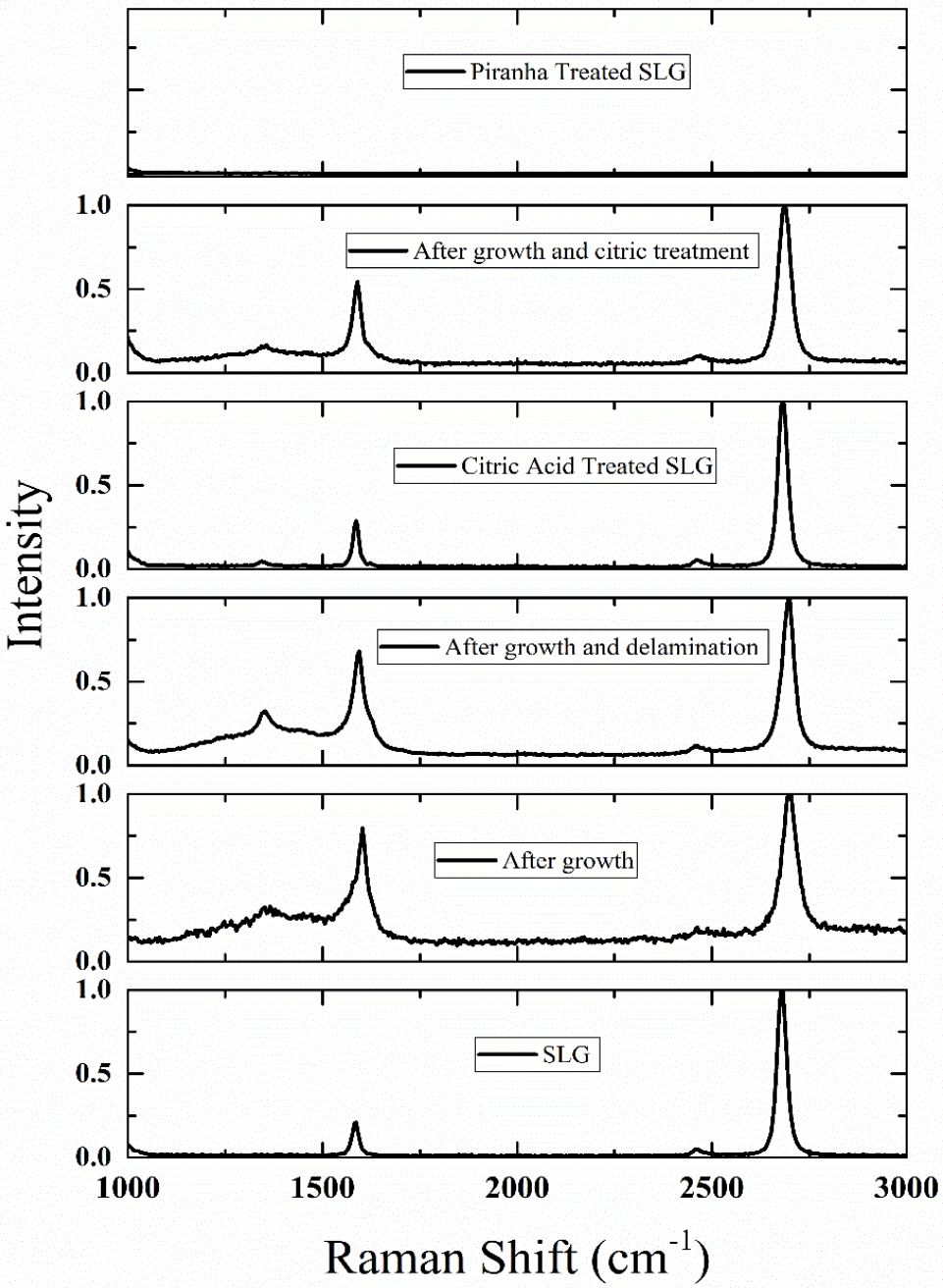

Figure 3.14. *Raman results of measurement at different steps of SLG substrate restoration process.*

3.5 InAs Nanowire Array Delamination, Transfer, and Device Fabrication

We now turn the focus back to InAs NWs grown on Si via the LSA approach and describe a method developed for their delamination and transfer to carrier wafers for the fabrication of substrate-free NW-based photodetector membranes. The NW array delamination and substrate reuse procedure is intended to enable the fabrication of substrate-free, III-V membranes for optoelectronic device applications, such as broadband photodetectors.

To transfer the delaminated NW arrays for subsequent device fabrication, the backside surfaces of the exfoliated polymer membranes were subjected to an RIE process to expose ~150 nm along the base segments of the embedded NWs. Next, a trilayer stack of Ti/Al/Ti (25 nm/300 nm/25 nm) was sputtered on the backside of the membranes to serve as a backside contact and supportive medium to preserve the as-grown vertical orientation and original position of the NWs in the delaminated arrays. The membranes were then bonded to corona-treated Si carrier wafers using uncured PDMS as the bonding matrix, followed by a 3-hour baking step at 60 °C. Next, the bonded membranes were submerged in the First Contact^{TM} Thinner solution for 12 hours to dissolve the delamination matrix. For device fabrication, a S1813 photoresist layer was spin-coated to encapsulate the transferred NW arrays and then thinned using an RIE treatment to expose the tip segments of the NWs. The samples were then submerged in a citric acid solution ($C_6H_8O_7$:H_2O_2, 20:1) for 30 second to selectively etch the exposed NW tips segments in order to generate a more homogeneous height profile for all NWs in the large-area arrays.

The photoresist layer was again subjected to a short RIE step to expose the NW tip segments prior to sputter deposition of a 300 nm indium-tin-oxide (ITO) layer as a transparent conductive topside contact. Lastly, samples were annealed at 250 °C for 1 hour.

Figure 3.15 illustrates the process flow utilized for NW array transfer and device fabrication, as described above. The black and yellow arrows in Steps 2 to 5 represent the NW array when positioned in the upright (i.e., as-grown) and inverted orientations, respectively. In contrast to alternative fabrication approaches for NW-embedded flexible membrane devices that require device processing on the growth substrate [113], the current approach allows direct transfer of NW arrays to any foreign platform (e.g., carrier wafer, contact layer, etc.) while preserving the orientation and position of as-grown NWs during subsequent processing steps.

Figure 3.16(a) shows a photograph of a delaminated membrane containing a NW array that is embedded in the CFC polymer layer and held by a pair of tweezers. A tilted-view SEM image of the membrane's backside surface is shown in Figure 3.16(b). The bases of the delaminated NWs are visible through the encapsulating polymer layer after an RIE step to expose NWs for contact deposition. In Figure 3.16(c), the same backside surface is shown after deposition of a Ti/Al/Ti trilayer stack, which simultaneously serves as a reflective rear contact layer and a mechanical anchor. This anchoring medium preserves the original NW array spacing and orientation upon transfer to foreign carriers and it ensures reliable fidelity of the original array geometry during subsequent processing steps. In Figure 3.16(c), the contact points of the anchoring contact layer to individual NWs appear as hemispherical protrusion beyond the surface of the enclosing polymer matrix.

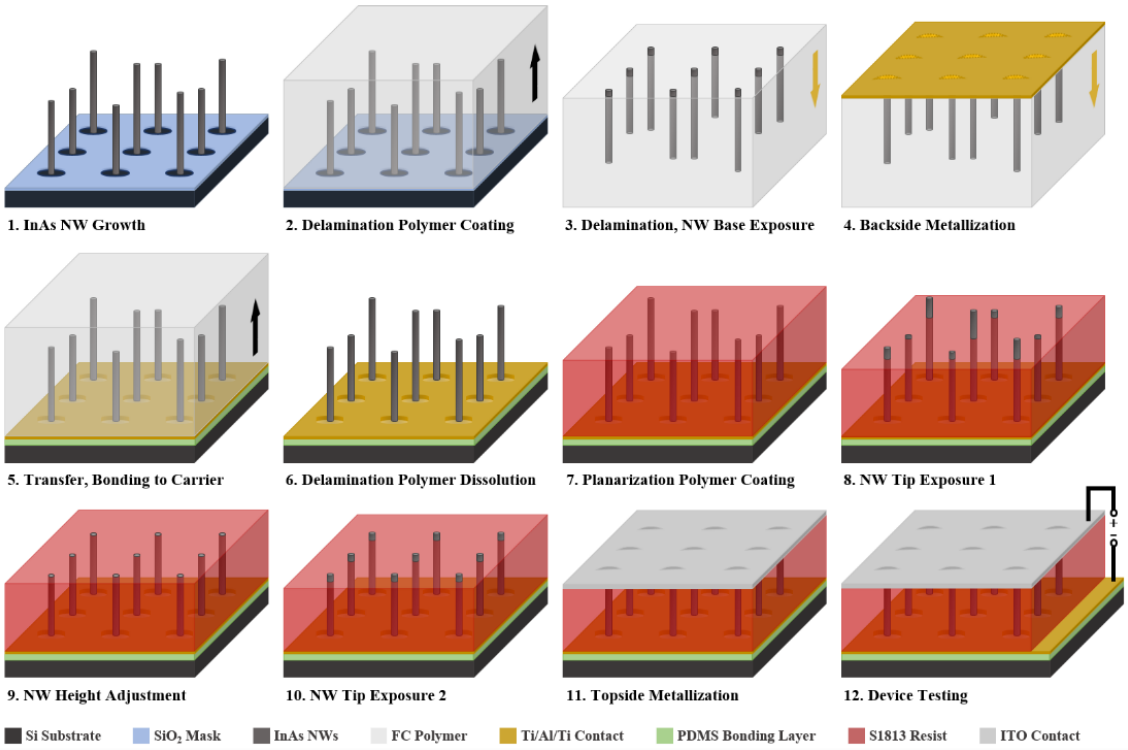

Figure 3.15. *Schematic diagram of NW array transfer and device fabrication process: (1) LSA growth of NW arrays via MOCVD; (2) CFC polymer deposition (black arrow shows the as-growth, upright array orientation); (3) delamination of NW-embedded polymer, followed by membrane inversion and RIE treatment to expose NW base segments (yellow arrow shows the inverted array orientation); (4) deposition of anchoring backside contact; (5) PDMS bonding of NW-embedded membrane to carrier wafer for further device fabrication; (6) dissolution of CFC polymer membrane, which results in NWs being transferred from their native growth substrate to a new carrier wafer with preserved position and vertical orientation; (7) coating and planarization of S1813 resist layer; (8) RIE treatment to expose the NW tip segments to a common height of ~1.75 μm; (9) wet-etching of exposed NWs tips using citric acid solution for height adjustment; (10) RIE treatment to expose NW tip segments for top contacting; (11) ITO top contact deposition followed by annealing treatment; (12) final device structure and probing configuration.*

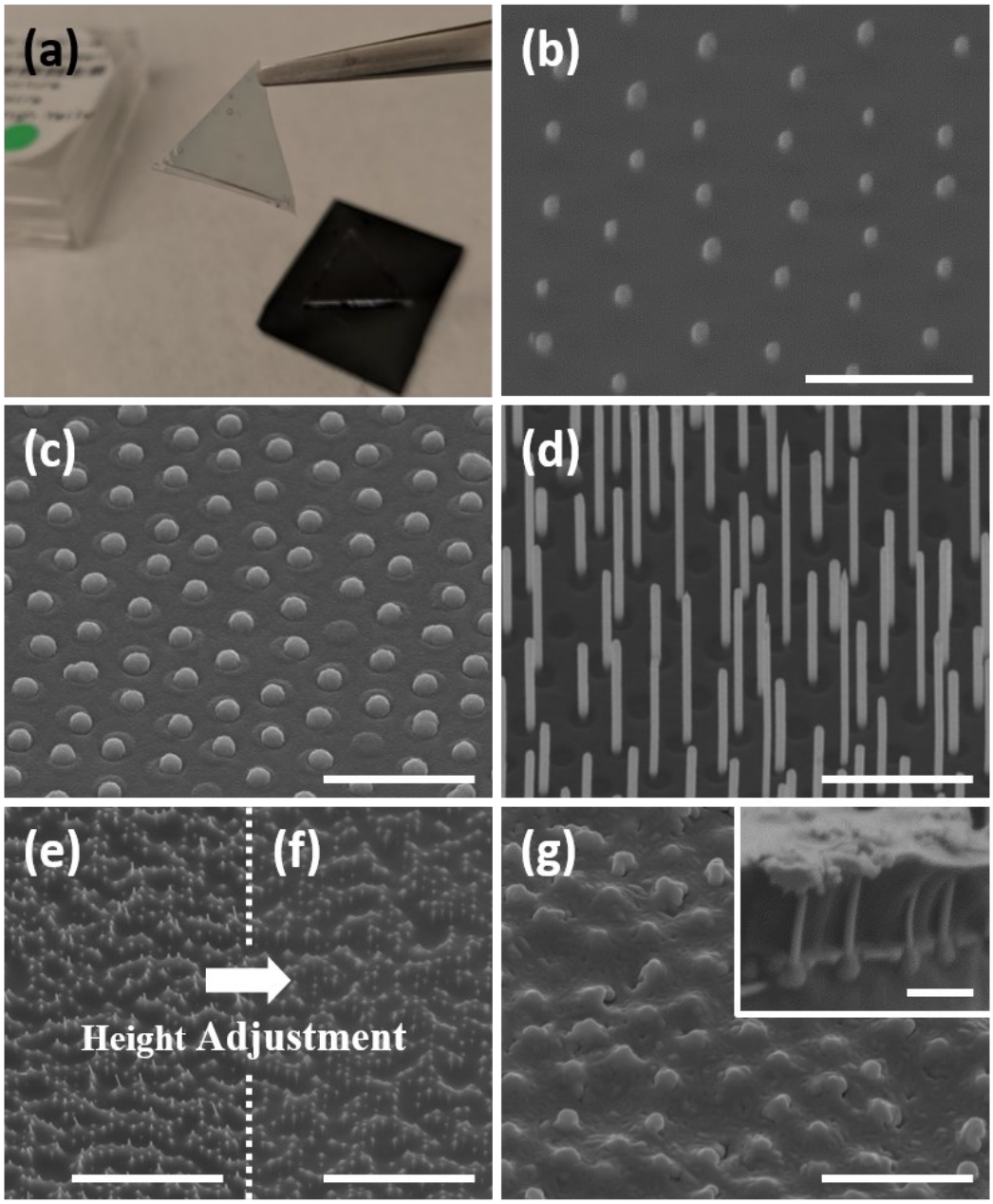

Figure 3.16. *(a) Photograph of InAs NW array membrane held with tweezers. Tilted-view SEM images obtained at various stages of the device fabrication process: (b) backside of delaminated membrane after RIE step to expose the NW base segments; (c) backside of delaminated membrane after Ti/Al/Ti trilayer stack deposition (hemispherical features represent location of NW base segments); (d) transferred, free-standing NW array on carrier wafer after backside PDMS bonding and CFC dissolution, showing that the original vertical orientation and positions of NWs is preserved; (e) S1813 polymer layer coating and planarization before height adjustment and (f) after citric acid treatment for height adjustment; (g) topside of NW membrane device after ITO top contact deposition. Inset shows a cross-sectional view of the fabricated device with 4 visible vertical NWs anchored in place by the backside contact (anchoring bulbs visible under each NW). Scale bars in (b)-(g) represent 3 μm. Scale bar in inset of (g) represents 1 μm.*

Since important optical properties of NW arrays, such as spectral range and wavelength-selective resonant absorption, can be engineered as a function of NW orientation, diameter, and pitch values [14], [153], [154], maintaining NW verticality and array geometry during fabrication is critical. An image of an upright NW array, anchored by the backside contact stack, after dissolution of the encapsulating CFC membrane is shown in Figure 3.16(d); this corresponds to Step 6 of the process flow in Figure 3.15. As seen in the micrograph, successful transfer of the NW array is realized with near-unity yield. After dissolution of the delamination polymer, the original orientation and relative position of each NW in the array is preserved.

Preserving the as-grown orientation of NWs after delamination and transfer to carrier wafers is necessary for processing simplicity and for reliable and reproducible performance of NW array-based membrane devices. Here, the CFC polymer is used as a delamination matrix that introduces minimal damage to the NWs and enables their as-grown separation and vertical orientation to be maintained upon peel-off and transfer to foreign carrier wafers. Figure 3.17(a) shows a representative distribution of the alignment angle of 100 NWs measured from an as-grown sample. A mean orientation angle of 89.95° is measured with a standard deviation value of 0.35°. Figure 3.17(b) shows the alignment angle distribution of 100 NWs measured after array transfer to a carrier wafer and CFC polymer dissolution. The free-standing and transferred NWs are anchored at their bases by the trilayer backside metallic contact stack. A mean orientation angle of 89.94° and standard deviation of 0.69° are measured after transfer. In the case of the transferred array, approximately 90% of all NWs are oriented between 89° to 91°. The remaining 10% of NWs are aligned between 88°-89° and 91°-92°. No NWs are observed with orientation

angles less than 88° or greater than 92°, demonstrating that their verticality is preserved upon peel-off, transfer, and dissolution of the delamination polymer.

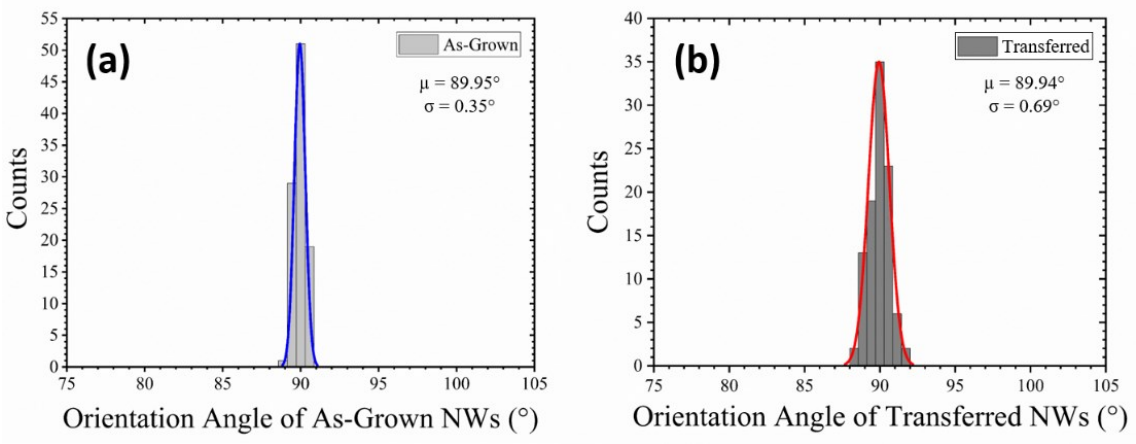

Figure 3.17. *Histogram of orientation angle of (a) as-grown and (b) transferred NWs. The blue curve in (a) and the red curve in (b) show data fit to a Gaussian distribution.*

Several alternative NW array peel-off and substrate reuse approaches have been presented to date. Spurgeon et al. first demonstrated delamination of Si NW arrays and reuse of a parent Si (111) substrate along with the porous oxide masking layer in 2008 [147]. After mechanical separation, the authors selectively etched the remnant NW bases segments inside the template nanopores prior to electrodeposition of Au inside the pores, which served as catalysts for Si NW regrowth via the VLS mechanism. Similarly, Cavalli et al. showed reuse of nanoimprint lithography-patterned InP (111) substrates through delamination of InP NW arrays using PDMS membranes. For substrate cleaning, diluted tetra-butyl-ammonium fluoride (TBAF) solution was used to remove the residual polymer followed by a dilute HCL treatment to remove the base part of the InP NWs [155]. More recently, Zhang et al. published an elegant approach for NW array peel-off. This involved spin-coating bilayers of S1818 and SU-8 polymers separated by Pd/Pt alloy films and

double-exposure to selectively remove the S1818 layer at the base of the NWs, while leaving the remainder of the NWs embedded in the SU-8 layer [156]. The authors noted that this approach enabled array delamination due to the built-in stress within the SU-8 layer and that it reduced potential inhomogeneity at the NW facture plane. Jafari Jam et al. also recently presented another practical method, which involved VLS growth of GaAs/AlAs/GaAs NWs through a patterned SiN_x porous template [157]. After growth, the NWs were embedded in a PDMS layer and mechanically fractured across the AlAs segment, which was subsequently selectively etched. Thus, the AlAs segment served as a sacrificial layer and generated a homogeneous surface for the underlying GaAs segment inside the pores of the masking template for selective re-electrodeposition of Au catalysts, enabling regrowth of NWs on the parent GaAs substrate. The NW array transfer and substrate reuse methods presented in the current work combines some of the strategic advantages of the recently demonstrated approaches, including: (a) use of high-throughput and reproducible *i*-line photolithography to pattern oxide masking templates on 150 mm wafers; (b) absence of foreign seeding agents in exchange for a simplified LSA growth mechanism; (c) use of the CFC polymer as a delamination medium, which enables process simplicity by eliminating the need for polymer bilayer deposition and double-exposure; and (d) ease of dissolving the CFC polymer membrane while preserving the vertical NW orientation, which enables potential use in biomedical applications [160]. A distinguishing aspect of the current work is that remnant NW base segments are exploited as preferential sites for NW re-growth on parent substrates, which avoids growth and selective etching of sacrificial NW segments as well as additional substrate restoration steps.

In comparison to the above approaches, however, the LSA growth mode utilized here has a notable disadvantage: The inhomogeneity in the length distribution of as-grown NWs presents a challenge for planarization and subsequent top contact deposition. During conventional SAE NW growth, the high degree of lateral confinement provided by the narrow-diameter template pores enables growth of NWs with uniform diameters and, therefore, more homogeneous length distributions. In contrast, during LSA of InAs on Si, the diameter of NWs is not strictly defined by the size of the larger template pores. Rather, the NW diameter and axial-to-radial growth rate ratio depend upon other parameters. These include the lattice-mismatch between InAs and Si, the number of nearest neighbor NWs, the spacing of nanopores, and the epitaxial growth conditions. The wider distribution of NW diameters resulting from LSA synthesis introduces NW length non-uniformities in the case of large-area arrays.

To normalize the NW height distribution and mitigate top contact deposition challenges, two planarization steps are introduced. After re-encapsulating the transferred NW array in a S1813 photoresist planarization medium (Figure 3.15, Step 7), an RIE procedure is used to expose ~90% of all NWs in the array, as shown in Figure 3.16(e) (corresponding to Figure 3.15, Step 8). At this stage, the embedded NWs are buried in the S1813 polymer to a common height of ~1.75 μm. Next, a citric acid treatment is used to etch the excess length of the NWs exposed beyond the surface of the encapsulation medium (Figure 3.15, Step 9). This process effectively corrects NW length disparities over large areas and generates a more homogeneous array height. Lastly, a short RIE treatment is used to uniformly expose the top 150 nm of the NWs for ITO deposition, as shown in Figure 3.16(f) (corresponding to Figure 3.15, Step 10). Figure 3.16(g) shows the planarized top

surface of the NW array after top contact deposition (corresponding to Figure 3.15, Step 11). The locations of individual NWs are visible through the ITO film. The inset of Figure 3.16(g) shows a cross-sectional view of the fabricated device, where four vertical NWs are seen that are partially embedded in the planarization medium and anchored in place by the backside trilayer contact. Each anchoring point can be seen as a bulb-like protrusion in the underlying PDMS bonding layer. Samples are subjected to a thermal annealing treatment prior to device testing to form Ohmic contacts, as well as to improve the transparency of the ITO film and reduce its sheet resistance.

The photoresponse of the substrate-free, vertical InAs NW array-based metal-semiconductor-metal (MSM) photoconductors is measured at room-temperature by probing the top and backside contacts, as depicted in Step 12 in Figure 3.14 [136], [137], [159]. A tungsten halogen lamp is used as the broadband source, which provides illumination over the 350 nm to 2000 nm wavelength range, with incident power density of 57 mW/cm^2. Figure 3.18 shows the semi-log current–voltage (I–V) characteristics of a representative NW array device under dark (black curve) and illuminated (red curve) conditions over the -1 V to +1V bias range. A reverse dark current of ~3 μA is measured at -1 V. Upon illumination, the production of photogenerated carriers results in a clear current enhancement, characterized by a photocurrent of roughly 0.3 mA at -1 V.

Thus, a room-temperature on/off current ratio (I_{ON}/I_{OFF}) of approximately 10^2 is measured. The detected photoresponse validates the feasibility of the fabrication process described above. It also demonstrates that the delaminated NWs that are regrown on reused Si substrates are optically active and remain structurally stable during the transfer process. Using the substrate reuse and processing protocols established here, the performance and

functionality of NW-based photodetectors can be improved in future works through implementation of several proven strategies, such as introduction of p-i-n junctions and heterojunctions during NW growth,[88] as well as modulation of NW diameter and array geometry for enhanced selective resonant absorption.[58], [160]

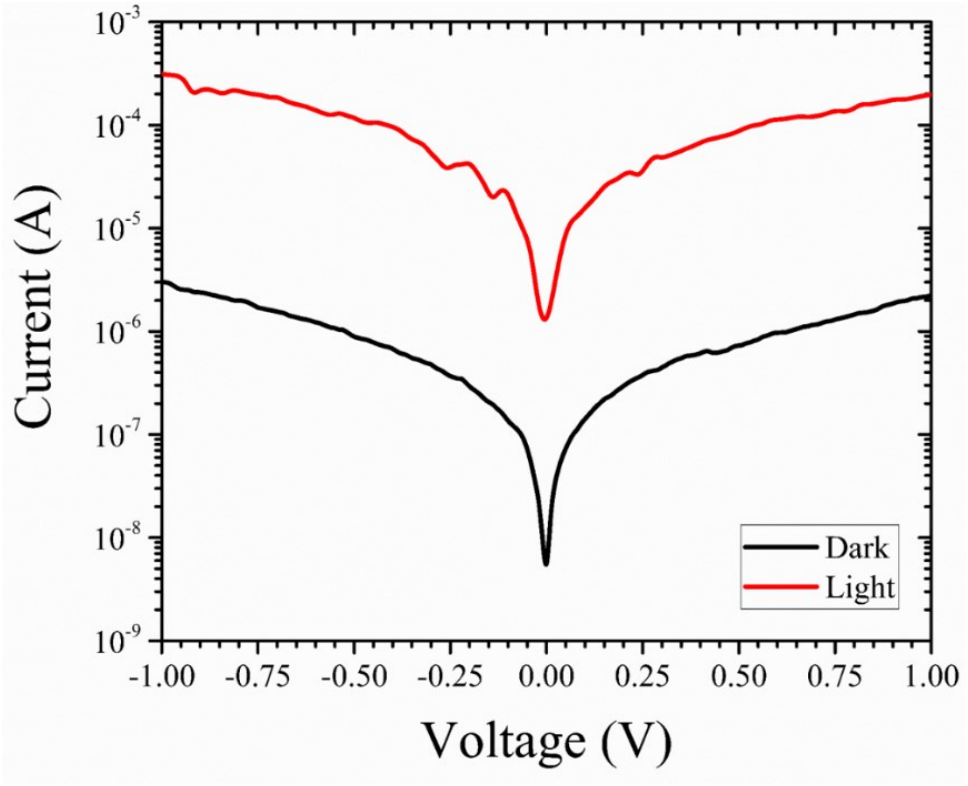

Figure 3.18. *Output characteristics of the substrate-free InAs NW array-based MSM photodetector under dark (black curve) and illuminated (red curve) conditions.*

While the LSA growth technique offers a series of practical advantages, it also has some notable limitations. The main drawbacks of the LSA method include: (a) inherent inhomogeneity in diameter and length of as-grown NWs and sample-to-sample variability in NW dimensions; (b) limited control over the exact position of NWs inside wider nanopores, which leads to array aperiodicity; (c) strain-limited self-assembly requires a

high degree of lattice mismatch between substrate and epi-layer, which limits the number of materials combinations that can be synthesized under this growth mode; and (d) challenges associated with growth of axial and coaxial NW heterostructures with equivalent geometries. However, the LSA growth mode enables heterogeneous epitaxy of vertical and high-aspect-ratio InAs NWs and micropillars with a wide range of tunable dimensions including diameters ranging from 100 nm to 1 μm and lengths tunable from 0.1 μm to greater than 10 μm, using template pores varying from 0.5 μm to 4 μm in diameter and array pitch values in the 1 μm to 10 μm range [161].

3.6 Conclusions

The LSA growth mode by MOCVD provides a low-cost path toward III-V NW array growth on large-area Si substrates. Scalable photolithography is employed for patterning of selective-area masking templates. The growth sequence uses flowrate-modulation, which provides global NW yields exceeding 80% and allows control over the arrangement of only a single NW per template nanopore. As-grown InAs NW arrays are embedded in a polymer encapsulation medium, mechanically delaminated from the growth surface, and anchored by a metallic trilayer stack. The latter serves as a backside device contact layer and ensures that the original position and vertical orientation of the free-standing NWs are preserved upon transfer to foreign carrier wafers for device processing. Parent Si wafers and their masking templates are reused for subsequent LSA growth runs using two separated regrowth approaches. In the first approach, a citric acid (or a piranha solution) treatment is used to restore the parent substrates and nanoporous oxide masking layers to their pre-growth state. In an alternative approach, the original substrates, which contain short NW base segments that remain inside the template pores after delamination, are directly reused without introduction of intermediate substrate restoration steps. In this case, the remnant NW base segments act as preferential sites for extension of the InAs lattice in the vertical direction. In both approaches, the original LSA masking template pattern fidelity is preserved upon substrate reuse and no parasitic nucleation is observed on the mask, consistent with crystal growth under a selective-area self-assembly regime. The transferred InAs NW arrays are processed for proof-of-concept demonstration of substrate-free MSM photodetectors with I_{ON}/I_{OFF} ratios of 10^2 under broadband illumination. Future extensions of the current work include detailed characterization of the optical properties of

delaminated InAs NW arrays of various dimensions in dissimilar encapsulating polymer media, analysis of the influence of anchoring backside contact layers on their optical properties, and detailed performance analysis of substrate-free membrane photodetectors fabricated using type-II heterojunction NWs. This work establishes the LSA growth mode as a feasible approach for heteroepitaxial synthesis of large-area III-V NW arrays on oxide-templated Si wafers that can be reused without dedicated restoration between regrowth cycles for applications in substrate-free and flexible optoelectronic membrane devices.

In this chapter, we demonstrated that InAs NW arrays can undergo delamination and can be easily transferred to carrier substrates. The delamination process offers notable advantages, including a significant reduction in dark current by eliminating substrate contributions. Additionally, delamination facilitates flexible device fabrication and contributes to a reduction in manufacturing costs. For NW-based device applications requiring a substrate-free architectures, the deposition of a backside metal layer becomes an essential step. This backside metal not only serves as a contact layer but also acts as a backside reflector, influencing light absorption.

In the subsequent Chapter 4, we investigate the impact of a backside reflector on the infrared IR light absorption properties of InAs NW array-based membranes.

Chapter IV

4 Modeling Selective Narrowband Light Absorption in Coaxial InAs-$GaAs_{0.1}Sb_{0.9}$ Nanowires with Partial Shell Segment Coverage

Vertical III-V nanowire (NW) arrays are promising candidates for infrared (IR) photodetection applications. Generally, NWs with large diameters are required for efficient absorption in the IR range. However, increasing the NW diameter results in a loss of spectral selectivity and an enhancement in the photodetector dark current. Here, we propose a nanophotonic engineering approach to achieving spectrally-selective light absorption while minimizing the volume of the absorbing medium. Based on simulations performed using rigorous coupled-wave analysis (RCWA) techniques, we demonstrate dramatic tunability of the short-wavelength infrared (SWIR) light absorption properties of InAs NWs with base segments embedded in a reflective backside Au layer and with partial $GaAs_{0.1}Sb_{0.9}$ shell segment coverage. Use of a backside reflector results in the generation of a delocalized evanescent field around the NW core segment that can be selectively captured by the partially encapsulating $GaAs_{0.1}Sb_{0.9}$ shell layer. By adjusting the core and

shell dimensions, unity absorption can be selectively achieved in the 2 to 3 μm wavelength range. Due to the transparency of the $GaAs_{0.1}Sb_{0.9}$ shell segments, wavelength-selective absorption occurs only along the InAs core segments where they are partially encapsulated. The design presented in this work paves the path toward spectrally-selective and polarization-dependent NW array-based photodetectors, in which carrier collection efficiencies can be enhanced by positioning active junctions at the predefined locations of the partial shell segments.

4.1 Background and Motivations

Vertical III–V nanowire (NW) arrays are promising materials for optoelectronic applications due to their distinct properties compared to the bulk and thin-film systems. It has been theoretically and experimentally shown that light can strongly be absorbed in arrays of III-V NWs with micron-scale lengths with an overall material savings of ~93% [56], [162]–[164]. In addition, their efficient defect-free strain relaxation allows for a broad range of III-V compounds to be heteroepitaxially grown on lattice-mismatched substrates such as Si [12], [129], [165].

Of particular interest is the use of III-V NW arrays for infrared (IR) photodetection applications, due to their potential to overcome traditional tradeoffs between response speed and external quantum efficiency [8]. For such applications, InAs NW arrays provide an excellent platform due to their small bandgap and high carrier mobility [166], [167]. Moreover, high detectivity at room-temperature can be realized through the use of NW-based photodetectors due to a reduction in the volume of the absorbing medium and, consequently, dark current [168], [169]. Generally, NWs with large diameters are required for efficient absorption in the IR range [58]. However, increasing the NW diameter results in a loss of spectral range selectivity and an enhancement in dark current due to the corresponding increase in material volume [54]. Therefore, novel methods for achieving spectrally-selective and narrowband light absorption while minimizing the volume of light absorption medium and array fill factor are highly desired for applications in NW-based IR photodetectors with low-size, weight, power, and cost (SWaP-C) metrics. To date, reports on nanophotonic engineering using delaminated NW array membranes and the

influence of the backside reflectors on the optical properties of substrate-free NW arrays are limited [170].

Regardless of the method used for NW growth, starting substrates are needed to guide their vertical orientation and can serve as robust handling carriers for further fabrication processes. However, it has been shown that NWs can be delaminated from their native substrate for further fabrication in substrate-free applications [155], [156], [171]. In addition, the use of delaminated NW arrays as the active medium can significantly reduce the photodetector dark current by eliminating the substrate contribution. In a Chapter 3, we demonstrated a complete fabrication procedure for substrate-free InAs NW-based photodetector, including epitaxial growth of InAs NW arrays followed by delamination, transferring, device processing, and Si substrate recycling for NW array regrowth. Successful delamination was realized through metal deposition on the backside of a NW array membrane. Such a backside metallic layer enables three key functions: (i) it serves as a backside contact; (ii) it acts as a mechanical anchor to hold the NWs in their original vertical orientation; and (iii) it functions as a backside reflector to enhance light absorption.

In this Chapter, we investigate the influences of a backside metal reflector layer on the absorption spectra of InAs NW arrays and take advantage of standing wave patterns generated above the metal reflector for wavelength-selective absorption in the short-wavelength infrared (SWIR) range. Coaxially heterostructured NW arrays consisting of InAs core segments that are partially encapsulated by $GaAs_{0.1}Sb_{0.9}$ shell layers are used for large tunability in the SWIR range, specifically through the consideration of the generated standing wave patterns. Embedding the bases of InAs NWs in Au backside contact layers results in periodic evanescent fields between adjacent NWs. However, often a single

optical mode dominates the optical response. The position, spatial extent, and coupling between neighboring NWs depend mainly on the NW geometry and wavelength of incident light, as well as on the periodicity of the array [14].

We show that the otherwise delocalized HE_{11} mode in the 2 to 3 μm wavelength range can be selectively absorbed in InAs NW core segments by adding partial $GaAs_{0.1}Sb_{0.9}$ shell layers with dimensions corresponding to the position and spatial extent of the evanescent field of the mode. The $GaAs_{0.1}Sb_{0.9}$ layers are transparent at this wavelength range and only act to enhance absorption of the otherwise delocalized HE_{11} mode. Wavelength-selective absorption is enhanced by a factor of ~10 at positions along the InAs core segments where they are encapsulated by the shell. The absorption wavelength can be manipulated as a function of core segment length and the partial shell segment geometry. Moreover, narrowband wavelength selectivity can be controlled by tuning the length of the InAs NW core segment. Such site-specific absorption in InAs NWs can be exploited for enhancement of carrier collection efficiency by positioning active *p-n* junctions at the predefined locations of $GaAs_{0.1}Sb_{0.9}$ shell layers. The design approaches highlighted in this work are anticipated to enable novel, low-SWaP-C, NW-based IR photodetector membranes with tunable narrowband selectivity along specific NW locations.

4.2 Theory of Rigorous Coupled-Wave Analysis

The rigorous coupled-wave analysis (RCWA) technique enables the simulation of optical properties for micro/nanostructured surfaces with tunable geometries, based on diffraction. This method provides a semi-analytical solution to Maxwell's electromagnetic equations for periodic structures, specifically those with laterally non-homogeneous refractive indices. Analytical solutions are identified only in the direction where the refractive index remains constant [172]. The accuracy of the solution relies on the number of terms retained in the space-harmonic expansion of the fields within diffracting structures. Consequently, the RCWA method proves suitable for investigating electromagnetic wave interactions within ordered nanowire arrays, due to their lateral periodicity [173].

Based on Huygens principle, when a plane electromagnetic wave interacts with a grating structure, numerous reflected waves are generated at the point of incidence. In Figure 4.1, a schematic illustrates a planar wave of wavelength λ with the plane of incidence being perpendicular to the grooves and an incident angle of θ_{inc} being diffracted from periodical three-dimensional (3D) structures. Region I characterized by an electric permittivity of $\varepsilon_I = 1$, is considered as free space, where $\varepsilon = (n + ik)^2$, with n and k representing the refractive index and extinction coefficient, respectively. Region II corresponds to the grating layer with a period Λ, resulting in a heterogeneous medium. The permittivity in this region varies periodically with respect to x, such that $\varepsilon_{(x+\Lambda)} = \varepsilon_x$. In the periodical structures, the dielectric function is ε_{II}, whereas in the grooves it is ε_I. Additionally, Region III is a homogenous medium with electric permittivity of ε_{III}.

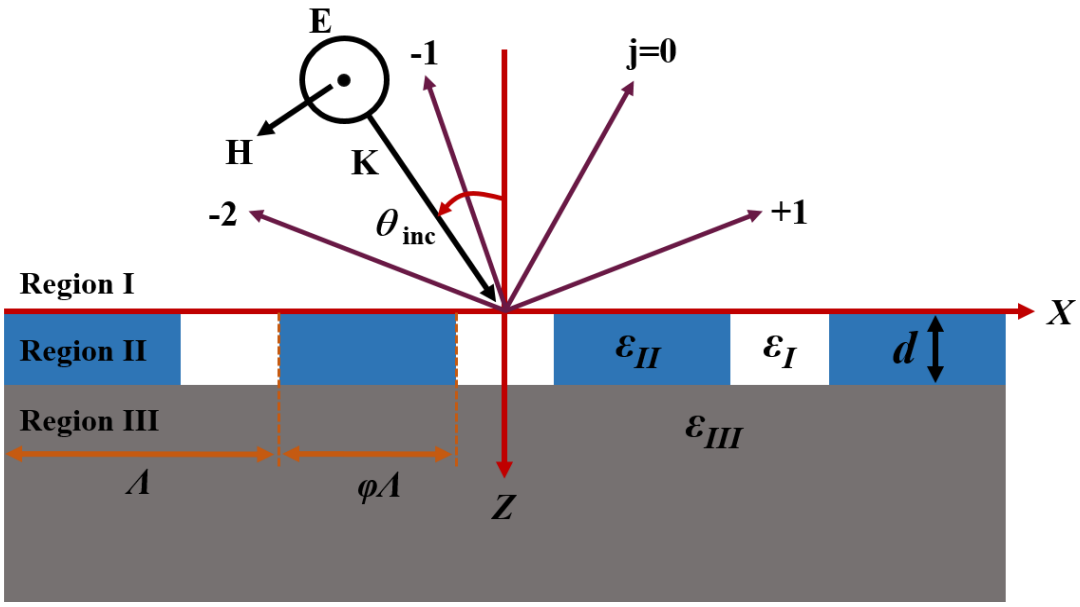

Figure 4.1. *Schematic of diffraction of electromagnetic radiation by a grating (for TE mode wave).*

Consider that k_{Ix} and k_{Iz} are the x and z components of the incident wave vector $\boldsymbol{k_I}$ in Region I, respectively. Therefore, the magnitude of the wave vector in Region I is given by:

$$k_I = \frac{2\pi n_I}{\lambda} = k, \tag{4.1}$$

and similarly for Region III,

$$k_{III} = \frac{2\pi n_{III}}{\lambda} = n_{III}k \tag{4.2}$$

The normalized incident electric field for a wave with TE mode can be written as:

$$E = e^{i(k_{Ix}x + k_{Iz}z)}\hat{y}, \tag{4.3}$$

where, for simplicity in Eq. (4.3), and all subsequent instances, the $\exp(-iwt)$ term has been omitted. Within the grating structure, the *x* component of each diffracted wave vectors is determined by the Bloch-Floquet condition as:

$$k_{x,m} = \frac{2\pi sin\theta}{\lambda} + \frac{2\pi}{\Lambda} m, \tag{4.4}$$

here, m represents the order of the diffracted wave. The continuity of tangential components for both electric and magnetic fields across an interface relies on phase matching conditions; therefore, k_x needs to be identical in all three media. In Region I, $k_{z,m}$ can be calculated by using:

$$k^2 = k_{x,m}^2 + k_{z,m}^2 \tag{4.5}$$

In the same way, using Eq. (4.5) with the corresponding wave vectors, $k_{z,m}$ can be calculated for Region II and III. The $k_{z,m}$ term is purely imaginary if $k_{x,m} > k_I$ and the m^{th} order diffracted wave decays exponentially towards the *z*-direction, resulting in an evanescent wave. The total magnitude of the electric field in Region I is determined by the superposition of incident and reflected waves, whereas the total electric field in Region III is given by the superposition of transmitted waves, as follows:

$$\boldsymbol{E_I}(x,z) = e^{i(k_x x + k_{Iz} z)} + \sum_m r_m e^{i\left(k_{Ix,m} x - k_{Iz,m} z\right)}, \tag{4.6}$$

$$\boldsymbol{E_{III}}(x,z) = \sum_m t_m \, e^{i\left(k_{x,m} x + k_{IIIz,m}(z-d)\right)}, \tag{4.7}$$

where r_m and t_m are the reflection and transmission coefficients for the interface between Regions I and II and the m^{th} order transmitted wave, respectively.

Due to the periodicity of Region II, the electric field, E_{II}, can be expanded in terms of its space harmonic components. These components are phase-matched with the diffraction orders in Regions I and III. Hence, the normalized E_{II} can be written as:

$$\boldsymbol{E_{II}}(x,z) = \sum_{m} \psi_m(z)\, e^{ik_{x,m}x}, \tag{4.8}$$

here, ψ_m represents the field amplitude for the m^{th} diffraction order. Additionally, the periodic nature of the relative permittivity in the grating layer allows for its expansion using a Fourier series as:

$$\varepsilon(x) = \sum_{u} \varepsilon_u\ e^{\left(\frac{i2u\pi}{\Lambda}x\right)}, \tag{4.9}$$

where ε_u is the uth Fourier coefficient given by:

$$\varepsilon_0 = \phi\varepsilon_{II} + (1-\phi)\varepsilon_I \tag{4.10.a}$$

$$\varepsilon_u = \frac{(\varepsilon_{II} - \varepsilon_I)sin(u\phi\pi)}{u\pi} \tag{4.10.b}$$

where ϕ is the surface filling factor of the periodic material in Region II.

Now, Maxwell's equations can be solved to obtain the wave equation for the electric field in Region II, which is non-homogeneous. Therefore, the wave equation can be written as:

$$\nabla^2\boldsymbol{E_{II}} + \nabla(\boldsymbol{E_{II}} \bullet \nabla ln\varepsilon) + \nabla ln\mu \times (\nabla \times \boldsymbol{E_{II}}) + k^2\mu\varepsilon\boldsymbol{E_{II}} = 0. \tag{4.11}$$

The second term in Eq. (4.11) becomes zero, since E_{II} and $\nabla \ln\varepsilon$ are perpendicular to each other. Also, $\ln\mu = 0$, since the medium is nonmagnetic. Hence, Eq. 4.11 can be re-written as:

$$\nabla^2 \boldsymbol{E_{II}}(x,z) + k^2 \varepsilon(x) \boldsymbol{E_{II}}(x,z) = 0. \tag{4.12}$$

Therefore, the final coupled wave formula can be obtained by substituting Eq. (4.7) and (4.8) into (4.12) as follows:

$$\sum_m \left(\frac{d^2\psi_m}{dz^2} - k_{x,m}^2 \psi_m + k^2 \sum_p \varepsilon_{m-p} \psi_p \right) e^{ik_{x,m}x} = 0. \tag{4.13}$$

This needs to be satisfied for every m^{th} term and, therefore, the $e^{ik_{x,m}x}$ coefficients must be identically zero for every m^{th} term. For Eq. (4.13), through the harmonics of the grating, each space harmonic term is coupled to the other terms. The numerical solution is obtained with a sufficiently large number of diffraction orders.

From Maxwell's equations, the magnetic field in Region II can be obtained as:

$$\nabla^2 \times \boldsymbol{E} + \frac{\partial(\mu \boldsymbol{H})}{\partial t} = 0 \tag{4.14}$$

Therefore, the magnetic field $\boldsymbol{H}$ in Region II, using the electric field in Eq. (4.8) can be written as:

$$\boldsymbol{H}_{II,x} = \frac{i}{\omega\mu} \sum_m k \gamma_m(z) e^{ik_{x,m}x} \tag{4.15.a}$$

$$\boldsymbol{H}_{II,z} = \frac{1}{\omega\mu} \sum_m k_{x,m} \psi_m(z) e^{ik_{x,m}x} \tag{4.15.b}$$

where γ_m and ψ_m are related by:

$$\frac{d\psi_m(z)}{dz} = k\gamma_m(z). \tag{4.16}$$

Another relation between γ_m and ψ_m is needed to solve the Eq. (4.16), which can be obtained by substituting Eq. (4.15.a), Eq. (4.15.a), and Eq. (4.8) into the following equation:

$$\nabla^2 \times \boldsymbol{H} + \frac{\partial(\varepsilon \boldsymbol{E})}{\partial t} = 0 \tag{4.17}$$

Another set of relationships between γ_m and ψ_m can be obtained from Eq. (4.17) by expansion as:

$$\frac{\partial \gamma_m(z)}{\partial z} = \left(\frac{k_{x,m}^2}{k} \psi_m(z) - k \sum_n \varepsilon_{m-n} \psi_m(z) \right) \tag{4.18}$$

The solution of Eqs. (4.16) and (4.18) can be expressed in matrix form as:

$$\left[\frac{\partial^2 \Psi}{\partial (kz)^2} \right] = [\boldsymbol{A}][\Psi] \tag{4.19}$$

where Ψ is the matrix form of $\psi_m(z)$. When the diffraction orders are specified as $m = 0, \pm1, \pm2, ..., \pm q$, the total number of diffraction orders N is defined as $N = 2q + 1$. Thus, both matrices Ψ and $\boldsymbol{A}$, have dimensions $N \times N$. Additionally, $\boldsymbol{A}$ is defined as:

$$\boldsymbol{A} = \boldsymbol{K}_x^2 - \boldsymbol{E}' \tag{4.20}$$

in this equation, a diagonal matrix $\boldsymbol{K}_x^2$ has elements determined by $\boldsymbol{K}_x(a, a) = \frac{k_{x,(a-q-1)}}{k}$, and $N \times N$ matrix $\boldsymbol{E}'$ is composed of the Fourier coefficients of the dielectric function. The solution to Eq. (4.20) involves Eigenvalue analysis and applying relevant boundary conditions [174]–[176].

4.3 Optical Modeling

Due to the lack of analytical solutions for light-scattering in nanowire arrays, optical simulations are performed using the rigorous coupled wave analysis (RCWA) technique via the DiffractMOD simulation engine of Synopsys TCAD RSoft®. Thanks to the lateral periodicity of NW arrays, the RCWA method is suitable for the study of electromagnetic wave interactions within ordered NW arrays with laterally non-homogeneous refractive indices.

In this method, the principle of conservation of energy is satisfied, therefore reflectance, transmittance and subsequently absorption can be calculated based on the incident electromagnetic field, and the light-scattering problem can be written in terms of a superposition of the coupled waves and Fourier transforms of the refractive indices perpendicular to the direction of the incident beam propagation. Reflection and transmission measurement planes are positioned above the maximum and minimum planes of simulation domain, respectively. Therefore, absorption through the structure can be calculated by $A(\lambda) = 1 - [R(\lambda) + T(\lambda)]$. Here, $R(\lambda)$ is the reflectance from the array and $T(\lambda)$ is the transmittance through the membrane. Absorption is calculated over an incident wavelength range of 1 to 3 μm using 11×11 number of plane-wave harmonics. For completeness, note that the contour plots shown in Figures 4.12 and 4.13 are calculated with the scattering matrix method [14], which is in essence equivalent to RCWA or the Fourier modal method (FMM) [177]. In addition, the accuracy of the RCWA method is examined by Finite element method (FEM), using Wave Optics Module in Comsol Multiphysics. Figure 4.2 shows the results of an accuracy evaluation performed for the structure illustrated in Figure 4.2(a). Both FEM and RCWA methods showed excellent

convergence as plotted in Figure 4.2(b) with an average point-to-point deviation of 0.16% and total absorption difference of 0.03% over the 1 to 3 μm spectral range. A detailed comparison of FEM and RCWA methods has been previously reported for modeling of optical properties of NW array systems [178].

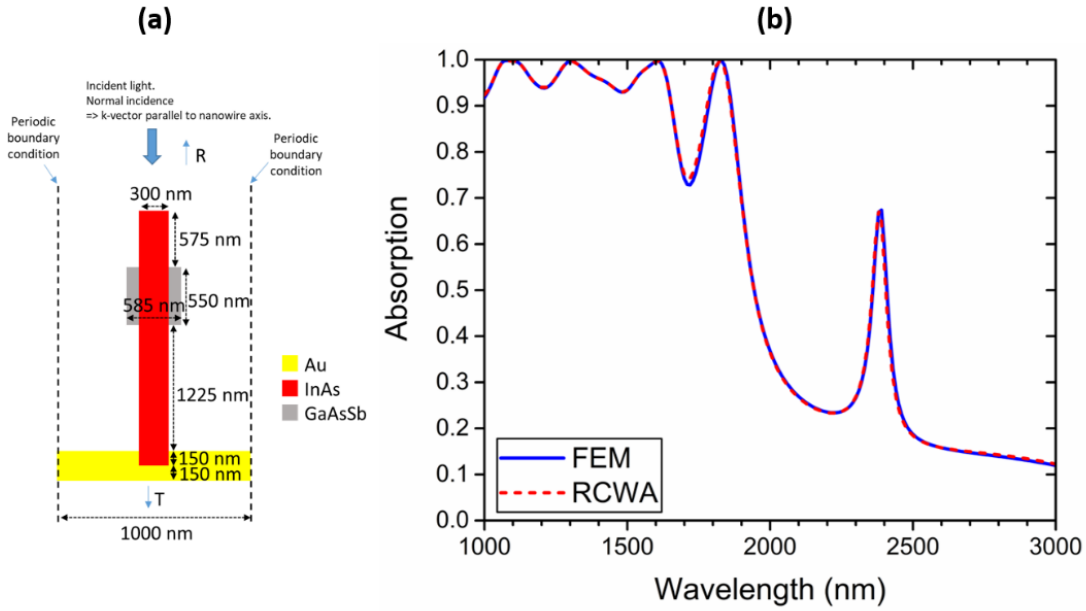

Figure 4.2. *(a) Simulated structure for accuracy evalauation; (b) simulated absorption spectra using FEM (solid blue curve) and RCWA (dashed red curve) methods.*

InAs NW core segments are used as the main absorption medium covered by partial $GaAs_{0.1}Sb_{0.9}$ shell segments to tune wavelength-selective absorption. The $GaAs_{0.1}Sb_{0.9}$ shell material is selected due to lattice matching with the InAs core. In addition, the InAs-$GaAs_{0.1}Sb_{0.9}$ material system provides a type-II broken gap which can be suitable for tunneling diode photodetectors with high responsivity [179], [180]. Geometrical parameters of the InAs-$GaAs_{0.1}Sb_{0.9}$ partial core-shell NW structure are defined as shown in Figure 4.3. The base of the InAs NW core segment is embedded with a depth of 150 nm

in a 300 nm-thick Au layer, which acts as the backside reflector. The length of the InAs core and $GaAs_{0.1}Sb_{0.9}$ shell segments are defined by L_C and L_S, respectively. The diameter of the InAs core segment is defined by D_C and the diameter of the $GaAs_{0.1}Sb_{0.9}$ shell segment is defined by $D_S = D_C + 2T_S$, where T_S is the shell thickness. Moreover, E_C and E_S are defined as the exposed core segment length and the length of the extension of the axial shell segment above the core segment, respectively.

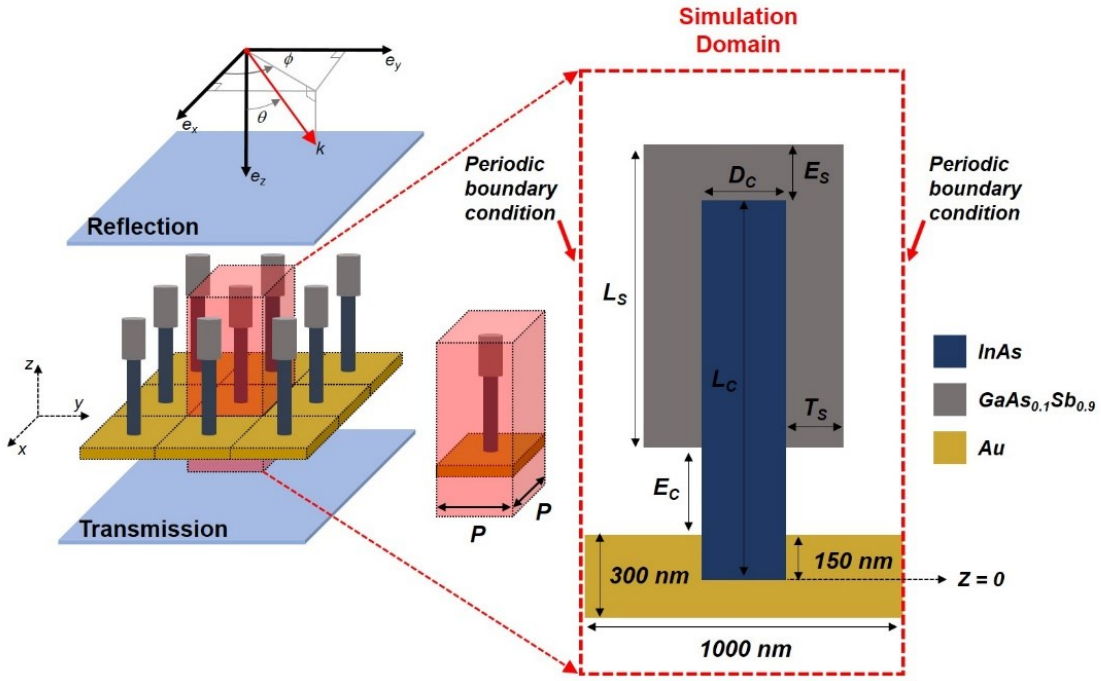

Figure 4.3. *Schematic representation of periodic InAs NWs with partial $GaAs_{0.1}Sb_{0.9}$ shell segments. Also shown is the simulation domain and the definition of related geometrical parameters where the L_C and D_C are defined as core length and diameter, respectively. The L_S and T_S are defined as shell length and thickness, respectively. The E_C and E_S are defined as the exposed core segment length and the length of the extension of the axial shell segment above the core segment, respectively.*

Unless otherwise stated, a square unit cell with constant pitch (P) of 1000 nm is used, which previously was demonstrated to be well-suited for SWIR absorption [58]. The real (n) and imaginary (κ) components of the refractive index for InAs and Au were obtained from the RSoft materials library and n-and κ-values for $GaAs_{0.1}Sb_{0.9}$ were obtained from Ref.[181]. Unless otherwise stated, the surrounding medium is set as air with n-value equal to 1. Where noted, different encapsulation media with refractive indices ranging from 1 to 1.54 are also investigated.

4.4 Light Absorption in InAs Nanowire Array Membranes with and without Backside Metal Reflectors

In Section 3.5, we demonstrated a complete procedure for fabrication of substrate-free InAs NW-based photodetectors, which was realized through NW array delamination and backside metal deposition. As reported for both thin-film and NWs geometries, the effective light path increases through introduction of a backside reflector [54], [155], [182]. In this section, the effect of the backside reflector on light absorption in InAs NW arrays is investigated via optical modeling. Figures 4.4(a) and (b) show the simulated absorption spectra of periodic arrays of InAs NWs with different diameters without and with a 300 nm-thick backside Au contact layer, respectively. The InAs NW core diameter (D_C) ranges from 100 nm to 600 nm with 100 nm increments for constant NW core segment length (L_C) of 2.5 μm. As depicted in Figure 4.4(a), increasing the NW diameter results in absorption at longer wavelength. For instance, selective absorption wavelength is increased from 1050 nm for D_C = 200 nm to 1400 nm for D_C = 300 nm. By further increasing the diameter, the absorption peak shifts toward longer wavelengths. However, wavelength-selective absorption effects due to radial mode resonance are diminished as the linewidth is expanded to the point that for D_C = 500 nm, only ~69% of the incident light over the SWIR range is absorbed in the InAs NW array. Since, the radial mode resonances depend primarily on D_C and are independent of the NW array pitch [183], increasing D_C while keeping the pitch constant leads to a rise in the surface filling factor (~79% for D_C = 500 nm and P = 1000 nm) making the NW array behave more like a planar medium. Therefore, as the fill factor increases, the top surface reflection from NWs also increases, which results in a loss of absorption intensity, as verified by the modeling results in Figure 4.4(a). In

addition, increasing D_C makes it possible for different modes to be coupled in the NWs and consequently leads to linewidth broadening or degradation of wavelength-selective absorption as shown in Figure 4.4(a) [184].

By embedding the base segments of InAs NWs to a height of 150 nm in a reflective Au film, the broadband light absorption effect is enhanced. As depicted in Figure 4.4(b) for D_C = 500 nm, ~92% of the incident light over the SWIR range is absorbed in InAs NW arrays. This can be explained by considering the effective light path increase through the NWs due to reflection from the Au backside film that acts as an almost perfect reflector in this wavelength range. Figure 4.5 shows contour plots of light absorption in InAs NW array membranes over the SWIR range (1-3 μm) for different core segment diameters ranging from 100 nm to 600 nm in 10 nm increments at a constant core segment length of 2500 nm. Figure 4.5(a) illustrates absorption in InAs NW array membranes without a Au backside contact layer. Increasing the NW diameter results in longer wavelength absorption with absorption intensity ≥ 90% (shown with dashed line) shifts to longer wavelength and broadens. However, increasing the NW diameter leads to a degradation in spectral selectivity of the absorption. This behavior is intensified when 150 nm of the base segment of the InAs NWs is embedded in a 300 nm-thick Au layer as shown in Figure 4.5(b). This trend is more noticeable for $D_C \geq 350$ nm with a backside reflector, demonstrating a tradeoff between longer wavelength absorption and selectivity for InAs NW arrays.

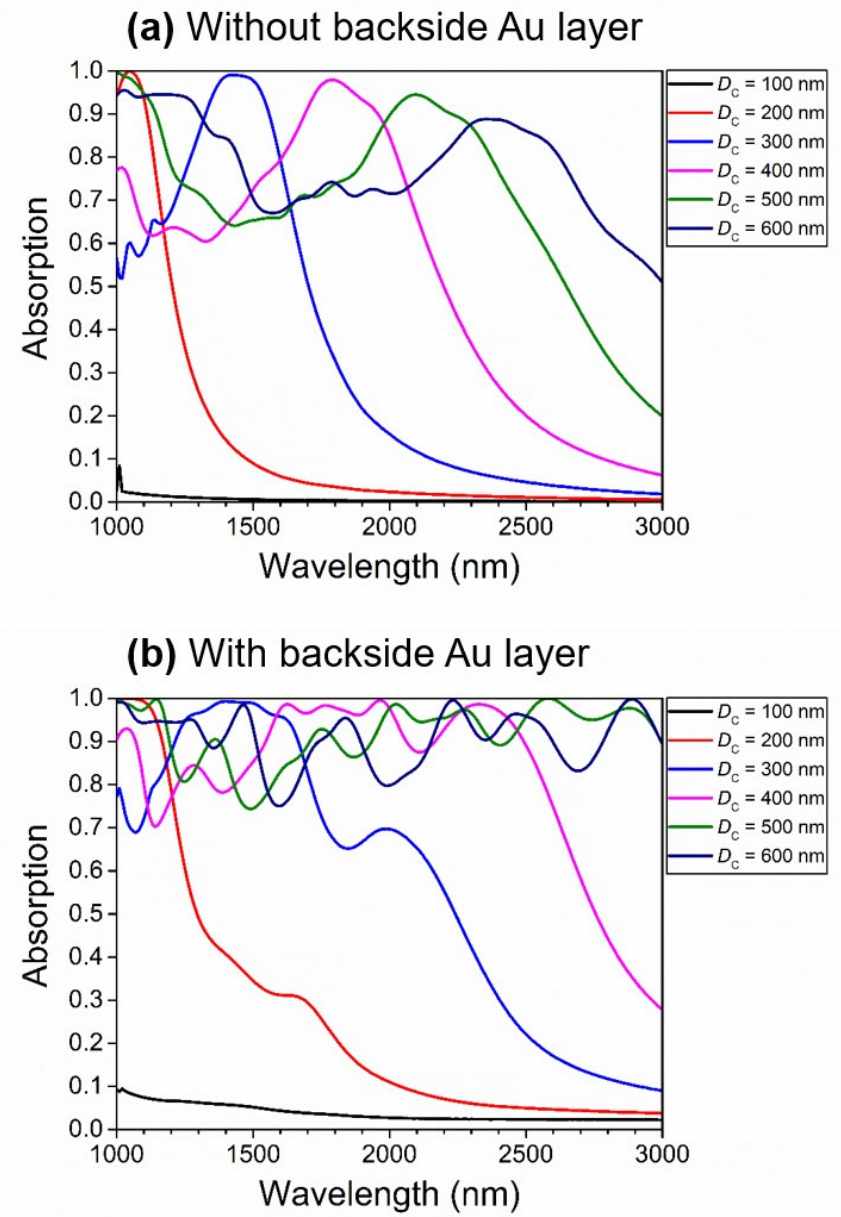

Figure 4.4. *Absorption spectra of InAs NW array membranes for diameters ranging from 100 to 600 nm (a) with and (b) without a backside Au reflector. The NW length is constant at 2500 nm for all data sets.*

Increasing the diameter of the NWs in periodic arrays can enhance broadband absorption. However, the key advantages of NW-based PDs are the possibilities of achieving room-temperature (i.e. uncooled) and ultra-high detectivity in the IR range due to the small volume of the absorbing materials [88], [185]. Minimizing the volume of the

NW array is very important, since the PD dark current scales typically with the dimensions of the absorbing medium. Additionally, increasing the NW diameter results in a loss of the radial mode resonance, which is one of the promising benefits of NW arrays for wavelength-selective absorption. Therefore, it is desirable to obtain strong wavelength-selective absorption while keeping the light absorption medium as low in volume as possible in order to break the trade-off between responsivity and dark current for high-detectivity in the SWIR spectral range.

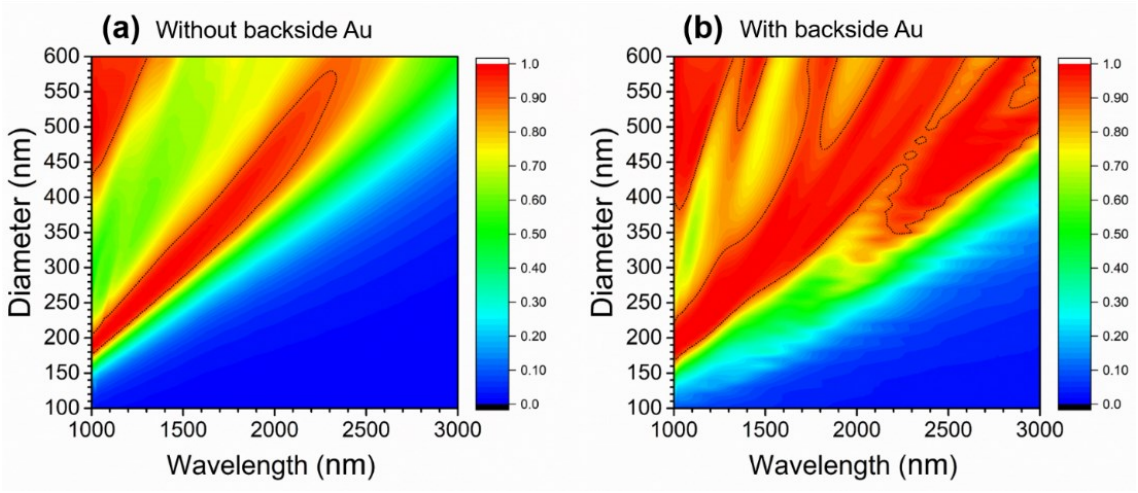

Figure 4.5. *Light absorption contour plots of InAs NW array membranes (a) without and (b) with a backside Au layer. The InAs NW core length is kept constant at* L_C *= 2500 nm.*

4.5 Absorption and E-Field Density Cross-Section Profiles

When considering the planar Au layer without NWs present, since Au serves as a near-perfect reflector in the IR range, non-absorbed incident light reflects back and consequently interferes with the incident light, which results in the formation of standing waves. For normally incident *x*-polarized light, the electric field associated with the incident beam ($\boldsymbol{E}_i$) can be described as $\boldsymbol{E}_i = E_0 e^{-ikz}\boldsymbol{e}_x$, where E_0 is the amplitude of the incident electric field, k is the wavenumber, z is the vertical distance from the center of the Au layer such that z = 150 nm marks the topside surface of the Au reflector, and $\boldsymbol{e}_x$ is the unit vector. Likewise, the electric field associated with the reflected beam ($\boldsymbol{E}_r$) can be described as $\boldsymbol{E}_r = E_r e^{ikz}\boldsymbol{e}_x$, where E_r is the amplitude of the reflected electric field. The peak intensity position of the standing waves can be calculated by considering $\boldsymbol{E}_i$ and $\boldsymbol{E}_r$. The total field in air, $\boldsymbol{E}_{tot}$, is the superposition of these components, namely: $\boldsymbol{E}_{tot} = \boldsymbol{E}_i + \boldsymbol{E}_r$ (for z > 150 nm). With good approximation of perfect reflection from the Au back contact film, it can be considered that $|E_r| = |E_0|$. The tangential component of $\boldsymbol{E}_{tot}$ should be close to zero at the interface of the perfect metal, which results in a phase change by π for $\boldsymbol{E}_r$; therefore, $\boldsymbol{E}_r = -\boldsymbol{E}_i$. As a result, standing waves in the region above of the Au film with $\boldsymbol{E}_{tot} = -2iE_0 \sin(k(z - z_0))e_x$ arise. In the absence of NWs above the mirror, the peak intensity positions of the standing wave pattern can be calculated as $z_{peak} = \lambda(\frac{1}{4} + \frac{m}{2})$, where λ is the incident wavelength and m is an integer. Figure 4.6(a) shows the E-field density profile of the standing wave pattern above the Au film for different wavelengths in the 1 to 3 μm range. As illustrated in Figure 4.6(a), as the incident

wavelength increases, the peak E-field density positions expand and the separation between the centers of the standing waves increases, since the separation is given by $\lambda/2$.

A similar effect is also expected when InAs NW arrays are introduced to the system even though the above equivalence $|E_r| = |E_0|$ is no longer valid due to incident beam absorption in InAs NW arrays. In order to comprehensively understand the light interaction behavior in InAs NW arrays, E-field density profiles are modeled for different incident wavelengths. Figures 4.6(b) and 4.6(c) show the *E*-field density profiles for different wavelengths from 1 to 3 μm in InAs NW array membranes without and with a backside reflector, respectively, at constant D_C = 300 nm and L_C = 2500 nm. Figures 4.6(d) and 4.6(e) show the light absorption profiles corresponding to Figures 4.6(b) and 4.6(c), respectively. In both cases, regardless of the inclusion of a backside Au contact layer, the incident light is absorbed in the InAs NW array membranes in the SWIR range, but optimal absorption occurs at a wavelength of ~1.4 μm due to radial mode resonance (i.e., diameter-dependent selective absorption through the HE_{11} guided mode in the NW) [14] at this wavelength, as shown in Figures 4.6(d) and 4.6(e), most of the incident light is absorbed near the top of the NWs up to a distance of 1 μm from the top surface.

For membranes without backside reflectors and for incident wavelengths > 1.4 μm, the absorption intensity decreases as the incident wavelength increases and light absorption occurs mainly along the edges of the NWs, as shown in Figure 4.6(d).The same behavior of the HE_{11} mode showing strong field intensity along the NW sidewalls has been previously shown for NWs with diameters ≤ 700 nm [54]. On the other hand, the effect of the backside reflector is observable for all wavelengths in the SWIR range, as shown in

Figure 4.6(c). When the incident light and non-absorbed reflected light interfere, periodic evanescent fields are generated around the NWs and extend between adjacent NWs.

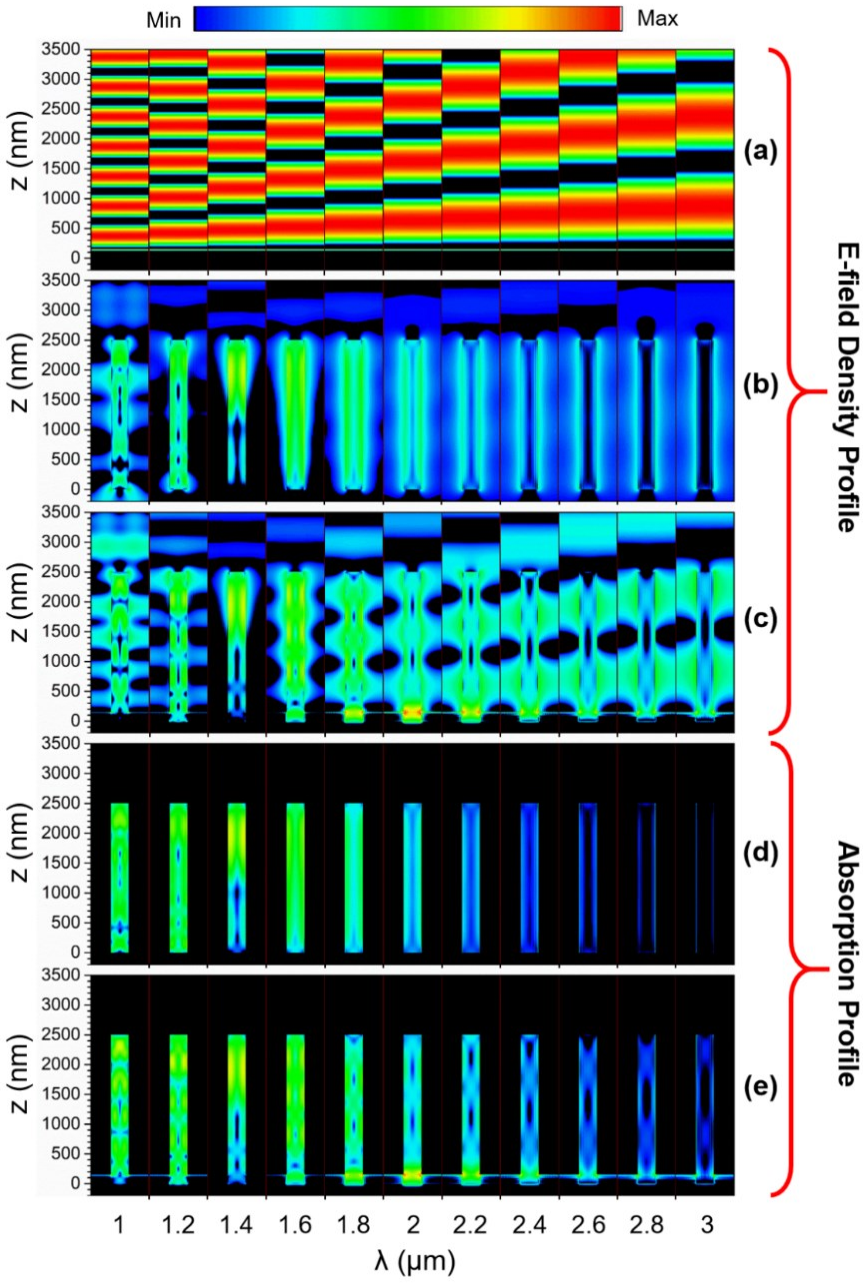

Figure 4.6. *E-field density profile at different wavelengths for (a) standing waves above the Au film, (b) InAs NWs without backside Au contact, and (c) InAs NWs with backside Au contact layer. (d) and (e) show the corresponding absorption profiles for InAs NW arrays without and with a backside Au contact layer, respectively. In all cases,* L_C *= 2500 nm and* D_C *= 300 nm. The colorbar represents values in logarithmic scale.*

These phenomena can be confirmed by observing the corresponding absorption profiles in Figure 4.6(e), where light absorption occurs periodically along the NW length compared to the absorption profile of NW arrays without backside reflectors in Figure 4.6(d). This effect is more obvious for longer wavelengths in the 2 to 3 μm range. The periodic evanescent modes are not coupled into NWs due to their small diameters and can be referred to as the delocalized mode [183], [186], [187]. Similar to standing waves formed over the Au reflector layer in Figure 4.6(a), by increasing the wavelength of incident light, the centers of the evanescent modes shift upward along the InAs NWs and their axial extent increases, resulting in a reduction of optical coupling for a given NW as illustrated in Figure 4.6(e).

The center of the decoupled modes for InAs NW arrays with backside Au contact approximately coincide with the center of the standing waves above the Au film (i.e., without InAs NW). This can be explained by the effective refractive index of the fundamental *HE11* mode ($n_{eff,HE11}$). The *HE11* guided mode is the dominant IR absorbing mode in small-diameter NWs [58], [54], [153], [115]. In the absence of NWs, the mode is a plane wave with phase propagation defined by $\exp(-ik_0zn)$, where n is the refractive index of the medium above the Au mirror and $k_0 = 2\pi/\lambda$. By introducing InAs NWs, the phase propagation becomes modified to $\exp(-ik_0zn_{eff,HE11})$, where $n_{eff,HE11}$ increases with NW diameter, D_C. Thus, increasing D_C results in a shorter spatial oscillation period for the mode at a given (free-space) wavelength. The Figure 4.7(a) shows calculated effective refractive index of the *HE11* mode ($n_{eff,HE11}$) over the 2 to 3 μm wavelength range for different InAs core diameters (D_C) at a constant pitch of 1000 nm. For small values of D_C, the change in $n_{eff,HE11}$ from n is minimal and only becomes influential for

D_C > 200 nm. For example, for D_C = 300 nm in the 2 to 3 µm range, $n_{eff,HE11}$ varies between 1.12 and 1.08. This causes a compression of the evanescent modes by 12% to 8% in the z-direction compared to the standing waves in the absence of NWs where $n = 1$. The effect of NW pitch on $n_{eff,HE11}$ at constant D_C = 300 nm is shown in Figure 4.7(b) where pitch is varied between 400 nm and 1000 nm. Increasing the pitch from 400 nm to 1000 nm (i.e., decreasing the filling factor) results in a significant drop of ~35% in $n_{eff,HE11}$ over 2 to 3 µm range. More details about effective refractive index calculations can be found in Ref. [14], [54], [188].

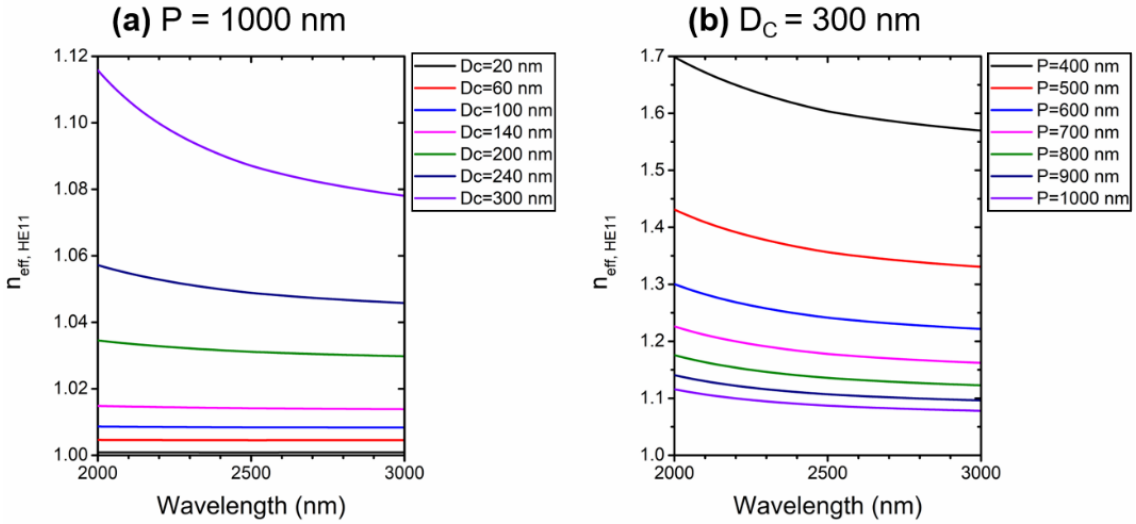

Figure 4.7. *Effective refractive index of the HE_{11} mode plotted as a function incident radiation wavelength for (a) different InAs NW core segment diameters at a constant pitch of 1000 nm and (b) different pitch values at a constant InAs NW core segment diameter of 300 nm.*

Figures 4.8(a) and 4.8(b) illustrate x-z views of the *E*-field density profile in InAs NW arrays with base segments embedded in a Au backside contact layer over the 1 to 3 µm range for D_C = 100 nm and D_C = 200 nm, respectively, with L_C = 2500 nm for direct comparison with the previous result of D_C = 300 nm. For all the three diameters, the

evanescent field is more noticeable at wavelengths longer than the diameter-dependent radial mode resonance and follows the same trend as described above. The main difference is in the position and axial extent of the evanescent field along the NWs. It is apparent that for NWs with smaller diameters, the position of the evanescent field between the NWs is more comparable with a standing wave above the bare Au film (i.e., Figure 4.6(a)). This is in good agreement with the calculated $n_{eff,HE11}$ shown in Figure 4.7, demonstrating that $n_{eff,HE11}$ becomes more comparable to the free space value for smaller NW diameters. Similarly, decreasing the NW array pitch results in an increase in the density of the light absorbing medium and, consequently, an increase in $n_{eff,HE11}$ and a corresponding compression of the decoupled modes in NW-adjacent fields at any given wavelength.

Figures 4.8(c) and 4.8(d) illustrate the corresponding absorption profiles of the NW arrays shown in Figures 4.8(a) and 4.8(b), respectively. As described above, the position, spatial extent, and separation of the evanescent modes depend mainly on the NW core segment diameter and wavelength of incident light. Based on this principle, we demonstrate a new approach for tuning the IR absorption spectra of coaxially heterostructured periodic NW arrays. We show that the otherwise decoupled mode in the 2 to 3 μm wavelength range can be selectively absorbed in InAs NW core segments by adding partial $GaAs_{0.1}Sb_{0.9}$ shell segments with dimensions and positions matched to the behavior of evanescent fields.

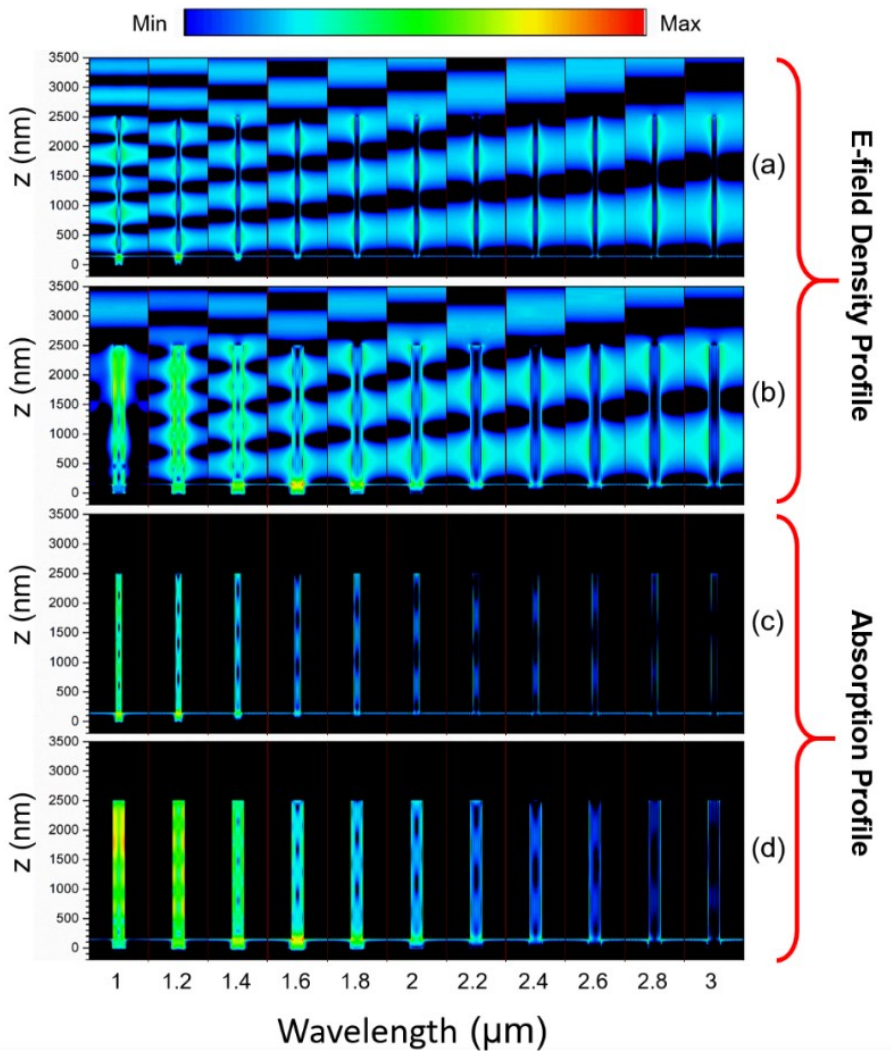

Figure 4.8. *E-field density profiles at different wavelengths spanning 1 to 3 μm for InAs NW array membranes with backside Au layer and (a) D_C = 100 nm, and (b) 200 nm. (c) and (d) show light absorption profiles coresponding to (a) and (b), respectively. In all cases, L_C = 2500 nm. The colorbar represents intensity in logarithmic scale.*

4.6 Light Absorption in Core-Shell InAs-$GaAs_{0.1}Sb_{0.9}$ NW Array Membranes

Simulations are performed for InAs-$GaAs_{0.1}Sb_{0.9}$ core-shell NW arrays with base segments embedded in Au contact layer to a depth of 150 nm. First, NW geometries with full shell layer coverage of the InAs core segment are considered. With reference to the schematic representation in Figure 4.2, the geometric parameters are defined as follows: L_C = 2500 nm, L_S = 2300 + T_S nm, D_C = 300 nm, where T_S = 25-150 nm. In this model, comparable axial and radial growth rate of the shell segment is assumed, such that $E_S = T_S$. In this way, for practical purposes of preventing short-circuit pathways between the shell segment and the Au contact, a spacer region of E_C = 50 nm is included in the modeled geometry.

Figure 4.9(a) shows the absorption spectrum over the SWIR range for InAs-$GaAs_{0.1}Sb_{0.9}$ core-shell NW array membranes with different shell thickness values ranging from 25-150 nm. The addition of a shell segment with 25 nm thickness extends the ≥ 90% absorption spectral range from 1.4 μm (peak absorption wavelength for InAs core segment alone with 300 nm diameter) to longer wavelengths (i.e., ~1.85 μm). Similar trends are observed by increasing the shell thickness, meaning that longer wavelengths can be absorbed. Considering that the shell material is completely transparent for wavelengths ≥ 1.9 μm, all of the incident light is absorbed by the InAs core segment. Therefore, the shell segment extends the absorption range to longer wavelengths without increasing the volume of the light absorbing medium. Some distinguishable peaks can be observed at wavelengths > 2500 nm for thicker shell segments, specifically at shell thickness values of 100, 125,

and 150 nm. This may be addressed by considering the influence of the evanescent field as discussed earlier, whereby the shell segment can trap the delocalized mode outside of the core such that it can be absorbed by the InAs segment.

In order to further explore this concept, simulations are performed for structures with partial shell coverage. The geometric parameters are defined as follows: L_C = 2500 nm, L_S = 700 nm, D_C = 300 nm, T_S = 25-150 nm, and E_C = 1350 nm. Here, the $GaAs_{0.1}Sb_{0.9}$ shell segment length and position are intentionally chosen to match the size and position of the evanescent field at 2.6 μm based on Figure 4.6(c). Figure 4.9(b) shows the absorption spectra of partial core-shell structures with the above dimensions. As shown, for all shell thicknesses ≥ 50 nm, only a single absorption peak is observed in the 2 to 3 μm wavelength range. As the thickness of the shell segment increases, the absorption peak undergoes a red shift towards longer wavelengths, exhibiting greater selectivity with a reduced linewidth. This phenomenon can be elucidated through F-P interference, as discussed in Section 1.4. The expansion of the shell segment thickness leads to enhanced reflections from both the top and bottom surfaces, contributing to a decrease in linewidth (i.e., FWHM).

For T_S = 150 nm, close to unity absorption at a peak wavelength of 2.62 μm is obtained, which is attributed to a suitable fit between the evanescent field position and shell geometry. This point can be demonstrated further by shifting the shell position along the length of the InAs core segment. For this set of simulations, partial core-shell structures with L_C = 2500 nm, L_S = 700 nm, D_C = 300 nm, T_S = 150 nm, and E_C = 1350 nm are chosen (solid dark blue line in panel (b) of Figure 4.9). Relative to its initial position in Figure 4.9(b), the shell segment is shifted in 100 nm increments upward and downward along the central InAs core, corresponding to values of E_C between 1150 nm and 1550 nm. As shown

in Figure 4.9(c), by shifting the $GaAs_{0.1}Sb_{0.9}$ shell downwards and upwards, the peak at 2.62 μm is shifted to shorter and longer wavelength, respectively. However, the peak absorption intensity is decreased noticeably, which indicates that for optimal narrowband wavelength-selective absorption, a specific shell geometry including thickness and position must be assigned.

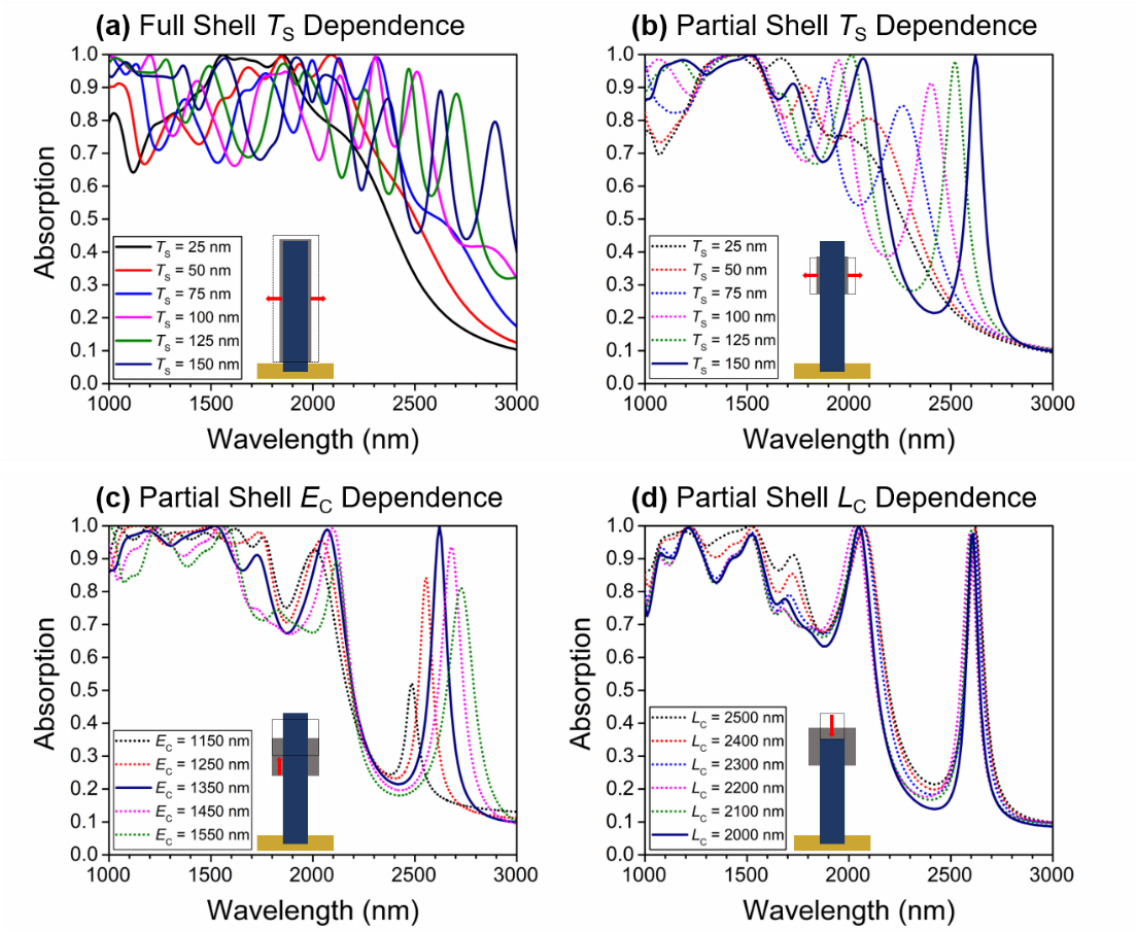

Figure 4.9. *Absorption spectrum over SWIR range of (a) InAs-$GaAs_{0.1}Sb_{0.9}$ core-shell with full core coverage for different shell thickness, (b) partial InAs-$GaAs_{0.1}Sb_{0.9}$ core-shell for different shell thickness, (c) partial InAs-$GaAs_{0.1}Sb_{0.9}$ core-shell with T_S = 150 nm and L_S = 700 nm for different E_C (shell segment position along core segment) and (d) partial InAs-$GaAs_{0.1}Sb_{0.9}$ core-shell with T_S = 150 nm, L_S = 700 nm and E_C = 1350 nm for different L_C = 2500-2000 nm.*

The partial core-shell geometry shown in the insets of Figures 4.9(b) and 4.9(c) requires selective $GaAs_{0.1}Sb_{0.9}$ shell formation along the InAs NW core segment. Although selective radial epitaxy has been demonstrated for NWs grown using the vapor-liquid-solid mechanism, the approach is mainly feasible when the core segment crystal structure can be well-controlled during particle-assisted synthesis. For example, Namazi et al. have demonstrated selective growth of GaSb shell segments on InAs NW core regions with zinc blende crystal structure, while GaSb growth was suppressed along wurtzite phase InAs core regions [189]. For NW growth via seed-free methods that are less conducive to crystal phase engineering, partial shell formation at site-specific locations along the core segment can be more reasonably achieved through multiple selective chemical etching steps. A process flow for the fabrication of coaxial nanowires with partial shell segments is depicted in Figure 4.10. Two different fabrication approaches are presented here corresponding to Figure 4.9(d) including: (1) a structure in which the NW core segment extends above shell segment as depicted in Figure 4.10(a), and (2) a structure in which the NW shell segment extends above core segment as depicted in Figure 4.10(b). In both cases, InAs NW core segments are first grown (Step 1). Next, the core segments are passivated with an oxide layer to encapsulate the full length of the NWs (Step 2). The NWs are then coated with photoresist (Step 3) and etched back to a desired height based on the shell position as determined from simulation results (Step 4). The passivation mask is selectively etched to expose the tip of the NWs for shell growth (Step 5), followed by photoresist removal (Step 6). Next, $GaAs_{0.1}Sb_{0.9}$ growth is carried out with the desired thickness (Step 7). For the first approach, the undesired shell segment length at the top of the NW must be removed to keep the $GaAs_{0.1}Sb_{0.9}$ shell segment at a specific location along the NW core segment

corresponding to the black dotted curve in Figure 4.9(d). This can be realized via photoresist coating (Step 8 in Figure 4.10(a)) and followed by RIE treatment to etch the photoresist to the desired height (Step 9 in Figure 4.10(a)). Then, the excess shell segment length is removed by selective chemical etching (Step 10 in Figure 4.10(a)).

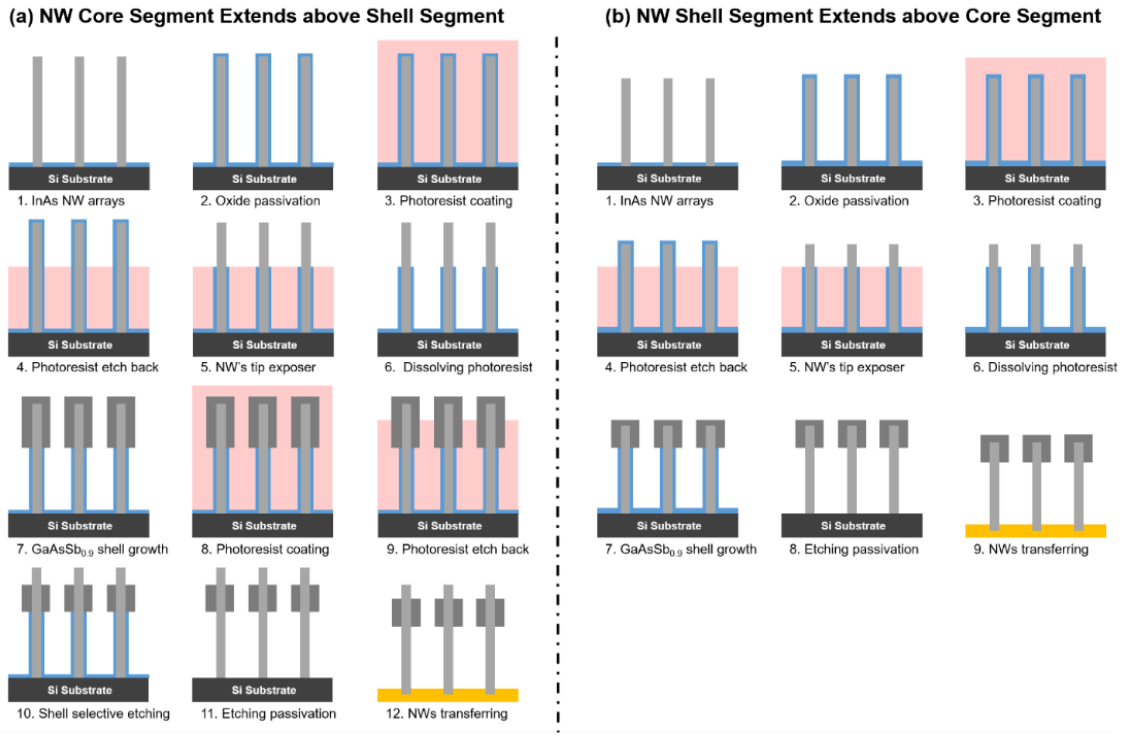

Figure 4.10. *Schematic diagram of partial $GaAs_{0.1}Sb_{0.9}$ shell segment growth processes: (a) 1. SAE growth of NW core segments; 2. Oxide mask deposition around the NWs; 3. Coating and planarization of photoresist layer; 4. RIE treatment to etch back the photoresist to the desired height based on simulation results; 5. Oxide mask chemical etching to expose the core segment for shell growth; 6. Photoresist dissolution; 7. $GaAs_{0.1}Sb_{0.9}$ shell segment growth; 8. Coating and planarization of photoresist layer; 9. RIE treatment to etch back the photoresist to desired shell segment height; 10. Selective chemical etching of shell segment along NW tip; 11. Chemical etching of passivation layer; 12. NW array delamination and transfer. (b) Steps 1-7 are the same procedure as shown in (a); Step 8. Chemical etching of passivation layer; 9. NW arrays delamination and transfer. The final structure at Step 12 in (a) and Step 9 in (b) correspond to the simulated structures in Figure 4.9(d) with dotted black curve and solid blue curve, respectively.*

In the second approach wherein the shell segment resides at the NW tip, the shell segment with desired dimensions is grown after Step 6, which eliminates the selective chemical etching step, as depicted in Figure 4.10(b). In both approaches, the final steps include etching of the passivation layer (Step 11 and 8 in Figure 4.10(a) and (b), respectively), followed by NW array delamination and transfer (Step 12 and 9 in Figure 4.10(a) and (b), respectively), as presented in Chapter 3.

Figure 4.11 illustrates *x*-*z* views of E-field density profiles in InAs NW array membranes embedded in a Au backside contact layer over the 1 to 3 μm range for different NW lengths of L_C = 1250 nm, 2500 nm, and 5000 nm for constant D_C = 300 nm. For the represented L_C range where the incident light is only weakly absorbed in the InAs NWs, the NW length has no significant impact on the position and spatial extend of the delocalized mode. Comparing the results shown in Figure 4.11 reveals that the axial extent and position of the evanescent field along the InAs NWs is periodic and not affected by the length of the core segment. Hence, the length and diameter of the InAs core segment can be rationally designed such that the desired evanescent field of specific wavelength is positioned near the NW tip and such that the deposition of a $GaAs_{0.1}Sb_{0.9}$ segment only in the corresponding tip location enables selective narrowband light absorption. In order to demonstrate this point, simulations are performed to study the effect of the InAs core length (L_C), while keeping the position of the shell segment at a fixed height above the Au mirror. The same geometry as in the previous simulation is used but with different core segment lengths decreasing from 2500 nm to 2000 nm in 100 nm increments. For L_C = 2500 nm, the top-most 300 nm region of the tip of the core segment is not covered by the $GaAs_{0.1}Sb_{0.9}$ shell; whereas, for L_C = 2000 nm, the top of the InAs core segment is covered by a

$GaAs_{0.1}Sb_{0.9}$ shell such that E_S = 200 nm. As represented in Figure 4.9(d), the length of the exposed core segment tip does not affect the intended absorption wavelength and all cases reveal > 95% absorption at ~2.6 μm.

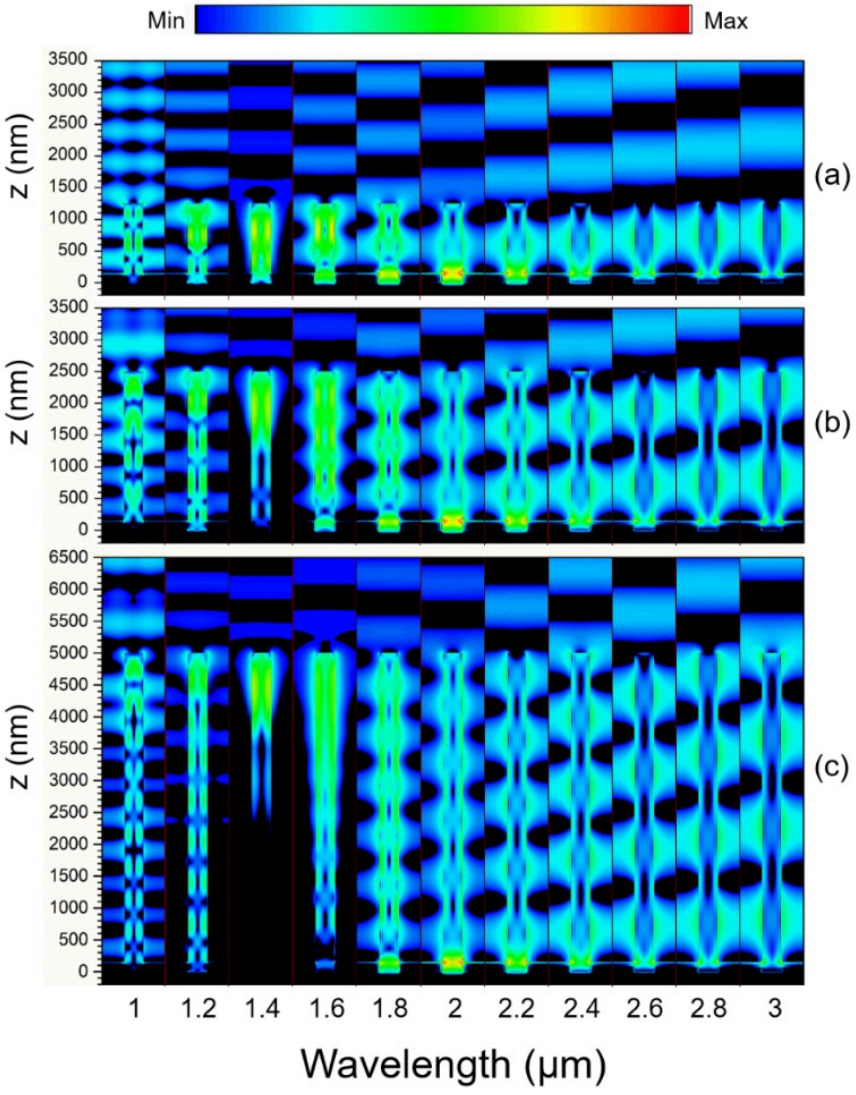

Figure 4.11. *E-field density profiles at selected wavelengths for InAs NWs with base segments embedded in a Au contact layer. The profiles are modeled for different NW core segement lengths of (a) L_C = 1250 nm, (b) L_C = 2500 nm, and (c) L_C = 5000 nm. In all cases, D_C = 300 nm. The colorbar represents intensity in logarithmic scale.*

The main influence is on the linewidth of the absorption line, insofar as increasing the core segment length results in linewidth broadening, which effectively represents a reduction in spectral selectivity. This can be explained by considering that as the length of the core segment decreases, the core-shell overlap also decreases. Thus, the evanescent field at any given wavelength can only be coupled through a shell segment that captures a portion of the otherwise decoupled mode. We show that otherwise decoupled modes in the 2 to 3 μm wavelength range can be selectively absorbed in InAs NW core segments by adding partial $GaAs_{0.1}Sb_{0.9}$ shell layers with thickness and position corresponding to the desired evanescent field. The $GaAs_{0.1}Sb_{0.9}$ layers are transparent in this wavelength range and only act to enhance absorption of the evanescent field. Wavelength-selective absorption is localized to positions along the InAs core segments where they are partially encapsulated. The absorption wavelength can be manipulated as a function of the partial shell segment position, length, and diameter. Moreover, narrowband wavelength selectivity can be controlled by tuning the length of the InAs NW core segment.

A series of additional simulations are performed based on the NW tip-encapsulated partial shell structure. Figure 4.12 shows contour plots of light absorption in arrays of NWs with InAs core segments of constant diameter, D_C = 300 nm, with $GaAs_{0.1}Sb_{0.9}$ shell segments at their tips with L_S = 700 nm and $E_S = T_S$. Absorption is plotted over the SWIR range while the InAs core segment length, L_C, is varied from 700 to 4000 nm for different shell segment thicknesses of 100, 150, and 200 nm. For wavelengths less than 2 μm most incident light is absorbed by the core and shell, and wavelength-selective absorption is not realized. For instance, for structures with T_S = 150 nm and L_C = 2050 nm, the total absorption over the 1 to 2 μm range is ~84%.

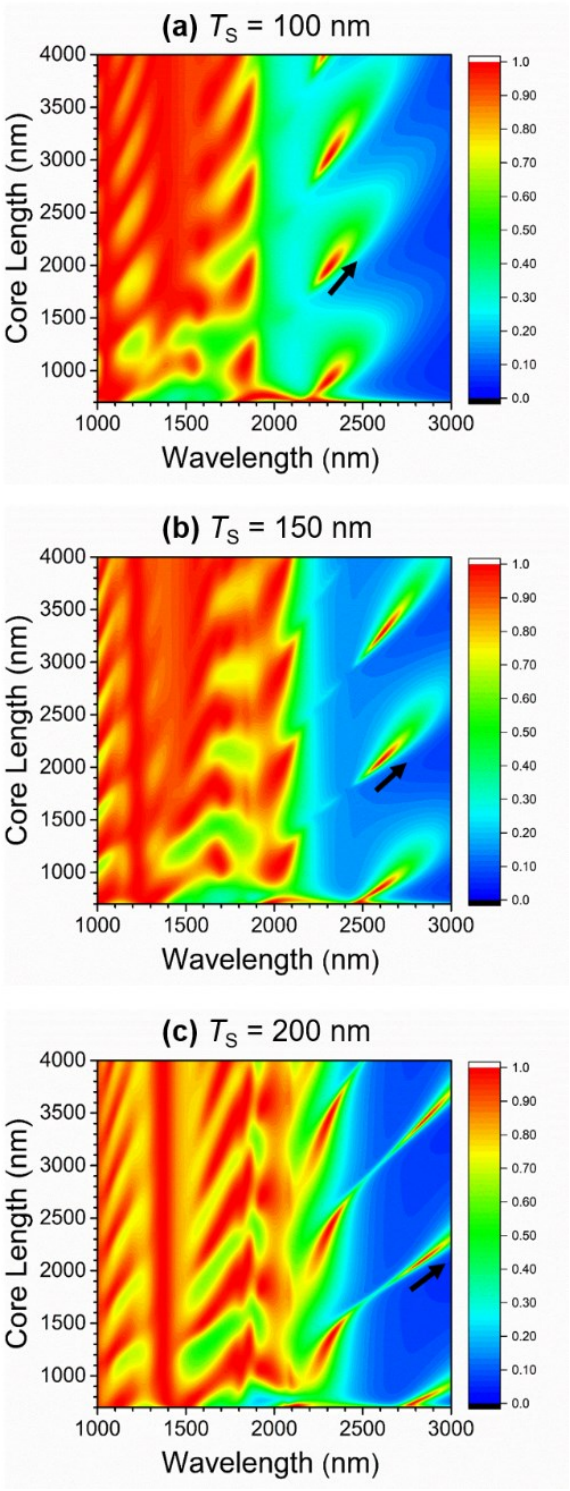

Figure 4.12. *Contour plots of absorption intensity over the 1000 to 3000 nm wavelength range for core-shell InAs-$GaAs_{0.1}Sb_{0.9}$ structures with partial shell segments at the NW tip, where the NW core segment length is varied between L_C = 700 and 4000 nm for different shell thickness values of (a) T_S = 100 nm, (b) T_S = 150 nm, and (c) T_S = 200 nm. In all cases, L_S = 700 nm and $E_S = T_S$.*

By tuning L_C and T_S, selective absorption peaks can be freely shifted in the 2 to 3 μm spectral range such that near-unity absorption is realized for particular core-shell geometries. By increasing L_C, the absorption peaks are shifted toward longer wavelengths for all values of T_S, as indicated by the black arrows in Figure 4.12, which shows good agreement with the trend in the position of the delocalized mode. This can be explained by the evanescent field pattern defined by $n_{eff,HE11}$ for the bare InAs core segment. As depicted in Figure 4.6(c), increasing the incident light wavelength shifts the position of the evanescent field upward along each InAs NW.

Additionally, Figure 4.11 demonstrates that for the range of NW lengths considered here, L_C does not affect the presence or position of the delocalized mode. Thus, at longer wavelengths, the anti-nodes of the standing wave of the otherwise decoupled mode, which are shifted upward along the InAs core segment, can coincide with the position of the partial $GaAs_{0.1}Sb_{0.9}$ shell segment at the NW tip as L_C increases.For all values of T_S in the incident wavelength range beyond 2 μm, the periodic nature of the near-unity absorption peaks along the L_C axis (i.e., red fringes in Figure 4.12) supports the notion that the position of the evanescent field at any given wavelength scales with $\lambda/2$.

As shown in Figure 4.12, thicker shell layers are needed to trap longer wavelength light, which is consistent with the observed trends in Figure 4.9(b). Therefore, the effect of the shell thickness must be considered for wavelength-selective absorption using partial core-shell NW geometries. With shell segment thickness of 200 nm, as shown in Figure 4.12(c), highly selective absorption can be realized when targeting the long-wavelength range (i.e., narrow red fringes) where InAs is otherwise weakly absorbing. This can be attributed to a similar effect as discussed above for Figure 4.9(b), resulting from the

increased thickness of the shell and consequently an enhancement in the reflections from the top and bottom interfaces of the shell. This effect, related to F-P interference discussed in Section 1.4, culminates in a decrease in linewidth. In addition, considering that the anomalous mode coupling effect of the shell promotes absorption, but the weak absorption of the underlying InAs core segment gives a sharp drop in peak absorption intensity, resulting in a narrow linewidth. At shorter wavelengths, absorption of the InAs core segment is increased as shown in Figure 4.12(b) causing a broadening of the absorption peak in comparison to the case where a thicker partial $GaAs_{0.1}Sb_{0.9}$ shell is employed.

The influence of the InAs core diameter is shown in Figure 4.13, where D_C is varied from 50 nm to 400 nm in 50 nm increments for L_C values ranging between 700 nm and 4000 nm, and at a constant T_C value of 150 nm. For $D_C \leq 150$ nm, absorption in the 2 to 3 μm range is less than 5%. However, for $D_C = 200$ nm, selective absorption is observed staring at a wavelength of approximately 2.25 μm and extended to 3 μm for $D_C = 400$ nm. As D_C increases, the selective absorption peak wavelength shifts toward longer wavelengths and broadens along both the L_C and light absorption is enhanced at larger NW core diameters. It is worth noting again that the extent of the evanescent field along the InAs core segment at any constant value of D_C is a function of the incident wavelength. For shorter incident wavelengths, the extent of the decoupled mode is correspondingly narrowed.

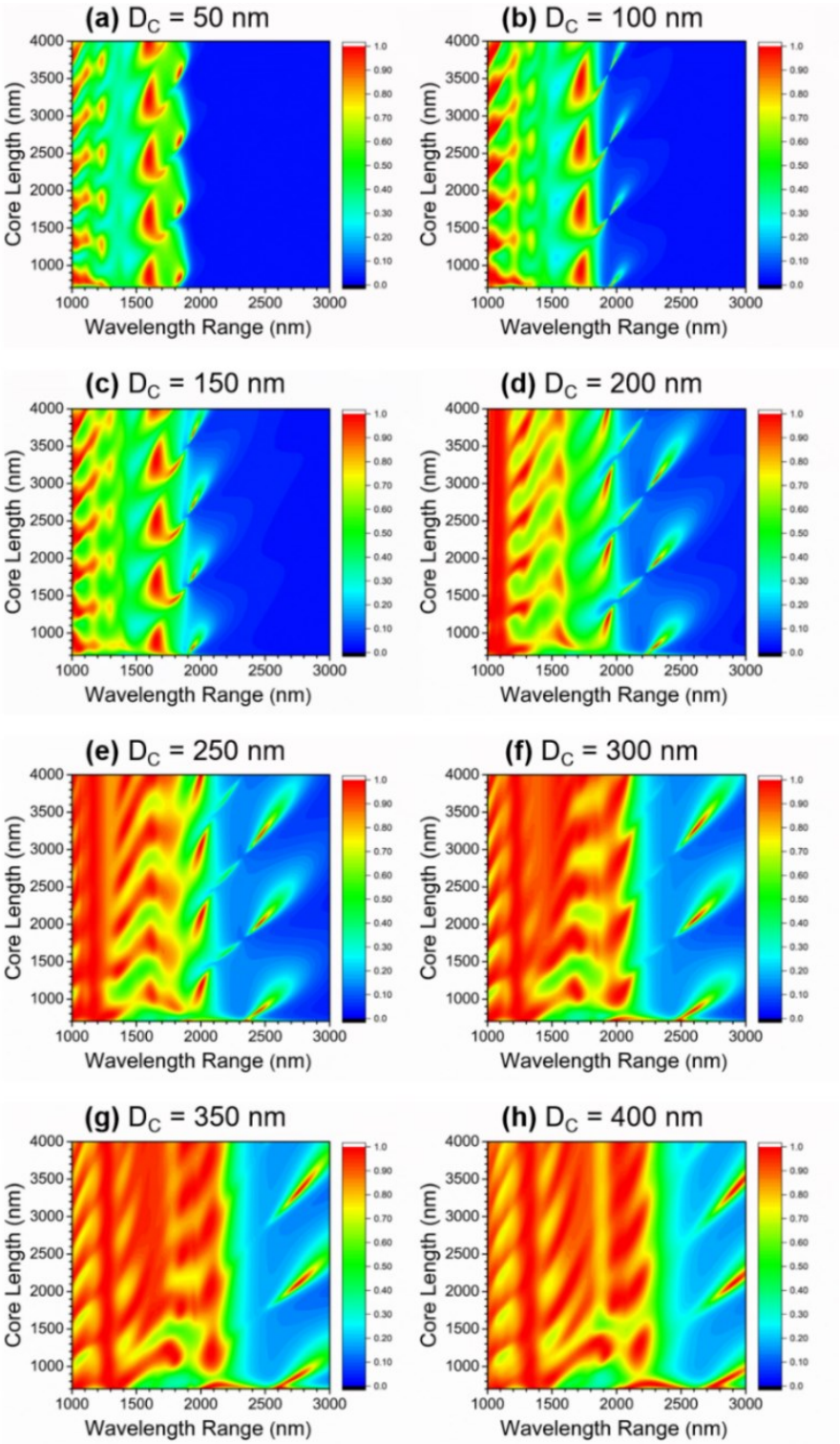

Figure 4.13. *Contour plots of absorption intensity over the 1 to 3 μm wavelength range for core-shell InAs-$GaAs_{0.1}Sb_{0.9}$ structures with partial shell segment coverage at the NW tip, where the NW core segment length is varied between L_C = 700 and 4000 nm for different shell thickness values of D_C = 50 to 400 nm in (a) through (h). In all cases, L_S = 700 nm, T_S = 150 nm, and E_S = T_S.*

In all of the above cases, a constant L_S value of 700 nm is used for the purposes of direct comparison. However, the shell length plays an important role and L_S = 700 nm is not optimally matched for incident wavelengths < 2 μm due to the $GaAs_{0.1}Sb_{0.9}$ shell segment absorptance, which results in a secondary absorption peak at shorter wavelengths. The effect of L_S is investigated for the same geometries in order to decrease the secondary peak absorption intensity as shown in Figure 4.14(a). Decreasing L_S results in a corresponding decrease in the secondary peak until it is quenched at L_S = 550 nm. However, the primary peak at ~2500 nm is also decreased in absorption intensity. The primary peak can be recovered through small adjustments in core segment length such that unity absorption is achieved at L_C = 1950 nm, without considerable re-appearance of the secondary peak, as shown in Figure 4.14(b).

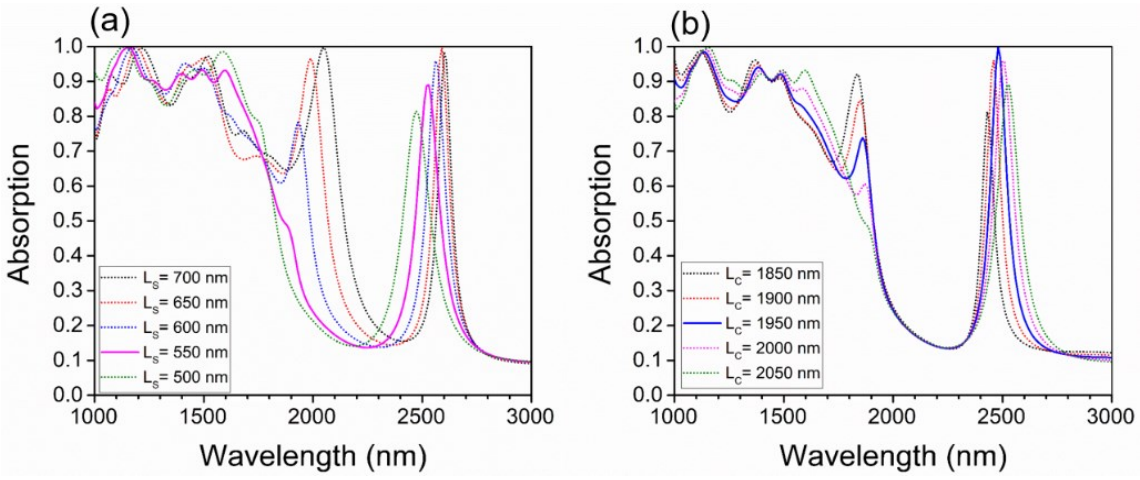

Figure 4.14. *(a) Absorption spectra showing the effect of (a) shell segment length, L_S and (b) core segment length, L_C. By adjusting L_C, unity absorption is recovered for the optimal NW geometry with L_S = 550 nm.*

Figure 4.15 shows the simulated absorption spectra various NW array geometries and summarizes the key features discussed above. Structure A defines an InAs-

$GaAs_{0.1}Sb_{0.9}$ core-shell NW with L_C = 1950 nm, D_C = 300 nm, L_S = 550 nm, E_C = 1400 nm and $E_S = T_S$ = 150 nm, such that the partial shell segment is situated at the tip of the NW. The absorption spectra of four different NW geometries are compared with that of structure A in order to highlight the attributes of the optimized structure for narrowband wavelength-selective light absorption. Structure B defines an InAs-$GaAs_{0.1}Sb_{0.9}$ core-shell NW with L_C = 2500 nm, D_C = 300 nm, L_S = 550 nm, E_C = 1400 nm and T_S = 150 nm, such that the shell segment does not encapsulate the NW tip. Structure C defines an InAs-InAs core-shell NW with L_C = 1950 nm, D_C = 300 nm, L_S = 550 nm, E_C = 1400 nm and $E_S = T_S$ = 150 nm. This structure is identical to Structure A, except for the distinction that the core and shell segments are both composed of InAs. Structure D defines an InAs NW with L_C = 1950 nm and D_C = 300 nm. Structure E defines an InAs NW with L_C = 1950 nm and D_C = 600 nm. To summarize and show the effect of the NW shell segment, absorption and E-field density profiles are shown at the primary absorption peak wavelength of 2.48 μm for Structure A in Figure 4.15. As noted above, the shell is transparent at this wavelength, corresponding to the dark absorption profile beyond the NW core segment. Observing the *E*-field profile reveals that at a wavelength of 2.48 μm, the field is localized at the position of the $GaAs_{0.1}Sb_{0.9}$ shell segment. Therefore, the shell segment can act as a light guide to localize and concentrate the incident light, such that it can be absorbed in the core segment; whereas, without a shell layer, the core segment itself is only absorbing around 20% of the incident light at a wavelength of 2.48 μm as shown in the absorption spectra in Figure 4.15.

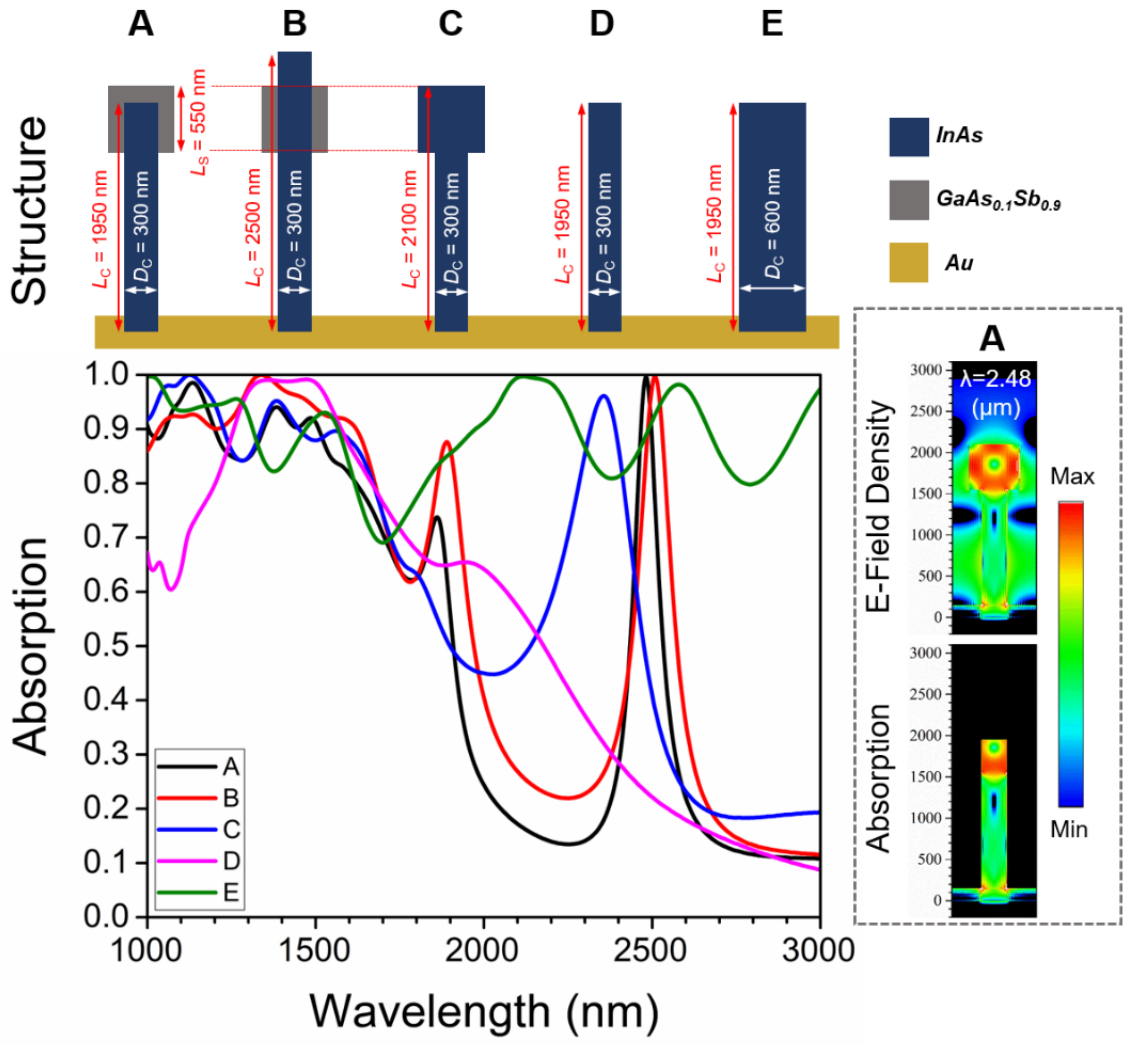

Figure 4.15. *Comparison of absorption spectrum for different structures. A: InAs-$GaAs_{0.1}Sb_{0.9}$ partial core-shell, where D_C = 300 nm, L_C = 1950 nm, L_S = 550 nm and E_S = T_S = 150 nm. B: InAs-$GaAs_{0.1}Sb_{0.9}$ partial core-shell, where D_C = 300 nm, L_C = 2500 nm, L_S = 550 nm and T_S = 150 nm, C: InAs-InAs partial core-shell, where D_C = 300 nm, L_C = 2100 nm, L_S = 550 nm and E_S = T_S = 150 nm. D: InAs core where D_C = 300 nm, L_C = 1950 nm. E: InAs core where D_C = 600 nm, L_C = 1950 nm. Insect shows E-field density profile and corresponding absorption profile at 2.48 μm for Structure A. The colorbar represents values in logarithmic scale.*

Comparing the absorption spectra of Structures A and B, the same behavior is observed except for a small red shift in the primary peak wavelength and a ~20% higher absorption intensity in secondary peak in the case of Structure B. This shows the benefit of Structure A over B, which is not only more practical in terms of synthesis but also

partially quenches the secondary peak. The geometry influence is also investigated via Structure C, as shown in Figure 4.15. Wavelength-selective absorption is observed at ~2.36 μm with 96% absorption. However, the selectivity is reduced compared to Structure A as the bandwidth is increased. This indicates that even though the NW geometry plays a bigger role in the selective absorption effect, both the material composition and geometry of the NW core and shell segments must be carefully optimized for the highest selectivity. The absorption spectrum shows negligible absorption beyond 2 μm in the case of the InAs NW with 300 nm core diameter (i.e., Structure D). However, for the InAs NW with 550 nm diameter (i.e., Structure E), 90% of the incident light is absorbed over 2 to 3 μm range. Increasing the InAs NW diameter results in higher absorption in the SWIR region, but the larger diameter is expected to also result in an increase in the undesired PD dark current. Importantly, wavelength-selective absorption cannot be realized in the case of larger diameter NWs. The nanophotonic engineering approach introduced in this work can be used to selectively absorb incident SWIR radiation in InAs NW core segments with smaller diameters. Moreover, using this method, the active region of the PD device can be placed in the designed absorption region near the NW tip, which can dramatically increase detectivity.

For all NW array cases discussed thus far, the refractive index of the background medium is selected as $n = 1$, meaning that no encapsulation medium is assumed. However, from a practical point of view, NW arrays are usually encapsulated in a spacer medium for surface planarization and contacting purposes during the device fabrication process. The encapsulation medium of higher refractive index than air shifts the standing wave pattern located above the Au layer, resulting in a loss of the desired wavelength-selective

absorption (unless another anti-node of the standing wave pattern happens to shift to coincide with the location of the shell segment). Figure 4.16 shows the influence of the background refractive index. Here, absorption spectra are simulated for the case of Structure A when fully embedded in benzocyclobutene (BCB), a common encapsulation medium with $n = 1.54$ [167], [190], [191].

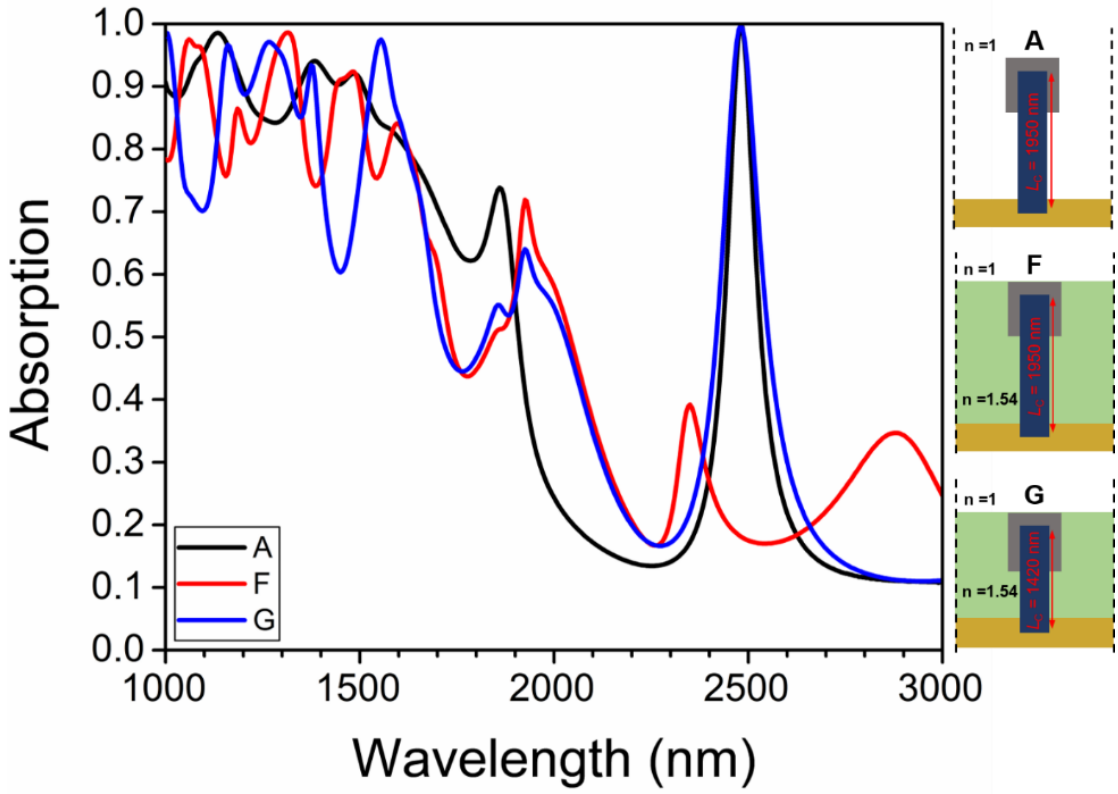

Figure 4.16. *A comparison of the absorption spectra of Structures A, F, and G showing the effect of BCB as an encapsulation medium.*

This structure is henceforth referred to as Structure F. The absorption spectrum (red curve) in the 2 to 3 μm range is no longer comparable with that of Structure A (black curve). However, considering that increasing the refractive index modifies the wavelength in the material by λ/n, the standing wave pattern becomes compressed along the length of

the NW. Figure 4.17 shows the E-field density profile for an InAs core segment with D_C = 300 nm and L_C = 2500 nm encapsulated in BCB. Hence, the center of decoupled modes is shifted down along the InAs core axis, which means the length of the core segment can be simply adjusted to capture the desired evanescent field. As shown in Figure 4.16, when L_C is shortened from 1950 nm to 1420 nm in the case of Structure G, the same absorption peak at 2.48 µm is recovered (blue curve).

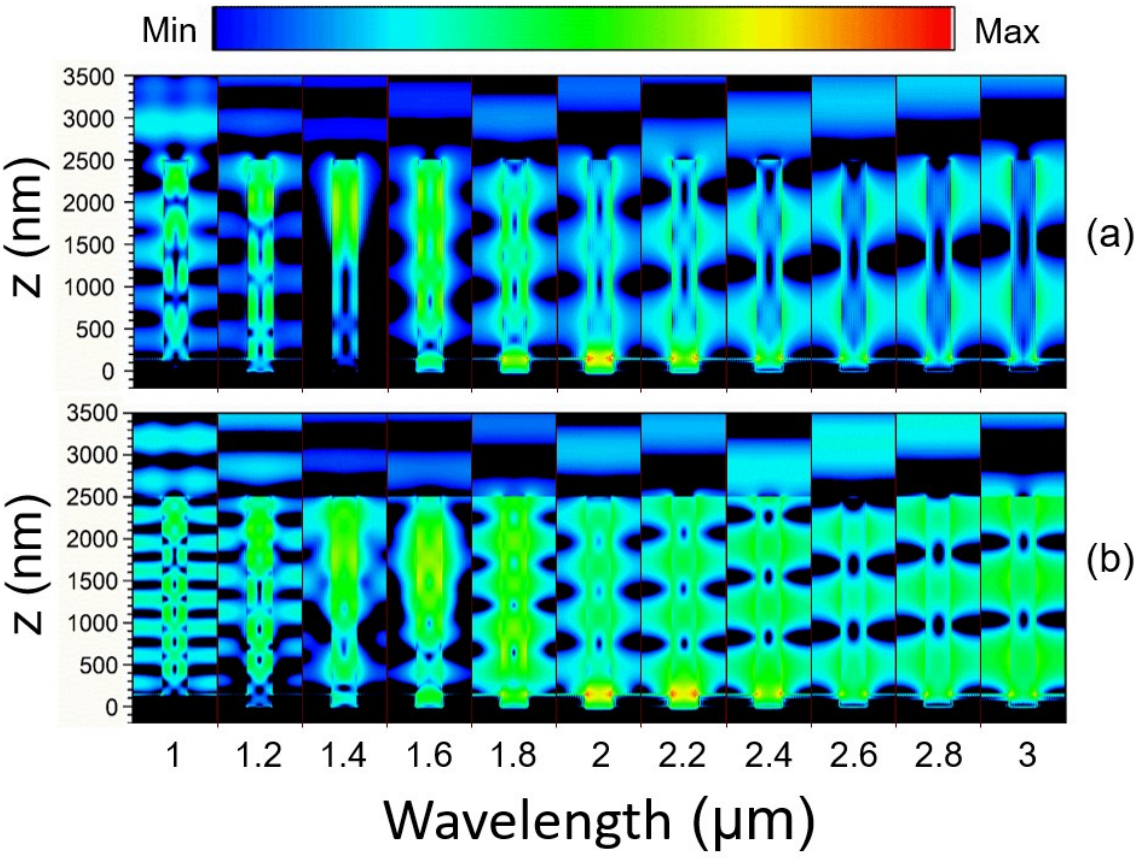

Figure 4.17. *E-field density profiles at different wavelengths for InAs NWs on a Au contact layer, where D_C = 300 nm and L_C = 2500 nm. The encapsulating medium is modeled as (a) air with n = 1 and (b) BCB with n = 1.54. The colorbar represents values on logarithmic scale.*

Figure 4.18 shows the effect of different encapsulation media with different refractive indices from 1 to 1.5 and 1.54 (i.e., BCB) on the absorption spectrum of Structure A depicted in Figure 4.15. By increasing n, the absorption peak shifts toward longer wavelength and is reduced in intensity. This is likely explained by the compression of the position of the evanescent field along the length of the NWs as shown in Figure 4.17.

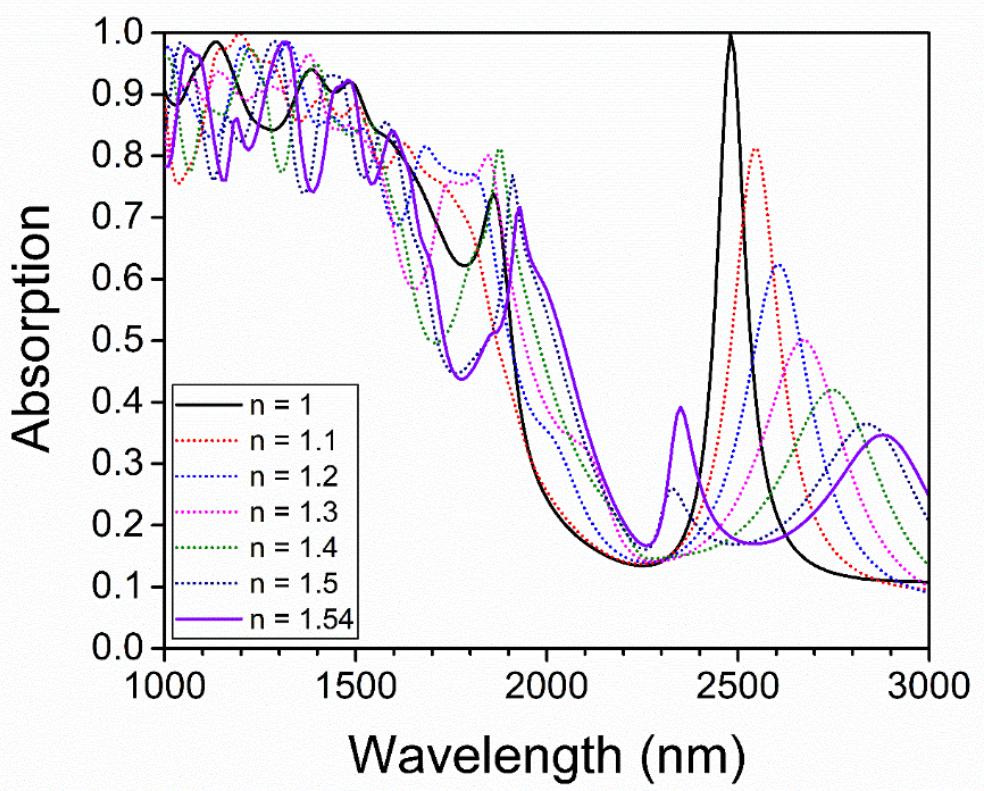

Figure 4.18. *Simulated absorption spectra for Structure A NW arrays embedded in encapsulation media with refractive indices varied between 1 and 1.54.*

Lastly, absorption spectrum dependence on the incidence polar angle (θ) is investigated for Structure A under two different azimuthal angles (ϕ) of 0° and 45° for both p and s polarizations, independently. Figure 4.19 shows absorption spectra for different polar angles ranging from 0° to 75° in 7.5° increments. A strong polarization dependence

is observed. For p-polarization and ϕ = 0°, the primary peak absorption intensity is decreased by increasing θ such that at θ = 37.5° the primary peak is completely quenched and by further increasing θ the primary peak is recovered at θ = 75°, while s-polarization maintains a primary peak absorption at > 90%. The observed behavior is promising for polarization detection with several applications including remote sensing, telecommunications, environmental monitoring and more [192]. The s/p ratio is calculated for all angles of θ, which reveals the important point that for the partial core-shell Structure A, both spectral- and polarization-dependent detection can be achieved.

Specifically, at θ = 37.5°, polarization-dependent optical filtration is realized using Structure A NW arrays with an s/p ratio of ~5, as shown in Figure 4.20. It is worth mentioning that Structure A has not been specifically designed for polarization-dependent detection and these polarization simulations are performed to demonstrate the concept that partial core-shell structures hold promise for such polarization filtration applications.

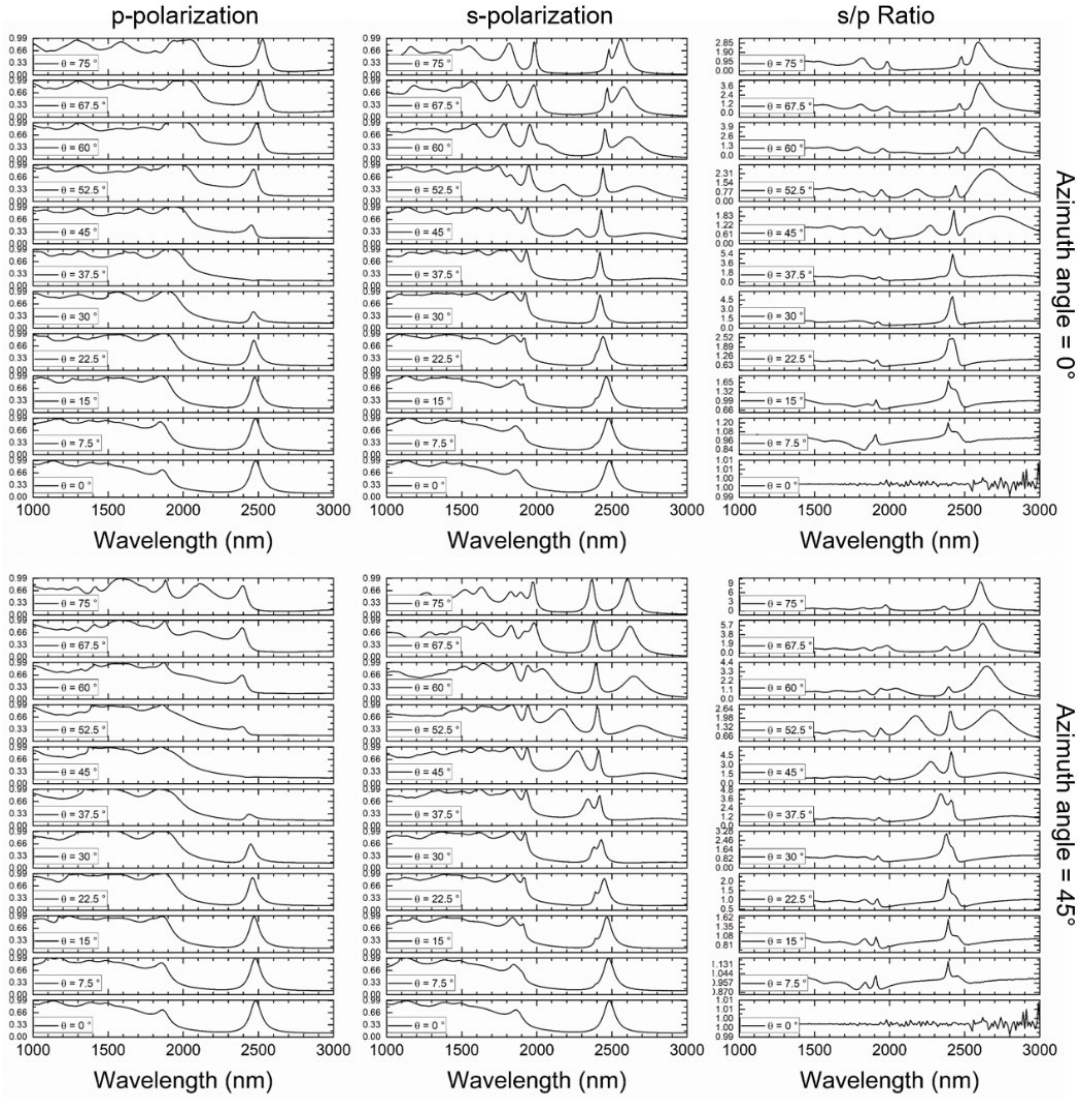

Figure 4.19. *p-polarization (left column) and s-polarization (center column) dependences for different polar angles of incidence ranging from 0° to 75° and for azimuthal angles of 0° (top row) and 45° (bottom row). In each case, the s/p polarization ratio is plotted (right column) in the 1 to 3 μm range.*

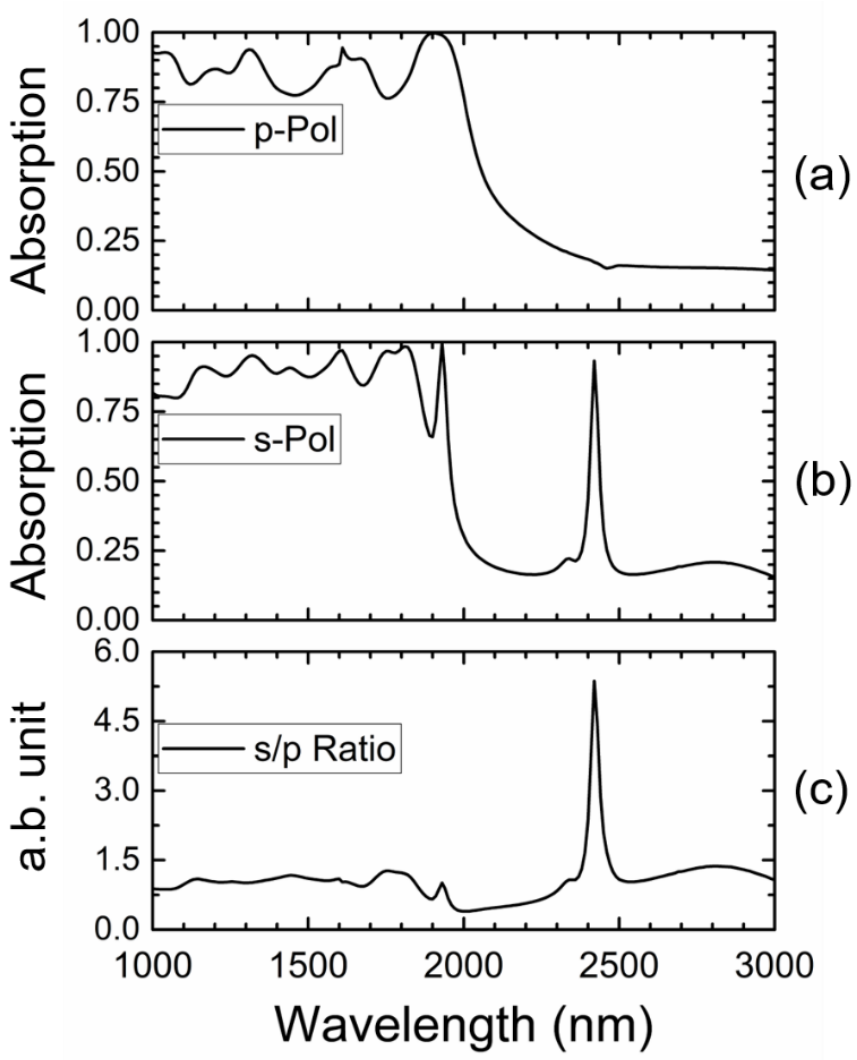

Figure 4.20. *(a), (b) absorption spectra for Structure A under polar incident angle of 37.5° and azimuth angle of 0° for p and s polarization, respectively. (c) s/p ratio.*

4.7 Conclusions

In conclusion, a novel method for achieving spectrally-selective light absorption was presented while minimizing the collection medium volume and NW array fill factor, which are highly desired for device applications in NW-based IR photodetectors. Dramatic tunability of the IR absorption spectrum is demonstrated based on coaxially heterostructured NW arrays consisting of InAs core segments that are partially encapsulated by $GaAs_{0.1}Sb_{0.9}$ shell layers. Embedding the bases of InAs NWs in Au backside contact layers results in periodic evanescent fields, where the position, spatial extent, and separation of the evanescent modes depend mainly on the NW geometry and wavelength of incident light. We show that the otherwise delocalized dominant mode in the 2 to 3 μm range can be selectively absorbed in InAs NW core segments by adding partial $GaAs_{0.1}Sb_{0.9}$ shell layers with dimensions corresponding to the position and spatial extent of the evanescent field. The absorption wavelength can be manipulated mainly as a function of NW core segment length such that the tip of the core segment coincides with the desired delocalized mode and where it can be captured via transparent $GaAs_{0.1}Sb_{0.9}$ shell layer coverage. Furthermore, the analysis of absorption spectra simulated for various polar and azimuthal angles of incidence reveals that both spectrally-selective detection and polarization-dependent optical filtration can be simultaneously achieved. The design approaches highlighted in this work are promising for novel NW-based IR photodetector membranes with enhanced carrier collection mechanisms since the wavelength-selective absorption is localized to positions along the InAs core segments where they are partially encapsulated.

As described in this chapter, the wavelength-selective absorption of IR light within NW arrays strongly depends on NW diameter. For optoelectronic device applications, achieving broadband absorption or multispectral detection would be optimally realized through a single-chip and single-epitaxial growth manufacturing process that enables NW arrays with diverse geometries and compositions. This would facilitate the tunable interaction of incident light with multiple unique NW arrays across predefined wavelength ranges.

In the next chapter, we explore the local manipulation of effective precursor flowrates during SAE growth of InAs-based NW arrays. This investigation aims to demonstrate the feasibility of growing multiple NW arrays, each with different geometries and compositions, in a single SAE run on the same Si substrate through equal-diameter patterned nanopores.

Chapter V

5 A Study of NW SAE Growth Rate Enhancement Effects

Here, we explore the influence of NW array size in selective area epitaxy (SAE) and present an innovative approach to locally manipulate effective precursor flowrates during the growth of InAs NWs. Our exploration reveals a controlled growth rate enhancement effect, yielding an eight-fold volumetric enhancement ratio compared to control samples. Notably, the largest array exhibited a 37% decrease in NW diameter and length compared to the smallest array on the same substrate grown in the same run. This SAE approach enables the synthesis of III-V NWs with tunable geometries on a single substrate, facilitated by a singular nanopore masking pattern. Additionally, via growth rate enhancement effect, we demonstrate the ability to vary the composition of adjacent $Al_xIn_{(1-x)}As$ NW arrays within the $0.11 \leq x \leq 0.54$ range during a single SAE run. This development opens new avenues for innovative approaches in manufacturing broadband NW-based optoelectronic devices, highlighting diverse absorption capabilities that prove particularly advantageous for multispectral photodetector applications, as an example.

5.1 Background and Motivations

One of the main challenges in the use of NW geometries for absorption-based applications is their limited sensitivity across the wavelength spectrum. To enable NW devices to detect multiple spectral ranges, the NW arrays must have diverse geometries. As discussed in Chapter 4, light can be selectively absorbed within NW arrays based on the diameter of the NWs. Increasing the NW diameter results in a shift of selective light absorption spectrum towards longer wavelengths as shown in Figure 4.5. For optoelectronic applications, it would be highly desirable to have a single chip with different growth arrays, each containing NWs of varied geometries and compositions. This design would enable selective interaction with incident light across different wavelength ranges for each individual growth array. Achieving this would require conducting multiple NW array growth cycles. To grow each individual NW array, the growth conditions and precursors flowrates must be adjusted. If multiple NW geometries are to be realized on a single wafer, then after each SAE run, the NW arrays would have to be isolated to prevent any unintended growth during subsequent growth cycles. This approach introduces process complexity, increases costs, and lacks time efficiency. Therefore, it would be highly advantageous to synthesize NW arrays with diverse geometries in just one growth run.

An alternative approach involves patterning a substrate with nanopores of varying sizes at distinct locations. However, achieving this for nanoscale pores poses significant challenges. Various lithography techniques, including electron-beam lithography (EBL) and nanoimprint lithography (NIL), can be employed to fabricate nanopore arrays with diverse diameters. However, each lithographic method has inherent limitations. EBL, for instance, is characterized by its high cost and low throughput. On the other hand, NIL faces

challenges related to reproducibility. Displacement Talbot lithography (DTL) is another method that can be used to pattern over larger wafer with high resolution and without the need for complex and expensive projection optics.

Hrachowina et al. showed the feasibility of achieving NWs with different geometries on a single growth run using the VLS growth mechanism, via DTL substrate patterning [193]. They successfully patterned an entire 2-inch (111) InP wafer using PMGI resist with varied diameters ranging from 140 nm to 200 nm. Following this patterning, the deposition of Au resulted in gold particles of different diameters. In the VLS growth mechanism, the diameter of the NW is dictated by the diameter of the catalyst particle. Thus, by controlling the size of the gold catalyst particle through substrate patterning and subsequent Au deposition, they effectively controlled the diameter of the as-grown InP NWs. As illustrated in Figure 5.1, increasing the diameter of the Au particle leads to NWs with a larger diameter, but smaller length. As reported, the length of the NWs decreased from approximately 4500 nm to 2000 nm as the Au diameter increased from 140 nm to 200 nm. This observation can be explained by understanding that the total volume of material for each nanowire remains consistent due to the identical growth conditions over the entire substrate.

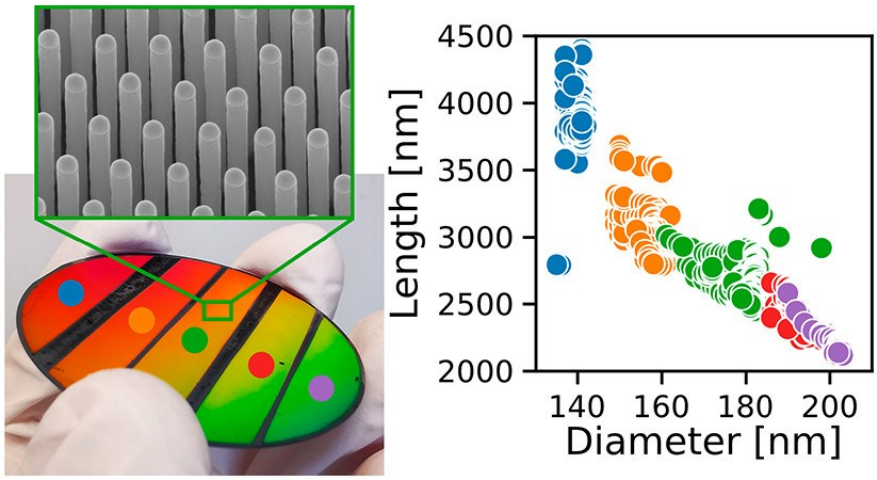

Figure 5.1. *(a) Representative SEM image and photograph of the wafer containing InP nanowires of different dimensions. (b) Length and diameter distribution of InP NW across the wafer. Adopted from Ref. [196].*

This DTL method for defining variable nanopore dimensions demands intricate patterning due to its high sensitivity to dose, and it is important to emphasize that the growth was achieved via the VLS method. This prompted us to explore the concept further for the SAE growth technique, for the first time, using a more straightforward patterning approach. Instead of varying the nanopore diameters across the wafer, we conceived the idea to modulate the growth conditions across the substrate. At first glance, this might seem implausible, especially considering that in each growth run, key growth conditions such as temperature, pressure, and time remain constant. Nevertheless, the only feasible growth parameter that can be selectively adjusted locally is the effective precursor flowrate and, therefore, the effective V/III ratio. Modulation of this growth parameter, however, can be achieved by manipulating the geometry of the NW growth array. To provide a more detailed explanation, let us consider two distinct regions: the SAE growth region (A, depicted in gray) and the SAE growth mask region (B, represented in blue), as illustrated in Figure 5.2. The extent of area B is determined by the surface migration length (λ) of

adatoms, particularly that of group-III adatoms, on the masking template. Here, λ describes the distance traveled on the oxide layer by adatoms before nucleation at the nanopores sites or before incorporation into the NW structure. This area essentially serves to collect growth species, directing them through their intrinsic surface migration toward the SAE growth region.Now, let us envision a scenario in which all the growth species that land on the oxide area B can actively contribute to the growth process. By expanding the growth area from A to A', we effectively reduce the proportion of oxide area to the total growth area (B/A > B/A'). Considering the fact that growth occurs in an environment enriched with group-V elements, the growth rate is predominantly determined by the flow of group-III elements. As a result, the effective group-III flow for growth area A is greater than that for growth area A'.

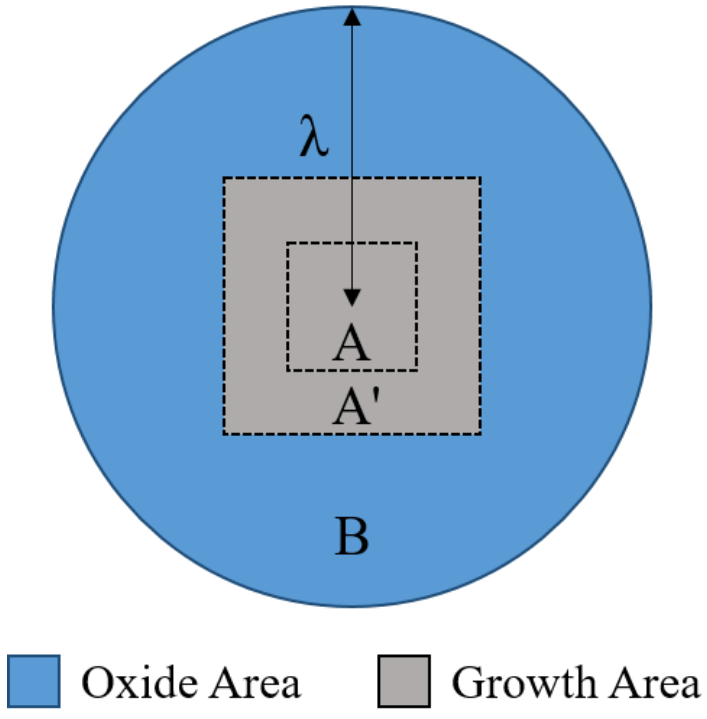

Figure 5.2. *Schematic of effective group-III flow modulation idea.*

5.2 InAs NW Growth Rate Modulation

5.2.1 Experiment Design

A potential approach to studying the effect of growth area geometry on SAE rate involves patterning different growth regions on a single substrate. To this end, an experiment was designed with various growth array geometries, ranging from 25×25 μm^2 to 400×400 μm^2 as depicted in Figure 5.3 with array indices A to E, respectively. An edge-to-edge separation of 600 μm, which is substantially greater than the surface migration length of group-III adatoms on oxide, was maintained between adjacent growth arrays to mitigate any potential mutual influence, guaranteeing no competition in the collection of adatoms. The blue and gray areas correspond to the oxide and growth regions, respectively.

The circles depicted by the dashed lines can be regarded as the effective group-III adatom collection zone. Therefore, all the adatoms within this dashed circle were likely to diffuse to the growth area and contribute to NW synthesis. Simple geometric calculations reveal that the ratio of the collection area (circular area subtracted by growth area) to the growth area decreases from 490 for the smallest array, A, to 4 for the largest array, E. This means there would be >100 times more group-III adatoms for array A compared to array E, leading to an enhancement of the NW growth rate. Therefore, arrays with different NW geometries can be obtained on the same substrate in a single growth run.

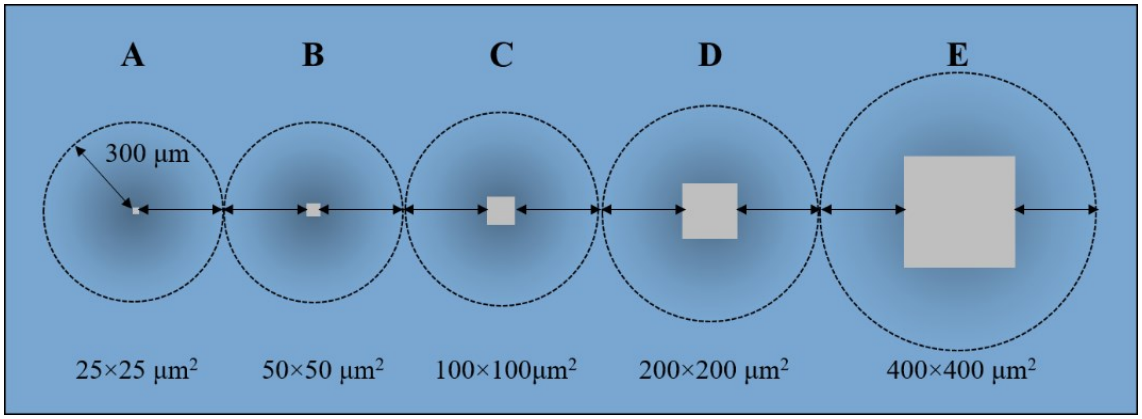

Figure 5.3. *Schematic representation of the designed substrate featuring varied growth areas, depicted in gray. These areas are encircled by the growth mask (oxide) illustrated in blue.*

5.2.2 Sample Fabrication

The intended samples were fabricated using 2-inch Si (111) substrates, which were already patterned with SAE growth masks suitable for NW growth. Ordered arrays of nanopores with diameter of ~140 nm and pitch of 500 nm were patterned through a 50 nm SiO_2 film using the Talbot displacement lithography (TDL) technique as shown in Figure 5.4. Here, the SiO_2 film acts as a masking template while the Si surface exposed through the nanopores serve as the adatom sinks, leading to vertical NWs. This substrate patterning process was carried out at the NanoLund Lab (Lund University, Sweden. The LSA method presented in Chapter 3 could not be used for this study, since the nanopore diameter is significantly larger than that of the intended NWs. Having multiple NWs per pore is undesirable, as it would unnecessarily complicate the evaluation of meaningful changes in NW geometry. Therefore, we had to proceed with a substrate where the nanopores are sized at less than 140 nm to ensure only a single NW per pore. Unfortunately, this substrate could not be fabricated at the RIT SMFL due to the limited resolution of our lithography tools.

The smallest feature size that we can achieve in the SMFL is over 300 nm, which is not suitable for our study.

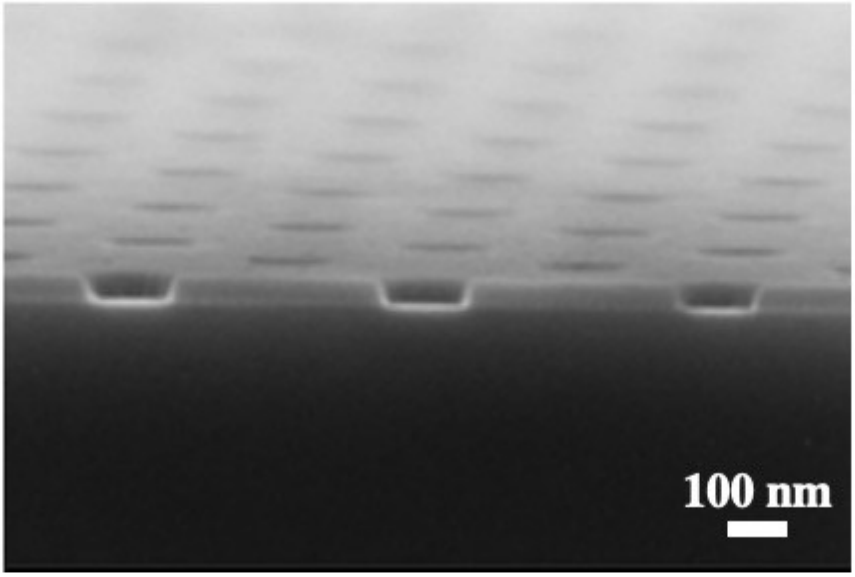

Figure 5.4. *Cross-sectional SEM image of patterned Si (111) substrate with SiO_2 SAE template using TDL method (prepared by NanoLund Lab).*

To define growth arrays with different geometries, we need to deposit SiO_2, which acts as the growth mask, while preserving the desired area with nanopores where the NWs will grow. An additive patterning approach was used to fabricate the designed substrate. This means the desired growth areas are protected, and SiO_2 is deposited on the remaining parts of the sample. The fabrication process is illustrated in Figure 5.5. First, the starting 2-inch Si (111) fully patterned with 150 nm nanopores was diced to 1×1 cm^2 chips, which were coated with the negative photoresist, Futurrex NR9g-1500 PY, spun at 2500 rpm for 40 sec and baked at 90 °C for 1 min to achieve a 1 μm thick film. A negative photoresist was chosen because of its natural undercut, which is required for the subsequent liftoff process. Next, the samples were exposed using the SUSS MicroTec MJB4 with exposure

wavelengths of 365 nm and 405 nm for 1.8 sec, followed by a 10 sec development in MF CD-26 developer. After this, the chips were loaded into the Kurt Lesker PVD 75 sputter tool for SiO_2 deposition. The sputtering technique were preferred over other oxide deposition methods available at the RIT facilities, such as PECVD and LPCVD, because of temperature limitations. These techniques operate at high temperatures, often exceeding 400 °C, which the photoresist cannot withstand. The SiO_2 mask was deposited using high power settings, with a forward (FWD) power of 185 W and a low deposition rate of less than 0.1 Å/s, achieved by adjusting the Argon flow to maintain a chamber pressure of 5 mTorr. The use of high FWD power ensures that process ions have sufficient energy to strongly scatter after striking the substrate. Additionally, high chamber pressure results in a shorter mean free path, leading to increased scattering and improved step coverage [194]. Finally, to complete the lift-off process, the samples were immersed in heated N-Methyl-2-pyrrolidone (NMP) at 50 °C using an ultrasonic bath, followed by O_2 plasma Asher. The growth arrays with dimensions 25×25 μm^2 to 400×400 μm^2 were pattered, henceforth referred to as Arrays A to E, respectively.

Figure 5.6 shows an SEM image of the sample following the fabrication process detailed above. The growth array is encircled by a deposited oxide mask, which can potentially serve as a region for the collection of adatoms on the wafer surface within the adatom migration length from the center of the growth array.

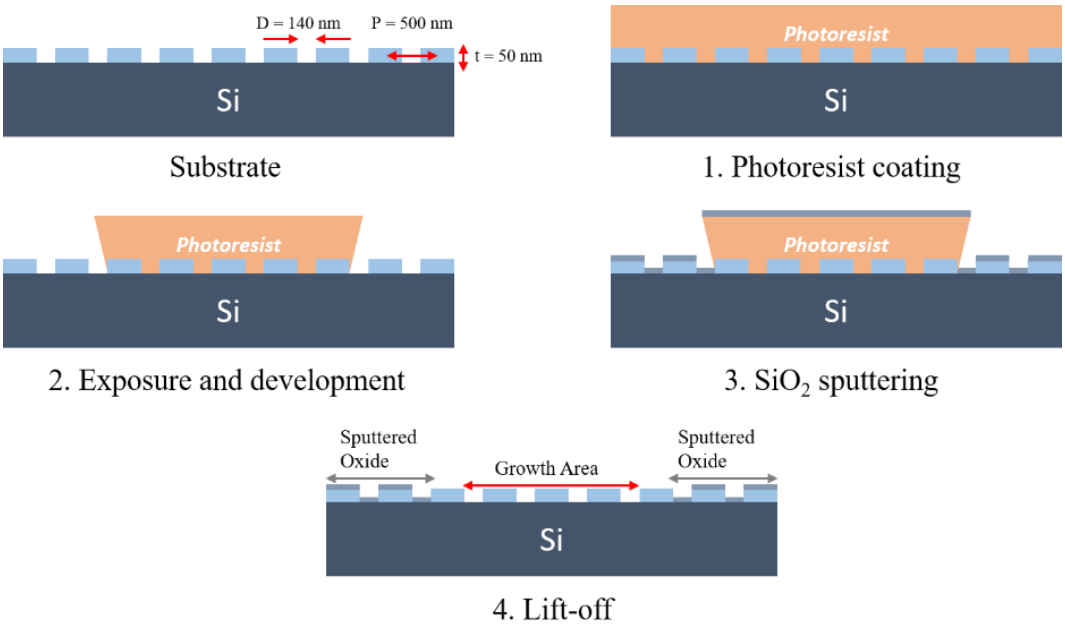

Figure 5.6. *Schematic of additive pattering process flow.*

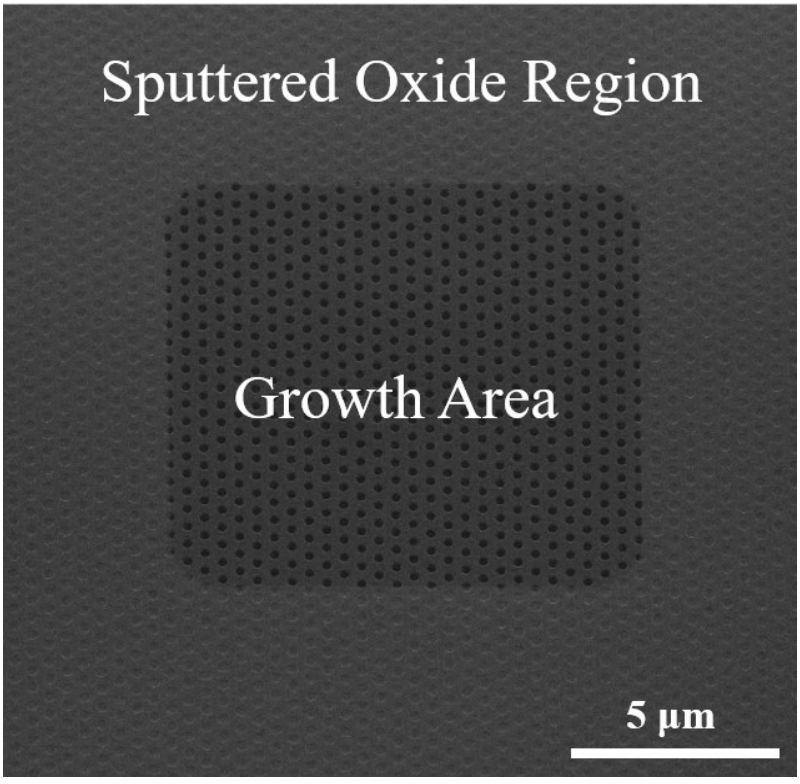

Figure 5.5. *45° tilted-view SEM image of the SAE sample after additive patterning process.*

Similar samples were also fabricated using a subtractive patterning approach, as depicted in Figure 5.7. First, a 50 nm-thick SiO_2 film was deposited over the entire substrate, covering all the nanopores and the primary oxide masking layer, using the PECVD method. This method achieves a better quality of deposited oxide compared to the sputtering technique. Then, the samples were coated with positive photoresist AZ MIR 701, spun at 3000 rpm for 30 sec, and baked at 90 °C to achieve a 1.1 μm thick film. The positive photoresist was chosen because it is more suitable for the dry etching process and makes it possible to use the same photolithography mask. Next, the substrates were exposed using the SUSS MicroTec MJB4 with exposure wavelengths of 365 nm and 405 nm for 2.1 sec, followed by baking at 110 °C for 1 min to improve the sidewall roughness and profile. This was followed by a 1 min development in MF CD-26 developer and baking at 140 °C to harden the photoresist for the subsequent dry etch process. Substrates were then placed into an RIE Phantom III reactor chamber. The goal was to selectively etch the deposited oxide in the growth region, but crucially, to leave the underlying nanopores intact. Given the nanopore mask thickness of just 50 nm, it was essential to employ a slow etch rate. An etch rate of 1 nm/s was achieved using 25 sccm of CF_4 and CHF_3, with a chamber pressure of 100 mbar and an RF power setting of 100 W. After performing RIE for 50 seconds, the photoresist was removed using an O_2 ash plasma technique for 180 sec.

Even though a superior quality oxide was obtained using PECVD outside the growth area, the issue with the subtractive patterning was that the nanopores within the growth area were not fully exposed after RIE etching and BOE treatment. Figure 5.8 presents SEM images post-InAs growth on a substrate patterned using the subtractive approach. As depicted, only some regions of nanopores are exposed from which the NWs

could potentially grow. Various RIE conditions were tested in an attempt to resolve the issue; however, none of them proved successful. The precise underlying reasons for this lack of success were not fully explored or understood. Other lab users were experiencing unstable etching and varying etching rates from one run to the next at the time. It could also have been due to chamber contamination or RF power supply that resulted in unstable plasma. However, due to time constraints, it was decided to proceed with the additive patterning method, as mentioned above.

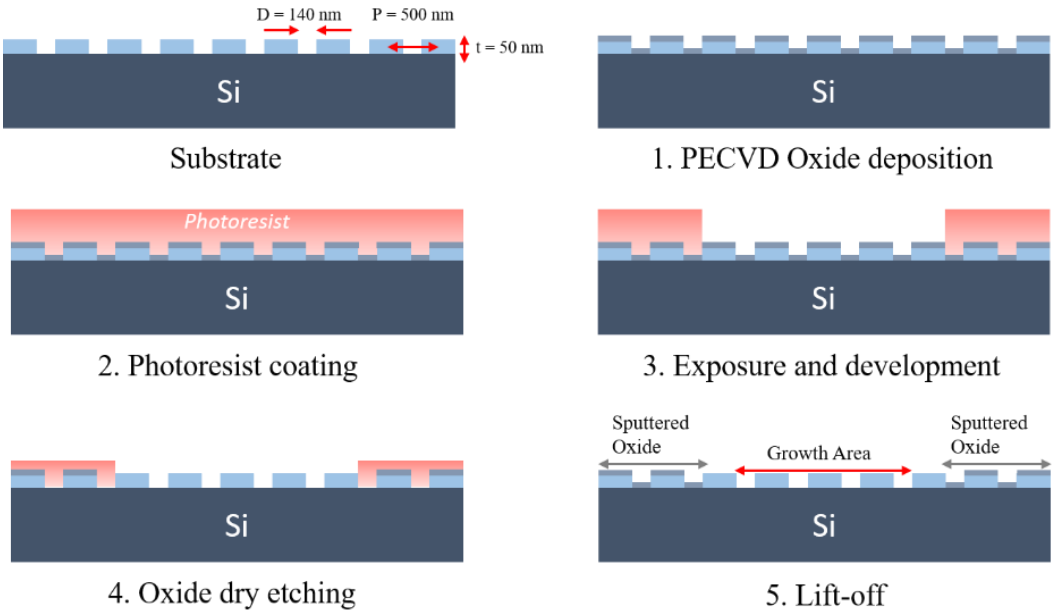

Figure 5.7. *Schematic of subtractive pattering process flow.*

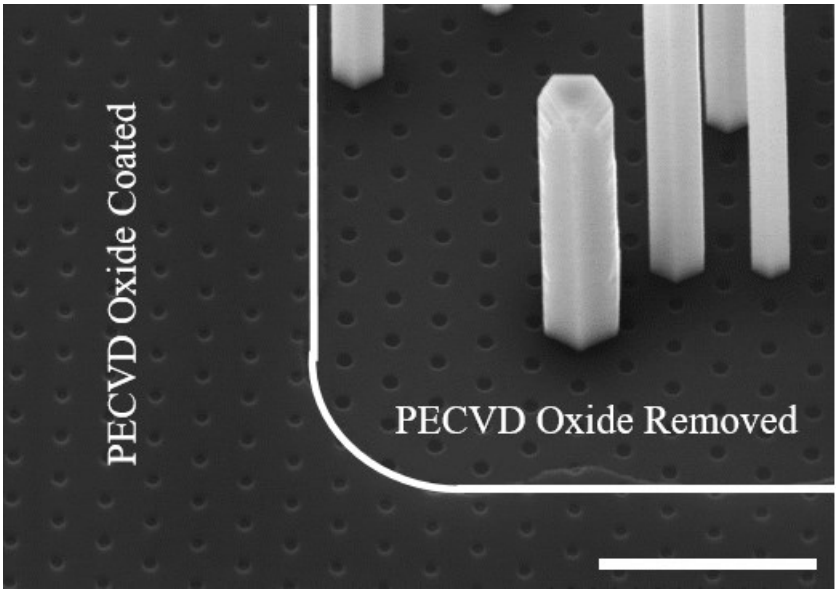

Figure 5.8. *45° tilted-view SEM image of the sample after the subtractive pattering process and InAs NWs growth. Scale bars represent 2 µm.*

5.2.3 InAs NW Growth and Analysis

As previously noted, a decrease in the dimensions of a growth array is expected to result in an increase of the NW growth rate. Therefore, to investigate the intended growth rate dependences on array geometry, the growth conditions need to be optimized to achieve well-controlled and slow growth rates for the smallest growth array (Array A), while also ensuring a high NW yield for all the arrays.

After a 5-second BOE treatment to remove the native oxide, the samples were loaded into the MOCVD reactor to grow vertical InAs NWs. The gas-phase precursors used were Trimethylindium (TMIn; $In(CH_3)_3$) for the supply of indium and arsine (AsH_3) for the supply arsenic. The samples underwent an annealing process at 850 °C for 5 minutes, saturated with a constant AsH_3 flow of 2230 µmol/min subsequently, the susceptor set-point temperature was reduced to 700 °C. The growth ensued with a 16

µmol/min TMIn flow and a 365 µmol/min AsH_3 flowrate for 5 minutes, while the chamber pressure was consistently maintained at 100 mbar. Figures 5.9 (a) to 5.9(e) show SEM images of InAs NW arrays grown on different Arrays A to E, respectively. The NWs geometry was evaluated by measuring the diameter and length of 35 individual NWs for each array, considering a correction factor due to the 45° tilt of the SEM stage for the length measurements.

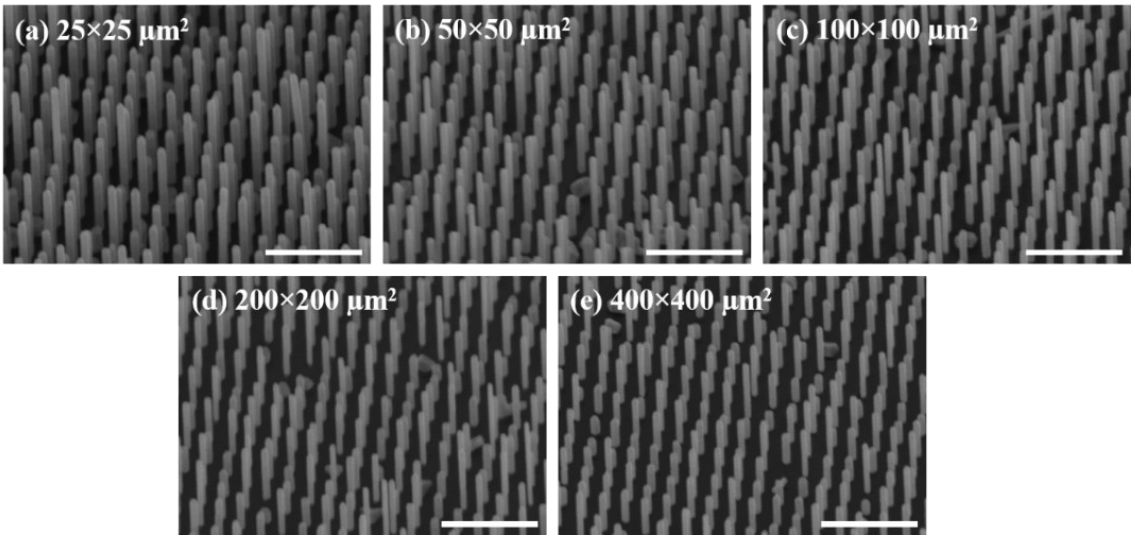

Figure 5.9. *45° tilted-view SEM images of SAE-grown InAs NWs under 16 µmol/min of TMIn flow. Showcasing different growth arrays with varying geometries, ranging from 25×25 µm² to 400×400 µm², as shown in panels (a) through (e), respectively. Scale bars represent 2 µm.*

The results of the dimensional analysis for this SAE run are shown in Figures 5.10 (a) and 5.10(b), respectively. As expected, NWs showed different average diameter and length for each array size. For the smallest growth array, labeled A, the growth rate was notably enhanced, resulting in the thickest and longest NWs. In contrast, the largest growth array, E, exhibited the thinnest and shortest NWs. Transitioning from array A to E, the mean diameter decreased from 250 ± 18 nm to 143 ± 8 nm, a difference of approximately 21%. Simultaneously, the mean length reduced from 1668 ± 344 nm to 927 ± 245 nm, a

substantial difference of about 44%. The quoted errors represent the calculated standard deviation from the mean.

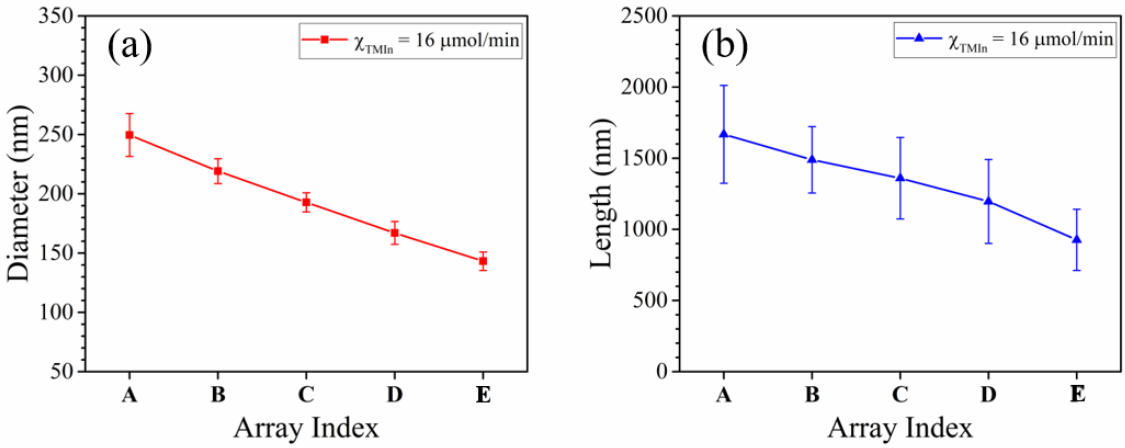

Figure 5.10. *Representations of (a) the mean NW diameter and (b) the mean NW length for each individual growth array. Error bars represent one standard deviation from the mean based on a minimum of 35 unique measurements per array.*

It is important to note that these NWs were grown in a single run on an identical substrate, with a single growth mask containing a common nanopore diameter of ~140 nm. The only experimental variable was the dimensions of the growth area. Therefore, these results unequivocally support the hypothesis that the geometry of the NWs can be modulated solely by adjusting the growth area size. Although we observed the anticipated SAE modulation effect, growth under 16 µmol/min of TMIn flow was not optimal with respect to the geometry of the resultant NWs. The InAs NWs lacked uniformity due to an overly aggressive growth environment (i.e., rapid growth rate). Figure 5.11 shows SEM image of edge of the Array A. As highlighted by red boxes, the NWs appear to merge together along the edge of the array, indicating an excessive radial growth rate and a departure from the layer-by-layer sidewall growth mode [195], [196].

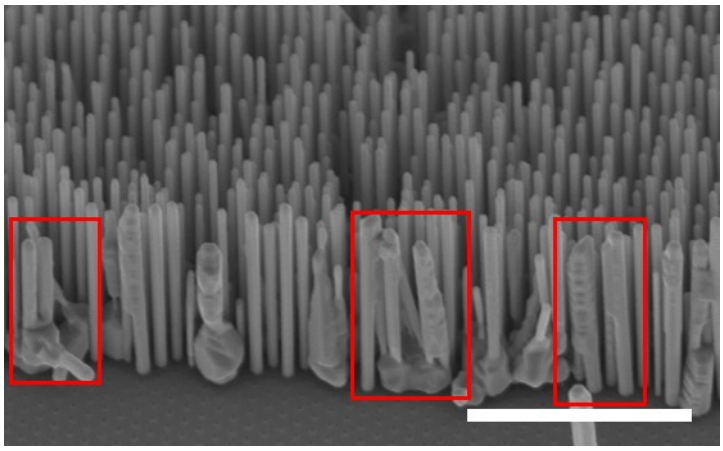

Figure 5.11. *45° tilted-view SEM images show InAs NWs under a 16 µmol/min TMIn flow for Array A, illustrating aggressive growth and merger of neighboring NWs along the sides of the array. Scale bars represent 6 µm.*

To address the issue, two separate growth runs were conducted. The first was carried out under 4 µmol/min of TMIn flow for 5 minutes, and the second under 2 µmol/min of TMIn flow for 10 minutes. This was done to conserve the total epitaxial volume in both runs for meaningful comparisons. Note that all of the other growth parameters remained unchanged. Figure 5.12 (a) and (b) show SEM images of InAs NW arrays grown under 4 and 2 µmol/min of TMIn flow for each growth array size from A to E, respectively. The geometry of the NWs was assessed and similar trends, as noted above, were observed. The NWs exhibited varying average diameters and lengths for each array size depending on the TMIn flow. Going from Array A to E for growth under 4 µmol/min of TMIn flow, the average diameter decreased from 192 ± 7 nm to 115 ± 10 nm, representing a difference of approximately 40%. At the same time, the average length decreased from 2650 ± 504 nm to 1531 ± 320 nm, marking a significant difference of about 42%. For growth under 2 µmol/min of TMIn flow, the average NW diameter decreased from 126 ± 9 nm to 79 ± 7 nm representing a difference of approximately 37%. For the

lower TMIn flowrate case, the average NW length decreased from 3347 ± 404 nm to 2119 ± 337 nm, again marking a difference of about 37%. The NW dimension data for each array are plotted in Figure 5.13 for both TMIn flowrates.

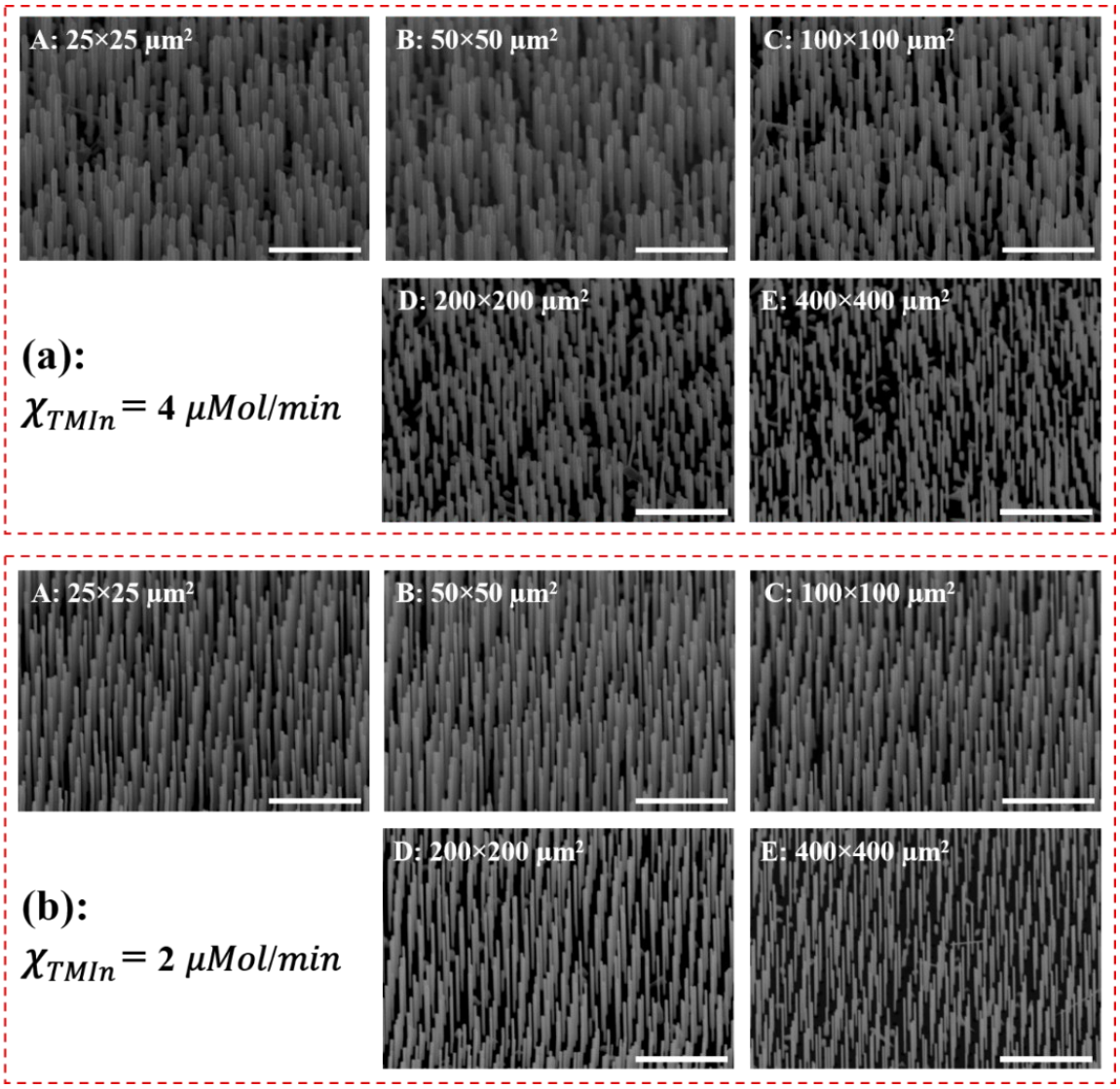

Figure 5.12. *45° tilted-view SEM images of SAE-grown InAs NWs grown under (a) 4 µmol/min of TMIn flow and (b) 2 µmol/min of TMIn flow, wherein each array is indicated with its corresponding label (A through E) and dimensions. All scale bars represent 2 µm.*

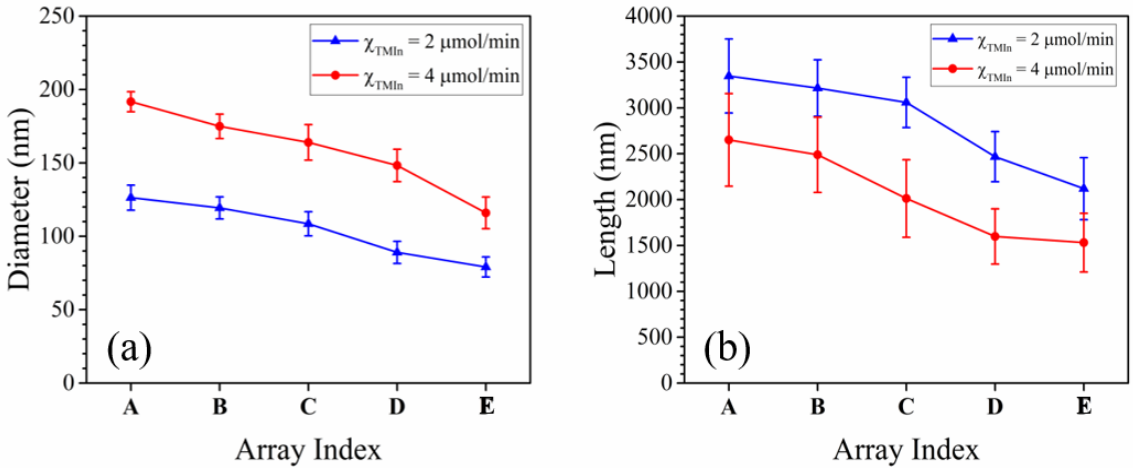

Figure 5.13. *(a) The measured mean NW diameter and (b) the mean NW length for each individual growth array for both TMIn flowrates, 4 µmol/min and 2 µmol/min, represented by red and blue line respectively. Error bars represent one standard deviation from the mean, as calculated based on a minimum of 35 unique measurement per array.*

It has been observed that decreasing the TMIn flow leads to a decrease in the mean NW diameter, but an increase in mean NW length. This observation can be explained by higher axial growth rate compared to the lateral growth rate at lower TMIn flows due to a longer diffusion length of adatoms at higher V/III ratios [197]–[199].

To understand the influence of array size on NW growth rate during SAE, a volumetric growth rate enhancement factor was calculated by comparing the total InAs volume of each array to a control sample. In every growth run, an additional SAE-templated sample, which was not subjected to the supplementary array patterning described in Section 5.2.2, was loaded into the reactor as a control sample. The total growth volume (TGV) of each array was calculated by considering a cylindrical shape for the NWs and the density of nanopores (i.e., ~2887 nanopores per 25×25 µm^2). Thus, we can define the total growth volume as

$$TGV = \frac{\pi}{4}(D_{Ave})^2 L_{Ave} N, \quad (5.1)$$

where D_{Ave} and L_{Ave} are measured average NW diameter and length values, respectively, and N is the number of nanopores in each array.

Figure 5.14 shows SEM images of control samples (i.e., those with an effectively infinite array size). For TGV calculation of the control sample, the growth yield of NWs was also taken into account by measuring the ratio of the number of grown NWs to the number of nanopores in a 25×25 μm^2 area. Yield calculation revealed ~60% and 56% for samples grown under 4 and 2 μmol/min of TMIn, respectively. The mean diameter and length measurements indicated 104 nm and 1967 nm, respectively, for growth under a 4 μmol/min TMIn flowrate. Meanwhile, for growth under a 2 μmol/min TMIn flowrate, the mean diameter and length values were measured to be 95 nm and 1366 nm, respectively.

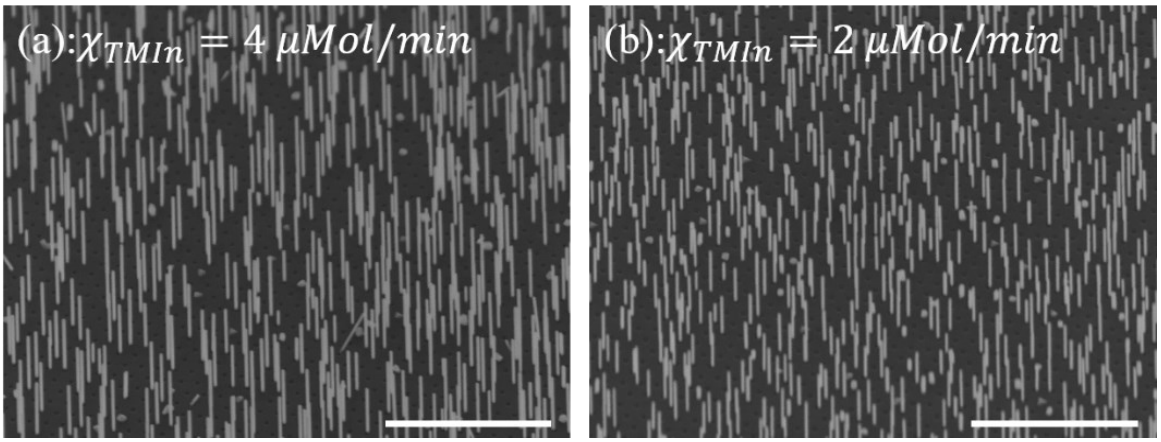

Figure 5.14. *45° tilted-view SEM images of InAs NWs grown on reference substrates (no specific array size pattering) under (a) 4 μmol/min and (b) 2 μmol/min of TMIn flowrates. Scale bars represent 5 μm.*

Figure 5.15 plots shows the total volumetric enhancement ratio based on the ratio of the TGV in Arrays A-E relative to the TGV of the control sample considering an equivalent area (e.g., TGV of Array A divided by TGV of control sample measured across a 25×25 μm^2 area, TGV of Array B divided by TGV of control sample measured across a 50×50 μm^2 area, etc.).

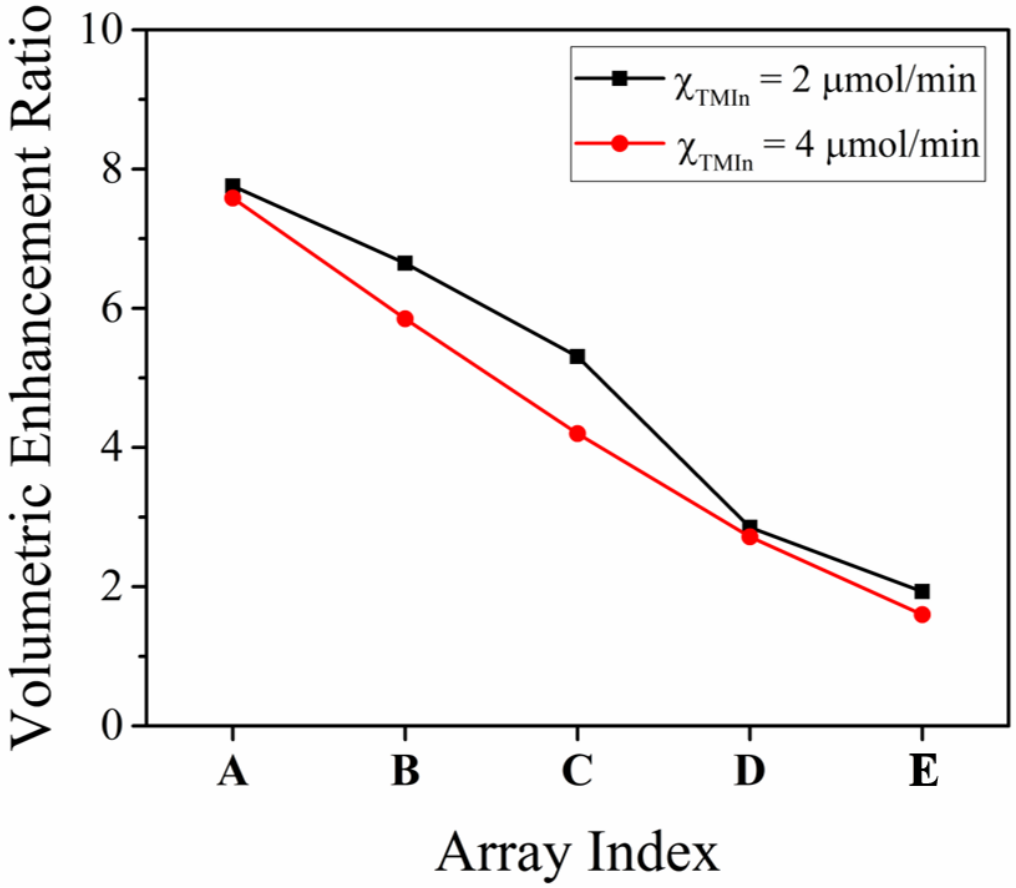

Figure 5.15. *Plot of the calculated volumetric enhancement ratio for different NW array sizes under 4 µmol/min (red) and 2 µmol/min (black) TMIn flowrates.*

As shown, by increasing the array size from 25×25 μm^2 (i.e., Array A) to 400×400 μm^2 (i.e., Array E), the total volumetric enhancement ratio decreased from approximately 8 to 2. Thus, increasing the array size leads to a decrease in the growth enhancement effect,

approaching the growth rate of the control sample. This provides strong evidence for growth rate dependence on array size, which can only be explained by the local effective enhancement of the TMIn flowrate. The obtained results confirm the hypothesis established at the start of the experiment. They illustrate that by simply adjusting the size of the growth area, the effective V/III ratio can be locally modulated. Consequently, growth conditions can be altered, resulting in a transformation of the NW geometry from one array to another on the same substrate within a single growth run.

5.2.4 Growth Rate Modulation Model

In this section, a geometrical model based on the surface migration length of In adatoms is presented to better justify the influence of array size on SAE growth rate. As experimentally demonstrated in Section 5.2.3, the SAE enhancement effect increases as a function of decreasing array size. Considering constant growth parameters in each growth run such as temperature, chamber pressure, and precursor flowrates, and considering that the AsH_3 flowrate is significantly higher than the TMIn flowrate (with a V/III ratio of 181 for the control sample), the only parameter that could account for the growth enhancement effect is the effective TMIn flowrate. As discussed in Section 5.1, the effective TMIn flow experiences a local enhancement that is determined by the ratio of the In adatom collection area to the growth array size.

Here, the growth area is considered as the dimensions of the array size. In order to simplify the model, a circular growth area was considered instead of square; however, the diameter values considered in the model with circular array geometry were selected in order to the match the total area of the square-shaped experimental arrays (i.e., model

diameter of 28.21 μm to 451.35 μm, results in the same area as experimental arrays of side length of 25 μm to 400 μm, respectively). Therefore, determining the collection area of the In adatoms is the crucial element to develop the model. The term 'collection area' refers to the region where all In adatoms within can contribute to growth by migrating on the oxide surface to reach the edge of the growth area. For this model, two main factors are considered for In adatoms. The first factor is the distance (l), representing the distance of In adatoms from the growth area. Only In adatoms whose distance to the edge of the growth area is less than the surface migration length ($l < \lambda$) can contribute to the formation of NWs as depicted in Figure 5.16. The second factor pertains to the migration direction of the adatoms. Considering the fact that adatoms can migrate in all directions spanning 360° with equal probability, only those adatoms with initial migration path within an angular range $\Delta\theta$, as illustrated in Figure 5.16 by orange angular range, stand a chance of reaching the growth area. This net probability can be represented by

$$P = \frac{\Delta\theta}{360°} \tag{5.2}$$

where $\Delta\theta$ is described as:

$$\Delta\theta = 2\sin^{-1}\left[\frac{(D/2)}{(D/2)+l}\right] \tag{5.3}$$

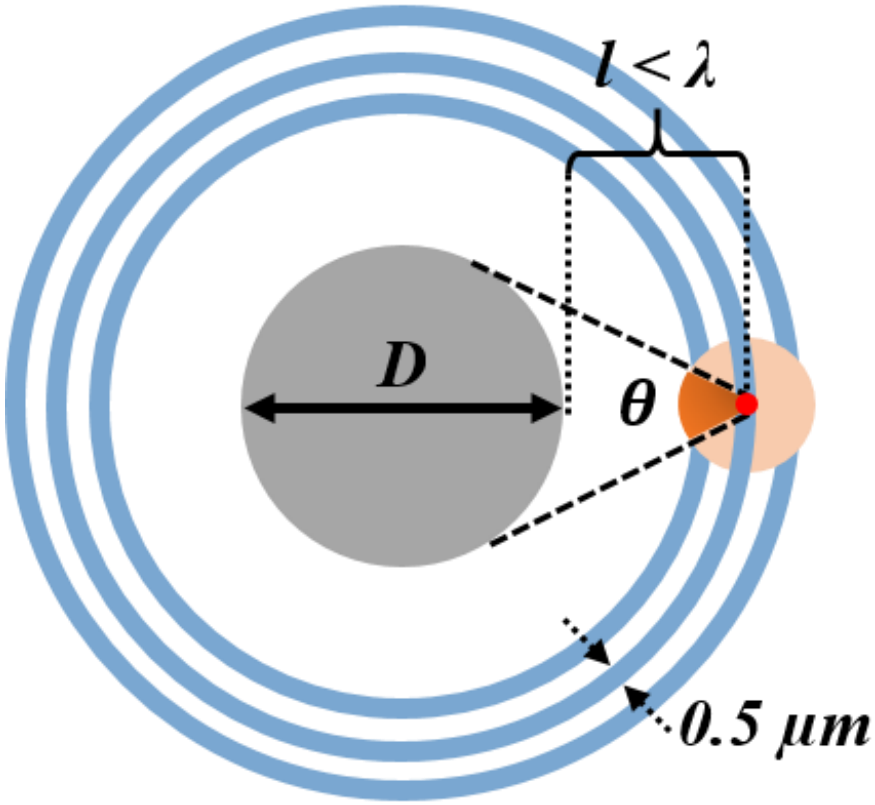

Figure 5.16. *Schematic representation of the growth rate enhancement effect model, depicting a growth area with diameter, D, and an In adatom impinging at a distance, d, away from its edge.*

All adatoms with initial impingement within distance, l, from the growth array, as depicted by the gray ring in Figure 5.16, have the same net probability, P, to migrate toward the growth area. Therefore, the effective collection area for those adatoms with distance l away from growth array can be calculated as:

$$P \times A_l \tag{5.4}$$

where A_l is the area of the ring with width of 0.5 μm, similar to pore-to-pore pitch, is defined by:

$$A_l = \pi\left[\left(\frac{D}{2} + l + 0.25\,\mu m\right)^2 - \left(\frac{D}{2} + l - 0.25\,\mu m\right)^2\right]. \quad (5.5)$$

It is assumed here that all adatoms within $l < \lambda$ can contribute to the growth. Therefore, it is necessary to calculate and sum for all l values from the edge of the growth area to λ within increments of 0.5 μm, according to:

$$A_{Total} = \int_0^{\lambda} P \times A_l \, dl. \quad (5.6)$$

Therefore, the relative volumetric enhancement ratio (*VER*) can be written as:

$$VER = \frac{A_{Total} + A_{NW}}{A_{NW}} \quad (5.7)$$

where A_{NW} is area of the NW growth array, such that $A_{NW} = \pi(D/2)^2$.

It worth mentioning that the probability of adatoms scattering along their migration path can be neglected, since this can be considered to be common for all the adatoms moving toward and away from the growth region.

Figure 5.17 presents the volumetric enhancement ratio, which represents the ratio of the effective collection area to the growth area for values of λ spanning from 100 to 350 μm (since the exact value is not determined), comparing them to the experimental results obtained from Figure 5.15.

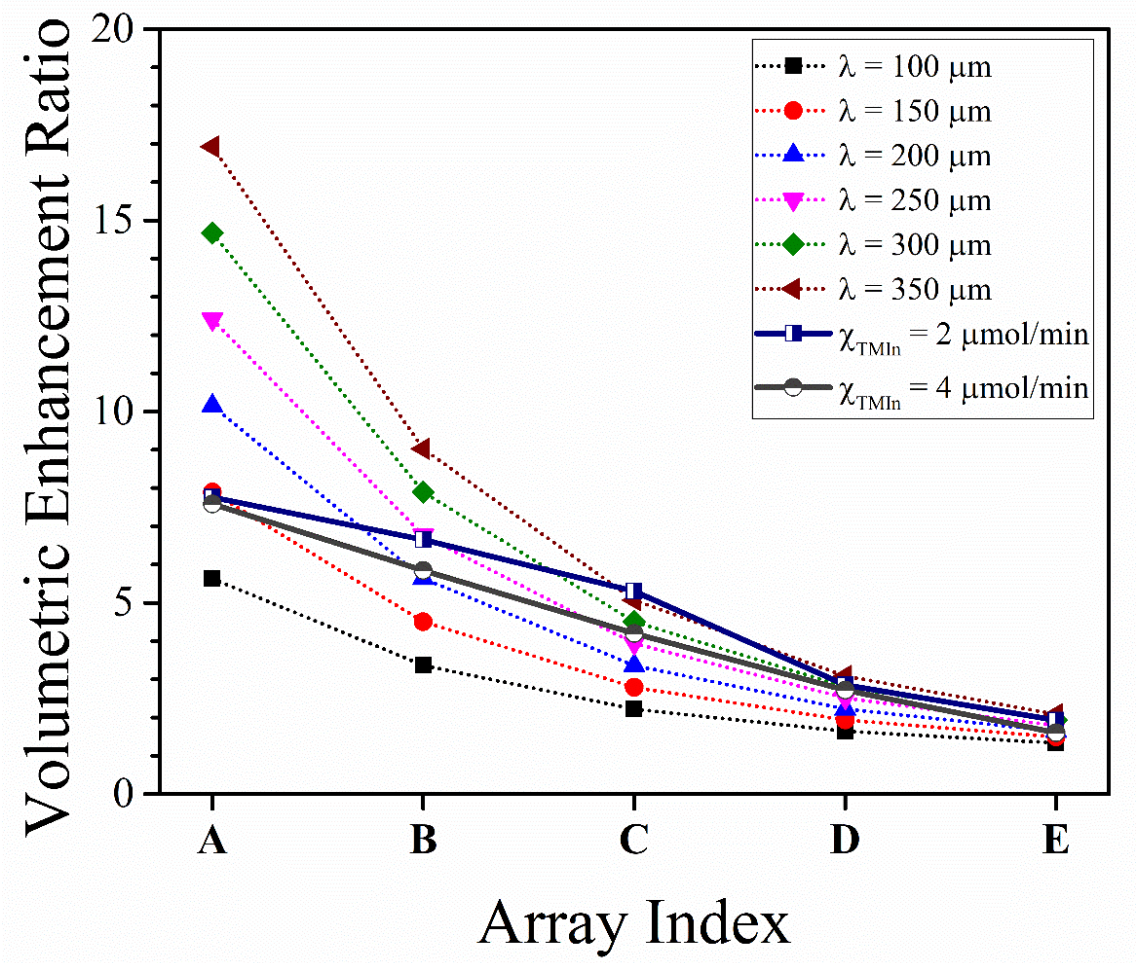

Figure 5.17. *Comparison of modeled volumetric enhancement ratio (represented by dotted lines) for different surface migration length ranging from λ = 100 μm to 350 μm, depicted by different colors, versus experimental volumetric enhancement ratio for 4 μmol/min and 2 μmol/min TMIn flowrates (represented by solid lines).*

As expected, the modeled volumetric enhancement effect diminishes as the array size expands from A to E. The difference in the volumetric enhancement effect between the smallest Array, A, and the largest, E, hinges significantly on λ. As illustrated, for Array A, the volumetric enhancement ratio surges approximately from 6 to 19 as λ grows from 100 to 350 μm. For Array E, an increase from 1.3 to 2.2 is obtained. The model with longest λ shows a good correlation with experimental data for Arrays C, D and E. However, for Arrays A and B, the experiment data shows a good fit with the models for shorter values

of λ. This discrepancy can be explained by parasitic NW growth outside of the intended arrays, which quenches the growth enhancement effect. Therefore, the collection area is effectively and disproportionately reduced for smaller arrays, and a departure from the above ideal-case model arises. Due to the poor quality of the sputtered oxide and nonuniformity of the deposited film, there were many pinholes in the deposited film. These pinholes expanded during the pre-growth BOE treatment, acting as undesirable sinks outside the intended growth area, as shown in Figure 5.18. Therefore, the growth enhancement effect becomes less pronounced because of the growth of InAs NWs outside the designated area.

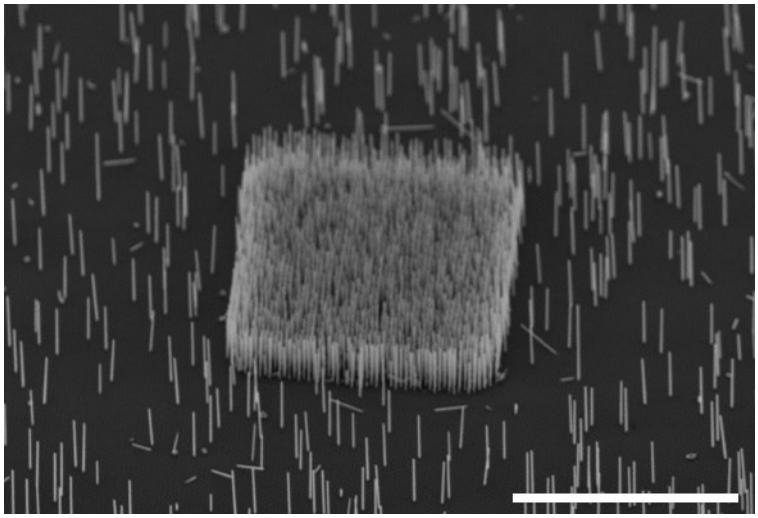

Figure 5.18. *45° tilted-view SEM images showing undesired InAs NWs grown outside of the intended growth region due to the presence of pinholes in the sputtered oxide layer. Scale bar represents 20 μm.*

As previously discussed, one of the practical applications of this growth method is the definition of arrays with unique wavelength-selective absorption spectra based on the NWs geometry. This can be promising for tunable multispectral photodetector applications. Additionally, this method can be employed to investigate the influence of the

V/III ratio on the NW axial and lateral growth rates and morphology from a fundamental epitaxy perspective. So far, it has been demonstrated that by adjusting the size of the growth array, one can effectively change the local V/III ratio for InAs NW growth. By applying the same concept, it would be promising to adjust the composition of each growth array by introducing Al into the system. This approach could potentially open new avenues in the growth dynamics and properties of the resulting NWs. In the following Section 5.3, we will investigate the NW composition modulation during SAE growth in a single growth run, using the test case of the AlInAs ternary compound.

5.3 Investigation of Composition Modulation

One of the advantages of ternary compound semiconductor is that bandgap of the material can be tuned by adjusting the composition (i.e., the ratio of group-III or group-V species). This property makes ternary compound semiconductors versatile material systems for a wide range of optoelectronic and electronic applications.[181] Among this material system, $Al_xIn_{(1-x)}As$ finds common use in high-speed electronics and optoelectronics, including quantum cascade lasers, high electron mobility transistors (HEMTs), and avalanche photodiodes. The relationship between the bandgap energy (E_g) and the Al composition (x) can be described by the equation: $E_g = 0.36 + 2.35x + 0.24x^2$. Therefore, by adjusting x from 0.1 to 0.6, the bandgap can be tuned from 0.6 eV to 1.85 eV. This corresponds to wavelengths of 2066 nm and 670 nm, respectively.

In the context of crystal growth, using the MOCVD method to synthesis, the composition is predominantly determined by the molar flowrates of the vapor-phase reactants. By altering the flowrates of the different gas-phase precursors, the composition of the NWs can be adjusted throughout the growth process. This implies that to achieve $Al_xIn_{(1-x)}As$ ternary compound with different compositions, the flowrates of group-III elements must be adjusted separately in different growth runs. Thus, it would be highly desirable to be able to tune the composition of $Al_xIn_{(1-x)}As$ within a single growth run. This capability would be particularly promising for optoelectronic applications. For instance, multispectral detector devices could benefit from having multiple NW arrays with varying compositions, enabling the detection of different wavelengths on the same chip. As of now, there is no recognized method to produce NWs of varying compositions on one wafer in a single growth run [200].

It is well-known that the Al adatom surface migration length is significantly shorter than that of In adatoms [201], [202]. This discrepancy can be theoretically expected to lead to variations in the ratio of In adatom collection area to Al adatom collection area during SAE. Thus, an experiment is designed here to test the hypothesis that neighboring arrays of $Al_xIn_{(1-x)}As$ NWs with distinct compositions can be realized in a single epitaxy run on the same chip by leveraging the above SAE enhancement effects.

To carry out this experiment, a new set of samples were designed and fabricated via additive pattering, as depicted in Figure 5.19. The regions labeled A to E represent the intended growth areas, ranging from 25×25 μm^2 to 400×400 μm^2, respectively, similar to the patterned samples described in Section 5.2.2. With an edge-to-edge separation of 600 μm, these arrays can be perceived as having a wide-open neighboring oxide region that serves as collection area for In adatoms.

Adjusting the growth rates by fine-tuning the area of the oxide region adjacent to the nanopores arrays could present a promising approach of further controlling $Al_xIn_{(1-x)}As$ composition, with the potential to decrease growth rate enhancement effects as the oxide area is reduced. In Section 5.2 the effect of the array size on NW growth rate was investigated. To also investigate the influence of the oxide area in this section, 6 more arrays are added to the design, all with a constant growth array size of 50×50 μm^2. Here, the area immediately outside the patterned nanopores arrays, colored in blue, represents an oxide field, which is designed with three different dimensions: 150×150 μm^2, 250×250 μm^2, and 450×450 μm^2. This field, henceforth referred to as the “skirt” region acts as the adatom collection area. The skirt area is defined by a square border region wherein the Si substrate surface is exposed; this region functions as an additional adatom sink. In order

to investigate the effect of the border on SAE growth, two different border widths of 12.5 µm and 50 µm are defined for oxide skirt area. Arrays with thin and thick borders are named B_1 to B_3, and B'_1 to B'_3, respectively. Here, the indices 1 to 3 denote the oxide skirt area size, ranging from 150×150 µm² to 450×450 µm². Table 6.1 shows the details for each SAE growth array.

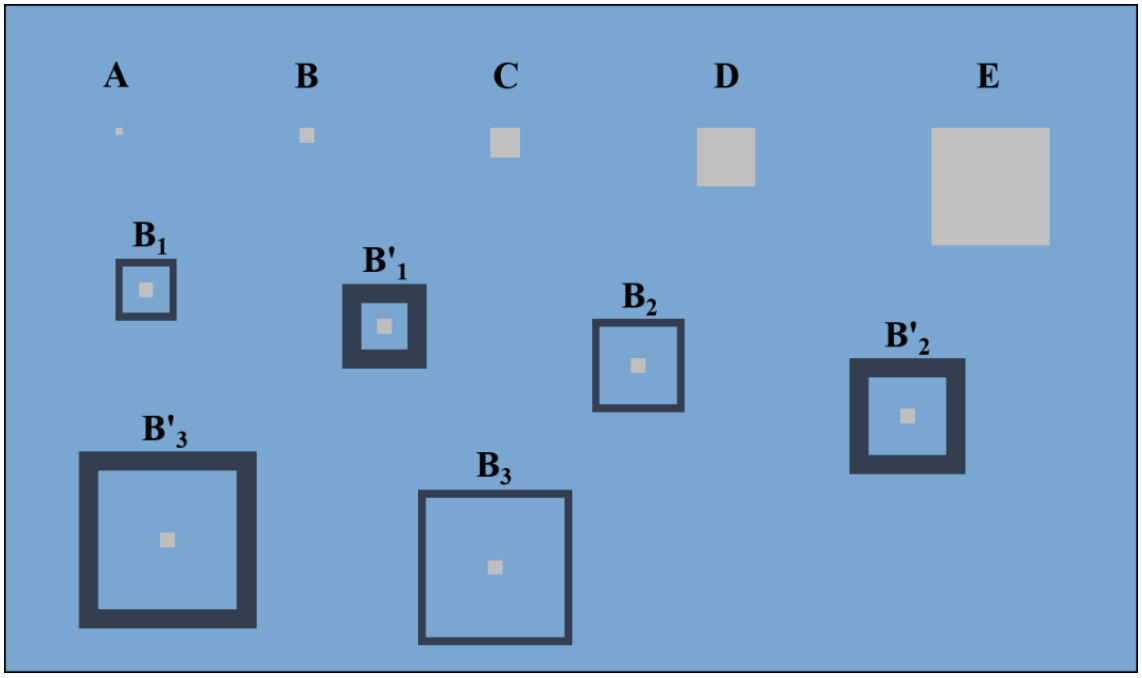

Figure 5.19. *Schematic representation of the sample design, showing different NW growth arrays and oxide skirt sizes. The blue color in the background and gray color represent the oxide and growth arrays, while the dark blue color represents the border.*

Table 5.1. *Dimensions of NW Growth Arrays, Oxide Skirt Regions, and Border for Compositional Analysis*

Array Index	A	B	C	D	E	B_1	B'_1	B_2	B'_2	B_3	B'_3
Growth Array Dimensions (μm^2)	25^2	50^2	100^2	200^2	400^2	50^2	50^2	50^2	50^2	50^2	50^2
Oxide Skirt Dimensions (μm^2)	N/A	N/A	N/A	N/A	N/A	150^2	150^2	250^2	250^2	450^2	450^2
Border Width (µm)	N/A	N/A	N/A	N/A	N/A	12.5	50	12.5	50	12.5	50

5.3.1 InAs-$Al_xIn_{(1-x)}As$ Core-Shell NW Array Growth

Achieving high-aspect ratio $Al_xIn_{(1-x)}As$ NWs with a high Al content is challenging due to the low diffusion length of Al [202]. The SAE growth of AlInAs necessitates a more systematic exploration to optimize growth conditions with respect to temperature and precursor flowrates. To investigate the composition modulation effects of $Al_xIn_{(1-x)}As$ during SAE growth of NWs, without introducing a large number of dedicated growth trials to optimize the synthesis of purely AlInAs NWs, a coaxial NW configuration with an InAs core segment and an AlInAs shell segment is used. This configuration allows for a broader tolerance of growth temperatures and precursor flowrates during the shell deposition, thereby facilitating and expediting the analysis of $Al_xIn_{(1-x)}As$ segment compositions.

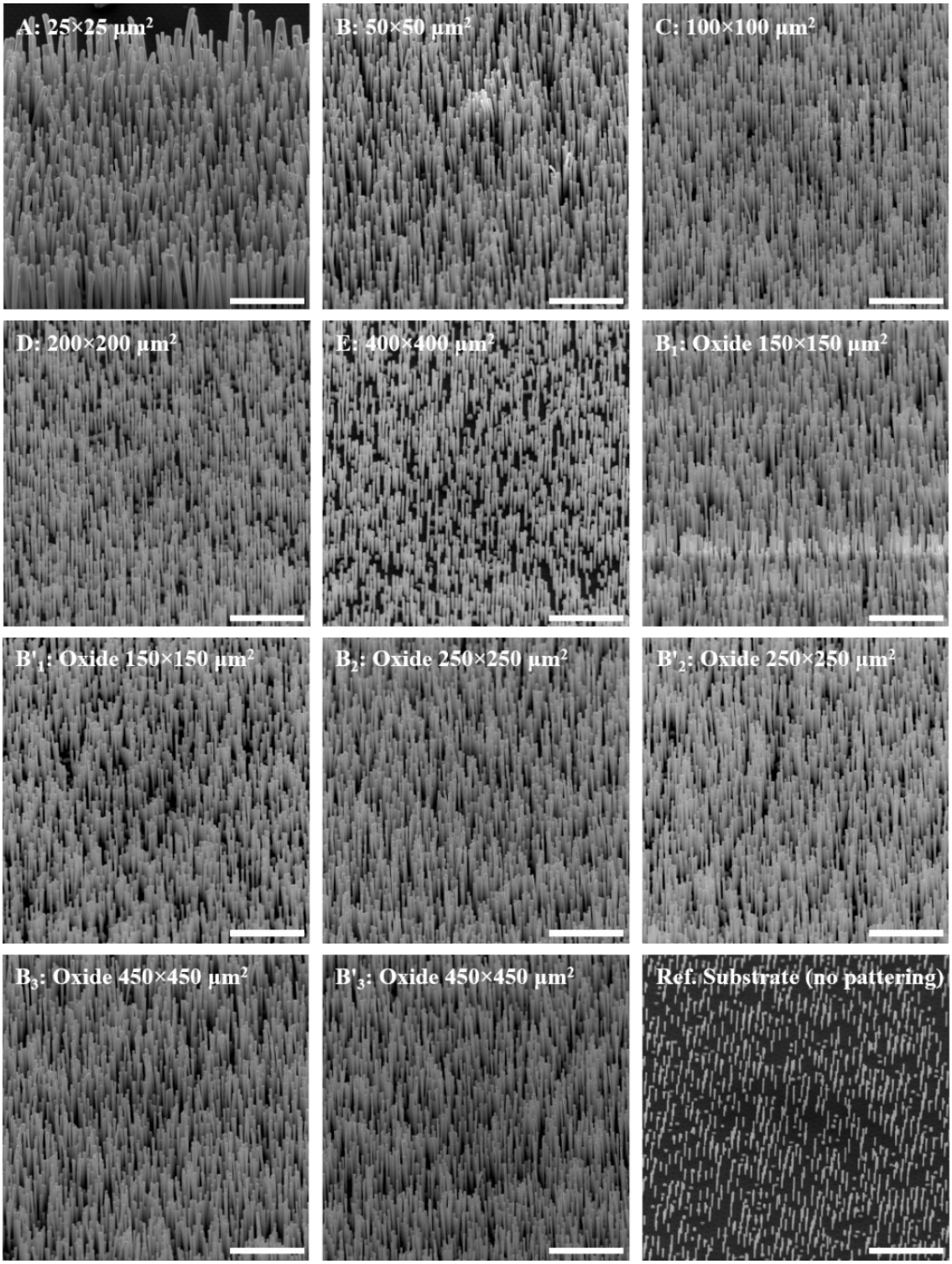

Figure 5.20. *45° tilted-view SEM images of SAE-grown InAs-AlInAs core-shell NWs, showing different array geometries A to E, B_1 to B_3, B'_1 to B'_3, and control sample with no additional array pattering. All scale bars represent 5 µm.*

After treating the samples with BOE for 5 seconds to remove the native oxide, they were loaded into the MOCVD reactor. The InAs core growth was initiated at a temperature of 700°C using flowrates of 2 µmol/min for TMIn and 365 µmol/min for AsH_3, maintained for 5 minutes. Throughout this process, the chamber pressure was kept constant at 100 mbar. Subsequently, the TMIn flow was turned off, terminating the core segment growth, and the temperature was decreased to 600°C. Upon reaching this set-point temperature, TMIn and TMAl were introduced at flowrates of 2 µmol/min and 3 µmol/min, respectively. Notably, the 3 µmol/min TMAl flowrate is the lowest that can be consistently maintained by the reactor's mass flow controller (MFC) during growth of InAs-$Al_xIn_{(1-x)}As$ core-shell NWs. SEM images of InAs-$Al_xIn_{(1-x)}As$ core-shell NWs grown on different arrays from A to E, B_1 to B_3 , B'_1 to B'_3, and control sample (i.e., with no isolated array pattering) are shown in Figure 5.20.

5.3.2 Results and Discussions

As the primary focus of this study was to assess Al composition modulation, dimensional analysis was not conducted for this specific growth run. Nonetheless, SEM images reveal a pattern similar to that of the InAs NWs discussed in Section 5.2.4. As the array size progresses from A to E, a discernible reduction in both NW length and diameter becomes evident, indicating slower rates of axial and lateral growth. To investigate composition, EDX measurements were performed, and subsequent analyses were carried out.

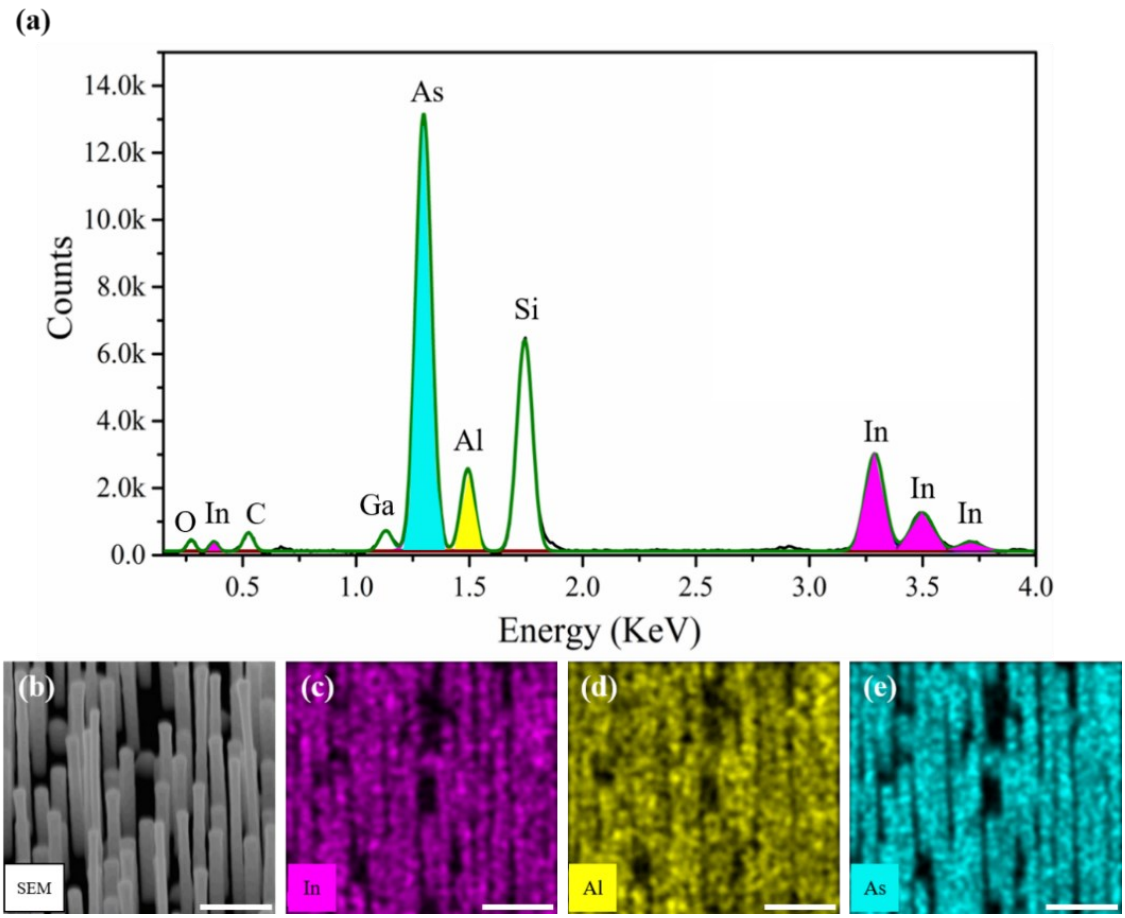

Figure 5.21. *(a) Representative EDX spectrum collected from Array D at the location shown in (b). EDX maps of elemental (c) In, (d) Al and (d) As, collected from the same region as SE micrograph (b).*

For EDX measurements performed using a Tescan Mira3 SEM instrument, an acceleration voltage of 10 keV and a narrow view field were selected, with an acquisition time of 2 minutes. The EDX data for each growth array was collected from 5 different locations. This data was then individually plotted and analyzed using Origin software to subtract the X-ray baseline, deconvolute the spectral features, and calculate the integrated area associated with each deconvoluted peak. Figure 5.21(a) displays a representative EDX spectrum for Array D (i.e., 200×200 μm²). Figures 5.21(b) and 5.21(c) show the corresponding SEM images and EDX elemental maps for As (blue), Al (yellow), and In

(pink), which are color matched in the spectrum plot. The area under the peaks associated with As, Al, and In, as depicted by the corresponding elemental map colors, were considered to define the relative Al composition of each array. To determine the In elemental content, we considered the summation of the areas under the peaks of all four different characteristic X-ray energies including M_V, $L_{\beta 1}$, $L_{\beta 2}$, and L_{γ}, sorted from low to high energy.

The ratio between the integrated intensities (i.e., total areas under the peaks) can be used as a metric for the measurement of the relative solid-phase content of the group-III species in the NWs. Eq. 5.8 shows Al composition (x):

$$x = \frac{I_{Al}}{I_{In} + I_{Al}} \tag{5.8}$$

where I_{Al} and I_{In} are the calculated integrated intensity of the Al EDX peak (total area under the peak represented by yellow color) and all four In EDX peaks (total area under the peaks represented by pink color). The I_{Al} and I_{In} for each spectrum were calculated, and the Al composition (x) was subsequently calculated for each array individually. The results are shown in two different plots, depicted in Figures 5.22(a) and 5.22(b), for Arrays A-E (with the unpatterned control sample as a reference for comparison) and B_1-B'_3 arrays (with the patterned Array B as a reference for comparison), respectively. As shown, when the array size is extended from A to E, the Al composition constantly increases from $x = 0.11$ to $x = 0.40$, with the control sample exhibiting the highest Al content at $x = 0.54$. The observed trend for arrays with varying oxide skirt sizes and border widths indicates that as the oxide skirt size increases, the Al composition constantly decreases. Specifically, when the oxide skirt is increased from Array B'_1 to B_3, the Al composition drops from $x = 0.29$ to $x = 0.21$.

Among those arrays patterned with a border region, Array B with the largest oxide skirt displays the lowest Al content, measuring at $x = 0.17$. Notably, for arrays with the same oxide skirt area, those arrays with a thicker border region exhibit the highest Al content, as depicted in Figure 5.22(c), which shows a similar trend for each border type.

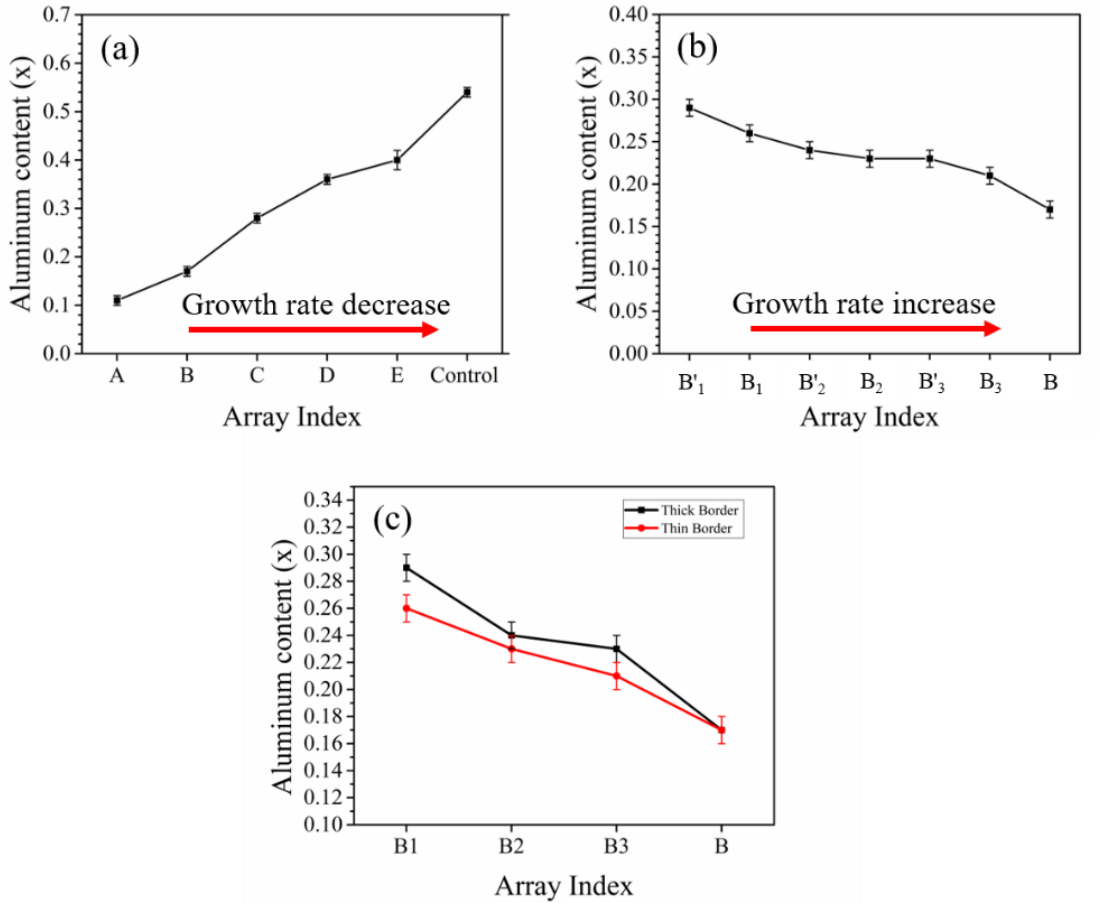

Figure 5.22. *Measured Al content, x, for (a) Arrays A-E and (b) B series arrays. (c) Comparison of Al content of B series arrays with thick (black) and thin (red) border regions.*

The trends observed in both sets of arrays are linked to the SAE growth enhancement effect. According to the results presented in Section 5.2, it is evident that the growth enhancement effect decreases as the array size increases from A to E. Therefore, it can be interpreted that as the growth enhancement effect decreases, the Al content

monotonically increases. The control sample with no SAE growth enhancement effect shows the highest Al content compared to all other arrays. This fact is further confirmed by the Array B series. Increasing the oxide skirt area leads to the collection of more group-III adatoms, resulting in an enhanced volumetric growth rate. Additionally, for arrays with the same oxide skirt area, the one with a larger border is expected to have a lower growth rate. This is due to the higher capacity of the wider border to capture more diffusive adatoms. Considering the impact of oxide skirt and border regions on growth rate, it can be inferred that Array B'_1, with the smallest oxide skirt area and a thick border, is likely to have the weakest growth enhancement effect among the arrays in the B series. Therefore, the arrays in the B series can be sorted based on their growth enhancement potential from weakest to strongest as follows: B'_1, B_1, B'_2, B_2, B'_3, B_3, with Array B having the most enhanced growth rate.

Thus, it is observed that as the growth enhancement effect is exaggerated, the Al content of the $Al_xIn_{(1-x)}As$ NWs decreases. This understanding is crucial in identifying the primary reason for the observed compositional differences. Generally, NWs grow through two distinct adatom collection mechanisms: direct impingement and surface diffusion, as schematically represented in Figure 5.23. In the first extreme, the adatoms directly strike the top facet of the NWs and contribute to their growth. In the second extreme, the adatoms migrate from the growth mask along the NWs sidewall until they reach the top facet.

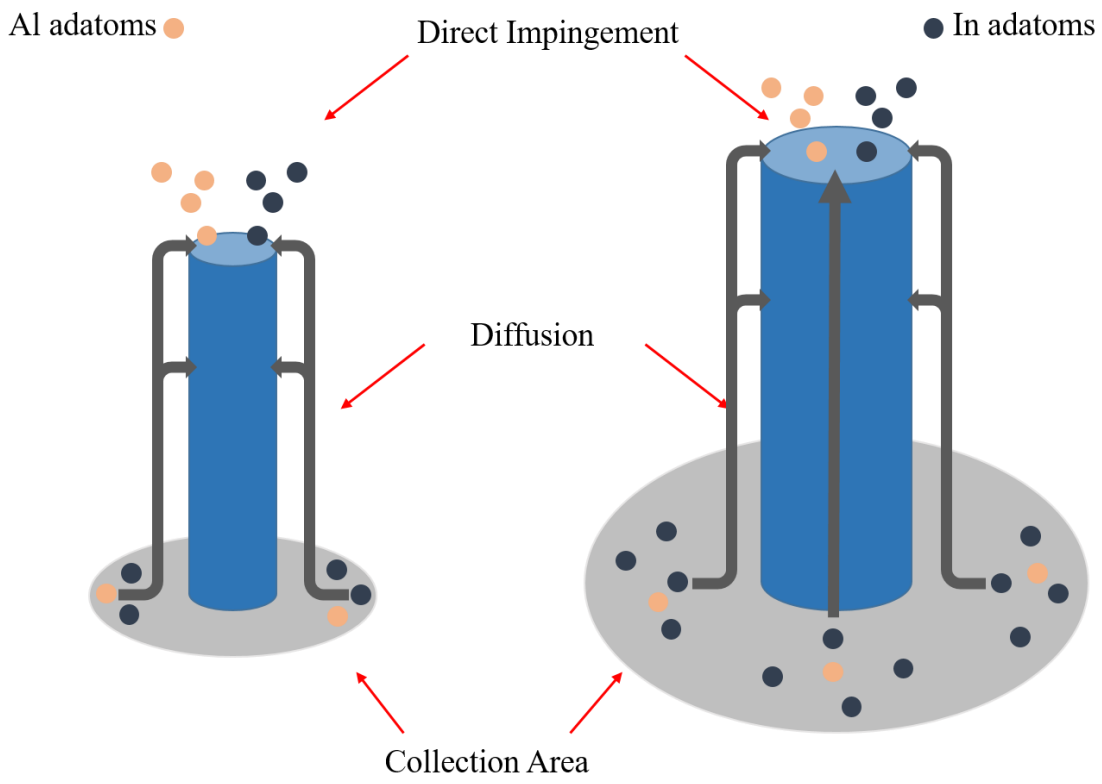

Figure 5.23. *Schematic model showing direct impingement vs. diffusion growth contributions for two distinct scenarios of AlInAs NW growth: one with a weak SAE enhancement effect (left) and the other with a strong SAE enhancement effect, predominantly influenced by the incorporation of diffusive In adatoms (right).*

As mentioned above, Al adatoms have a much shorter surface migration length, thereby reducing the contribution from the diffusion mechanism. Consequently, Al adatoms primarily contribute to growth via direct impingement within or immediately adjacent to the growth region (i.e., patterned array). In contrast, the SAE growth rate enhancement effect is primarily governed by surface migration of In adatoms from regions beyond the growth area, as described in Section 5.2. This implies that for arrays with a reduced growth enhancement effect, such as array E, In adatoms contribute to growth more evenly via both direct impingement and diffusion mechanisms, whereas for arrays with a greater growth enhancement effect, such as array A, In adatoms contribute to growth

predominantly via the diffusion mechanism. However, considering the short surface migration length of Al, we can consider that the Al adatoms mainly contribute to growth via the direct impingement mechanism, regardless of the array size. Therefore, In and Al adatoms can contribute more evenly to AlInAs NW formation for large arrays, resulting in a higher Al content, as shown in Figure 5.23. On the other hand, for arrays with a strong growth enhancement effect, such as array A, a balanced contribution from In and Al growth species no longer exists due to the dominant In surface migration mechanism, and the relative Al content is consequently reduced.

5.4 Conclusions

In this chapter, a novel approach was explored for the simultaneous growth of InAs-based nanowire (NW) arrays with diverse geometries on a single substrate during a single growth run. The study demonstrated that adjusting the dimensions of NW growth arrays can significantly influence the effective flowrate of group-III elements, subsequently impacting the growth rate of the NWs. Regions of NW growth were patterned with varying dimensions, ranging from 25×25 μm^2 to 400×400 μm^2, on a (111) Si substrate with a nanopore-templated SiO_2 mask. In a singular InAs growth run, both the diameter and length of the NWs exhibited a 37% decrease when transitioning from the smallest-area to the largest-area array. This highlights the substantial impact of NW growth array size on the overall growth rate. The observed trend was attributed to the ratio of the collation area for In adatoms, defined by the surface migration length, to the size of the NW growth region. As the size of the NW growth array increased, this ratio decreased, consequently diminishing the enhancement effect on growth rate.

To further support our experimental findings, a geometrical model was presented. This model was based in surface migration length and the probability of adatoms reaching the NW growth region. Moreover, employing the same concept, the investigation extended to composition modulation of $Al_xIn_{(1-x)}As$ through the growth of an InAs-AlInAs nanowire core-shell structure. It was observed that with a decrease in the growth rate, the Al content increased. This occurrence can be attributed to the considerably shorter surface migration length of Al compared to In adatoms, which boosts the surface diffusion growth mechanism of In adatoms for smaller arrays. Therefore, there will be more In compared to Al adatoms to incorporate to NWs structure. This study not only provides valuable insights

into the correlation between NW growth array dimensions and growth rates, but also offers a theoretical framework to explain these observations.

Chapter VI

6 Conclusions and Future Work

6.1 Summary and Conclusions

III-V semiconductor nanowires (NWs) are promising for future electronic, optoelectronic, and photonic devices. However, their high manufacturing costs, primarily due to the initial III-V substrates and substrate patterning, hinder large-scale integration. The research presented here aims to create substrate-free optoelectronic devices through selective area epitaxy (SAE) of InAs-based NW arrays.

In Chapter 3, a cost-effective method for producing InAs NW arrays on reusable Si wafers using the localized self-assembly (LSA) method was developed. Key achievements include using conventional *i*-line lithography for growth mask patterning, growth of sub-lithographic InAs NW arrays with yield of over 80%, and the successful delamination of as-grown NW arrays for fabrication of substrate-free devices. This process allows for multiple reuses of a Si substrate for NW growth and establishes, for the first time, the LSA approach for NW growth without the need for intermediary processing steps.

In Chapter 4, a nanophotonic engineering approach was also developed for achieving spectrally-selective light absorption in coaxial III-V NW arrays. Tunable short-wavelength infrared (SWIR) absorption in InAs NW array membranes with a backside reflector and partial $GaAs_{0.1}Sb_{0.9}$ shell segment coverage was explored through optical simulations. Near-unity and wavelength-selective absorption in the 2 to 3 μm wavelength range was achieved by tuning the geometry and dimensions of the core/shell NW segments. This approach enables novel design of spectrally-selective, polarization-dependent NW photodetectors with enhanced carrier collection.

In Chapter 5, the growth rate enhancement effect that arises during SAE synthesis of InAs NW arrays was investigated. This effect was controlled to achieve an eight-fold volumetric enhancement ratio, allowing for the growth of a tunable range of different NW dimensions on the same substrate. Similarly, it was demonstrated for the first time that the composition of adjacent $Al_xIn_{(1-x)}As$ NW arrays can be varied in the $0.11 \leq x \leq 0.54$ range during the same SAE run, which enables new approaches for the fabrication of multi-spectral NW-based optoelectronic devices.

These discoveries present new opportunities for the design and engineering of semiconductor NW materials and contribute to the advancement of flexible and cost-effective optoelectronic devices. These materials have broad applications in numerous sectors, including defense, healthcare, communications, and consumer electronics.

6.2 Outline for Future Work

There are several potential avenues for future research to extend the current work, which are discussed in this section. These are preliminary results stemming from the main research branches of this work that require further experimentation and/or analysis. These extensions are expected to make meaningful contributions to the field of NW research.

6.2.1 InAs Films on Si

The growth of III-V thin films on cost-effective substrates, such as silicon, has been a subject of extensive research. However, certain materials, like InAs on Si, present challenges due to significant differences in lattice mismatch, thermal expansion coefficient, and polarity between the epilayers and the substrate [203]. In this study, a novel approach was explored for growing InAs thin films on (111) Si substrates using a nanoporous template similar to the SAE samples employed in Chapter 5.

A two-step SAE growth mode was employed to achieve a continuous InAs film on Si. In the first step, InAs NW core segment growth proceeded on patterned Si (111) substrates. Subsequently, a change in growth conditions was implemented to suppress axial growth and encourage lateral growth. During lateral growth, the sidewalls of the NWs extended until they reached adjacent NWs, merging during the process to form a cohesive, smooth film of InAs on the Si substrate, as illustrated in Figure 6.1(a).

In SAE growth mode, lateral growth consistently occurs during epitaxy, albeit at a slower rate compared to axial growth [199]. The {111}-oriented top facet of NWs, which represent the lowest surface energy family of planes, provide the highest axial growth rate.

To suppress axial growth and stimulate lateral growth, it is necessary to reduce the surface migration length of adatoms, preventing them from reaching the top facet of the NWs. Instead, they are compelled to incorporate into the NWs from the sidewalls. Two common approaches for promoting lateral growth in SAE-grown NWs involve increasing the V/III ratio and decreasing the growth temperature [36], [199]. In this work, a patterned Si substrate, similar to the one used in Chapter 5, was employed for growth. This substrate featured pores with diameters of ~150 nm and pitch of 500 nm, as depicted in Figure 6.1(b).

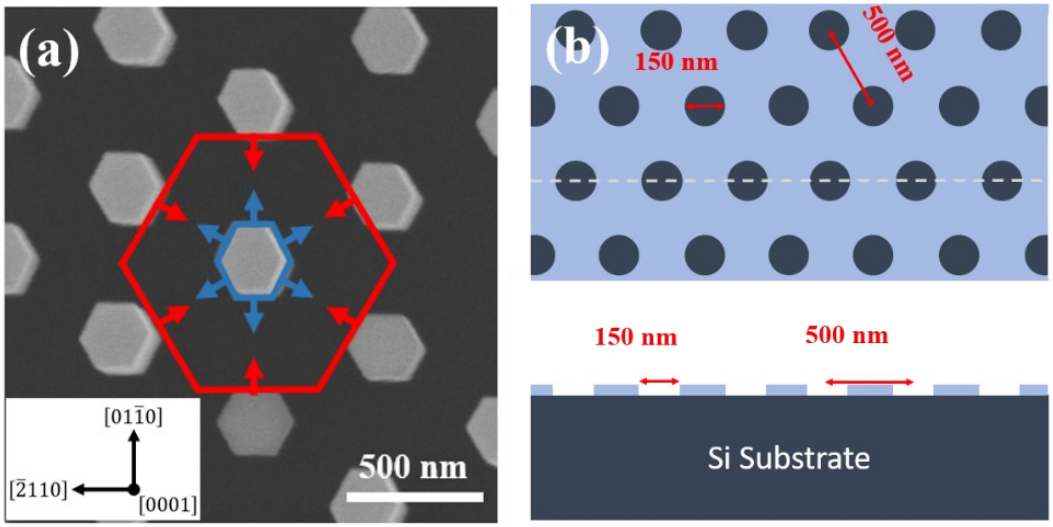

Figure 6.1. *(a) Top view on InAs SAE-grown NWs on Si substrate and potential for coalescence of neighboring NWs through lateral growth, indicated by arrows that are perpendicular to the NW sidewall growth front. (b) Schematic of patterned Si growth substrate, top and cross-section view.*

In order to remove native silicon oxide inside the pores, substrates were subjected to a 5 seconds buffered-oxide etching (BOE) treatment, then immediately loaded into the MOCVD reactor. TMIn and AsH_3 were used as gas-phase precursors for the supply of In and As growth species, respectively. All samples were first subjected to a 5-minute heat treatment at 850°C under an AsH_3 flow of 2000 µmol/min. In order to grow InAs film via

NW coalescence, we need to first grow short NW core segments and then switch to a predominantly radial growth mode to laterally expand the NWs. A two-step flowrate modulated SAE growth technique was performed for all of the samples in this work. The first step (i.e., core segment growth) was performed under the exact same growth conditions for all samples. Here, the substrate surface was flooded with a high TMIn and AsH_3 flowrates of 16 µmol/min and 365 µmol/min (i.e., V/III ratio of 22.8), respectively, for a period of 30 seconds at a 700 °C set-point temperature and a chamber pressure of 100 mbar. In order to promote lateral growth, during the second growth step, the set-point temperature was dropped to 600 °C under TMIn and AsH_3 flowrates of 32 and 1460 µmol/min (i.e., V/III ratio of 45.6), respectively, for 10 minutes. As-grown samples were then observed using SEM as shown in Figure 6.2(a). The average diameter and length of the NWs measured under these growth conditions were measured to be 209 ± 15 nm and 1804 ± 277 nm, respectively (errors represent one standard deviation from mean as measured for sample sets of 40 NWs).

Since the substrate pattern pitch is 500 nm, the NW diameter must exceed 500 nm in order to observe the intended coalescence effect. Therefore, for the second growth run, the temperature was dropped to 500 °C under the same V/III and over the same growth time as the previous sample. Average diameter and length values of 374 ± 18 nm and 927 ± 163 nm, respectively, were measured; this sample is shown in Figure 6.2(b). Here, the mean NW diameter was increased by approximately 165 nm; however, this was insufficient for NW coalescence. Moreover, SEM inspection revealed that the NW sidewalls did not have vertical and smooth facets, likely due to the low growth temperature. Therefore, a third sample was grown, where the set-point temperature of the second growth step was

increased to 550 °C under same V/III ratio for 20 minutes. This resulted in NWs with mean diameter and length values of 436 ± 54 nm and 987 ± 356 nm, respectively.

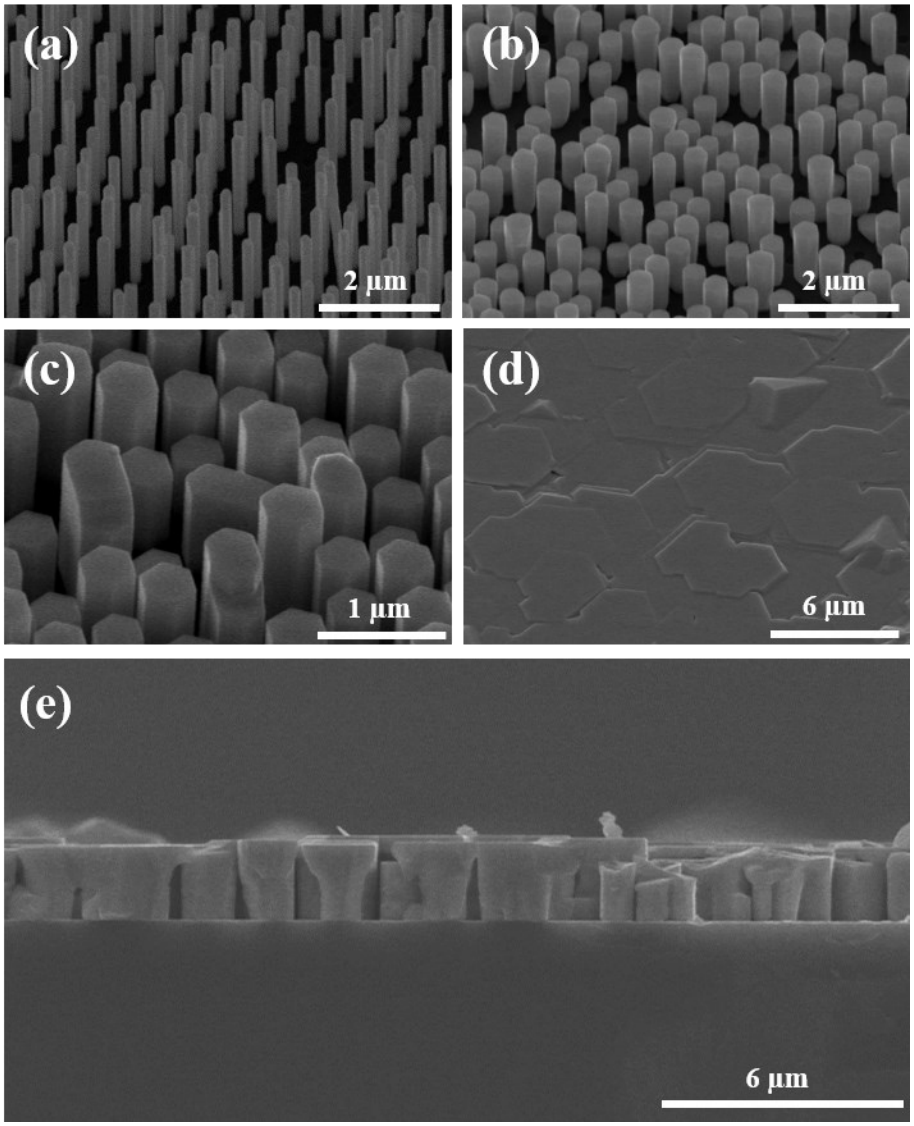

Figure 6.2. *45° tilted-view SEM image of two-step growth with the same conditions in the first step (i.e., "nucleation step" at T_G = 700 °C, V/III = 22.8, t = 30 s), but under different conditions for the second "lateral extension" step as follows: (a) T_G = 600 °C, V/III = 45.6, t = 10 min; (b) T_G = 500 °C, V/III = 45.6, t = 10 min; (c) T_G = 550 °C, V/III = 45.6, t = 20 min; and (d) T_G = 550 °C, V/III = 45.6, t = 60 min. (e) Cross-sectional view of sample shown in (d).*

In Figure 6.3(c), it is evident that some of the NWs have coalesced with their nearest neighbors or are in the early stages of coalescence. Additionally, the NWs exhibited the desired smooth sidewall facet under a temperature of 550 °C. Consequently, a subsequent sample was grown under the same conditions, but for an extended step-two duration of 1 hour. The SEM image in Figure 6.2(d) shows the coalesced NWs, which are observed to form an InAs film on the Si substrate. While most of the samples displayed a predominantly stepped surface, which is attributed to variations in the height of the NWs formed during the first growth step, some regions exhibited a smooth and uniform surface. The presence of polycrystalline island defects was also observed. To investigate the coalescence interface, a sample was cleaved to inspect the cross-section using SEM. Figure 6.2(e) shows tapered NWs with a larger diameter at the top compared to the bottom of the NWs, suggesting that a 2D growth mode begins at a certain point in the growth process. This likely occurred when the neighboring NW tips started to coalesce, resulting in the formation of a cohesive InAs film on top of the NWs.

The study holds considerable promise for future investigation, particularly regarding its potential applications in thin film growth. Evaluating the merging interface, optimizing growth conditions, and exploring growth on different templates could be promising avenues for future research in the realm of thin film growth, especially when dealing with high lattice mismatch.

6.2.2 InAs NW Doping

Doping is an essential process in semiconductor electronic and optoelectronic devices, necessitating a thorough investigation of growth conditions, including dopant precursor flowrate ratios. Given the significant difference in growth rates between NWs and thin films, doping conditions can vary. Therefore, Si_2H_6 doping of InAs NWs was explored for achieving high *n*-type doping.

A growth was carried out under 2 μmol/min of TMIn and 365 μmol/min of AsH_3 flowrates with dopant-to-group-III precursor ratio (i.e., Si_2H_6/III) of 2×10^{-2} at a set-point temperature of 700 °C for 30 min. The objective was to achieve *n*-type InAs NWs with length of > 5 μm and target dopant concentration of $n = 5 \times 10^{18}$ cm^{-3}. This sample was shipped to a collaborator at the University of Illinois to measure the doping level. Generally, evaluating doping levels in NWs poses more challenges compared to thin films. The NWs need to be sufficiently tall to allow for easy detachment and transfer to a substrate, ensuring their horizontal orientation. This setup enables the contacting and measurement of conductivity for individual NWs. These measurements are currently pending and will be continued by our collaborators in the future. Doping measurement results can be very helpful to know the exact Si incorporation in the NW structure, such that the desired doping levels can be adjusted by tuning the growth condition such as temperature, V/III ratio, and TMIn and Si_2H_6 flowrates.

6.2.3 InAsSb Optical Simulations for LWIR Absorption

In Chapter 4, the focus of our investigations was the tuning of coaxial NW geometries for selective absorption in the short-wavelength infrared (SWIR) range of the electromagnetic spectrum. The same approach could be applied to the mid-wavelength infrared (MWIR) range (i.e., 3-5 μm) and the long-wavelength infrared (LWIR) range (i.e., 8-14 μm), which are of significant interest for defense applications. A suitable ternary III-V alloy with the smallest semiconductor bandgap is $InAs_{(1-x)}Sb_x$ with $x = 0.63$. This ternary material covers the entire LWIR range, extending up to 17 μm at room temperature. The utilization of InAsSb NWs could open new possibilities for enhancing military applications that rely on MWIR and LWIR wavelengths [204]. Therefore, preliminary optical simulations were conducted for $InAs_{0.37}Sb_{0.63}$ NW array membranes without a backside reflection layer, as depicted in Figure 6.3. The diameter of the NWs was varied from 100 nm to 2000 nm while maintaining a constant length of 4 μm. Arrays with pitch values of 3 μm, 4 μm, and 5 μm were explored. As the NW diameter and pitch increase, selective absorption demonstrates a consistent red shift toward longer wavelengths, mirroring the trends discussed in Section 5.3. This observation can be further investigated by incorporating a back contact reflector and adding a partial shell to enhance selective absorption while minimizing the absorption volume.

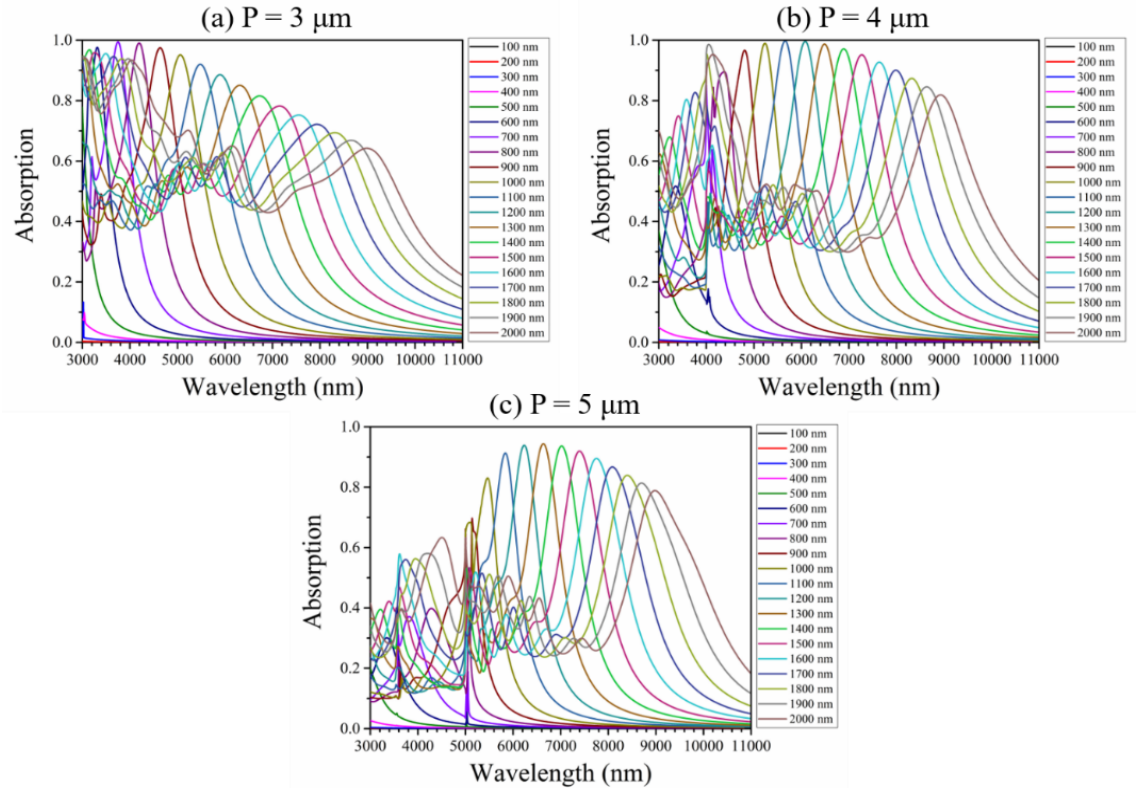

Figure 6.3. *Absorption spectra of $InAs_{0.37}Sb_{0.63}$ NW array membranes without backside reflectors for diameters ranging from 100 to 600 nm and different pitch values of (a) 3 μm, (b) 4 μm, and (c) 5 μm.*

6.2.4 Mixed-Dimensional III-V/2D Heterostructures

Lastly, as part of an ongoing collaborative study with Pennsylvania State University, we explore the self-assembly process of InAs nanostructures via MOCVD on continuous MoS_2 monolayers on sapphire substrates. Our findings indicate that the MOCVD growth temperature significantly influences the morphology and number density of InAs nanostructures on MoS_2. The remote epitaxy effect is investigated by comparing the growth of InAs on different platforms, including epitaxial MoS_2 on sapphire, MoS_2 on SiO_2, as well as on graphene on sapphire and graphene on SiO_2 systems. To delve deeper into the interfacial atomic order at the InAs/MoS_2 heterojunction, TEM analysis is

conducted. The results unveiled that NWs grown at 600 °C exhibited an arsenic-polar orientation, indicating the presence of an In-terminated interface. Conversely, the triangular nanoflakes grown at 750 °C demonstrated an In-polar orientation, signifying an arsenic-terminated interface. This exploration sheds light on the temperature-dependent growth behavior and interfacial characteristics of InAs nanostructures on MoS_2, providing valuable insights for tailored van der Waals epitaxy of mixed-dimensional heterostructures.

Semiconductor heterostructures are promising materials for novel electronics and optoelectronics applications. However, integrating dissimilar materials with pristine interfaces is very challenging. Conventionally, the formation semiconductor heterostructures relies on one-to-one chemical boding between dissimilar materials and, therefore, limits the integrating process to those material with similar lattice constants and symmetry, similar electronic properties, similar processing conditions [205]. This means that integration of chemically-bonded systems of dramatically different lattice parameters leads to built-in strain relaxation, which results in interface disorder and consequently to degradation of material properties like carrier transport at the interface. Alternatively, dislocation-free and electronically clean interfaces can be achieved via van der Waals (vdW) integration approach for a wide range of two-dimensional (2D) materials through weak vdW forces between layers, as shown in Figure 6.4 [205], [206]. This approach is not limited to 2D material systems alone, and can be principally applicable for different material dimensions, which opens new opportunities for fundamental studies and possible novel device applications.

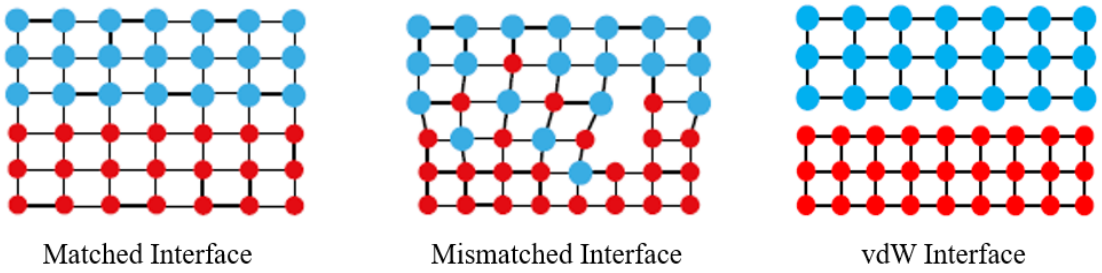

Figure 6.4. *Schematic of bonded heterostructures interfaces: lattice-matched interface (left), lattice mismatched interface (middle), and a van der Waals interface (right).*

Mixed-dimensional heterostructures (MDHs) are very promising material systems since they allow the inherent properties of their distinct components to be synergistically exploited. For example, coupling one-dimensional NWs that provide high optical absorption with two-dimensional van der Waals monolayer materials that provide high in-plane carrier mobility is desirable for many device applications. In fact, in recent years, numerous exciting examples have been reported that use MDHs for high-responsivity multispectral photodetectors, gate-tunable high-efficiency photovoltaic solar cells, and multicolor high-current-injection light-emitting diodes; these new device architectures also are suitable for flexible, wearable, stretchable, and low-weight applications [206], [207]. Moreover, vdW MDHs are promising material systems for next generation electronic and optoelectronic applications because they can give rise to new physical properties stemming from interlayer coupling interactions and redistribution of charge states across the van der Waals gap. Hence, they are interesting from a basic science perspective and, recently, these systems have been investigated for their unique properties such as tunable interlayer microwave absorption, enhanced terahertz emission, and formation of indirect and hybrid exciton states with binding energies on the order of 100 meV [208]–[213].

Epitaxial integration of III-V semiconductor nanostructures with 2D materials enables tremendous freedom in the synthesis of widely tunable MDHs. Such III-V/2D hybrid nanosystems give rise to otherwise inaccessible physical properties stemming from novel interlayer coupling effects and heterojunction carrier dynamics for a versatile combination of materials. They also provide opportunities for the discovery of new crystal growth mechanisms. As mentioned, direct integration of III-V compounds with foreign lattices, and in a manner that allows pristine interfaces to be preserved, is very challenging by conventional epitaxy. However, dislocation-free and electronically clean interfaces can be realized via the van der Waals (vdW) epitaxial integration approach for III-V crystal growth on various monolayer nanomaterials. For example, III-V epi-structure properties can be tuned, such that room-temperature bandgap energies ranging from 0.17 eV for InSb to 2.45 eV for AlP [214]. The type, concentration and profile of foreign impurities through in-situ doping can be controlled to manipulate transport properties and exciton dynamics. In addition, the number density, size and dimensionality of the III-V nanostructures can be controlled as a function of the MOCVD growth conditions. So, all of these options provide the capability to tune the critical parameters of the heterostructures including interfacial charge distributions, and heterojunction barriers heights, and band alignments, which is critical for engineering optoelectronic response behavior.

Furthermore, using MOCVD integration has some inherent benefits compared to other approaches forming MDHs. For example, unlike micro-mechanical exfoliation, MOCVD growth is more scalable for practical applications [215]. Unlike solution transfer, it can enable clean and abrupt interfaces without introducing contamination during transfer. Moreover, unlike some physical vapor deposition methods that can damage the 2D surface

through bombardment and heating, the MOCVD approach maintains more pristine heterojunctions interfaces [215], [216]. This provides opportunities for discovery of new crystal growth phenomena from unique coincident-site lattice coupling and vacancy-mediated buckling effects when covalent lattices are integrated with van der Waals layered materials. Therefore, pseudo van der Waals epitaxy allows a covalently bonded III-V lattice to be coupled with a monolayer materials through a van der Waals gap such that there is no strain sharing across the interface [215], [216]. This allows strain free III-V crystals to be integrated without suffering from threading dislocation defects despite their different crystal structures and large lattice mismatch with the 2D film.

Of particular interest is the InAs/MoS_2 nanosystem, which provides a type-I heterojunction band alignment and tunable interlayer band structure that depends largely on lattice polarity and presence of vacancy defects at the heterointerface [217], [218]. In this study, we have investigated the self-assembly of InAs nanostructures via MOCVD on continuous MoS_2 monolayers on sapphire substrates. All the samples were grown under the same growth conditions as shown in Table 6.1, with constant flow of TMIn and AsH_3 at a V/III ratio of 25 and at growth temperatures ranging from 600 to 750° C to study the growth temperature dependence.

Table 6.1. *Growth Conditions InAs on continuous MoS_2 on Sapphire*

Bake Temp (°C)	Bake Time (s)	Growth Temp (°C)	Growth Time (s)	TMIn Flowrate (µmol/min)	V/III Ratio	Reactor Pressure (mBar)
850	300	600 650 700 750	300	16	25	100

For InAs growth on MoS_2 on sapphire, it was observed that the MOCVD growth temperature dramatically influences the morphology and number density of InAs nanostructures. Figure 6.5(a)-(d) show the samples grown at 600 – 750 °C. The density of parasitic islands considerably decreased by increasing the growth temperature. More importantly, it was observed that self-assembly of vertical NWs is favored at a growth temperature of 600 °C, as shown in Figure 6.5(e). No vertically aligned NWs were observed for the sample grown at 750 °C. Instead, triangular nanoplates with two common self-aligned in-plane orientations were observed as shown in Figure 6.5(f) indicated by dotted lines.

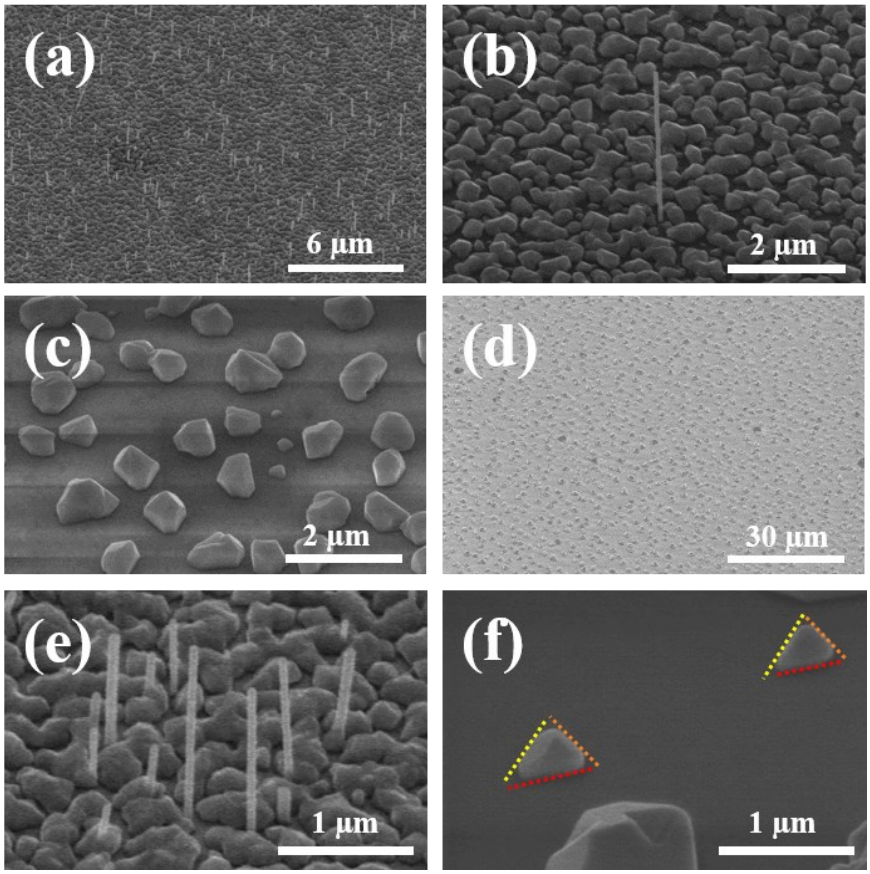

Figure 6.5. *Tilted-view SEM imagea of InAs growth on MoS_2 on sapphire substrate: at (a) 600 °C, (b) 650 °C, (c) 700 °C, and (d) 750 °C. (e) and (f) show magnified views of samples grown at 600 °C and 750 °C, respectively.*

Many of the growth trends that have been observed for InAs on MoS_2 follow similar trends that have been long reported in the literature for self-assembly and selective-area epitaxy of III-Vs. For example, Figure 6.6(a) shows a phase diagram for formation of hexagonal crystals versus truncated tetrahedral structures based on partial pressure of the group-V precursor, AsH_3, on the vertical axis and reciprocal temperature on the horizontal axis. The solid line labelled B represents the boundary between the 2×2 and $\sqrt{19} \times \sqrt{19}$ surface reconstructions [219]. Here, the cartoons of the hexagonal and pyramidal structures show the likelihood of low-temperature conditions leading to NWs at high effective arsine pressures, and high-temperature conditions leading to the truncated nanoflakes at low effective arsine partial pressures [219].

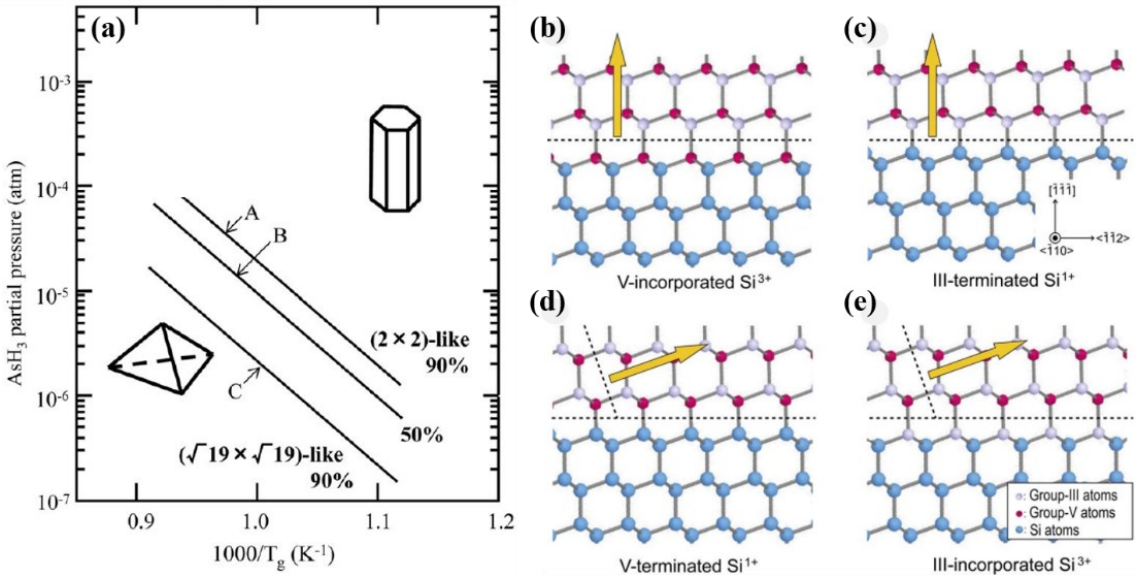

Figure 6.6. *(a) Phase diagram of hexagonal or tetrahedral island growth as functions of AsH_3 partial pressure and temperature. Illustrations of interfacial crystal structure for: (a) Group-V incorporated Si interface, (b) group-III terminated Si interface, (c) group-V terminated Si interface, and (d) group-III incorporating Si interface. The yellow arrows indicate III–V NW-growth direction. Adopted from Ref. [219] and [220].*

In our investigation, the arsine flow has not been modified at different temperatures, meaning that lower effective group-V supply is expected due to surface desorption at the high temperature of 750° C. Also during growth of polar III-V crystals on dissimilar substrates, the lattice polarity and termination at the interface can strongly influence the epi-structure growth direction and morphology. For example, in the case of III-V growth on non-polar silicon, whether the interface is group-V incorporated or group-V terminated as shown in Figures 6.6(b) and 6.6(d), respectively. Whether it is group-III terminated or group-III incorporated is depicted in Figures 6.6(c) and 6.6(e), respectively [140], [220].

In order to investigate the lattice polarity at the heterojunction interface, samples grown at 600° C (for NWs) and 750 °C (for nanoflakes) have been selected for further TEM analysis. Figure 6.7(a) shows a HAADF image of the growth interface formed by an InAs NWs on MoS_2 at 600 °C, where the sapphire substrate, 2D layers, and III-V lattice are contrast-differentiated based on Z-number. EDXS mapping of elemental indium (in blue), molybdenum (in red), and aluminum (in teal) are also shown in Figures 6.7(b), 6.7(c), and 6.7(d), respectively. High-resolution HAADF images for InAs crystals grown at 600° C (for NWs) and 750° C (for nanoflakes) are shown in Figures 6.7(e) and 6.7(f), respectively. In both cases, the white arrows indicate the growth direction of InAs crystals. Interestingly, it appears that the InAs NWs grown at 600 °C are arsenic-polar, implying that they have an In-terminated interface, while the triangular InAs nanoflakes grown at 750 °C are In-polar implying that they have an arsenic-terminated interface. The intensity linescans collected from the lattice-resolved images, shown in the insets of Figure 6.7(e) and 6.7(f), support the same point. These observations follow the aforementioned trends regarding group-III termination resulting in a vertical growth direction for nanowires and

group-V termination resulting in a non-vertical growth direction for truncated nanoflakes, as depicted in Figures 6.6(c) and 6.6(d), respectively.

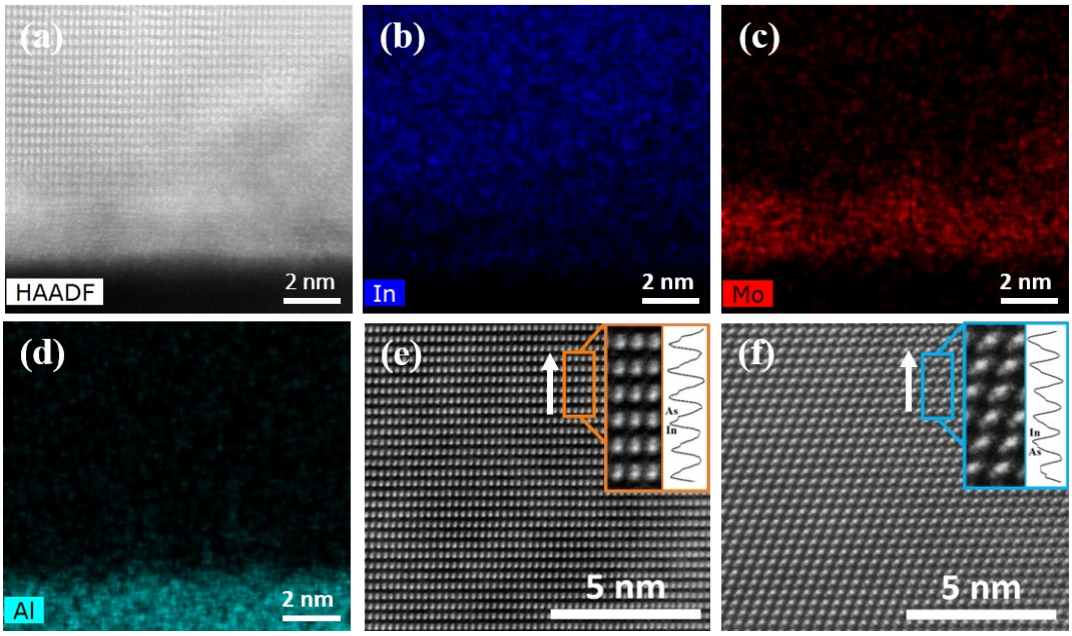

Figure 6.7. *a) HAADF image of InAs/MoS_2/sapphire interface grown at 600° C, EDX mapping of elemental (b) indium, (c) molybdenum, and (d) aluminum. High-resolution HAADF images of (e) InAs NW grown at 600 °C on MoS_2 and (f) nanoflakes grown at 750 °C on MoS_2. Insets show the intensity linescans collected from the lattice-resolved images, and white arrows indicate the growth direction.*

To investigate whether the nanostructure formation is influenced by the lattice order and a likely stronger potential field of the underlying substrate, which is the so-called remote epitaxy effect, we simultaneously carried out growths on 2D materials that were transferred to oxide films on silicon substrates, as well as 2D materials that were CVD-grown on sapphire. Figures 6.8(a) and 6.8(b) show InAs crystal growth performed at 750 °C under a V/III ratio of 25 on single layer graphene (SLG)-on-SiO_2 and SLG-on-sapphire samples, respectively. Growth of InAs on SLG resulted in polycrystalline islands with no regular faceting structure regardless of the underlying substrate. However, growth on

MoS_2-on-SiO_2 and on MoS_2-on-Sapphire, as shown in Figures 6.8(c) and 6.8(d), respectively, resulted in the same type of triangular nanoflakes with common sidewall facets as noted above. This was observed at the higher temperatures regardless of whether or not the underlying substrate was sapphire or SiO_2. This is a strong indication that the common in-plane orientation of the InAs nanoflakes is mediated by the MoS_2 layer itself, and this is seen more clearly in the Figure 6.8(c), where the sidewalls of the InAs nanostructure, marked by orange dotted lines, appear to be aligned with the sidewalls of the MoS_2 domain, which are marked by the white dashed lines. Accordingly, it is less likely that the underlying sapphire substrate is causing any influential remote epitaxy effect here; rather, that InAs growth is epitaxially guided by the MoS_2 lattice.

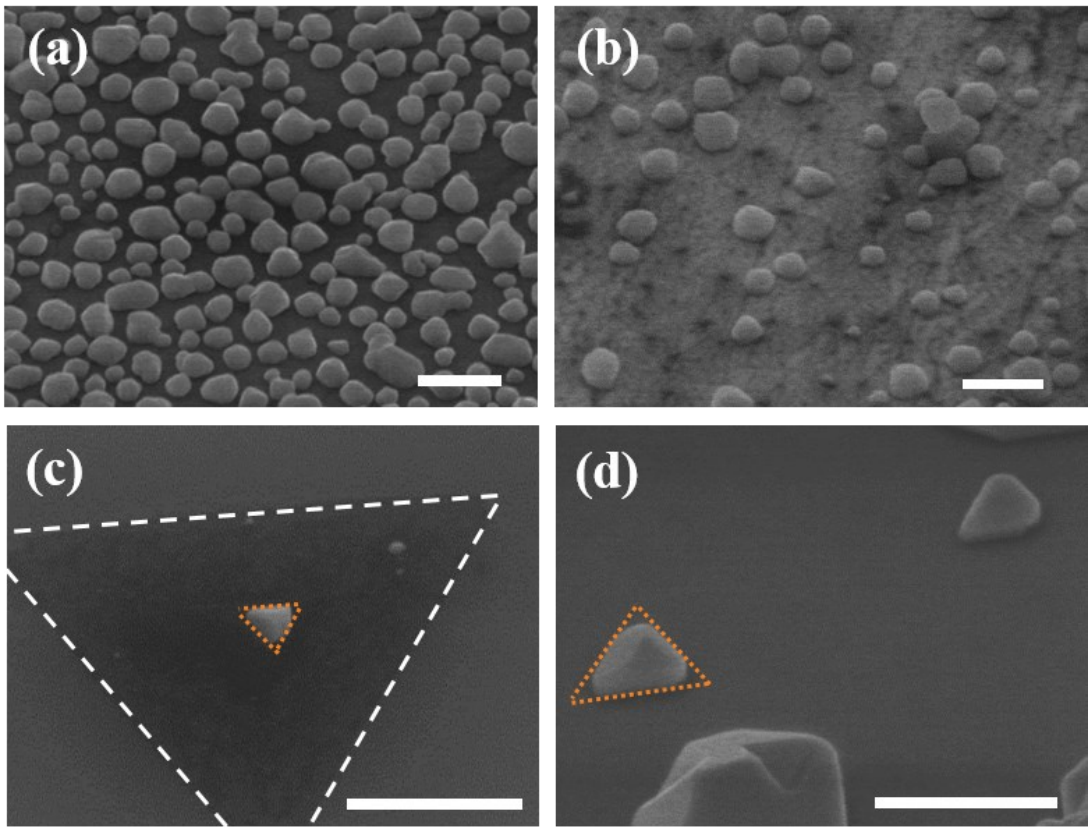

Figure 6.8. *Tilted-view SEM image of InAs growth on (a) SLG on oxide, (b) SLG on Sapphire (c) MoS_2 on oxide (d) MoS_2 on Sapphire at same growth temperature.*

Our research group has previously reported a model for a nearly-commensurate super-cell configuration for the epitaxial InAs on MoS_2 system [152]. In Figure 6.9, molybdenum and sulfur atoms are shown as blue and yellow, while indium and arsenic atoms are shown as gray and orange, respectively. The image shows a top view of the $(\bar{1}\bar{1}\bar{1})$ plane of the cubic InAs lattice over the $(000\bar{1})$ plane of the hexagonal MoS_2 lattice. At the top, the 2×2 InAs unit cell is shown with a blue border, and along the center of the image we can see those 3 multiples of the InAs unit cell along the $(2\bar{1}\bar{1})$ direction become coincident with 14 multiples of the Mo-to-Mo spacing along the $(10\bar{1}0)$ direction of the MoS_2 lattice. Therefore, this represents a pseudo-commensurate relationship between InAs and MoS_2, which is shown as the likely basis of the lattice registry effect discussed above.

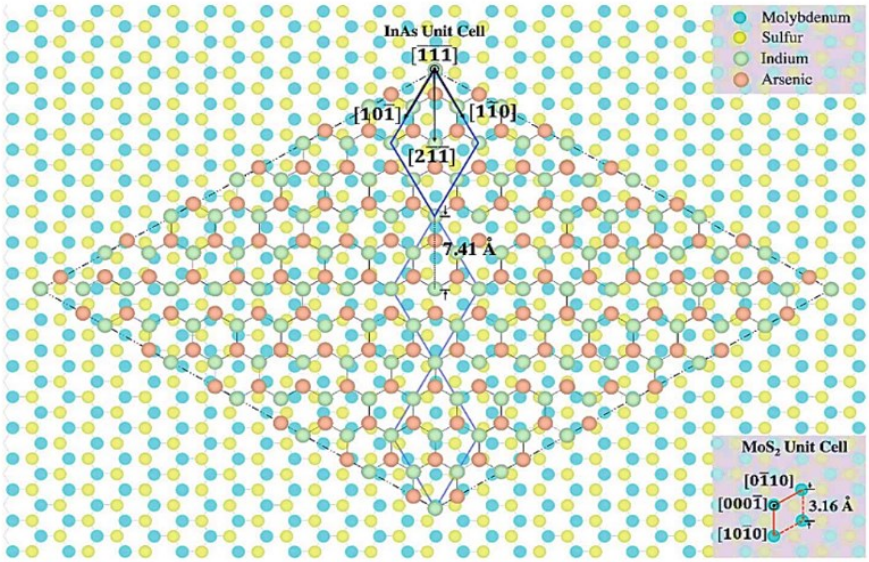

Figure 6.9. *Plan-view model of a nearly-commensurate super-cell configuration composed of a* $(\bar{1}\bar{1}\bar{1})$ *oriented InAs cubic lattice on* $(000\bar{1})$ *oriented* MoS_2 *hexagonal lattice. Adopted from Ref. [152].*

Furthermore, photoluminescence (PL) spectroscopy was carried out after and before InAs growth on MoS_2 to investigate the influence of nanostructure growth on the optical properties of MoS_2. The PL spectroscopy measurements showed a large red shift for the dominant MoS_2 peak from 1.87 eV to 1.58 eV, specifically for growth under 600 °C and 650 °C. Figure 6.4 shows the PL spectrum for MoS_2 before (black) and after (red) InAs growth at 650 °C. The basis of this redshift is currently not well-understood and further investigations but may be related to InAs/MoS_2 interfacial states and/or strain effects.

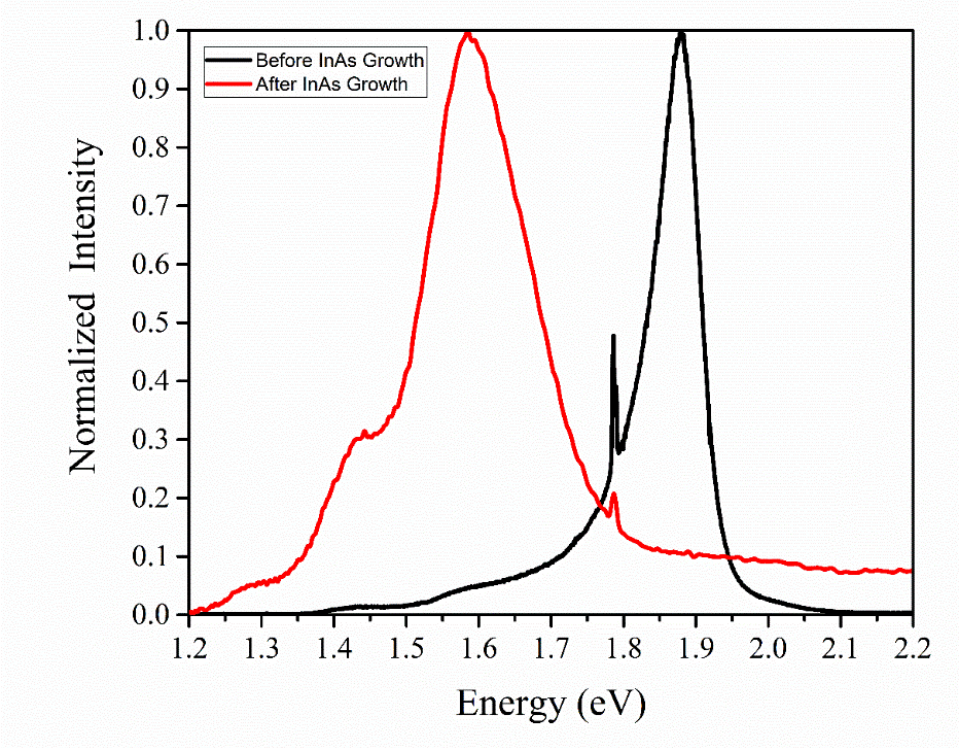

Figure 6.10. *Pl spectrum of on MoS_2 substrate before and after growth of InAs nanostructure at 650 °C.*

To conclude, self-assembly of InAs nanostructures via MOCVD on continuous MoS_2 monolayers on sapphire substrates was investigated. It was demonstrated that MOCVD growth temperature dramatically influences the morphology and number density of InAs nanostructures grown on MoS_2. Whereas self-assembly of vertical NWs is favored at a growth temperature 600 °C, triangular nanoplates with two common self-aligned in-plane orientations are observed at 750 °C. No remote epitaxy effect was observed by comparing growth of InAs on different platforms including epitaxial MoS_2-on-sapphire, MoS_2-on-SiO_2, as well as on graphene-on-sapphire and graphene-on-SiO_2 systems. The interfacial atomic order at the InAs/MoS_2 heterojunction was investigated by TEM analysis. The results revealed that NWs grown at 600 °C exhibited an arsenic-polar orientation, indicating the presence of an In-terminated interface. On the other hand, the triangular nanoflakes grown at 750 °C were found to be In-polar, implying an arsenic-terminated interface.

This study can be expanded by performing additional characterization techniques, including electron energy-loss spectroscopy (EELS) and scanning tunneling spectroscopy (STS), to obtain more detailed insights into the interlayer characteristics of the MDH systems, such as the materials-specific interfacial density of states and interfacial band structure. Moreover, similar investigations can be conducted for other MDHs, like InP or GaAs, on various 2D materials such as MoS_2 or WSe_2.

Chapter VII

7 Research Contributions

7.1 Journal Articles

7.1.1 First-Authored Peer-Reviewed Journal Publications (2)

- **A. Abrand**, N. Anttu, P. K. Mohseni, "Modeling Selective Narrowband Light Absorption in Coaxial InAs-$GaAs_{0.1}Sb_{0.9}$ Nanowires with Partial Shell Segment Coverage", *Nano Express*, 4 (2), 025003, 2023.

- **A. Abrand**, M. A. Baboli, A. Fedorenko, S. J. Polly, E. Manfreda-Schulz, S. M. Hubbard, P. K. Mohseni, "Localized Self-Assembly of InAs Nanowire Arrays on Reusable Si Substrates for Substrate-Free Optoelectronics", *ACS Applied Nano Materials*, 5 (1), 840-851, 2022.

7.1.2 Co-Authored Peer-Reviewed Journal Publications (3)

- M. A. Baboli, **A. Abrand**, R. A. Burke, A. Fedorenko, T. S. Wilhelm, S. J. Polly, M. Dubey, S. M. Hubbardab and P. K. Mohseni, "Mixed-dimensional InAs nanowire on

layered molybdenum disulfide heterostructures via selective-area van der Waals epitaxy", *Nanoscale Advances*, 3 (10), 2802-2811, 2021.

- T. S. Wilhelm, I. L. Kecskes, M. A. Baboli, **A. Abrand**, M. S. Pierce, B. J. Landi, I. Puchades, P. K. Mohseni, "Ordered Si Micropillar Arrays via Carbon-Nanotube-Assisted Chemical Etching for Applications Requiring Nonreflective Embedded Contacts", *ACS Applied Nano Materials*, 2 (12), 7819-7826, 2019.

- T. S. Wilhelm, A. P. K, M. A. Baboli, **A. Abrand**, K. A. Bertness, P. K. Mohseni,"Black GaAs with Sub-Wavelength Nanostructures Fabricated via Lithography-Free Metal-Assisted Chemical Etching", *ECS Journal of Solid State Science and Technology*, 8 (6), Q134, 2019.

7.1.3 First-Authored Conference Presentations (4)

- **A. Abrand**, N. Anttu, P. K. Mohseni, "Tuning Selective Narrowband Infrared Absorption Using Coaxial InAs-$GaAs_{0.1}Sb_{0.9}$ Nanowires with Partial Shell Segment Coverage", *64th Electronic Materials Conference (EMC)*, June 2022. (Oral Presentation)

- **A. Abrand**, M. A. Baboli, B. P. Huet, Z Santos, P. P. Dholabhai, J. M. Redwing, and P. K. Mohseni, "Growth and characterization of Mixed-Dimensional InAs/MoS_2 Heterostructure", *63rd Electronic Materials Conference (EMC)*, June 2021. (Oral Presentation)

- **A. Abrand**, M. A. Baboli, T. S. Wilhelm, and P. K. Mohseni, "Flexible III-V Nanowire-Based Photodetectors via Selective-Area Epitaxy on Reusable Si Substrates", *62nd Electronic Materials Conference (EMC)*, June 2020. (Oral Presentation)

- **A. Abrand**, M. A. Baboli, T. S. Wilhelm, and P. K. Mohseni, "Reuse of Si Substrates for Selective-Area Epitaxy of Large-Area III-V Nanowire Array-Based Flexible Infrared Photodetectors", *Virtual Material Research Society Conference (MRS)*, Nov 2020. (Oral Presentation)

7.1.4 Co-Authored Conference Presentations (2)

- A. Fedorenko, **A. Abrand**, P. K. Mohseni, S. M. Hubbard, "Multi-Terminal Dual-Junction $GaAs_{0.73}P_{0.27}/In_{0.22}Ga_{0.78}As$ Nanowire Solar Cell: An Integrated Approach to Simulation" *Photovoltaic Specialists Conference (PVSC)*, Jun 2020. (Publication)

- J. W. Morrell, **A. Abrand**, N. H. Manimarand, P. K. Mohseni and K Xu, "Realizing Gate-All-Around Vertical Nanowire Field-Effect Transistors based on Van Der Waals Epitaxial InAs-on-2D Heterostructures" *Graphene and Beyond*, May 2023. (Poster)

Chapter IIX

8 References

[1] S. M.Sze and K. K. Ng, *Physics of Semiconductor Devices*. John Wiley & Sons, 2006.

[2] F. Dimroth, "High-efficiency solar cells from III-V compound semiconductors," *Phys. Status Solidi C*, vol. 3, no. 3, pp. 373–379, 2006, doi: 10.1002/pssc.200564172.

[3] "3. III-V compound semiconductor material systems." Accessed: Mar. 30, 2020. [Online]. Available: http://web.tiscali.it/decartes/phd_html/node4.html

[4] H. A. Fonseka, "Growth and Characterisation of InP Nanowires and Nanowire-Based Heterostructures for Future Optoelectronic Device Applications," 2015, doi: 10.25911/5d6e4a7eefdfa.

[5] T. Bryllert, L.-E. Wernersson, L. E. Froberg, and L. Samuelson, "Vertical high-mobility wrap-gated InAs nanowire transistor," *IEEE Electron Device Lett.*, vol. 27, no. 5, pp. 323–325, May 2006, doi: 10.1109/LED.2006.873371.

[6] J. Wallentin *et al.*, "InP Nanowire Array Solar Cells Achieving 13.8% Efficiency by Exceeding the Ray Optics Limit," *Science*, vol. 339, no. 6123, pp. 1057–1060, Mar. 2013, doi: 10.1126/science.1230969.

[7] R. R. LaPierre *et al.*, "III–V nanowire photovoltaics: Review of design for high efficiency," *Phys. Status Solidi RRL – Rapid Res. Lett.*, vol. 7, no. 10, pp. 815–830, 2013, doi: 10.1002/pssr.201307109.

[8] R. R. LaPierre, M. Robson, K. M. Azizur-Rahman, and P. Kuyanov, "A review of III–V nanowire infrared photodetectors and sensors," *J. Phys. Appl. Phys.*, vol. 50, no. 12, p. 123001, Feb. 2017, doi: 10.1088/1361-6463/aa5ab3.

[9] L. Samuelson, "Self-forming nanoscale devices," *Mater. Today*, vol. 6, no. 10, pp. 22–31, Oct. 2003, doi: 10.1016/S1369-7021(03)01026-5.

[10] M. T. Björk *et al.*, "One-dimensional heterostructures in semiconductor nanowhiskers," *Appl. Phys. Lett.*, vol. 80, no. 6, pp. 1058–1060, Feb. 2002, doi: 10.1063/1.1447312.

[11] L. C. Chuang, M. Moewe, C. Chase, N. P. Kobayashi, C. Chang-Hasnain, and S. Crankshaw, "Critical diameter for III-V nanowires grown on lattice-mismatched

substrates," *Appl. Phys. Lett.*, vol. 90, no. 4, p. 043115, Jan. 2007, doi: 10.1063/1.2436655.
[12] T. Mårtensson *et al.*, "Epitaxial III−V Nanowires on Silicon," *Nano Lett.*, vol. 4, no. 10, pp. 1987–1990, Oct. 2004, doi: 10.1021/nl0487267.
[13] Y. Du *et al.*, "Review of Highly Mismatched III-V Heteroepitaxy Growth on (001) Silicon," *Nanomaterials*, vol. 12, no. 5, p. 741, Feb. 2022, doi: 10.3390/nano12050741.
[14] N. Anttu and H. Q. Xu, "Efficient light management in vertical nanowire arrays for photovoltaics," *Opt. Express*, vol. 21, no. 103, pp. A558–A575, May 2013, doi: 10.1364/OE.21.00A558.
[15] N. P. Dasgupta *et al.*, "25th Anniversary Article: Semiconductor Nanowires – Synthesis, Characterization, and Applications," *Adv. Mater.*, vol. 26, no. 14, pp. 2137–2184, 2014, doi: 10.1002/adma.201305929.
[16] H. Kind, H. Yan, B. Messer, M. Law, and P. Yang, "Nanowire Ultraviolet Photodetectors and Optical Switches," *Adv. Mater.*, vol. 14, no. 2, pp. 158–160, 2002, doi: 10.1002/1521-4095(20020116)14:2<158::AID-ADMA158>3.0.CO;2-W.
[17] Y. Cui, Q. Wei, H. Park, and C. M. Lieber, "Nanowire Nanosensors for Highly Sensitive and Selective Detection of Biological and Chemical Species," *Science*, vol. 293, no. 5533, pp. 1289–1292, Aug. 2001, doi: 10.1126/science.1062711.
[18] C. Soci, A. Zhang, X.-Y. Bao, H. Kim, Y. Lo, and D. Wang, "Nanowire photodetectors," *J. Nanosci. Nanotechnol.*, vol. 10, no. 3, pp. 1430–1449, Mar. 2010.
[19] L. Shen, E. Y. B. Pun, and J. C. Ho, "Recent developments in III–V semiconducting nanowires for high-performance photodetectors," *Mater. Chem. Front.*, vol. 1, no. 4, pp. 630–645, 2017, doi: 10.1039/C6QM00279J.
[20] F. Dimroth and S. Kurtz, "High-Efficiency Multijunction Solar Cells," *MRS Bull.*, vol. 32, no. 3, pp. 230–235, Mar. 2007, doi: 10.1557/mrs2007.27.
[21] W. Shockley and H. J. Queisser, "Detailed Balance Limit of Efficiency of p-n Junction Solar Cells," *J. Appl. Phys.*, vol. 32, no. 3, pp. 510–519, Mar. 1961, doi: 10.1063/1.1736034.
[22] I. Åberg *et al.*, "A GaAs Nanowire Array Solar Cell With 15.3% Efficiency at 1 Sun," *IEEE J. Photovolt.*, vol. 6, no. 1, pp. 185–190, Jan. 2016, doi: 10.1109/JPHOTOV.2015.2484967.
[23] E. Garnett and P. Yang, "Light trapping in silicon nanowire solar cells," *Nano Lett*, pp. 1082–1087, 2010.
[24] B. Monemar, B. J. Ohlsson, N. F. Gardner, and L. Samuelson, "Chapter Seven - Nanowire-Based Visible Light Emitters, Present Status and Outlook," in *Semiconductors and Semimetals*, vol. 94, S. A. Dayeh, A. Fontcuberta i Morral, and C. Jagadish, Eds., in Semiconductor Nanowires II: Properties and Applications, vol. 94. , Elsevier, 2016, pp. 227–271. doi: 10.1016/bs.semsem.2015.10.002.
[25] M. Djavid and Z. Mi, "Enhancing the light extraction efficiency of AlGaN deep ultraviolet light emitting diodes by using nanowire structures," *Appl. Phys. Lett.*, vol. 108, no. 5, p. 051102, Feb. 2016, doi: 10.1063/1.4941239.

[26] Q. Yue, K. Li, F. Kong, J. Zhao, and W. Li, "Analysis on the Light Extraction Efficiency of GaN-Based Nanowires Light-Emitting Diodes," *IEEE J. Quantum Electron.*, vol. 49, no. 8, pp. 697–704, Aug. 2013, doi: 10.1109/JQE.2013.2265167.
[27] M. D. Brubaker *et al.*, "UV LEDs based on p–i–n core–shell AlGaN/GaN nanowire heterostructures grown by N-polar selective area epitaxy," *Nanotechnology*, vol. 30, no. 23, p. 234001, Mar. 2019, doi: 10.1088/1361-6528/ab07ed.
[28] G. T. Wang, Q. Li, J. J. Wierer, D. D. Koleske, and J. J. Figiel, "Top–down fabrication and characterization of axial and radial III-nitride nanowire LEDs," *Phys. Status Solidi A*, vol. 211, no. 4, pp. 748–751, 2014, doi: 10.1002/pssa.201300491.
[29] Y. Zhang, J. Wu, M. Aagesen, and H. Liu, "III–V nanowires and nanowire optoelectronic devices," *J. Phys. Appl. Phys.*, vol. 48, no. 46, p. 463001, Nov. 2015, doi: 10.1088/0022-3727/48/46/463001.
[30] K. A. Dick, "A review of nanowire growth promoted by alloys and non-alloying elements with emphasis on Au-assisted III–V nanowires," *Prog. Cryst. Growth Charact. Mater.*, vol. 54, no. 3, pp. 138–173, Sep. 2008, doi: 10.1016/j.pcrysgrow.2008.09.001.
[31] K. A. Dick and P. Caroff, "Metal-seeded growth of III–V semiconductor nanowires: towards gold-free synthesis," *Nanoscale*, vol. 6, no. 6, pp. 3006–3021, Feb. 2014, doi: 10.1039/C3NR06692D.
[32] G.-C. Yi, *Semiconductor Nanostructures for Optoelectronic Devices: Processing, Characterization and Applications*. Springer Science & Business Media, 2012.
[33] *Nanowires*. New York, NY: Springer Berlin Heidelberg, 2016.
[34] S. Breuer *et al.*, "Suitability of Au- and Self-Assisted GaAs Nanowires for Optoelectronic Applications," *Nano Lett.*, vol. 11, no. 3, pp. 1276–1279, Mar. 2011, doi: 10.1021/nl104316t.
[35] M. Heurlin, O. Hultin, K. Storm, D. Lindgren, M. T. Borgström, and L. Samuelson, "Synthesis of Doped InP Core–Shell Nanowires Evaluated Using Hall Effect Measurements," *Nano Lett.*, vol. 14, no. 2, pp. 749–753, Feb. 2014, doi: 10.1021/nl404039d.
[36] K. Tomioka *et al.*, "Selective-area growth of III-V nanowires and their applications," *J. Mater. Res.*, vol. 26, no. 17, pp. 2127–2141, Sep. 2011, doi: 10.1557/jmr.2011.103.
[37] S. D. Hersee, X. Sun, and X. Wang, "The Controlled Growth of GaN Nanowires," *Nano Lett.*, vol. 6, no. 8, pp. 1808–1811, Aug. 2006, doi: 10.1021/nl060553t.
[38] C. H. Joyner, "Chapter 5 - Advances in Semiconductor Laser Growth and Fabrication Technology," in *Optical Fiber Telecommunications IIIB (Third Edition)*, I. P. Kaminow and T. L. Koch, Eds., Boston: Academic Press, 1997, pp. 163–199. doi: 10.1016/B978-0-08-051317-1.50009-7.
[39] M. Yao *et al.*, "GaAs Nanowire Array Solar Cells with Axial p–i–n Junctions," *Nano Lett.*, vol. 14, no. 6, pp. 3293–3303, Jun. 2014, doi: 10.1021/nl500704r.
[40] D. S. Hobbs, B. D. MacLeod, and J. R. Riccobono, "Update on the development of high performance anti-reflecting surface relief micro-structures," in *Window and Dome Technologies and Materials X*, International Society for Optics and Photonics, May 2007, p. 65450Y. doi: 10.1117/12.720672.

[41] E. Yablonovitch and G. D. Cody, “Intensity enhancement in textured optical sheets for solar cells,” *IEEE Trans. Electron Devices*, vol. 29, no. 2, pp. 300–305, Feb. 1982, doi: 10.1109/T-ED.1982.20700.
[42] N. Anttu, “Nanophotonics in absorbing III-V nanowire arrays,” p. 81, 2013.
[43] E. C. Garnett, M. L. Brongersma, Y. Cui, and M. D. McGehee, “Nanowire Solar Cells,” *Annu. Rev. Mater. Res.*, vol. 41, no. 1, pp. 269–295, 2011, doi: 10.1146/annurev-matsci-062910-100434.
[44] N. Anttu, “Absorption of Light in Vertical III-V Semiconductor Nanowires for Solar Cell and Photodetector Applications,” *Crystals*, vol. 13, no. 9, p. 13091292, Aug. 2023, doi: 10.3390/cryst13091292.
[45] N. Anttu, “Nanophotonics in absorbing III-V nanowire arrays,” Lund University, 2013.
[46] Y. Hu, R. R. LaPierre, M. Li, K. Chen, and J.-J. He, “Optical characteristics of GaAs nanowire solar cells,” *J. Appl. Phys.*, vol. 112, no. 10, p. 104311, Nov. 2012, doi: 10.1063/1.4764927.
[47] N. Huang, C. Lin, and M. L. Povinelli, “Broadband absorption of semiconductor nanowire arrays for photovoltaic applications,” *J. Opt.*, vol. 14, no. 2, p. 024004, Jan. 2012, doi: 10.1088/2040-8978/14/2/024004.
[48] N. Anttu, “Physics and design for 20% and 25% efficiency nanowire array solar cells,” *Nanotechnology*, vol. 30, no. 7, p. 074002, Dec. 2018, doi: 10.1088/1361-6528/aaf3f5.
[49] K. T. Fountaine, W.-H. Cheng, C. R. Bukowsky, and H. A. Atwater, “Near-Unity Unselective Absorption in Sparse InP Nanowire Arrays,” *ACS Photonics*, vol. 3, no. 10, pp. 1826–1832, Oct. 2016, doi: 10.1021/acsphotonics.6b00341.
[50] N. Anttu, “Geometrical optics, electrostatics, and nanophotonic resonances in absorbing nanowire arrays,” *Opt. Lett.*, vol. 38, no. 5, pp. 730–732, Mar. 2013, doi: 10.1364/OL.38.000730.
[51] A. W. Snyder and J. Love, *Optical Waveguide Theory*. Springer Science & Business Media, 1983.
[52] D. J. Traviss, M. K. Schmidt, J. Aizpurua, and O. L. Muskens, “Antenna resonances in low aspect ratio semiconductor nanowires,” *Opt. Express*, vol. 23, no. 17, pp. 22771–22787, Aug. 2015, doi: 10.1364/OE.23.022771.
[53] K. Seo *et al.*, “Multicolored Vertical Silicon Nanowires,” *Nano Lett.*, vol. 11, no. 4, pp. 1851–1856, Apr. 2011, doi: 10.1021/nl200201b.
[54] J. Svensson, N. Anttu, N. Vainorius, B. M. Borg, and L.-E. Wernersson, “Diameter-Dependent Photocurrent in InAsSb Nanowire Infrared Photodetectors,” *Nano Lett.*, vol. 13, no. 4, pp. 1380–1385, Apr. 2013, doi: 10.1021/nl303751d.
[55] N. Anttu, “Absorption of light in a single vertical nanowire and a nanowire array,” *Nanotechnology*, vol. 30, no. 10, p. 104004, Jan. 2019, doi: 10.1088/1361-6528/aafa5c.
[56] N. Anttu *et al.*, “Absorption of light in InP nanowire arrays,” *Nano Res.*, vol. 7, no. 6, pp. 816–823, Jun. 2014, doi: 10.1007/s12274-014-0442-y.
[57] G. Otnes and M. T. Borgström, “Towards high efficiency nanowire solar cells,” *Nano Today*, vol. 12, pp. 31–45, Feb. 2017, doi: 10.1016/j.nantod.2016.10.007.

[58] K. M. Azizur-Rahman and R. R. LaPierre, “Wavelength-selective absorptance in GaAs, InP and InAs nanowire arrays,” *Nanotechnology*, vol. 26, no. 29, p. 295202, Jul. 2015, doi: 10.1088/0957-4484/26/29/295202.
[59] B. E. A. Saleh and M. Carl Teich, *Fundamentals of Photonics*. Wiley, 2007.
[60] A. Konar *et al.*, “Carrier Transport in High Mobility InAs Nanowire Junctionless Transistors,” *Nano Lett.*, vol. 15, no. 3, pp. 1684–1690, Mar. 2015, doi: 10.1021/nl5043165.
[61] V. Jain *et al.*, “Study of photocurrent generation in InP nanowire-based p+-i-n+ photodetectors,” *Nano Res.*, vol. 7, no. 4, pp. 544–552, Apr. 2014, doi: 10.1007/s12274-014-0422-2.
[62] Y. Zhang and H. Liu, “Nanowires for High-Efficiency, Low-Cost Solar Photovoltaics,” *Crystals*, vol. 9, no. 2, Art. no. 2, Feb. 2019, doi: 10.3390/cryst9020087.
[63] B. M. Kayes, H. A. Atwater, and N. S. Lewis, “Comparison of the device physics principles of planar and radial p-n junction nanorod solar cells,” *J. Appl. Phys.*, vol. 97, no. 11, p. 114302, May 2005, doi: 10.1063/1.1901835.
[64] G. Leilei, “Semiconductor Nanowire Array-Based Photodetectors,” PhD Thesis, Hong Kong University of Science and Technology, 2016.
[65] C. L. Tan and H. Mohseni, “Emerging technologies for high performance infrared detectors,” *Nanophotonics*, vol. 7, no. 1, pp. 169–197, 2018, doi: 10.1515/nanoph-2017-0061.
[66] Pik-Yiu Chan and J. D. Enderle, “Automatic door opener,” in *Proceedings of the IEEE 26th Annual Northeast Bioengineering Conference (Cat. No.00CH37114)*, Apr. 2000, pp. 139–140. doi: 10.1109/NEBC.2000.842418.
[67] K. Kato, A. Kozen, Y. Muramoto, Y. Itaya, T. Nagatsuma, and M. Yaita, “110-GHz, 50%-efficiency mushroom-mesa waveguide p-i-n photodiode for a 1.55-μm wavelength,” *IEEE Photonics Technol. Lett.*, vol. 6, no. 6, pp. 719–721, Jun. 1994, doi: 10.1109/68.300173.
[68] S. Fedderwitz *et al.*, “Multigigabit 1.3μm GaNAsSb⁄GaAs Photodetectors,” *Appl. Phys. Lett.*, vol. 93, no. 3, p. 033509, Jul. 2008, doi: 10.1063/1.2960540.
[69] A. Rogalski, “Infrared detectors: an overview,” *Infrared Phys.*, p. 24, 2002.
[70] S. O. Kasap, *Optoelectronics and photonics: principles and practices*, 2nd ed. Boston: Pearson, 2013.
[71] L. VJ *et al.*, “A Perspective on Nanowire Photodetectors: Current Status, Future Challenges, and Opportunities,” *IEEE J. Sel. Top. Quantum Electron.*, vol. 17, no. 4, pp. 1002–1032, Jul. 2011, doi: 10.1109/JSTQE.2010.2093508.
[72] W. Herschel, “XIV. Experiments on the refrangibility of the invisible rays of the sun,” *Philos. Trans. R. Soc. Lond.*, vol. 90, pp. 284–292, Jan. 1800, doi: 10.1098/rstl.1800.0015.
[73] G. Gaussorgues and S. Chomet, *Infrared Thermography*. Springer Science & Business Media, 2012.
[74] “Linden’s Handbook of Batteries 4th Edition by Thomas Reddy – Instant Reading.” Accessed: Dec. 10, 2018.
[75] V. Jain, “III-V Nanowire-based Infrared Photodetectors : Design, Fabrication and Characterization,” thesis/doccomp, Lund University, 2016. Accessed: Jun. 09, 2020.

[76] R. S. Quimby, “Photonics and Lasers: An Introduction,” in *Photonics and Lasers: An Introduction*, John Wiley & Sons, Ltd, 2006.
[77] X. Dai, M. Tchernycheva, and C. Soci, “Compound Semiconductor Nanowire Photodetectors,” in *Semiconductors and Semimetals*, vol. 94, Elsevier, 2016, pp. 75–107. doi: 10.1016/bs.semsem.2015.08.001.
[78] M. Razeghi, *Fundamentals of Solid State Engineering*. Springer Science & Business Media, 2002.
[79] K. S. Giboney, M. J. W. Rodwell, and J. E. Bowers, “Traveling-wave photodetector design and measurements,” *IEEE J. Sel. Top. Quantum Electron.*, vol. 2, no. 3, pp. 622–629, Sep. 1996, doi: 10.1109/2944.571760.
[80] K. Tanabe, K. Watanabe, and Y. Arakawa, “III-V/Si hybrid photonic devices by direct fusion bonding,” *Sci. Rep.*, vol. 2, Apr. 2012, doi: 10.1038/srep00349.
[81] X. Zhang *et al.*, “Giant UV photoresponse of a GaN nanowire photodetector through effective Pt nanoparticle coupling,” *J. Mater. Chem. C*, vol. 5, no. 17, pp. 4319–4326, 2017, doi: 10.1039/C7TC00594F.
[82] F.-X. Liang, J.-Z. Wang, Z.-P. Li, and L.-B. Luo, “Near-Infrared-Light Photodetectors Based on One-Dimensional Inorganic Semiconductor Nanostructures,” *Adv. Opt. Mater.*, vol. 5, no. 14, p. 1700081, 2017, doi: 10.1002/adom.201700081.
[83] H. Wang, “High gain single GaAs nanowire photodetector,” *Appl. Phys. Lett.*, vol. 103, no. 9, p. 093101, Aug. 2013, doi: 10.1063/1.4816246.
[84] H. Xia *et al.*, “Distinct Photocurrent Response of Individual GaAs Nanowires Induced by n-Type Doping,” *ACS Nano*, vol. 6, no. 7, pp. 6005–6013, Jul. 2012, doi: 10.1021/nn300962z.
[85] M. A. Seyedi, M. Yao, J. O’Brien, S. Y. Wang, and P. D. Dapkus, “Large area, low capacitance, GaAs nanowire photodetector with a transparent Schottky collecting junction,” *Appl. Phys. Lett.*, vol. 103, no. 25, p. 251109, Dec. 2013, doi: 10.1063/1.4852136.
[86] L.-B. Luo *et al.*, “Near-Infrared Light Photovoltaic Detector Based on GaAs Nanocone Array/Monolayer Graphene Schottky Junction,” *Adv. Funct. Mater.*, vol. 24, no. 19, pp. 2794–2800, 2014, doi: 10.1002/adfm.201303368.
[87] C. L. Tan and H. Mohseni, “Emerging technologies for high performance infrared detectors,” *Nanophotonics*, vol. 7, no. 1, pp. 169–197, 2018, doi: 10.1515/nanoph-2017-0061.
[88] M. D. Thompson *et al.*, “Low Leakage-Current InAsSb Nanowire Photodetectors on Silicon,” *Nano Lett.*, vol. 16, no. 1, pp. 182–187, Jan. 2016, doi: 10.1021/acs.nanolett.5b03449.
[89] A. C. Farrell, W.-J. Lee, P. Senanayake, M. A. Haddad, S. V. Prikhodko, and D. L. Huffaker, “High-Quality InAsSb Nanowires Grown by Catalyst-Free Selective-Area Metal–Organic Chemical Vapor Deposition,” *Nano Lett.*, vol. 15, no. 10, pp. 6614–6619, Oct. 2015, doi: 10.1021/acs.nanolett.5b02389.
[90] D. Ren *et al.*, “Room-Temperature Midwavelength Infrared InAsSb Nanowire Photodetector Arrays with Al $_2$ O $_3$ Passivation,” *Nano Lett.*, p. acs.nanolett.8b04420, Jan. 2019, doi: 10.1021/acs.nanolett.8b04420.

[91] U. Otuonye, H. W. Kim, and W. D. Lu, “Ge nanowire photodetector with high photoconductive gain epitaxially integrated on Si substrate,” *Appl. Phys. Lett.*, vol. 110, no. 17, p. 173104, Apr. 2017, doi: 10.1063/1.4982648.
[92] K. Chiba, A. Yoshida, K. Tomioka, and J. Motohisa, “Vertical InGaAs Nanowire Array Photodiodes on Si,” *ACS Photonics*, vol. 6, no. 2, pp. 260–264, Feb. 2019, doi: 10.1021/acsphotonics.8b01089.
[93] “Organometallic Vapor-Phase Epitaxy - 2nd Edition.” Accessed: Aug. 30, 2023.
[94] K. Ploog, “Molecular Beam Epitaxy of III-V Compounds: Technology and Growth Process,” *Annu. Rev. Mater. Sci.*, vol. 11, no. 1, pp. 171–210, 1981, doi: 10.1146/annurev.ms.11.080181.001131.
[95] A. G. Thompson, “MOCVD technology for semiconductors,” *Mater. Lett.*, vol. 30, no. 4, pp. 255–263, Mar. 1997, doi: 10.1016/S0167-577X(96)00215-7.
[96] E. Hecht, *Optics*. Addison-Wesley, 2002.
[97] L. Reimer, *Scanning Electron Microscopy: Physics of Image Formation and Microanalysis*, vol. 45. in Springer Series in Optical Sciences, vol. 45. Berlin, Heidelberg: Springer, 1998. doi: 10.1007/978-3-540-38967-5.
[98] D. B. Williams and C. B. Carter, *Transmission Electron Microscopy: A Textbook for Materials Science*. Springer Science & Business Media, 2009.
[99] R. F. Egerton, *Physical Principles of Electron Microscopy*. Boston, MA: Springer US, 2005. doi: 10.1007/b136495.
[100] P. W. Hawkes and E. Kasper, *Principles of Electron Optics: Wave Optics*. Academic Press, 1996.
[101] D. K. Schroder, *Semiconductor Material and Device Characterization*. John Wiley & Sons, 2005.
[102] C. B. Carter and D. B. Williams, Eds., *Transmission Electron Microscopy*. Cham: Springer International Publishing, 2016. doi: 10.1007/978-3-319-26651-0.
[103] J. Bernardi, “Energy-dispersive X-ray spectroscopy,” in *Imaging Modalities for Biological and Preclinical Research: A Compendium, Volume 1: Part I: Ex vivo biological imaging*, IOP Publishing, 2021. doi: 10.1088/978-0-7503-3059-6ch41.
[104] B. Voigtländer, *Atomic Force Microscopy*. in NanoScience and Technology. Cham: Springer International Publishing, 2019. doi: 10.1007/978-3-030-13654-3.
[105] V. J. Logeeswaran *et al.*, “A Perspective on Nanowire Photodetectors: Current Status, Future Challenges, and Opportunities,” *IEEE J. Sel. Top. Quantum Electron.*, vol. 17, no. 4, pp. 1002–1032, Jul. 2011, doi: 10.1109/JSTQE.2010.2093508.
[106] B. Tian *et al.*, “Coaxial silicon nanowires as solar cells and nanoelectronic power sources,” *Nature*, vol. 449, no. 7164, pp. 885–889, Oct. 2007, doi: 10.1038/nature06181.
[107] R. Yan, D. Gargas, and P. Yang, “Nanowire photonics,” *Nat. Photonics*, vol. 3, no. 10, Art. no. 10, Oct. 2009, doi: 10.1038/nphoton.2009.184.
[108] M. T. Björk *et al.*, “One-dimensional Steeplechase for Electrons Realized,” *Nano Lett.*, vol. 2, no. 2, pp. 87–89, Feb. 2002, doi: 10.1021/nl010099n.
[109] G. Kästner † and U. Gösele, “Stress and dislocations at cross-sectional heterojunctions in a cylindrical nanowire,” *Philos. Mag.*, vol. 84, no. 35, pp. 3803–3824, Dec. 2004, doi: 10.1080/14786430420002813 89.

[110] R. Könenkamp, R. C. Word, and C. Schlegel, “Vertical nanowire light-emitting diode,” *Appl. Phys. Lett.*, vol. 85, no. 24, pp. 6004–6006, Dec. 2004, doi: 10.1063/1.1836873.
[111] C. K. Chan, X. F. Zhang, and Y. Cui, “High Capacity Li Ion Battery Anodes Using Ge Nanowires,” *Nano Lett.*, vol. 8, no. 1, pp. 307–309, Jan. 2008, doi: 10.1021/nl0727157.
[112] A. Nadarajah, R. C. Word, J. Meiss, and R. Könenkamp, “Flexible Inorganic Nanowire Light-Emitting Diode,” *Nano Lett.*, vol. 8, no. 2, pp. 534–537, Feb. 2008, doi: 10.1021/nl072784l.
[113] J.-H. Seo, E. Swinnich, Y.-Y. Zhang, and M. Kim, “Low dimensional freestanding semiconductors for flexible optoelectronics: materials, synthesis, process, and applications,” *Mater. Res. Lett.*, vol. 8, no. 4, pp. 123–144, Apr. 2020, doi: 10.1080/21663831.2020.1718231.
[114] N. Guan *et al.*, “Flexible White Light Emitting Diodes Based on Nitride Nanowires and Nanophosphors,” *ACS Photonics*, vol. 3, no. 4, pp. 597–603, Apr. 2016, doi: 10.1021/acsphotonics.5b00696.
[115] S. Mokkapati, D. Saxena, H. H. Tan, and C. Jagadish, “Optical design of nanowire absorbers for wavelength selective photodetectors,” *Sci. Rep.*, vol. 5, no. 1, p. 15339, Dec. 2015, doi: 10.1038/srep15339.
[116] R. S. Wagner and W. C. Ellis, “Vapor-liquid-solid mechanism of single crystal growth,” *Appl. Phys. Lett.*, vol. 4, no. 5, pp. 89–90, Mar. 1964, doi: 10.1063/1.1753975.
[117] P. Caroff, J. Bolinsson, and J. Johansson, “Crystal Phases in III–V Nanowires: From Random Toward Engineered Polytypism,” *IEEE J. Sel. Top. Quantum Electron.*, vol. 17, no. 4, pp. 829–846, Jul. 2011, doi: 10.1109/JSTQE.2010.2070790.
[118] J. Bolinsson, P. Caroff, B. Mandl, and K. A. Dick, “Wurtzite–zincblende superlattices in InAs nanowires using a supply interruption method,” *Nanotechnology*, vol. 22, no. 26, p. 265606, May 2011, doi: 10.1088/0957-4484/22/26/265606.
[119] P. K. Mohseni and R. R. LaPierre, “A growth interruption technique for stacking fault-free nanowire superlattices,” *Nanotechnology*, vol. 20, no. 2, p. 025610, Dec. 2008, doi: 10.1088/0957-4484/20/2/025610.
[120] D. L. Dheeraj *et al.*, “Growth and Characterization of Wurtzite GaAs Nanowires with Defect-Free Zinc Blende GaAsSb Inserts,” *Nano Lett.*, vol. 8, no. 12, pp. 4459–4463, Dec. 2008, doi: 10.1021/nl802406d.
[121] Y.-N. Guo *et al.*, “Phase Separation Induced by Au Catalysts in Ternary InGaAs Nanowires,” *Nano Lett.*, vol. 13, no. 2, pp. 643–650, Feb. 2013, doi: 10.1021/nl304237b.
[122] J. E. Allen *et al.*, “High-resolution detection of Au catalyst atoms in Si nanowires,” *Nat. Nanotechnol.*, vol. 3, no. 3, Art. no. 3, Mar. 2008, doi: 10.1038/nnano.2008.5.
[123] K. A. Dick, J. Bolinsson, B. M. Borg, and J. Johansson, “Controlling the Abruptness of Axial Heterojunctions in III–V Nanowires: Beyond the Reservoir Effect,” *Nano Lett.*, vol. 12, no. 6, pp. 3200–3206, Jun. 2012, doi: 10.1021/nl301185x.
[124] V. G. Dubrovskii and N. V. Sibirev, “Factors Influencing the Interfacial Abruptness in Axial III–V Nanowire Heterostructures,” *Cryst. Growth Des.*, vol. 16, no. 4, pp. 2019–2023, Apr. 2016, doi: 10.1021/acs.cgd.5b01613.

[125] N. Anttu, V. Dagytė, X. Zeng, G. Otnes, and M. Borgström, "Absorption and transmission of light in III–V nanowire arrays for tandem solar cell applications," *Nanotechnology*, vol. 28, no. 20, p. 205203, May 2017, doi: 10.1088/1361-6528/aa6aee.
[126] E. Barrigón *et al.*, "GaAs Nanowire pn-Junctions Produced by Low-Cost and High-Throughput Aerotaxy," *Nano Lett.*, vol. 18, no. 2, pp. 1088–1092, Feb. 2018, doi: 10.1021/acs.nanolett.7b04609.
[127] M. Heurlin *et al.*, "Continuous gas-phase synthesis of nanowires with tunable properties," *Nature*, vol. 492, no. 7427, pp. 90–94, Dec. 2012, doi: 10.1038/nature11652.
[128] A. L. Roest, M. A. Verheijen, O. Wunnicke, S. Serafin, H. Wondergem, and E. P. A. M. Bakkers, "Position-controlled epitaxial III–V nanowires on silicon," *Nanotechnology*, vol. 17, no. 11, pp. S271–S275, May 2006, doi: 10.1088/0957-4484/17/11/S07.
[129] P. K. Mohseni, C. Maunders, G. A. Botton, and R. R. LaPierre, "GaP/GaAsP/GaP core–multishell nanowire heterostructures on (111) silicon," *Nanotechnology*, vol. 18, no. 44, p. 445304, Oct. 2007, doi: 10.1088/0957-4484/18/44/445304.
[130] G. Barbillon, F. Hamouda, and B. Bartenlian, "Large Surface Nanostructuring by Lithographic Techniques for Bioplasmonic Applications," in *Manufacturing Nanostructures*, One Central Press, 2014, pp. 244–262.
[131] R. Md. M. Hasan and X. Luo, "Promising Lithography Techniques for Next-Generation Logic Devices," *Nanomanufacturing Metrol.*, vol. 1, no. 2, pp. 67–81, Jun. 2018, doi: 10.1007/s41871-018-0016-9.
[132] S. Hertenberger, D. Rudolph, M. Bichler, J. J. Finley, G. Abstreiter, and G. Koblmüller, "Growth kinetics in position-controlled and catalyst-free InAs nanowire arrays on Si(111) grown by selective area molecular beam epitaxy," *J. Appl. Phys.*, vol. 108, no. 11, p. 114316, Dec. 2010, doi: 10.1063/1.3525610.
[133] G. Koblmüller *et al.*, "Self-induced growth of vertical free-standing InAs nanowires on Si(111) by molecular beam epitaxy," *Nanotechnology*, vol. 21, no. 36, p. 365602, Sep. 2010, doi: 10.1088/0957-4484/21/36/365602.
[134] J. C. Shin *et al.*, "In $_x$ Ga $_{1-x}$ As Nanowires on Silicon: One-Dimensional Heterogeneous Epitaxy, Bandgap Engineering, and Photovoltaics," *Nano Lett.*, vol. 11, no. 11, pp. 4831–4838, Nov. 2011, doi: 10.1021/nl202676b.
[135] J. C. Shin *et al.*, "Wafer-Scale Production of Uniform InAs $_y$ P $_{1-y}$ Nanowire Array on Silicon for Heterogeneous Integration," *ACS Nano*, vol. 7, no. 6, pp. 5463–5471, Jun. 2013, doi: 10.1021/nn4014774.
[136] W. Wei, X.-Y. Bao, C. Soci, Y. Ding, Z.-L. Wang, and D. Wang, "Direct Heteroepitaxy of Vertical InAs Nanowires on Si Substrates for Broad Band Photovoltaics and Photodetection," *Nano Lett.*, vol. 9, no. 8, pp. 2926–2934, Aug. 2009, doi: 10.1021/nl901270n.
[137] Y. Jing *et al.*, "Catalyst-Free Heteroepitaxial MOCVD Growth of InAs Nanowires on Si Substrates," *J. Phys. Chem. C*, vol. 118, no. 3, pp. 1696–1705, Jan. 2014, doi: 10.1021/jp406428z.
[138] A. C. Farrell, W.-J. Lee, P. Senanayake, M. A. Haddad, S. V. Prikhodko, and D. L. Huffaker, "High-Quality InAsSb Nanowires Grown by Catalyst-Free Selective-Area

Metal–Organic Chemical Vapor Deposition," *Nano Lett.*, vol. 15, no. 10, pp. 6614–6619, Oct. 2015, doi: 10.1021/acs.nanolett.5b02389.
[139] M. T. Björk, H. Schmid, C. M. Breslin, L. Gignac, and H. Riel, "InAs nanowire growth on oxide-masked ⟨111⟩ silicon," *J. Cryst. Growth*, vol. 344, no. 1, pp. 31–37, Apr. 2012, doi: 10.1016/j.jcrysgro.2012.01.052.
[140] K. Tomioka, J. Motohisa, S. Hara, and T. Fukui, "Control of InAs Nanowire Growth Directions on Si," *Nano Lett.*, vol. 8, no. 10, pp. 3475–3480, Oct. 2008, doi: 10.1021/nl802398j.
[141] K. Tomioka, T. Tanaka, S. Hara, K. Hiruma, and T. Fukui, "III–V Nanowires on Si Substrate: Selective-Area Growth and Device Applications," *IEEE J. Sel. Top. Quantum Electron.*, vol. 17, no. 4, pp. 1112–1129, Jul. 2011, doi: 10.1109/JSTQE.2010.2068280.
[142] V. G. Dubrovskii, W. Kim, V. Piazza, L. Güniat, and A. Fontcuberta i Morral, "Simultaneous Selective Area Growth of Wurtzite and Zincblende Self-Catalyzed GaAs Nanowires on Silicon," *Nano Lett.*, vol. 21, no. 7, pp. 3139–3145, Apr. 2021, doi: 10.1021/acs.nanolett.1c00349.
[143] Q. Gao *et al.*, "Simultaneous Selective-Area and Vapor–Liquid–Solid Growth of InP Nanowire Arrays," *Nano Lett.*, vol. 16, no. 7, pp. 4361–4367, Jul. 2016, doi: 10.1021/acs.nanolett.6b01461.
[144] P. K. Mohseni *et al.*, "InxGa1–xAs Nanowire Growth on Graphene: van der Waals Epitaxy Induced Phase Segregation," *Nano Lett.*, vol. 13, no. 3, pp. 1153–1161, Mar. 2013, doi: 10.1021/nl304569d.
[145] J. S. Ward *et al.*, "Techno-economic analysis of three different substrate removal and reuse strategies for III-V solar cells," *Prog. Photovolt. Res. Appl.*, vol. 24, no. 9, pp. 1284–1292, 2016, doi: 10.1002/pip.2776.
[146] C.-W. Cheng, K.-T. Shiu, N. Li, S.-J. Han, L. Shi, and D. K. Sadana, "Epitaxial lift-off process for gallium arsenide substrate reuse and flexible electronics," *Nat. Commun.*, vol. 4, no. 1, p. 1577, Mar. 2013, doi: 10.1038/ncomms2583.
[147] J. M. Spurgeon, K. E. Plass, B. M. Kayes, B. S. Brunschwig, H. A. Atwater, and N. S. Lewis, "Repeated epitaxial growth and transfer of arrays of patterned, vertically aligned, crystalline Si wires from a single Si(111) substrate," *Appl. Phys. Lett.*, vol. 93, no. 3, p. 032112, Jul. 2008, doi: 10.1063/1.2959184.
[148] K. R. Williams, K. Gupta, and M. Wasilik, "Etch rates for micromachining processing-Part II," *J. Microelectromechanical Syst.*, vol. 12, no. 6, pp. 761–778, Dec. 2003, doi: 10.1109/JMEMS.2003.820936.
[149] Z. Liu *et al.*, "Correlation between surface reconstruction and polytypism in InAs nanowire selective area epitaxy," *Phys. Rev. Mater.*, vol. 1, no. 7, p. 074603, Dec. 2017, doi: 10.1103/PhysRevMaterials.1.074603.
[150] K. Tomioka, F. Izhizaka, and T. Fukui, "Selective-Area Growth of InAs Nanowires on Ge and Vertical Transistor Application," *Nano Lett.*, vol. 15, no. 11, pp. 7253–7257, Nov. 2015, doi: 10.1021/acs.nanolett.5b02165.
[151] M. A. Baboli *et al.*, "Improving pseudo-van der Waals epitaxy of self-assembled InAs nanowires on graphene via MOCVD parameter space mapping," *CrystEngComm*, vol. 21, no. 4, pp. 602–615, 2019, doi: 10.1039/C8CE01666F.

[152] M. A. Baboli *et al.*, "Mixed-dimensional InAs nanowire on layered molybdenum disulfide heterostructures via selective-area van der Waals epitaxy," *Nanoscale Adv.*, vol. 3, no. 10, pp. 2802–2811, 2021, doi: 10.1039/D0NA00768D.
[153] B. Wang and P. W. Leu, "Tunable and selective resonant absorption in vertical nanowires," *Opt. Lett.*, vol. 37, no. 18, p. 3756, Sep. 2012, doi: 10.1364/OL.37.003756.
[154] M. Aghaeipour, N. Anttu, G. Nylund, L. Samuelson, S. Lehmann, and M.-E. Pistol, "Tunable absorption resonances in the ultraviolet for InP nanowire arrays," *Opt. Express*, vol. 22, no. 23, pp. 29204–29212, Nov. 2014, doi: 10.1364/OE.22.029204.
[155] A. Cavalli, A. Dijkstra, J. E. M. Haverkort, and E. P. A. M. Bakkers, "Nanowire polymer transfer for enhanced solar cell performance and lower cost," *Nano-Struct. Nano-Objects*, vol. 16, pp. 59–62, Oct. 2018, doi: 10.1016/j.nanoso.2018.03.014.
[156] Y. Zhang, L. Hrachowina, E. Barrigon, I. Åberg, and M. Borgström, "Self-Limiting Polymer Exposure for Vertical Processing of Semiconductor Nanowire-Based Flexible Electronics," *ACS Appl. Nano Mater.*, vol. 3, no. 8, pp. 7743–7749, Aug. 2020, doi: 10.1021/acsanm.0c01314.
[157] R. J. Jam *et al.*, "Embedded sacrificial AlAs segments in GaAs nanowires for substrate reuse," *Nanotechnology*, vol. 31, no. 20, p. 204002, Feb. 2020, doi: 10.1088/1361-6528/ab7680.
[158] X. Li *et al.*, "Vertical nanowire array-based biosensors: device design strategies and biomedical applications," *J. Mater. Chem. B*, vol. 8, no. 34, pp. 7609–7632, 2020, doi: 10.1039/D0TB00990C.
[159] A. D. Mallorquí *et al.*, "Characterization and analysis of InA *s* / *p* –Si heterojunction nanowire-based solar cell," *J. Phys. Appl. Phys.*, vol. 47, no. 39, p. 394017, Oct. 2014, doi: 10.1088/0022-3727/47/39/394017.
[160] P. M. Wu, N. Anttu, H. Q. Xu, L. Samuelson, and M.-E. Pistol, "Colorful InAs Nanowire Arrays: From Strong to Weak Absorption with Geometrical Tuning," *Nano Lett.*, vol. 12, no. 4, pp. 1990–1995, Apr. 2012, doi: 10.1021/nl204552v.
[161] Y. H. Song *et al.*, "Position Control of Self-Grown III–V Nanowire Arrays on Si Substrates via Micrometer-Size Patterns by Photolithography," *Cryst. Growth Des.*, vol. 22, no. 4, pp. 2266–2271, Apr. 2022, doi: 10.1021/acs.cgd.1c01351.
[162] N. Anttu and H. Q. Xu, "Coupling of light into nanowire arrays and subsequent absorption," *J. Nanosci. Nanotechnol.*, vol. 10, no. 11, pp. 7183–7187, Nov. 2010, doi: 10.1166/jnn.2010.2907.
[163] M. Heiss *et al.*, "III–V nanowire arrays: growth and light interaction," *Nanotechnology*, vol. 25, no. 1, p. 014015, Jan. 2014, doi: 10.1088/0957-4484/25/1/014015.
[164] A. Fedorenko, M. A. Baboli, P. K. Mohseni, and S. M. Hubbard, "Design and Simulation of the Bifacial III-V-Nanowire-on-Si Solar Cell," *MRS Adv.*, vol. 4, no. 16, pp. 929–936, ed 2019, doi: 10.1557/adv.2019.127.
[165] F. Giubileo, A. D. Bartolomeo, Y. Zhong, S. Zhao, and M. Passacantando, "Field emission from AlGaN nanowires with low turn-on field," *Nanotechnology*, vol. 31, no. 47, p. 475702, Aug. 2020, doi: 10.1088/1361-6528/abaf22.
[166] Z. Liu *et al.*, "High-detectivity InAs nanowire photodetectors with spectral response from ultraviolet to near-infrared," *Nano Res.*, vol. 6, no. 11, pp. 775–783, Nov. 2013, doi: 10.1007/s12274-013-0356-0.

[167] H. Wook Shin *et al.*, "Short-wavelength infrared photodetector on Si employing strain-induced growth of very tall InAs nanowire arrays," *Sci. Rep.*, vol. 5, no. 1, p. 10764, Sep. 2015, doi: 10.1038/srep10764.
[168] M. Karimi *et al.*, "Room-temperature InP/InAsP Quantum Discs-in-Nanowire Infrared Photodetectors," *Nano Lett.*, vol. 17, no. 6, pp. 3356–3362, Jun. 2017, doi: 10.1021/acs.nanolett.6b05114.
[169] D. Ren, Z. Rong, K. M. Azizur-Rahman, S. Somasundaram, M. Shahili, and D. L. Huffaker, "Feasibility of achieving high detectivity at short- and mid-wavelength infrared using nanowire-plasmonic photodetectors with p–n heterojunctions," *Nanotechnology*, vol. 30, no. 4, p. 044002, Nov. 2018, doi: 10.1088/1361-6528/aaed5c.
[170] A. Fedorenko, M. A. Baboli, P. K. Mohseni, and S. M. Hubbard, "Towards High-Efficiency Triple-Junction Bifacial III-V Nanowire-on-Silicon Solar Cells: Design Approaches Enabling the Concept," in *2019 IEEE 46th Photovoltaic Specialists Conference (PVSC)*, Jun. 2019, pp. 3191–3194. doi: 10.1109/PVSC40753.2019.8981265.
[171] N. Gagrani, K. Vora, L. Fu, C. Jagadish, and H. H. Tan, "Flexible InP–ZnO nanowire heterojunction light emitting diodes," *Nanoscale Horiz.*, vol. 7, no. 4, pp. 446–454, Mar. 2022, doi: 10.1039/D1NH00535A.
[172] M. G. Moharam and T. K. Gaylord, "Rigorous coupled-wave analysis of planar-grating diffraction," *JOSA*, vol. 71, no. 7, pp. 811–818, Jul. 1981, doi: 10.1364/JOSA.71.000811.
[173] M. G. Moharam and T. K. Gaylord, "Three-dimensional vector coupled-wave analysis of planar-grating diffraction," *JOSA*, vol. 73, no. 9, pp. 1105–1112, Sep. 1983, doi: 10.1364/JOSA.73.001105.
[174] C.-H. Lin, K. M. Leung, and T. Tamir, "Modal transmission-line theory of three-dimensional periodic structures with arbitrary lattice configurations," *JOSA A*, vol. 19, no. 10, pp. 2005–2017, Oct. 2002, doi: 10.1364/JOSAA.19.002005.
[175] M. G. Moharam, E. B. Grann, D. A. Pommet, and T. K. Gaylord, "Formulation for stable and efficient implementation of the rigorous coupled-wave analysis of binary gratings," *JOSA A*, vol. 12, no. 5, pp. 1068–1076, May 1995, doi: 10.1364/JOSAA.12.001068.
[176] L. Li, "Multilayer modal method for diffraction gratings of arbitrary profile, depth, and permittivity," *JOSA A*, vol. 10, no. 12, pp. 2581–2591, Dec. 1993, doi: 10.1364/JOSAA.10.002581.
[177] N. Anttu, H. Mäntynen, A. Sorokina, J. Turunen, T. Sadi, and H. Lipsanen, "Applied electromagnetic optics simulations for nanophotonics," *J. Appl. Phys.*, vol. 129, no. 13, p. 131102, Apr. 2021, doi: 10.1063/5.0041275.
[178] N. Anttu, H. Mäntynen, T. Sadi, A. Matikainen, J. Turunen, and H. Lipsanen, "Comparison of absorption simulation in semiconductor nanowire and nanocone arrays with the Fourier modal method, the finite element method, and the finite-difference time-domain method," *Nano Express*, vol. 1, no. 3, p. 030034, Dec. 2020, doi: 10.1088/2632-959X/abd0d6.
[179] M. P. Mikhailova, K. D. Moiseev, and Y. P. Yakovlev, "Interface-induced optical and transport phenomena in type II broken-gap single heterojunctions," *Semicond.*

Sci. Technol., vol. 19, no. 10, pp. R109–R128, Sep. 2004, doi: 10.1088/0268-1242/19/10/R03.
[180] F. Wang *et al.*, "Band structure engineered tunneling heterostructures for high-performance visible and near-infrared photodetection," *Sci. China Mater.*, vol. 63, no. 8, pp. 1537–1547, Aug. 2020, doi: 10.1007/s40843-020-1353-3.
[181] I. Vurgaftman, M. P. Lumb, and J. R. Meyer, *Bands and Photons in III-V Semiconductor Quantum Structures*. in Series on Semiconductor Science and Technology. Oxford: Oxford University Press, 2020. doi: 10.1093/oso/9780198767275.001.0001.
[182] J. R. D'Rozario, S. J. Polly, G. T. Nelson, D. Wilt, and S. M. Hubbard, "Modeling free-carrier absorption in ultrathin III-V solar cells with light management," *Opt. Express*, vol. 30, no. 5, pp. 7096–7109, Feb. 2022, doi: 10.1364/OE.452170.
[183] K. T. Fountaine, C. G. Kendall, and H. A. Atwater, "Near-unity broadband absorption designs for semiconducting nanowire arrays via localized radial mode excitation," *Opt. Express*, vol. 22, no. 103, pp. A930–A940, May 2014, doi: 10.1364/OE.22.00A930.
[184] K. M. Azizur-Rahman and R. R. LaPierre, "Optical design of a mid-wavelength infrared InSb nanowire photodetector," *Nanotechnology*, vol. 27, no. 31, p. 315202, Aug. 2016, doi: 10.1088/0957-4484/27/31/315202.
[185] D. Ren *et al.*, "Uncooled Photodetector at Short-Wavelength Infrared Using InAs Nanowire Photoabsorbers on InP with p–n Heterojunctions," *Nano Lett.*, vol. 18, no. 12, pp. 7901–7908, Dec. 2018, doi: 10.1021/acs.nanolett.8b03775.
[186] L. Cao, J. S. White, J.-S. Park, J. A. Schuller, B. M. Clemens, and M. L. Brongersma, "Engineering light absorption in semiconductor nanowire devices," *Nat. Mater.*, vol. 8, no. 8, pp. 643–647, Aug. 2009, doi: 10.1038/nmat2477.
[187] S. A. Mann and E. C. Garnett, "Extreme Light Absorption in Thin Semiconductor Films Wrapped around Metal Nanowires," *Nano Lett.*, vol. 13, no. 7, pp. 3173–3178, Jul. 2013, doi: 10.1021/nl401179h.
[188] N. Anttu and H. Q. Xu, "Scattering matrix method for optical excitation of surface plasmons in metal films with periodic arrays of subwavelength holes," *Phys. Rev. B*, vol. 83, no. 16, p. 165431, Apr. 2011, doi: 10.1103/PhysRevB.83.165431.
[189] L. Namazi, M. Nilsson, S. Lehmann, C. Thelander, and K. A. Dick, "Selective GaSb radial growth on crystal phase engineered InAs nanowires," *Nanoscale*, vol. 7, no. 23, pp. 10472–10481, 2015, doi: 10.1039/C5NR01165E.
[190] Z. Li *et al.*, "Investigation of light–matter interaction in single vertical nanowires in ordered nanowire arrays," *Nanoscale*, vol. 14, no. 9, pp. 3527–3536, Mar. 2022, doi: 10.1039/D1NR08088A.
[191] H. Kim, H. Bae, T.-Y. Chang, and D. L. Huffaker, "III–V nanowires on silicon (100) as plasmonic-photonic hybrid meta-absorber," *Sci. Rep.*, vol. 11, no. 1, Art. no. 1, Jul. 2021, doi: 10.1038/s41598-021-93398-z.
[192] F. Snik *et al.*, "An overview of polarimetric sensing techniques and technology with applications to different research fields," in *Polarization: Measurement, Analysis, and Remote Sensing XI*, SPIE, May 2014, pp. 48–67. doi: 10.1117/12.2053245.
[193] L. Hrachowina, N. Anttu, and M. T. Borgström, "Wafer-Scale Synthesis and Optical Characterization of InP Nanowire Arrays for Solar Cells," *Nano Lett.*, vol. 21, no. 17, pp. 7347–7353, Sep. 2021, doi: 10.1021/acs.nanolett.1c02542.

[194] “Handbook of Sputter Deposition Technology - 2nd Edition.” Accessed: Oct. 31, 2023.
[195] C. Chen, M. C. Plante, C. Fradin, and R. R. LaPierre, “Layer-by-layer and step-flow growth mechanisms in GaAsP/GaP nanowire heterostructures,” *J. Mater. Res.*, vol. 21, no. 11, pp. 2801–2809, Nov. 2006, doi: 10.1557/jmr.2006.0341.
[196] C. B. Maliakkal *et al.*, “Independent Control of Nucleation and Layer Growth in Nanowires,” *ACS Nano*, vol. 14, no. 4, pp. 3868–3875, Apr. 2020, doi: 10.1021/acsnano.9b09816.
[197] Y. Liu, Y. Peng, J. Guo, D. La, and Z. Xu, “The effect of V/III ratio on the morphology and structure of GaAs nanowires by MOCVD,” *AIP Adv.*, vol. 8, no. 5, p. 055108, May 2018, doi: 10.1063/1.5028350.
[198] Z. Li *et al.*, “InAs nanowire arrays for room-temperature ultra-broadband infrared photodetection,” *Nanoscale*, vol. 15, no. 23, pp. 10033–10041, Jun. 2023, doi: 10.1039/D3NR00340J.
[199] K. Tomioka, P. Mohan, J. Noborisaka, S. Hara, J. Motohisa, and T. Fukui, “Growth of highly uniform InAs nanowire arrays by selective-area MOVPE,” *J. Cryst. Growth*, vol. 298, pp. 644–647, Jan. 2007, doi: 10.1016/j.jcrysgro.2006.10.183.
[200] K. Seshan, *Handbook of Thin Film Deposition*. William Andrew, 2012.
[201] T. Shitara, J. H. Neave, and B. A. Joyce, “Reflection high-energy electron diffraction intensity oscillations and anisotropy on vicinal AlAs(001) during molecular-beam epitaxy,” *Appl. Phys. Lett.*, vol. 62, no. 14, pp. 1658–1660, Apr. 1993, doi: 10.1063/1.108618.
[202] Chen, S. Shehata, C. Fradin, R. LaPierre, C. Couteau, and G. Weihs, “Self-Directed Growth of AlGaAs Core−Shell Nanowires for Visible Light Applications,” *Nano Lett.*, vol. 7, no. 9, pp. 2584–2589, Sep. 2007, doi: 10.1021/nl070874k.
[203] R. Alcotte *et al.*, “Low temperature growth and physical properties of InAs thin films grown on Si, GaAs and In0.53Ga0.47As template,” *Thin Solid Films*, vol. 645, pp. 119–123, Jan. 2018, doi: 10.1016/j.tsf.2017.10.006.
[204] K. Murawski *et al.*, “Bandgap energy determination of InAsSb epilayers grown by molecular beam epitaxy on GaAs substrates,” *Prog. Nat. Sci. Mater. Int.*, vol. 29, no. 4, pp. 472–476, Aug. 2019, doi: 10.1016/j.pnsc.2019.08.005.
[205] Y. Liu, Y. Huang, and X. Duan, “Van der Waals integration before and beyond two-dimensional materials,” *Nature*, vol. 567, no. 7748, pp. 323–333, Mar. 2019, doi: 10.1038/s41586-019-1013-x.
[206] D. Jariwala, T. J. Marks, and M. C. Hersam, “Mixed-dimensional van der Waals heterostructures,” *Nat. Mater.*, vol. 16, no. 2, pp. 170–181, Feb. 2017, doi: 10.1038/nmat4703.
[207] S. Padgaonkar, J. N. Olding, L. J. Lauhon, M. C. Hersam, and E. A. Weiss, “Emergent Optoelectronic Properties of Mixed-Dimensional Heterojunctions,” *Acc. Chem. Res.*, vol. 53, no. 4, pp. 763–772, Apr. 2020, doi: 10.1021/acs.accounts.9b00581.
[208] A. Boulesbaa *et al.*, “Ultrafast Charge Transfer and Hybrid Exciton Formation in 2D/0D Heterostructures,” *J. Am. Chem. Soc.*, vol. 138, no. 44, pp. 14713–14719, Nov. 2016, doi: 10.1021/jacs.6b08883.
[209] Y. Sun *et al.*, “MoS $_2$ -Based Mixed-Dimensional van der Waals Heterostructures: A New Platform for Excellent and Controllable Microwave-Absorption

Performance," *ACS Appl. Mater. Interfaces*, vol. 9, no. 39, pp. 34243–34255, Oct. 2017, doi: 10.1021/acsami.7b10114.
[210] Y. Tsuboi *et al.*, "Enhanced photovoltaic performances of graphene/Si solar cells by insertion of a MoS2 thin film," *Nanoscale*, vol. 7, no. 34, pp. 14476–14482, Aug. 2015, doi: 10.1039/C5NR03046C.
[211] Y. Ye *et al.*, "Multicolor graphene nanoribbon/semiconductor nanowire heterojunction light-emitting diodes," *J. Mater. Chem.*, vol. 21, no. 32, p. 11760, 2011, doi: 10.1039/c1jm11441g.
[212] D.-H. Kwak, P. Ramasamy, Y.-S. Lee, M.-H. Jeong, and J.-S. Lee, "High-Performance Hybrid InP QDs/Black Phosphorus Photodetector," *ACS Appl. Mater. Interfaces*, vol. 11, no. 32, pp. 29041–29046, Aug. 2019, doi: 10.1021/acsami.9b07910.
[213] Y. Liang, S. Huang, R. Soklaski, and L. Yang, "Quasiparticle band-edge energy and band offsets of monolayer of molybdenum and tungsten chalcogenides," *Appl. Phys. Lett.*, vol. 103, no. 4, p. 042106, Jul. 2013, doi: 10.1063/1.4816517.
[214] A. W. Bett, F. Dimroth, G. Stollwerck, and O. V. Sulima, "III-V compounds for solar cell applications," *Appl. Phys. A*, vol. 69, no. 2, pp. 119–129, Aug. 1999, doi: 10.1007/s003390050983.
[215] S. Zhang, J. Liu, M. M. Kirchner, H. Wang, Y. Ren, and W. Lei, "Two-dimensional heterostructures and their device applications: progress, challenges and opportunities—review," *J. Phys. Appl. Phys.*, vol. 54, no. 43, p. 433001, Aug. 2021, doi: 10.1088/1361-6463/ac16a4.
[216] T. H. Choudhury, X. Zhang, Z. Y. Al Balushi, M. Chubarov, and J. M. Redwing, "Epitaxial Growth of Two-Dimensional Layered Transition Metal Dichalcogenides," *Annu. Rev. Mater. Res.*, vol. 50, no. 1, pp. 155–177, Jul. 2020, doi: 10.1146/annurev-matsci-090519-113456.
[217] V. O. Özçelik, J. G. Azadani, C. Yang, S. J. Koester, and T. Low, "Band alignment of two-dimensional semiconductors for designing heterostructures with momentum space matching," *Phys. Rev. B*, vol. 94, no. 3, p. 035125, Jul. 2016, doi: 10.1103/PhysRevB.94.035125.
[218] Z. Santos and P. P. Dholabhai, "Thermodynamic stability of defects in hybrid MoS2/InAs heterostructures," *Comput. Mater. Sci.*, vol. 194, p. 110426, Jun. 2021, doi: 10.1016/j.commatsci.2021.110426.
[219] H. Yoshida *et al.*, "Analysis of twin defects in GaAs nanowires and tetrahedra and their correlation to GaAs(111)B surface reconstructions in selective-area metal organic vapour-phase epitaxy," *J. Cryst. Growth*, vol. 312, no. 1, pp. 52–57, Dec. 2009, doi: 10.1016/j.jcrysgro.2009.10.006.
[220] K. Tomioka, T. Tanaka, S. Hara, K. Hiruma, and T. Fukui, "III–V Nanowires on Si Substrate: Selective-Area Growth and Device Applications," *IEEE J. Sel. Top. Quantum Electron.*, vol. 17, no. 4, pp. 1112–1129, Jul. 2011, doi: 10.1109/JSTQE.2010.2068280.